

THÈSE

Pour obtenir le grade de

DOCTEUR DE LA COMMUNAUTE UNIVERSITE GRENOBLE ALPES

Spécialité : Matériaux, Mécanique, Génie civil, Electrochimie

Arrêté ministériel : 25 mai 2016

Présentée par

Dorjan DAUTI

Thèse dirigée par **Stefano DAL PONT**, Professeur, UGA

Codirigée par **Benedikt WEBER**, Ingénieur de Recherche, Empa

Encadrée par **Matthieu BRIFFAUT**, Maître de Conférences, UGA

préparée au sein du **Laboratoire Sols, Solides, Structures-Risques**
dans l'**École Doctorale I-MEP2 - Ingénierie - Matériaux, Mécanique,**
Environnement, Energétique, Procédés, Production

A combined experimental and numerical approach to spalling of high-performance concrete due to fire

Thèse soutenue publiquement le **26 Septembre 2018**
devant le jury composé de :

M. Christian LA BORDERIE

Professeur, Université de Pau et des Pays de l'Adour, Rapporteur et Président du jury

M. Roberto FELICETTI

Professeur, Politecnico di Milano, Rapporteur

M. Alain MILLARD

Ingénieur de Recherche, CEA Saclay, Examineur

M. Stefano DAL PONT

Professeur, Université Grenoble Alpes, Directeur de thèse

M. Benedikt WEBER

Ingénieur de Recherche, Empa, Co-directeur de thèse

M. Matthieu BRIFFAUT

Maître de conférences, Université Grenoble Alpes, Encadrant de thèse

M. Pierre PIMIENTA

Chef de Division adjoint, CSTB, Invité



Acknowledgements

The research presented in this doctoral thesis has been mainly financed by Tec21 Laboratory of Excellence, which is greatly acknowledged.

I would like to express my deep gratitude to my three supervisors who have guided me throughout these years and from whom I have learnt a lot. First, Stefano Dal Pont, for his persistence and determination, which "pushed" me through any obstacle of this doctoral work. I'm lucky and grateful for the endless time he dedicated to me, it has been a big help! Second, Benedikt Weber, for his sharp and detailed feedback on everything, not only during the time I spent at Empa, but also during the supervision "in-distance", which is not always easy, but he succeeded it in his unique way. And third, Matthieu Briffaut, for his energy and motivation. His advice has helped me in clearing many doubts in the scientific context but also in the personal one.

Besides my supervisors, I would like to thank the rest of my thesis committee: Mr. Christian La Borderie, Mr. Roberto Felicetti, Mr. Alain Millard and Mr. Pierre Pimienta. It was an honour to have them as jury members and a pleasure to discuss the various aspects of my PhD thesis.

I would like to highlight some other contributors to this PhD project: the "Cast3M expert" Giuseppe Sciumé for his input in numerical modeling, the "neutron expert" Alessandro Tengtattini for his precious help in performing and analysing the neutron tomography experiments, the Concrete/Construction Chemistry Laboratory at Empa for sharing their experimental expertise and Liliana Gramegna for the work performed during her master thesis. Thank you!

During this PhD project, which lasted 3 years, I have spent most of the time in Laboratory 3SR, in Grenoble. I want to thank Cino Viggiani for being the very first reason I got to know this lab where I met people (friends, staff, football team ...) that cherished my daily life. The particularly friendly environment of 3SR made the "bumpy road" of a PhD journey easier. A special mention for my special fellows, with whom we planted our PhD seeds together and who have been an inexhaustible source of motivation. I would also like to thank Empa Structural Engineering Laboratory, where I spent one-third of my PhD time. Since my first visit at Empa during my master project, I always received a warm welcome from this lab and the people working there.

This thesis, as everything else I achieved in my life, wouldn't have been the same without the warm support of my family (my dad, my mum, my brother), to whom I dedicate this work. I also want to express a heartfelt gratitude to my French family who have always been by my side.

Among all the satisfactions that this PhD life had reserved for me, the biggest gift was, undoubtedly, meeting Jeanne, whose love and support, made and continue making me stronger day after day.

Abstract

Concrete has been extensively used in the construction industry as a building material. A major drawback of this material is its instability at high temperature, expressed in the form of violent or non-violent detachment of layers or pieces of concrete from the surface of a structural element. This phenomenon, known as fire spalling, can lead to the failure of concrete structures such as tunnels, high rise buildings, nuclear power-plants, underground parkings etc. because the reinforcement steel is directly exposed to high temperature and the designed cross section of the concrete elements (*e.g.*, columns, beams, slabs) is reduced. A lot of research has been dedicated on developing preventing methods for spalling and also on determining the parameters that have an influence on it. However, the physics behind this phenomenon is not yet fully understood. The objective of this thesis is to contribute to the understanding of spalling mechanisms through a combined experimental and numerical approach, *i.e.*, neutron tomography coupled with advanced numerical modeling in an adequate scale.

In this doctoral work, the first 3D measurements of moisture content in heated concrete, which is believed to be one of the processes directly related to spalling, have been performed using in-situ neutron tomography. In order to follow the fast dehydration process of concrete, one 3D scan (containing 500 radiographs) per minute was captured thanks to the world leading flux at the Institute Laue Langevin (ILL) in Grenoble France. This acquisition speed, which is ten times faster than any other experiment reported in the literature, was sufficient to follow the dehydration process. A dedicated setup, adapted to neutron imaging and high temperature, has been developed for performing such kind of experiments. Concrete samples with different aggregate size have been tested. Quantitative analysis showing the effect of the aggregate size on the moisture distribution is presented. Results on the moisture accumulation behind the drying front, known as the moisture-clog, are also presented and discussed.

In parallel, a numerically-efficient coupled thermo-hydro-mechanical (THM) model has been implemented in the finite element software Cast3M for understanding and predicting the complex behaviour of concrete at high temperature in the context of spalling. The newly implemented code is remarkably faster (20-30 times) than an existing one, on which it is based. A mesoscopic approach has been adapted to the model for taking into account the heterogeneity of concrete. First the model is applied to experiments from literature monitoring standard parameters such as temperature, gas pressure and mass loss. Then, 1D moisture profiles obtained from neutron radiography experiments are used for verifying and improving the model in terms of some critical constitutive laws such as dehydration and water retention curves. Finally, the model is employed for predicting the 3D moisture distribution measured in this doctoral work via neutron tomography. Among others, mesoscopic THM simulations are performed for investigating the influence of an aggregate on the drying front.

Résumé en Français

Le béton est un matériau très utilisé dans l'industrie de construction. Une limite essentielle à l'utilisation de ce matériau est sa dégradation par écaillage lorsqu'il est exposé au feu. Le phénomène d'écaillage consiste au détachement sous forme d'écailles de la surface du béton exposée au feu, réduisant ainsi progressivement la section résistante. De plus, ce phénomène expose les armatures et peut conduire à une rupture prématurée de structures telles que les tunnels, les gratte-ciels, les centrales nucléaires etc. De nombreuses recherches ont été consacrées à la mise au point de méthodes de prévention de l'écaillage et à la détermination des paramètres qui ont une influence sur ce phénomène. Cependant, la physique qui contrôle l'écaillage n'est pas encore entièrement comprise. L'objectif principal de la thèse est de fournir une meilleure compréhension des mécanismes impliqués dans l'écaillage du béton en utilisant une approche numérique-expérimentale, *i.e.*, la tomographie neutronique couplée à la modélisation numérique avancée à une échelle adéquate.

Dans ce travail, les premières mesures 3D de la teneur en eau du béton (grandeur locale indispensable au suivi du processus de déshydratation potentiellement responsable de l'écaillage) soumis à un chargement thermique sévère ont été réalisées à l'aide de tomographies neutroniques rapides. Le suivi de la déshydratation rapide du béton a été possible en réalisant un scan 3D toutes les minutes grâce à la source neutrons de l'Institut Laue Langevin (leader mondial), à Grenoble, France. Cette vitesse d'acquisition est dix fois plus rapide que toute autre étude tomographique rapportée dans la littérature. Un dispositif, adapté à l'imagerie neutronique et aux essais à haute température, a été développé pour réaliser de telles expériences. L'influence de la taille des agrégats sur la distribution de l'humidité au sein de l'échantillon est présentée. Les résultats quantitatifs sur l'accumulation d'humidité derrière le front de déshydratation, connue sous le nom de 'moisture-clog' et considérée comme un des facteurs principaux engendrant un excès de pression, sont également présentés et discutés.

En parallèle, un modèle thermo-hydro-mécanique (THM) entièrement couplé a été mis en œuvre sur le logiciel élément fini Cast3M afin d'étudier et prédire le comportement du béton à haute température. Le code nouvellement implémenté est remarquablement plus rapide (20-30 fois) que le code existant sur lequel il est basé. Une approche mésoscopique a été adaptée au modèle pour prendre en compte l'hétérogénéité du béton. D'abord, le modèle est appliqué à des expériences de la littérature, qui étudient les paramètres standards tels que la température, la pression du gaz et la perte de masse. Ensuite, des profils d'humidité 1D obtenus à partir d'expériences de radiographie neutronique sont utilisés pour vérifier et améliorer le modèle en termes de lois de comportement critiques telles que les courbes de déshydratation et les isothermes de sorption. Enfin, le modèle est utilisé pour prédire la distribution d'humidité 3D mesurée dans ce travail de doctorat par tomographie neutronique. Entre autres, des simulations THM mésoscopiques sont effectuées pour étudier l'influence d'un agrégat sur le front de séchage.

Contents

Acknowledgements	iii
Abstract	iv
Nomenclature	x
1 Introduction	1
1.1 Concrete Spalling	1
1.2 Main physical phenomena when concrete is exposed to fire	4
1.3 Numerical models for concrete at high temperature with respect to spalling . . .	7
1.3.1 Engineering models	7
1.3.2 Advanced numerical modeling	9
1.3.2.1 Homogenized continuum models	9
1.3.2.2 Mesoscopic scale models	11
1.4 Experiments in heated concrete with respect to spalling	12
1.4.1 Full-scale tests	12
1.4.2 Medium-scale tests	12
1.4.3 Small-scale tests	13
1.4.4 Ambiguity of pore pressure measurements	17
1.5 Motivation and structure of the thesis	18
1.5.1 Limitations of the current experimental and numerical approaches with respect to spalling	18
1.5.2 Objective of this thesis and proposed methodology	19
1.5.3 Layout of the thesis	19
2 Numerical model for concrete behavior at high temperature	22
2.1 Conservation Equations	22
2.1.1 Mass Conservation	22
2.1.2 Energy Conservation	24
2.1.3 Momentum Conservation	25
2.1.4 Final form of model equations	25
2.2 Constitutive Equations	25
2.2.1 Density and pressure relationships	26
2.2.2 Mass transfer properties	27
2.2.2.1 Permeability	27
2.2.2.2 Diffusivity	27
2.2.3 Thermal properties	28
2.2.3.1 Thermal Conductivity	28
2.2.3.2 Thermal capacity	28
2.2.3.3 Enthalpy of evaporation	28
2.2.4 Fluid viscosities	28
2.2.5 Porosity	29
2.2.6 Dehydration	29

2.2.7	Retention curves: $S_l - p_c$ relationship	29
2.2.8	Effective stress principle	31
2.2.9	Strain decomposition	31
2.2.10	Damage constitutive law	32
2.3	Model Parameters	33
2.4	Finite element formulation	33
2.4.1	Spatial discretization	33
2.4.2	Temporal discretization	35
2.4.3	Initial and Boundary conditions	35
2.5	Implementation	36
2.5.1	A new monolithic procedure for THM problems	36
2.5.2	Cast3M Implementation	38
2.5.3	COMSOL Implementation	39
2.6	Extension of the model to the mesoscale	40
2.6.1	Mesoscale modeling of concrete	40
2.6.2	Mesh Generation	41
3	Application to experiments from literature	43
3.1	Simulation of temperature and gas pressure measurements	43
3.1.1	Experiments by Kalifa et al. (2000)	44
3.1.2	Numerical Analysis	44
3.1.3	Results and Discussion	45
3.1.3.1	Comparison: Monolithic vs. Staggered approach	46
3.1.3.2	Comparison: Cast3M vs. COMSOL Multiphysics	47
3.1.4	Conclusions: Application 1	48
3.2	Simulation of PTM tests by Mindeguia (2009) in the framework of RILEM TC256	49
3.2.1	Experiments by Mindeguia (2009)	49
3.2.2	Numerical Analysis	50
3.2.3	Results and discussion	51
3.2.3.1	Temperature evolution	51
3.2.3.2	Gas pressure evolution	52
3.2.3.3	Mass loss evolution	53
3.2.4	Discussion on Intrinsic Permeability	54
3.2.5	Mechanics	55
3.2.6	Conclusions: Application 2	55
3.3	Simulation of moisture migration measured by neutron radiography	57
3.3.1	Experimental data from neutron radiography	57
3.3.2	Numerical Analysis	60
3.3.2.1	Temperature results	61
3.3.2.2	Water loss profiles based on Harmathy dehydration evolution	62
3.3.3	Influence of dehydration of concrete on water loss profiles	63
3.3.3.1	Dehydration of concrete	63
3.3.3.2	Adjusted dehydration law	64
3.3.4	Influence of retention curves on water loss profiles	65
3.3.4.1	Water retention curves	65
3.3.4.2	Adjusted water retention curves	67
3.3.5	Role of permeability on water loss profiles	68
3.3.6	Conclusions: Application 3	69
3.4	Mesoscale Modeling	70
3.4.1	Numerical Analysis	70
3.4.2	Results	70

3.5	Chapter Conclusions	72
4	In-situ neutron tomography of heated concrete	73
4.1	Neutron imaging	73
4.1.1	X-ray vs. neutron radiography	73
4.1.2	Basic components of a neutron imaging facility	75
4.1.3	Mathematics of neutron imaging	77
4.1.3.1	Neutron radiography	77
4.1.3.2	Neutron tomography	78
4.2	Material and methods	80
4.2.1	Sample preparation	80
4.2.2	Heating Cell	82
4.2.3	Neutron tomography setup and image reconstruction	83
4.3	Results and discussion	86
4.3.1	Temperature measurements	86
4.3.2	Global dehydration speed: HPC 8 mm vs HPC 4 mm	87
4.3.2.1	Segmentation of aggregates and cement paste	88
4.3.2.2	Computing the volume of the dried cement paste	91
4.3.3	Evolution of moisture content	94
4.3.4	Discussion on the moisture accumulation	97
4.3.5	Thermocouple-induced cavities	100
4.3.6	Influence of a crack on the drying front	101
4.3.7	Additional drying at the boundary	102
4.3.7.1	Heat and moisture insulation	102
4.3.7.2	Radiography vs. Tomography	102
4.4	Chapter Conclusions	103
5	Simulation of moisture content: from continuum towards a 3D mesoscopic approach	105
5.1	Introduction	105
5.2	Front speed, moisture accumulation and boundary effects	105
5.2.1	Numerical Analysis	105
5.2.2	Case 1: Moisture escape from the lateral boundaries	108
5.2.2.1	Temperature and gas pressure results	108
5.2.2.2	Moisture profiles	109
5.2.2.3	Boundary effect	111
5.2.3	Case 2: Perfect moisture insulation	112
5.2.3.1	Temperature and gas pressure results	112
5.2.3.2	Moisture profiles	112
5.3	Simulations in 3D of moisture distribution	114
5.3.1	Homogeneous HPC 4 mm	114
5.3.2	Simplified mesoscopic approach	116
5.3.2.1	TH simulations	116
5.3.2.2	THM simulations with damage-permeability coupling	120
5.4	Chapter Conclusions	122
6	Conclusions and Perspectives	123
6.1	Summary of this doctoral work	123
6.1.1	Numerical model for concrete at high temperature	123
6.1.2	Neutron tomography experiments on heated concrete	124
6.2	Main Findings	125
6.3	Perspectives	127

Appendix A Operators C and K	128
Bibliography	130

Nomenclature

v	velocity [m/s]
\dot{m}	rate of mass change [$\text{kg m}^{-3}\text{s}^{-1}$]
C_{ij}	Capacity matrix
g	acceleration of gravity [m^2/s]
I	second order unit tensor [-]
K_{ij}	Conductivity matrix
t	stress tensor [Pa]
u	displacement [m]
Y	approximated solution in terms of state variables
C	heat capacity [$\text{Jkg}^{-1}\text{K}^{-1}$]
D	diffusion coefficient [m^2/s]
d	total damage [-]
d_t, d_c	tension/compression damage [-]
D_{v0}	ambient diffusion [m^2/s]
E	parameter for sorption isotherms linked with surface tension[-]
f_c	cement mass[-]
f_m	dehydration parameter for concrete's age[-]
f_s	stoichiometric factor for dehydration [-]
H	enthalpy [J/kg]
h_g	mass transfer coefficient [m/s]
h_T	heat transfer coefficient [$\text{Wm}^{-2}\text{K}^{-1}$]
I	Intensity of the neutron beam [$\text{ns}^{-1}\text{m}^{-2}$]
i	distance of the object from the imaging plane [m]
j	mass flux [$\text{kg m}^{-2}\text{s}^{-1}$]
K	permeability [m^2]
K_0	intrinsic permeability [m^2]
K_T	bulk modulus of the porous medium [Pa]
$k_{r\pi}$	relative permeability [-]
L	collimator tube length [m]
l_c	internal length [m]
M	molar mass [kg/kmol]
m	mass [kg]
p	pressure [Pa]
R	universal gas constant [$8314.41 \text{ JK}^{-1}\text{kmol}^{-1}$]
RH	relative humidity [-]
S	saturation [-]
T	temperature [K]
t	time [s]
N	shape function
α	Biot's constant [-]
β	thermal dilation coefficient [$1/\text{K}$]

ϵ	emissivity of the interface [-]
γ	surface tension [Pa]
κ	threshold of damage [-]
λ	thermal conductivity [$\text{Wm}^{-1}\text{K}^{-1}$]
λ_d	thermal conductivity of dry material [$\text{Wm}^{-1}\text{K}^{-1}$]
μ	dynamic viscosity [$\text{Pa}\cdot\text{s}$]
Ω	whole geometrical domain
ϕ	porosity [-]
ρ	density [kg/m^3]
Σ	boundaries of the geometrical domain
σ	Stefan-Boltzmann constant [$5.670 \times 10^{-8} \text{ Wm}^{-2}\text{K}^{-4}$]
σ	total stress tensor [Pa]
σ'	effective stress tensor [Pa]
Σ_i	Effective cross-section attenuation of the material i [cm^{-1}]
ϵ	strain [-]

Subscripts

0	reference state/initial state
∞	ambient
<i>ag</i>	aggregate
<i>atm</i>	atmospheric
<i>a</i>	air
<i>crit</i>	critical
<i>c</i>	capillary
<i>dehyd</i>	dehydration
<i>eq</i>	equivalent
<i>g</i>	gas
<i>i</i>	initial
<i>l</i>	liquid water
<i>sh</i>	shrinkage
<i>s</i>	solid
<i>th</i>	thermal
<i>vap</i>	evaporation
<i>vs</i>	saturation vapor
<i>v</i>	vapor water
π	liquid water, vapour water, dry air

Chapter 1

Introduction

1.1 Concrete Spalling

Concrete is the most used building material in the construction industry and there is no doubt that it will remain in use as a construction material well into the future (Gagg, 2014). However, a major limitation of the widespread use of concrete is that it is prone to spalling when exposed to fire. This phenomenon may apply to commonly used concrete (Ordinary Concrete) as well as to more recently developed types of concrete (High Performance Concrete, Self Compacting Concrete etc.) which are characterized by a higher mechanical and durability performance.

Spalling can be defined as the violent or non-violent detachment of layers or pieces of concrete from the surface of a structural element, during or after it is exposed to high and rapidly rising temperatures as experienced in fires (Khoury et al., 2007). This phenomenon can lead to the premature failure of concrete structures due to:

- *Reinforcement exposure*: The depth of spalling usually coincides with the concrete cover. The detachment of the concrete cover in the form of spalling exposes the reinforcement to a thermal load which can lead to reduction of the yield strength of steel.
- *Cross-section reduction*: The dimensions of the concrete members are optimized for a certain fire resistance designed with the assumption that the cross-section remains unchanged.

Several catastrophic tunnel fires (Channel tunnel fire in 1996, Mont-Blanc tunnel fire in 1999, St. Gotthard tunnel in 2002 etc.), which have caused a huge economical damage and even loss of life, have emphasized the vulnerability of concrete in case of fire induced spalling.



(a)



(b)

Figure 1.1: Examples of concrete spalling: (a) Channel Tunnel Fire, 1996 (www.tunneltalk.com) (b) concrete slab after a fire test (www.cstb.fr)

For decades, research has concentrated on fire testing and determining the influence of various parameters promoting spalling. The main parameters are: moisture content (Harmathy, 1965), heating rate (Hertz, 1992; Anderberg, 1997), external loading (Boström et al., 2007; Carré

et al., 2013), mineralogical character of aggregates (Ingberg et al., 1921), geometry (Guerrieri and Fragomeni, 2013; Werner and Rogge, 2015), concrete age (Jansson and Boström, 2013), element size, and cement type (Iravani and Anders, 2017).

Among the different measures employed against spalling like the use of super absorbent polymers and polypropylene fibers (Lura and Terrasi, 2014), recycled tire polymer fibers (Figueiredo et al., 2017), steel fibers (Chen and Liu, 2004), basalt fibers, coatings (Lu and Fontana, 2017) or air entraining agent (D'Aloia et al., 2013), the most popular one is the use of polypropylene fibers (Long, 1983; Kalifa et al., 2001; Zeiml et al., 2006; Liu et al., 2008; Jansson, 2013). Usually used in a recommended dosage of 2 kg/m^3 in the concrete mix, polypropylene fibers start melting around 160°C , which is lower than the temperature when spalling is usually encountered. The melting of fibers contributes to creating open paths for vapor release. On the other hand, their use comes with an economical cost and decreases the workability of concrete.

Despite the extensive research on determining the different factors influencing spalling and measures against it, the mechanisms behind this phenomenon are not yet fully understood. Several spalling theories have emerged but explanations are mostly qualitative and no general consensus on a single theory has been reached. A complete list and a historical overview are provided by Jansson (2013). The two principal mechanisms more broadly accepted are:

- (i) the differential thermal gradients (Saito, 1966; Bažant, 1997)
- (ii) the pore pressure build-up, also known as moisture clog theory (Harmathy, 1965)

The first mechanism is related to the thermo-mechanical processes. The exposure of a face of a concrete member to high temperature gives rise to a considerable temperature gradient which provokes significant thermal dilation. The major effect of the thermal dilation is the significant compressive stress ensuing in the cover. The restraint of this dilation, induces thermal stresses in deeper layers of the material. Fractures induced by the thermo-mechanical processes can contribute to spalling. The sudden unstable release of the potential energy of thermal stresses stored in the structure can cause the brittle fracture. According to this theory, the fact that the high performance concrete is far more brittle than normal strength concrete, makes the former more prone to spalling. In (Bažant, 1997) it was also noted that high pore pressure can only be assumed as a "trigger" to a crack but can not drive the explosion (see Figure 1.2(a)).

The pore pressure build-up theory is related to the evolution of water content in concrete. This theory is schematically represented in Figure 1.2(b). When the concrete face is heated, the free water evaporates and the chemically bound water is released in the form of vapor, forming a dry zone and rising the pressure in the pores. Due to pressure gradients, part of this vapor is evacuated to the heated face and part of it is driven toward the cold face where it condenses once the thermodynamic conditions are satisfied. This process continues until a quasi-saturated zone is formed, known as the moisture clog, which acts as an impermeable layer that restricts the vapor to "travel" further towards the colder region giving rise to high pressure build-up. In addition, the thermal dilation of water in saturated pores also induces pressure build-up. The later is believed to contribute in "triggering" spalling. Permeability of concrete and initial moisture content play a major role in the pore pressure spalling of concrete.

Explosive spalling generally occurs under the combined action of pore pressures and thermal stresses in the fire exposed zone. When the sum of the stresses exceeds the tensile strength of the material, cracks develop parallel to the surface often leading to a violent failure of the fire exposed region. Khoury presented a general sketch (see Figure 1.3) of combined thermal stress and pore-pressure induced explosive spalling (Khoury et al., 2007).

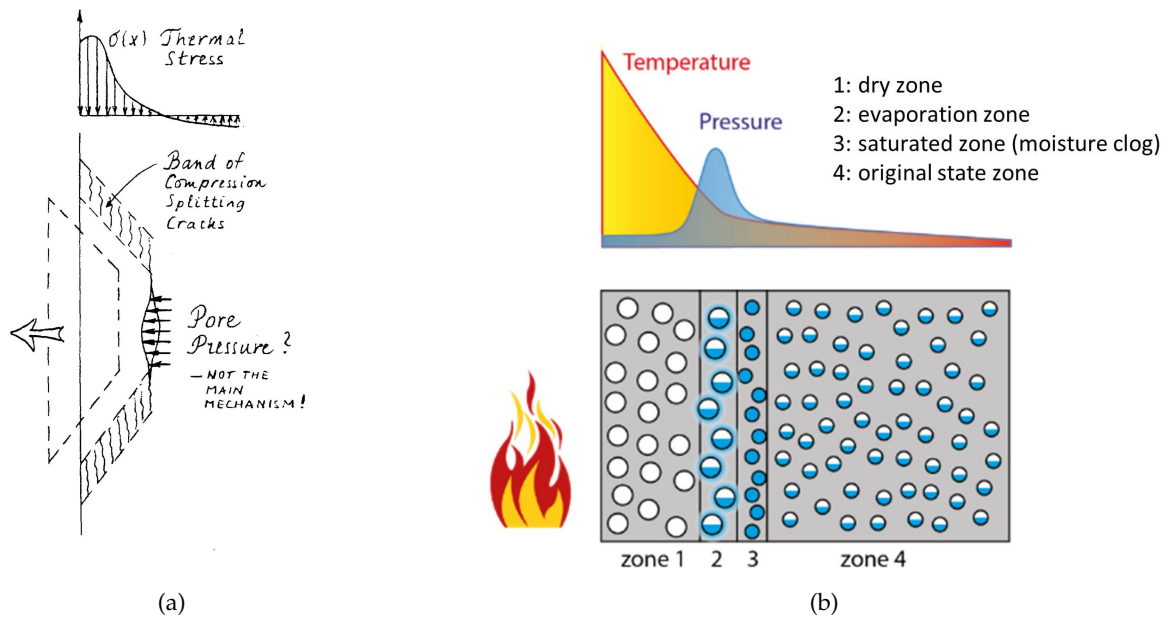


Figure 1.2: Spalling mechanisms: (a) Thermal stresses theory (Bažant, 1997) (b) Moisture clog theory

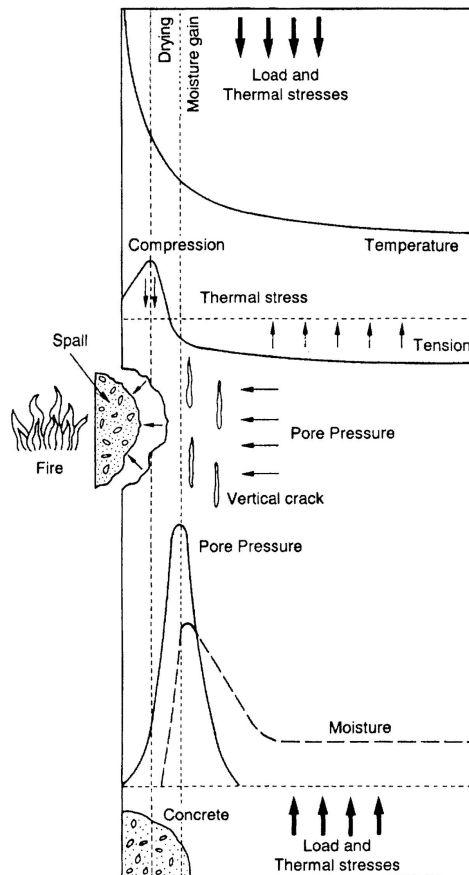


Figure 1.3: Combined thermal stresses and pore pressure spalling (Khoury et al., 2007)

Different methods are employed for spalling assessment. Although the large-scale tests are the most reliable, they are very costly. On the other hand, due to the complex nature of spalling (combined thermal stresses and pore pressure, heterogeneous material, evolving pore structure etc.), theoretical models are not able to provide useful predictions. Among these methods of analysis, the numerical modeling, which considers the fully coupled thermo-hydro-mechanical behavior of concrete, complemented with experiments seems the most promising approach in providing satisfactory explanation of not only the fundamental spalling mechanisms but also of their orders of magnitude.

In Section 1.3 and 1.4, an overview of the numerical models and experiments on heated concrete with respect to spalling is presented. Before that, the main physical phenomena occurring inside concrete at high temperature are presented in the next section.

1.2 Main physical phenomena when concrete is exposed to fire

Concrete is inherently a heterogeneous material made of aggregates and cement paste. The latter is a multiphase porous material, whose voids can be filled with water, air and other fluids. The water in the cement paste exists in two forms: pore water (free water) and chemically-bound water (solid water). The former is also known as evaporable water, as it evaporates when the thermodynamic conditions are met (*i.e.*, at $T = 100^\circ\text{C}$ and atmospheric pressure) and may be present in 3 main forms (Feldman and Sereda, 1968; McDonald et al., 2010; Wyrzykowski et al., 2017):

- *capillary and inter-hydrate water*: is the water filling the capillary pores (size = 100s of nanometers) and the interhydrate pores (size = 10s of nanometers). In other words, it is the water corresponding to a saturation greater than solid saturation point $S_{ssp} < S < 1$.
- *physically adsorbed water*: also known as the gel water is the water retained by the surface of the solid matrix due to Van der Waals forces. As shown in the Figure 1.4, this water is confined in the gel pores (size = a few nanometers)
- *interlayer water*: is the water which is confined in about 1 nanometer space between the C-S-H layers

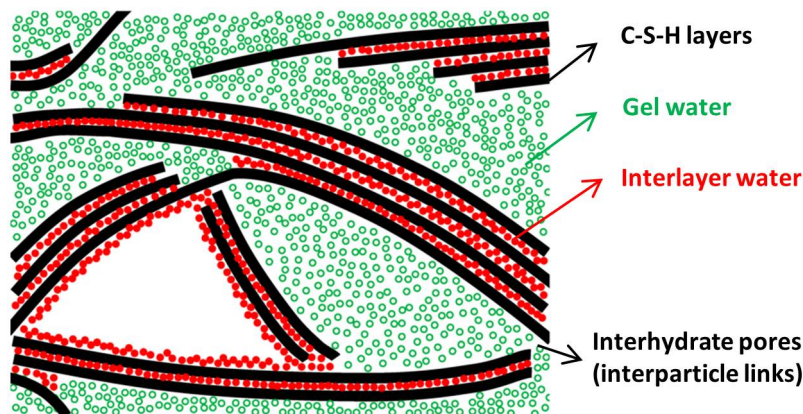


Figure 1.4: Schematic representation of C-S-H microstructure according to Wyrzykowski et al. (2017)

Voids greater than 10 μm , created from unintentional entrapment of air during mixing, often exist in concrete and can be filled with water (Neville, 2012). It is important to note that the

range of pore sizes, mentioned above, is a continuous one and the stated dimensional boundaries between capillary, interhydrate and gel pores are simply approximations to inherently blurred boundaries.

The chemically bound water (non-evaporable) is the water which is combined with anhydrous cement phase during hydration and potentially released from the solid skeleton due to phase changes occurring at certain temperatures. Thermogravimetric Analysis (TGA), Differential Scanning Calorimetry (DSC) and Differential Thermal Analysis (DTA) are usually adopted for investigating the thermal reactions such as: dehydration, dehydroxylation, decarbonation, oxidation, decomposition, phase transition or melting, occurring in cementitious materials heated up to 1000°C (Harmathy, 1970; Diederichs et al., 1989; Scrivener et al., 2015). In Figure 1.5 the TGA of a hydrating portland cement containing 4 wt.% of limestone is presented. Up to 300°C, the water is removed from hydrated products which include C-S-H phases. Between 400-500°, the dehydration of the calcium hydroxide (portlandite) takes place in a reaction known as dehydroxylation. Quartz, which is present in some aggregates and sands is transformed at 570°C (Diederichs et al., 1989). Above 600°C, decomposition of the limestone (CaCO_3) occurs on a process known as decarbonation.

It is important to note that thermal analysis such as TGA, DTA, DSC are often not representative of the thermal behavior of a representative concrete elementary volume. Heating rate, thermodynamic conditions, specimen size etc. might influence the reaction temperature of the hydrated products (Scrivener et al., 2015). A more detailed discussion on this topic will be provided in Section 3.3.3.1.

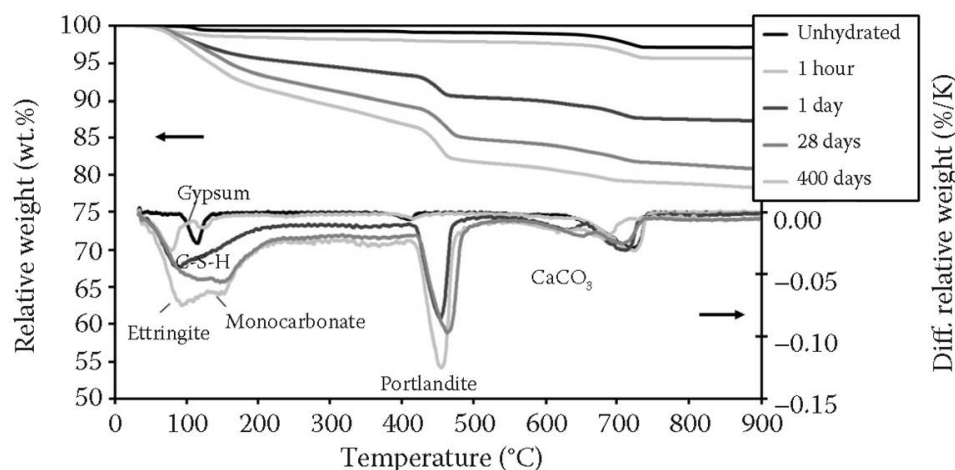


Figure 1.5: Identification of the main reactions in hydrating portland cement as shown by TGA (Scrivener et al., 2015)

Many non-linear thermo-hydro-mechanical phenomena and interactions are involved in concrete behavior when exposed to fire. A short summary of thermal, hydal and mechanical mechanisms is given in the following.

Thermal

There is heat provided by the convection from the surrounding hot air and due to radiation from the flames. This heat is transferred through the concrete material by conduction but also due to the movement of the fluid phases (advection). At the fire exposed surface, the capillary free water starts to evaporate and at sufficiently high temperatures the chemically bound water starts to be released. Both these phase changes consume energy and together with the relatively

low conductivity of concrete contribute to high-temperature gradients between the exposed and non-exposed face.

Hydral

In parallel, the phase changes (evaporation and dehydration) increase the vapor pressure in the pores. The pressure and moisture gradients result in mass transfer toward the exposed face as well as toward the non-exposed face. This mass transfer is strongly linked with the porosity, permeability and diffusion of concrete. While traveling toward the non-exposed face, vapor may condense back to liquid water forming a saturated zone usually referred as the moisture clog. An additional increase of the liquid water volume in the pores is due to the liquid thermal dilation, which is particularly important above 160°C (Gawin et al., 2002a). These cause a significant decrease of the gas permeability, because the space available for the gas is decreased.

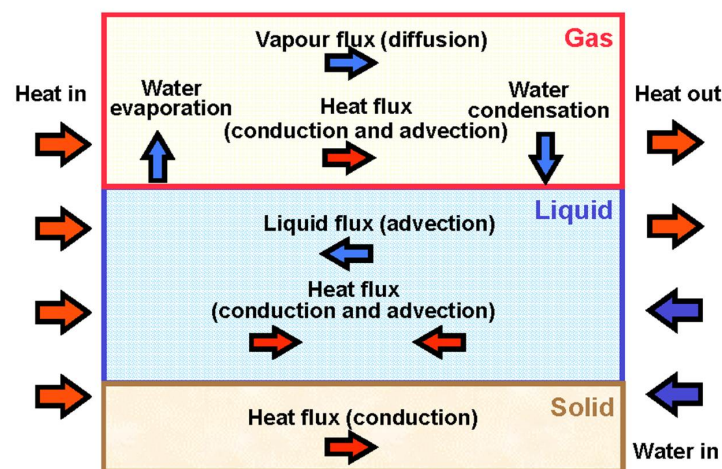


Figure 1.6: Schematic representation of thermal (arrows in red) and hydral phenomena (arrows in blue) occurring in heated porous medium (Gens and Olivella, 2001)

Mechanical

In addition to thermo-hydral phenomena, shown schematically in Figure 1.6, mechanical ones are also present. At high temperature, concrete dilation is observed. This dilation is due to:

- *normal thermal dilation of the solid skeleton*, which often depends on the type of the aggregate used in the concrete mix
- *concrete dehydration*, i.e., products of thermal dissolution of concrete components have greater volume than their initial volume
- *material cracking and progressive crack opening* which is caused by the heterogeneity of concrete. The incompatibility of the thermal dilation of the aggregates and cement paste (see Figure 1.7) causes the development of micro-cracks resulting in the degradation of the concrete strength properties gradually.

The thermal dilation of the external layer of a heated element is restrained by the core material which has lower temperature. This causes a macro-stress in the external layer of the element (traction in the direction perpendicular to the surface). The cracks, developed from this macro-stress, but also from thermo-chemical origin, cause a considerable increase of permeability which has a direct influence in the hydral behavior. The decomposition of strains is discussed in more detail in Section 2.2.9.

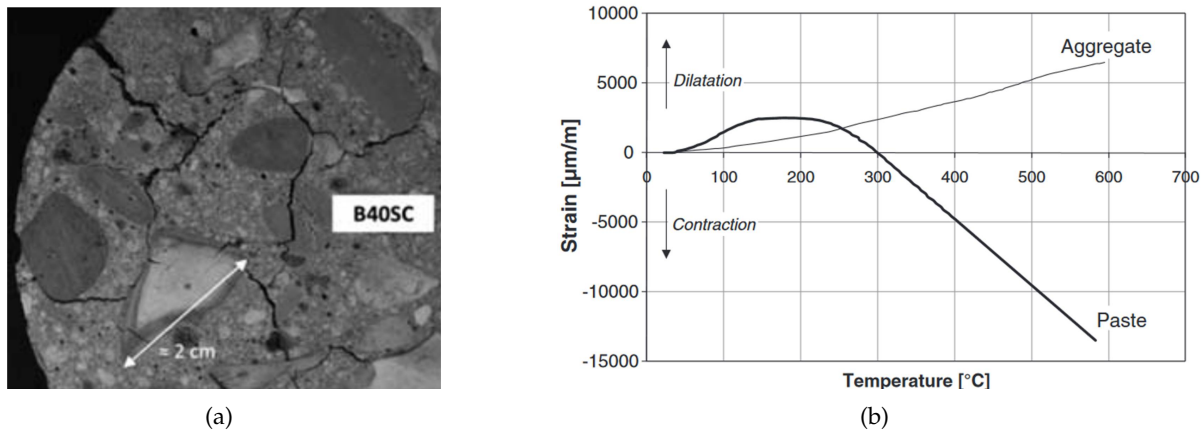


Figure 1.7: (a) Picture from (Mindeguia et al., 2013a) showing a concrete sample after being heated at 400° highlighting the cracks between aggregates and cement paste due to their different thermal behavior (Mindeguia et al., 2013b) as shown by in (b)

Given the complexity of the thermo-hydro-mechanical phenomena and their strong interaction, a combined experimental-numerical approach is indispensable for understanding the behavior of concrete at high temperature, in particular the spalling phenomenon. First, in next section a review of numerical models is presented. Then, in Section 1.4 the most well known experiments described in literature in the context of spalling are summarized.

1.3 Numerical models for concrete at high temperature with respect to spalling

1.3.1 Engineering models

Most engineering models consist on thermo-mechanical models. In these models the thermal field is determined first. Based on the distribution of the temperatures, the mechanical behavior is simulated by taking into consideration the mechanical material properties, evaluated at the calculated temperatures, and the generated strains and stresses.

Such engineering models are described on national and international design standards, such as Eurocodes. For the thermal analysis, the fire curve is chosen accordingly (see Figure 1.8). The standard temperature fire curve according to EN 1991-1-2 (which also corresponds to ISO 834 standard) represents the temperature experienced during a cellulosic fire (typical for buildings) in which the fire source comes from wood, paper, fabric etc. Another example of a more harsh fire curve is the hydrocarbon fire curve (*i.e.*, combustion of liquid fuels).

The thermal field can be obtained by solving the energy equation. The thermal material properties of concrete, obtained experimentally and modeled phenomenologically are given in Eurocode 2 in the form of empirical temperature-dependent functions. In Figure 1.9(a), the evolution of the heat capacity of concrete with siliceous aggregates at 3 different moisture contents is presented. The evaporation of water is considered implicitly in the heat capacity by the peaks (whose magnitude depends on the moisture content) starting at 100 °C. In Figure 1.9(b), the upper and lower limits of the evolution of conductivity with temperature are shown.

Alternatively, for the case of a standard fire curve, the thermal field can also be obtained from Eurocode 2 (Anex A, EN1991-1-2), where pre-calculated temperature profiles are available for typical concrete members *e.g.* slabs, beams, columns with moisture content 1.5%. The temperature graphs are conservative for moisture content greater than 1.5%.

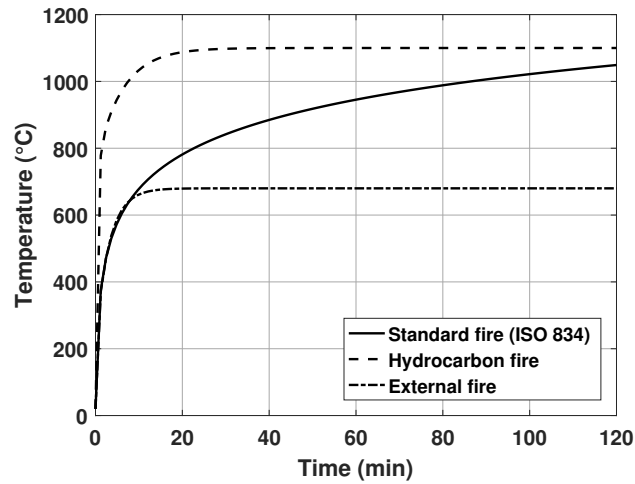
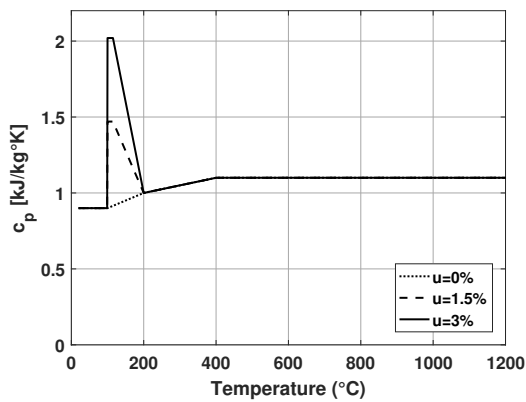


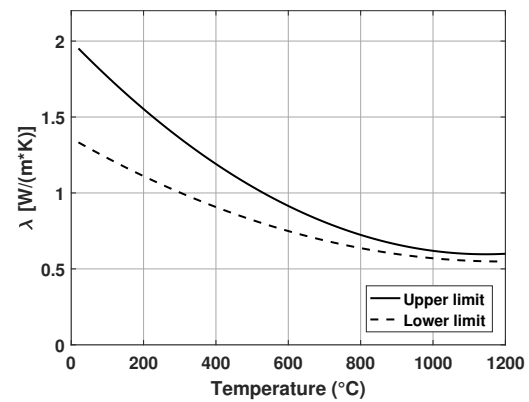
Figure 1.8: Fire curves according to design standards

For simulating the mechanical behavior, Eurocode 2 proposes three design methods:

- *Simplified calculation methods:* Once the thermal field is determined, the structural resistance of a structural components or the critical section of a substructure is determined by reducing its cross-section, in other words by disregarding the damaged concrete zones.
- *Advanced calculation methods:* A more realistic analysis of structures exposed to fire is based on fundamental physical behavior leading to a reliable approximation of the expected behavior of the relevant structural component under fire conditions. The changes of the mechanical properties (compressive strength, tensile strength, thermal elongation etc.) with temperature is taken into account. All strain components (thermal strain, creep strain, transient strain etc.) are implicitly taken into account into a mathematical stress strain model (see EN 1991-1-2 for details). Among others, a "check" on spalling, particularly on the compressive zone, is mentioned in the advanced calculation method.
- *Tabulated data or testing:* Based on experimental results, Eurocode 2 gives minimum design requirements e.g. structural components' dimensions. The method applies only for structures submitted to the standard temperature curve (see Figure 1.8).



(a)



(b)

Figure 1.9: Thermal properties necessary for thermal analysis according to EN1992-1-2 (a) Heat capacity for different moisture contents (b) Upper and lower limits of thermal conductivity

Spalling remains an open point in the design standards and recommendations on this subject are limited. In Eurocode, it is stated that explosive spalling is unlikely to occur when the moisture content is less than a certain moisture content ($k\%$). The latter is given for each country in the National Annex of the code and the recommended value is 3%. Above $k\%$, a more accurate assessment of moisture content, type of aggregate, permeability of concrete and heating rate is suggested.

While it is true that the moisture content has an important influence on spalling, it is certainly not the only factor. The spalling phenomenon is known to occur due to a combination/interaction of several thermo-hydro-mechanical mechanisms as discussed in Section 1.1. Therefore it is clear that the recommendations on spalling in standards are limited, mainly due to a lack of deep understanding. The limited recommendations show the necessity for further research in this field.

1.3.2 Advanced numerical modeling

1.3.2.1 Homogenized continuum models

The numerical models simulating heat and mass transfer in heated concrete are based on the thermodynamics of irreversible processes. The fundamental hypotheses underlying this theory is the local equilibrium assumption according to which all the local relations between the thermal, hydral, chemical and mechanical properties of a physical system are the same as for a uniform system at equilibrium. Luikov was the first to apply the theory for modeling of porous materials at normal temperature (Luikov, 1966). The model is essentially based on three partial differential equations describing the mass conservation of moisture (vapor and liquid water) and energy (Luikov, 1975).

Whitaker (1977) and Hassanizadeh and Gray (1979a; 1979b; 1980) obtained volume averaged conservation equations starting from point equations in each phase. Although their theory doesn't differ substantially from Luikov's, it offers an important justification for the continuum mechanics approach to the modelling of heat and mass transfer in order to make a rigorous connection between the microscale and the macroscale.

Partially based on Luikov's theory, Bažant and Thonguthai (1978; 1979) presented field equations for the coupled heat and moisture transfer in concrete at high temperatures. The model is based on a typical phenomenological approach where the moisture and heat transport are described by diffusive type differential equations obtained by means of irreversible thermodynamics. The coefficients of these differential equations are temperature and moisture content dependent and they are determined by inverse problem solution, *i.e.*, using known results of experimental tests to obtain the best agreement with the theoretical predictions. Such models give accurate predictions when applied to phenomena similar to those used to adjust the model parameters, but are often inaccurate when applied to situations different from the experimental tests. Some semi-empirical relationships are given for the desorption isotherms, for the dependence of permeability on temperature, for the change of porosity with dehydration etc. The model considers a single moisture flux *i.e.*, single fluid phase, which includes both liquid water and moist air. Thus, it is not possible to distinguish between the components of the gas phase *i.e.*, vapor and air or the different phases of water. Hence, there is no distinction between the vapor, liquid or air diffusion and phase changes can not be taken into account. The effect of the phase changes in the energy balance equations can only be considered through a temperature dependency of the thermal capacity. The mass flux is simplified by taking into consideration only the gradient of pressure. The model is limited to the description of the thermo-hydral behavior of concrete and there is no coupling with mechanical behavior.

Another single fluid phase model is the one presented in (England and Khoylou, 1995; Ichikawa and England, 2004) where the heat and the moisture transfer in concrete is described

by two differential equations derived from the conservation of heat and mass transfer. The heat transfer is only governed by heat conduction (neglecting heat convection) and the moisture transfer results from the combined effects of pressure induced flow (Darcy's law) and diffusion based flow (Fick's law).

The model formulated by Consolazio et al. (Consolazio et al., 1998; Chung et al., 2006) is based in the irreversible thermodynamics but in contrast to the previous models it considers the pores of the solid skeleton filled with two fluid phases: liquid water and gas phase. However, there is no distinction between the gas components (*i.e.*, vapor and air). Thus, the diffusion of water vapor, which becomes important in elevated vapor pressure gradients, is omitted.

Based on previous works of (Whitaker, 1977; Hassanizadeh and Gray, 1979a; Hassanizadeh and Gray, 1979b; Hassanizadeh and Gray, 1980), Gawin et al. (Gawin et al., 1999; Gawin et al., 2002b; Gawin et al., 2011a; Gawin et al., 2011b) presented a numerical model where concrete is treated as a multiphase system with the voids of the solid skeleton partly filled with liquid water and partly with the gas phase. The gas phase is a mixture of dry air and water vapor. The model considers many coupled thermo-hydral phenomena occurring in concrete at high temperature. In addition to the heat and moisture transfer, the mechanical behavior of heated concrete is also described. The thermo-hydral (TH) model is coupled with a mechanical model which considers the thermo-chemical and the mechanical degradation. In (Gawin et al., 1999), damage of concrete is first considered, following the model of scalar isotropic damage by Mazars (1986). Later, the non-local formulation of the damage theory (Pijaudier-Cabot and Bazant, 1987) is followed in (Gawin et al., 2003). A damage-permeability coupling is also proposed (Gawin et al., 2002b) for the first time.

In recent years, the thermo-hydro-mechanical (THM) model of Gawin et al. has been extensively used and further improved in the literature (Dal Pont and Ehrlicher, 2004; Dal Pont et al., 2007; Dal Pont et al., 2011; Meftah et al., 2012). The improvements consist on an extension of the model to 3D and a rigorous treatment of boundary conditions. The mathematical model used in this thesis and presented in detail in Chapter 2 is also based on this formulation.

Tenchev et al. (2001) also proposes a multiphase formulation that considers water vapor, liquid water and moist air separately. The TH model is based on Luikov's theory and similar to the model by Gawin et al. considers the most important heat and mass transfer phenomena. The model has been later extended by Tenchev and Purnell (2005) to include the mechanical behavior of concrete through a material damage model originally proposed by Ortiz (1985) and extended by the authors to account for the effects of high temperature. The effect of pore pressure on damage is considered by applying a body force.

A limitation of this THM model was the assumption that the gas pressure is equal to the liquid pressure (*i.e.*, $p_g = p_l$), so the capillary effects couldn't be properly considered. Davie et al. (2006) extended the model of Tenchev et al. (2001) by including the capillary effects and the adsorbed water.

In parallel to many similarities between the models proposed by Tenchev et al., Davie et al. and the one by Gawin et al., there are some significant differences including some critical constitutive relationships and most notably the choice of state variables. While temperature (T) and displacement vector (\mathbf{u}) are rather obvious and common choices for both models, the hydrometric state variables differ. Due to the fact that very different moisture contents may be encountered at the same moment in heated concrete, ranging from full saturation with liquid water (see England and Khoylou (1995)) up to completely dry material, it is not possible to use a single state variable that describes the whole range of moisture content. In the models presented by Tenchev et al. (2001) and Davie et al. (2006), the density of vapor (ρ_v) is chosen as a state variable for describing the hydrometric state. Similarly, vapor pressure (p_v) has been used as a state variable in (Dal Pont and Ehrlicher, 2004). While state variables ρ_v and p_v are valid in dry concrete, they cease to function when full saturation with liquid water occurs. Gawin et al. have selected capillary pressure p_c as a state variable. Analogously, this variable

has no physical meaning when the liquid water content drops below the solid saturation point (below which water is present only in an adsorbed state). However, as it was shown in (Gawin et al., 2002a), it is possible to use the capillary pressure in all saturation and temperature ranges by changing its meaning depending on the state. The capillary pressure can be interpreted as thermodynamic potential of the physically adsorbed water, which is valid both above the critical temperature of water (*i.e.*, 374.15 °C) and when only adsorbed water is present.

1.3.2.2 Mesoscopic scale models

Concrete has a highly heterogeneous microstructure with various components with different thermo-hydro-mechanical properties which interact among each other influencing the macroscopic behavior of the material. Different thermal dilations of concrete components (see Figure 1.7(b)) result in internal stresses at high temperature. Aggregates are relatively impermeable compared to cement paste and the differences in porosity influence the mass transport. In addition, different chemical composition also influences the respective phase changes at high temperature. In order to take into account explicitly the heterogeneous nature of concrete, models on a mesoscopic scale are required. These models, in contrast to the homogenized continuum models mentioned previously, consider concrete as an assembly of several components (aggregates, sand, mortar, ITZ etc.) in a scale smaller or equal to the Representative Elementary Volume (REV).

For concrete at high temperature, most of the existing mesoscopic models in literature (Grondin et al., 2007; La Borderie et al., 2007; Nguyen et al., 2010) take into account only the thermo-mechanical behavior of concrete, neglecting the influence of pressure and the hydal incompatibility between aggregates and cement paste. In Figure 1.10 an example of such study, performed by La Borderie et al. (2007) is shown.

Due to the complexity of the fully coupled THM modeling of concrete in a mesoscopic scale and also due to the lack of experimental data for validating such modeling approach, very few studies are found in literature (Le, 2011; Xotta et al., 2015) which take into account also the hydal aspect by modeling concrete as solid inclusions (aggregates) embedded in a partially saturated porous medium (cement paste). In (Xotta et al., 2015), the hydal model is limited to single fluid phase, based on the phenomenological approach originally proposed by Bažant and Thonguthai (1978).

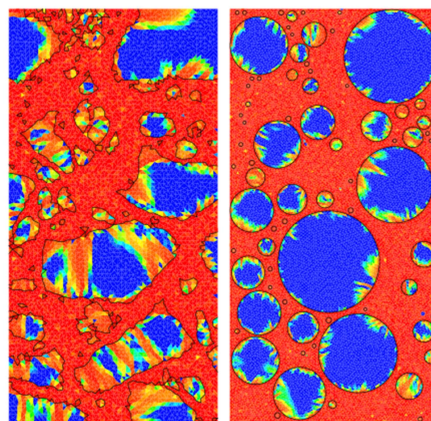


Figure 1.10: Mesoscale thermo-mechanical simulations of concrete heated up to 600° (La Borderie et al., 2007)

Therefore, there is a clear need for developing coupled THM numerical models in a mesoscopic scale. These models should be complemented and validated with experimental studies which also reveal information in the mesoscale (interaction aggregate-cement paste, influence

of the aggregates on the THM behavior etc). Such an approach is useful and necessary for understanding the phenomenon of spalling, which is inherently a local phenomenon.

After having presented the state-of-the-art models for concrete at high temperature, an overview of the experiments performed in heated concrete with respect to spalling is presented in the next section. These experiments are vital for shedding light on the mechanisms of spalling and for validating the numerical models discussed previously.

1.4 Experiments in heated concrete with respect to spalling

A standardized testing guidance for the assessment of fire spalling is missing. Nevertheless, laboratory tests on concrete specimens with different sizes and shapes have been performed for investigating high-temperature behavior of concrete, notably its susceptibility to spalling. The testing procedures can be categorized into three groups according to the sample dimensions: full-scale tests, medium-scale tests and small-scale tests.

1.4.1 Full-scale tests

Full-scale tests are carried out on full-sized concrete elements (columns, beams, slabs) that fit into large furnaces with typical size of 3 m. The boundary conditions, external load and conditioning of the concrete members correspond to the design assumptions. Furnaces with different dimensions and able to apply different fire curves (ISO, HC etc.) have been used in literature (Richter, 2004; Boström and Robert, 2008) for testing various structural elements (beams, columns, slab etc.). In addition to the furnace, the full-scale setup configurations often include hydraulic jacks and/or pre-stressing elements for applying mechanical loads. The real-time measured parameters in the full-scale tests can be: temperature, pressure, deflection and displacement. After the test, spalling can be quantified by analyzing the fire exposed surface using detailed photographic evidence. These tests are the most representative because they permit real structural members to be tested and provide information on the qualitative and quantitative behavior of these members. However, at the same time they are the most expensive and therefore not suitable for parametric experimental studies.



Figure 1.11: Example of full-scale fire test on a slab equipped with temperature and gas pressure sensors and loaded with post tensioning bars (Jansson and Boström, 2013)

1.4.2 Medium-scale tests

Medium-scale tests are performed using medium-scale furnaces with a typical heating surface of 1 m² for the assessment of the susceptibility of a specific concrete to spalling. This approach is less expensive than the full-scale tests. The spalling assessment methods can be grouped in

two main categories. The first one consist on measurements carried out during the spalling event for identifying its beginning, duration and frequency. Examples of such measurement techniques are: acoustic emission methods (Pereira et al., 2011) that allow counting the acoustic events which are directly linked to spalling and image analysis from a digital camera (Carré et al., 2013) which allows registering the volume and time of spalling. The second one consist in a spalling assessment after the test (also known as post-mortem analysis) by measuring the size, shape and amount of the spalled concrete material. Often loading conditions are applied in one direction using pre/post tensioning (Boström and Robert, 2008), in two directions via a restraining frame (Carré et al., 2013) or using hydraulic jacks (Lo Monte and Felicetti, 2017). A more extensive overview of such tests can be found in (Krzemień and Hager, 2015).

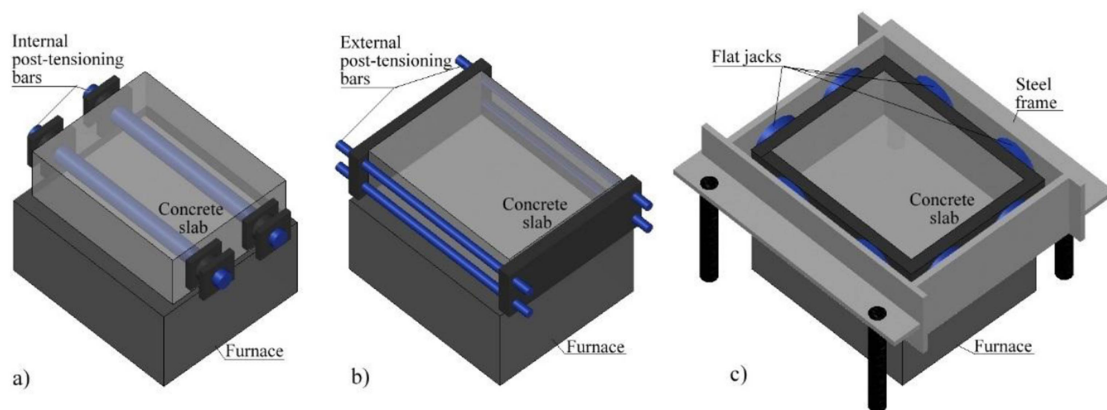


Figure 1.12: Example of medium-scale tests with different loading conditions (Figure from (Krzemień and Hager, 2015))

1.4.3 Small-scale tests

Small-scale tests are performed for understanding the behavior of concrete at high temperature in the context of spalling. These tests are carried out on small concrete specimens (*e.g.* rectangular prisms or cylinders with edges or diameter/height less than 300 mm), which are able to represent the phenomena occurring in real structures. In 1991, in his PhD thesis Connolly (1995) developed a setup for measuring temperature and gas pressures inside cylindrical specimens with diameter 150 mm and height 100 mm mounted inside a steel ring which can be loaded peripherally. Spalling was assessed by analyzing the exposed surfaces in terms of damaged area. The pressure measurements were unsuccessful due to large cracks around the pressure probes, which caused an immediate drop to zero.

One of the most well-known small-scale tests is the Kalifa experiment (Kalifa et al., 2000), in which measurements of gas pressure (P), temperature (T) and mass loss (M) are performed while a prismatic specimen with size 300 mm \times 300 mm \times 120 mm is being heated by a radiator up to 600°C (see Figure 1.13(a)). Such kind of test is often referred to as PTM test. The lateral faces are heat-insulated with porous ceramic blocks. Heating is provided by means of a radiant heater placed 3 cm above it. The specimens were equipped with gauges made of a round sintered metal plate crimped in a metal cup ($d = 12$ mm). The latter is brazed to a thin metal tube (inner diameter 1.6 mm), which comes out of the rear face of the specimen. At the time of the testing, a tight connector is placed at the free end of the tube. A flexible tube filled with silicon oil connects the gauge to the piezoelectric pressure transducer. A thermocouple (Φ 1.5 mm) is inserted in the tube through the connector down to the metal plate. The specimen is placed on a balance in order to monitor its mass during heating. The maximum pressure given by the sensors was 3.7 MPa.

In his PhD thesis, Mindeguia (2009) performed PTM tests using the same experimental setup with different heating rates. In that work, an extensive characterization of the tested concretes has been performed. The maximum measured pressure was 2.5 MPa. In a similar study by the same author (Mindeguia et al., 2010), lower measured pressures (less than 1 MPa) are reported.

Experiments similar to the ones by Kalifa et al. and Mindeguia have been performed by Phan (2002), who measured temperatures and gas pressures in prismatic sample with size $100\text{ mm} \times 200\text{ mm} \times 200\text{ mm}$ heated on one side by an electric furnace and insulated on the other sides. The maximum measured pressure was 2 MPa.

In his PhD thesis, Dal Pont (2004) also obtained temperature and gas pressure measurements, but on a larger specimen and with a slow heating rate. The experiment was performed on a 1.5 m high hollow cylinder ($d_{\text{int}} = 0.25\text{ m}$, $d_{\text{ext}} = 0.55\text{ m}$). These dimensions aim at reproducing a real structure *e.g.* a wall of 30 cm thickness. For temperature measurements type K thermocouples were used. Pressure gauges different from the ones used by Kalifa were employed. Four cylindrical electrical sensors (model XCQ, Kulite) of 3 cm in height and 1.5 cm in diameter are placed at 3, 9, 16 and 25 cm from the heated surface. The cylinder has been heated on the internal face up to 250°C with a 5°C/h velocity. The maximum measured pressure was $\sim 0.3\text{ MPa}$.

Temperature and gas pressure measurements have also been reported in (Dal Pont et al., 2005). A disc, 150 mm diameter and 50 mm thick, was heated by a thermal heater which allowed the temperature at the specimen's lower surface to reach 280°C . The pressure gauge is made of a steel tube, which has been stuck into concrete by means of a high-resistance glue for sealing, at 20-25 mm from the heated face. Tests have been performed by filling the steel tube with different types of oil (*i.e.*, silicon oil as in (Kalifa et al., 2000) and decasting oil) but also leaving it empty. The maximum pressure given by the gauges didn't exceed 1 MPa.

Hertz and Sørensen (2005) used a steel ring for restraining cylindrical concrete specimens with diameter 150 mm and height 300 mm, while heating them in one side using an electrical oven with an opening 100 mm (see the setup in Figure 1.13(b)). Susceptibility to spalling is assessed by measuring the area of spalling and acoustic emission is used for determining the spalling initiation.

Tanibe et al. (2014), also used a steel ring to restrain concrete cylinders with diameter 284 mm and height 100 mm. In addition, the samples were equipped with thermocouples, pressure gauges (steel tube filled with hydraulic jack oil) and strain gauges. A more violent heating curve (1200°C in 5 min) was applied. The measured pressures didn't exceed 0.3 MPa. The setup is shown in Figure 1.13(d). Spalling was assessed by monitoring the time of spalling and by measuring its depth post-mortem. In a later study (Akashi et al., 2016), the measured pressures reached 6 MPa, using the same setup.

Felicetti et al. (2013; 2017) developed a new test method for studying the influence of the pore pressure on the fracture behavior of concrete during heating. The setup is presented in Figure 1.13(e). A cubic specimen is heated on two opposite faces, whereas the lateral sides are sealed and thermally insulated, so as to instate a mono-dimensional thermo-hydral transient field. Pore pressures was measured using capillary steel pipes ($\Phi = 2\text{ mm}$) fitted with sintered metal heads ($d \simeq 5\text{ mm}$). The pipes were filled with silicon oil. Just after the maximum pore pressure was reached, the insulating boards were removed and the specimen was positioned under the press for the splitting test. The results show that pore pressure has a significant effect on the mechanical response of heated concrete. The measured pressures didn't exceed 1.3 MPa.

Van der Heijden et al. (2012) studied the moisture transport in heated concrete by nuclear magnetic resonance (NMR). The experimental setup is shown in Figure 1.14(a). Cylindrical specimens with diameter 80 mm and height 100 mm are heated by 4 halogen lamps which can reach a temperature up to $400\text{-}500^\circ\text{C}$. The spatial resolution is in the order of 3-5 mm. Results in terms of temperature and one dimensional moisture profiles are presented in this study.

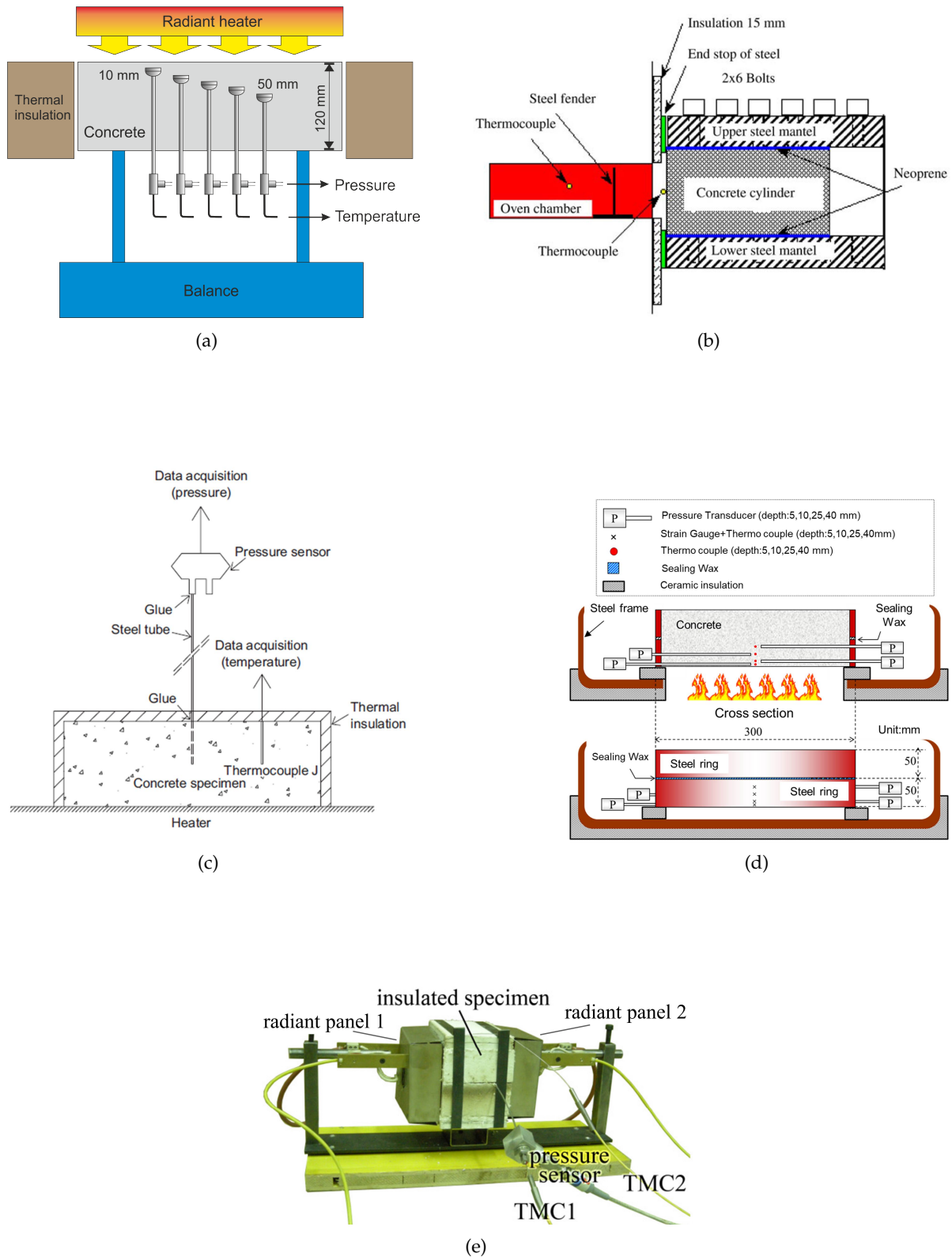


Figure 1.13: Examples of small scale tests: (a) PTM (pressure, temperature, mass loss) test (Kalifa et al., 2000; Mindeguia, 2009) (b) Concrete cylinder restrained in steel mantle for spalling assessment (Hertz and Sørensen, 2005) (c) Concrete disc equipped with thermocouples and various types pressure gauges (Dal Pont et al., 2005) (d) Concrete disc restrained in a steel ring and equipped with temperature, pressure and strain gauges (Tanibe et al., 2014) (e) Temperature, gas pressure and tensile strength in heated concrete (Felicetti et al., 2017)

Toropovs et al. (2015) performed real-time measurements of temperature, gas pressure and one dimensional moisture profiles by neutron radiography. Prismatic samples with size $100 \text{ mm} \times 100 \text{ mm} \times 25 \text{ mm}$ and equipped with temperature and pressure sensors were used for the test. While the samples were being heated by the thermal plate, neutron radiography was performed at PSI in Switzerland. The samples were laterally isolated for heat and moisture using glass foam and self adhesive aluminium tape as shown in Figure 1.14(b).

More recently, Lo Monte et al. (2017) monitored the location of the water front through Ground-Penetrating Radar (GPR) while measuring simultaneously the pore pressures in a square concrete slab, with a 800 mm-side and 100 mm-thickness, subjected to a heating at the bottom face. The objective of the study was to detect the water front position, rather than to directly measure the water content. The setup is shown in Figure 1.14(c).

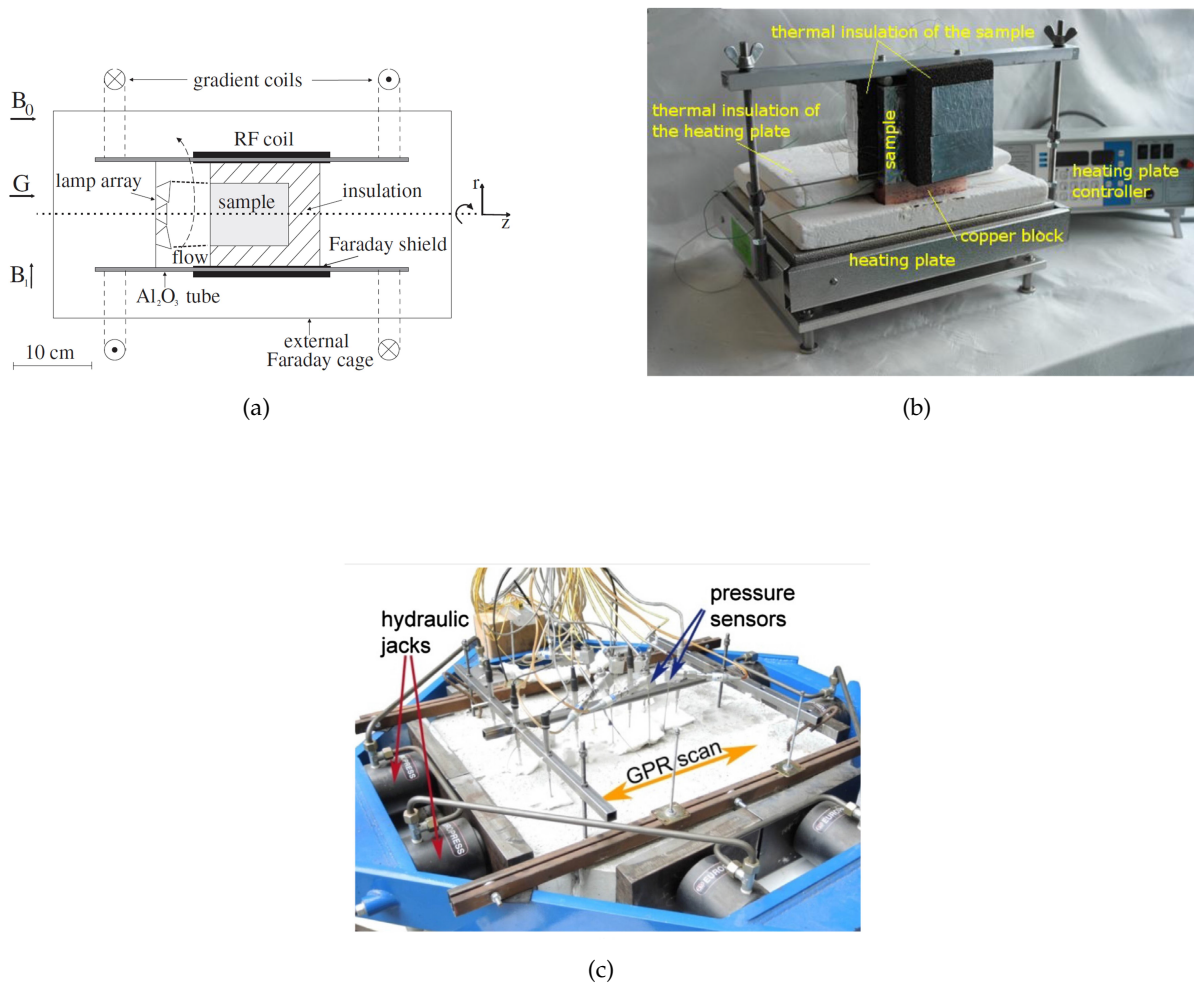


Figure 1.14: Other examples of small-scale tests, including moisture measurements: (a) Temperature and 1D moisture profiles by NMR van der Heijden et al. (Van der Heijden et al., 2012) (b) Temperature, gas pressure and 1D moisture profiles by neutron radiography (Toropovs et al., 2015) (c) Pore pressure and position of water front by Ground-Penetrating Radar (Lo Monte et al., 2017)

1.4.4 Ambiguity of pore pressure measurements

The overview of the experiments on heated concrete in the context of spalling shows that gas pressure is one the most widely measured parameters, due to the direct link with pore pressure build-up theory. However, the data reported in the experimental studies in literature (Kalifa et al., 2000; Dal Pont and Ehrlacher, 2004; Dal Pont et al., 2005; Mindeguia, 2009; Felicetti and Lo Monte, 2013; Guerrieri and Fragomeni, 2013; Carré et al., 2013; Mugume and Horiguchi, 2013; Tanibe et al., 2014; Akashi et al., 2016) spread over a large range of values (0.3 - 6 MPa) for similar type of concrete and thermal load (see Figure 1.15).

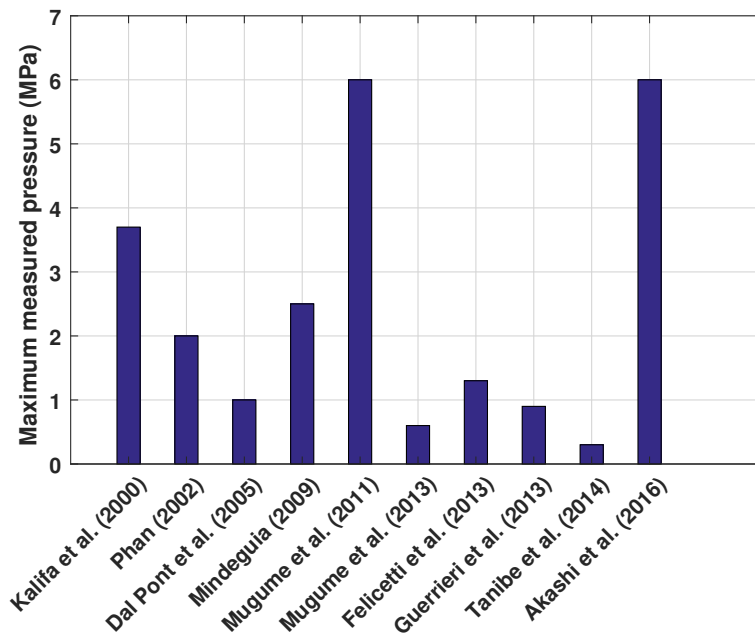


Figure 1.15: Large range of measured pressure for similar type of concrete and thermal load

One possible explanation for this spread is the disparate type of pressure measuring techniques employed in the tests. These methodologies have been used for measuring pressures directly, using embedded electrical sensors as in (Dal Pont and Ehrlacher, 2004), or indirectly by conducting the pressure out of the specimen using an empty pipe (Dal Pont et al., 2005; Mugume and Horiguchi, 2011), a pipe filled with oil (Dal Pont et al., 2005; Mugume and Horiguchi, 2011), pipes with clamped sintered material (Kalifa et al., 2000; Mugume and Horiguchi, 2011) or with sintered metal heads (Felicetti and Lo Monte, 2013). The Figure 1.16 shows the different types of sensors used in the experimental domain.

Another explanation for wide range of measured pressures is the intrusive nature of the methodology itself. The size of pressure gauges ranges between 2 and 12 mm. Introducing such a gauge, with a considerable size and more importantly with different THM behavior compared to concrete, means introducing an important heterogeneity which can alternate the behavior of the material (*i.e.*, induce cracks). These cracks can potentially build an escape channel for vapor which would effect the measurement.

Moreover, pressure gauges provide point-wise measurements. The heterogeneous nature of concrete induces some randomness in the flow paths of vapor and might result in a non-uniform pressure distribution. In other words, the measured pressures might be influenced by the position of the gauge with respect to the aggregates and/or pores.

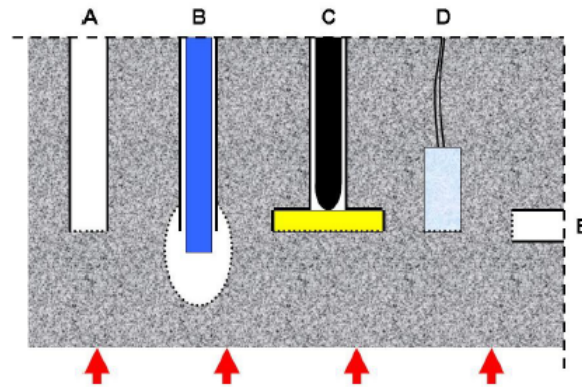


Figure 1.16: Different pressure measurement techniques: (A,E) Metal tube placed horizontally (Dal Pont et al., 2005) or vertically; (B) Sintered metal head (Felicetti and Lo Monte, 2013); (C) Cup with or without sintered metal (Kalifa et al., 2000; Mugume and Horiguchi, 2011); (D) Embedded electrical sensor (Dal Pont and Ehrlacher, 2004). Figure taken from Jansson (2013).

1.5 Motivation and structure of the thesis

1.5.1 Limitations of the current experimental and numerical approaches with respect to spalling

As mentioned previously, the two principal spalling mechanisms more broadly accepted are the differential thermal gradients and the pore pressure build-up. The latter is related to the evolution of the moisture content in concrete due to phase changes such as dehydration, evaporation, condensation, and mass transfer caused by pressure gradients. A combination of these physical processes may result in the formation of a moisture clog that leads to pore pressure build-up to which spalling itself is attributed.

Numerous experiments based on temperature and gas pressure measurements (Kalifa et al., 2000; Dal Pont and Ehrlacher, 2004; Dal Pont et al., 2005; Mindeguia et al., 2010; Felicetti and Lo Monte, 2013; Tanibe et al., 2014) have been performed to investigate the processes underlying spalling. Nonetheless, the pressures measured in these studies spread over a large range of values (0.3–6 MPa) for comparable types of concrete. This discrepancy can be ascribed to the disparate types of pressure sensor used for the measurements as well as to the intrusive and point-wise nature of experimental procedures themselves.

Other studies have attempted the investigation of moisture distribution in heated concrete following alternative approaches, notably employing nuclear magnetic resonance (Van der Heijden et al., 2011; Van der Heijden et al., 2012) and neutron radiography (Weber et al., 2013; Toropovs et al., 2015). One-dimensional moisture profiles were obtained in these experiments, albeit none of them has been able to track the moisture distribution in three dimensions. Spalling is an intrinsically three-dimensional process, since it locally depends on the heterogeneity of concrete. As a consequence, one dimensional moisture profiles are not sufficient for investigating the role of aggregates in the moisture distribution.

Therefore, experimental studies that follow locally the phenomena in heated concrete in real time but also in a quantitative and non-destructive manner are of paramount importance. Moreover, these experimental studies should take into consideration the heterogeneous nature of concrete.

On the other hand, the inherent complexity of spalling induces the need of complementing the experimental tests by numerical modeling. The latter would contribute in quantifying the orders of magnitude of spalling mechanisms and in identifying the most influential parameters, all this in a reduced cost and time compared to the experimental tests.

Despite the significant development of some advanced numerical models (see Section 1.3.2), a critical area for consideration lies on some key aspects of the behavior of concrete at high temperature described by a set of constitutive relations. Some of these relations are: (i) permeability and its evolution with temperature which is obtained from residual measurements, (ii) sorption isotherms which are numerically extrapolated to high temperature due to lack of experimental data, (iii) dehydration which is based on experiments performed on crushed samples etc.

Furthermore, the numerical models are validated mainly by pore pressure experiments. The latter are limited by their point-wise-measurement nature, and more importantly are dependent on the measurement technique.

Another critical area, which is usually not taken into account by the numerical models, is the heterogeneous nature of concrete which requires modeling in a mesoscopic scale. Advanced THM numerical models on a mesoscale are missing in literature.

Finally, the computational cost is also an issue, especially when considering mesoscopic modeling. Most of the simulations in literature are one-dimensional. Computationally efficient numerical codes are necessary not only for performing 3D simulations, but also for handling mesoscopic geometries.

1.5.2 Objective of this thesis and proposed methodology

The main objective of this PhD project is to better understand the mechanisms involved in spalling, a phenomenon which is not yet fully understood despite the extensive research dedicated over the last decades.

The methodology proposed in this thesis is a combined experimental-numerical strategy, *i.e.*, neutron tomography coupled with advanced numerical modeling in an adequate scale.

During this thesis, the first ever neutron tomography of concrete during exposure to high temperature for obtaining real-time and 3D measurements of moisture transport, a factor directly linked with spalling, has been achieved. This experimental work is complemented with the implementation of a numerically efficient coupled thermo-hydro-mechanical model for describing the complex physical phenomena in concrete at high temperature at mesoscale. Some constitutive relations, which on the one hand play a key role in the state-of-the-art numerical models but on the other hand are not strongly supported by experiments, have been identified and analyzed by the aid of neutron imaging experiments. Given the difficulty of measuring such properties directly, neutron imaging coupled with advanced numerical models is proposed for improving the current knowledge about these constitutive laws.

1.5.3 Layout of the thesis

In the following a description of the work performed in this thesis, chapter by chapter, is given.

Chapter 2 - Numerical model for concrete behavior at high temperature

Chapter 2 describes the advanced numerical model, used in this project as the starting point, for simulating the high-temperature behavior of concrete. The chapter provides the conservation equations that build up the mathematical model, which is based on the hybrid mixture theory of Lewis and Schrefler (1998). In addition, the set of constitute laws, retrieved mainly from the work of Pesavento (2000) and Gawin et al. (2002b) are presented. Some of these constitutive laws, which play a critical role in the numerical model, are identified and discussed in Chapter 3. Given that the main critic to such advanced numerical models is the high number of parameters, special attention is dedicated in this chapter to summarizing them in a synthetic way.

One of the challenges when dealing with such advanced models is the numerical implementation. Furthermore, an important objective is the achievement of a numerically efficient

model, with respect to an existing one (Dal Pont et al., 2007), for being able to deal with 3D and mesoscopic simulations. The details of the numerical implementation in the finite element softwares, Cast3M (2006) and COMSOL Multiphysics (1998), done in the framework of this PhD project, are also given in this chapter.

During this doctoral work, the model has also been enriched with a mesoscale approach for capturing the heterogeneous nature of concrete. Mesoscale meshes come with the cost of high computational time which brings out the need of a numerically efficient model.

Chapter 3 - Application to experiments from literature

In Chapter 3, the numerical model described in Chapter 2 has been used for modeling three case studies from literature. The main goals of these numerical analyses are: (i) the verification of results and the numerical performance of the newly implemented code (ii) improvement of the model in terms of some critical constitutive laws after having identified them.

The first case study is the experiment of Kalifa et al. (2000). The objective in this case study is the numerical validation of the thermo-hydral part of the newly implemented code against standard measurements of temperature and gas pressure and the investigation of its numerical performance.

In the second case study, similar experiments performed by Mindeguia (2009), where most of the material properties and their evolution with temperature are provided, are used for numerical analysis. This case study was proposed by the RILEM TC 256 Working Group 5, as a numerical benchmark of experiments in heated concrete.

The main critic of the so-called PTM (pressure, gas pressure, mass loss) experiments, used for numerical validation in the first two case studies in this work, but also commonly in the validation of numerical models in literature, is the reliability of the gas pressure measurements due to their intrusive nature. Therefore, a third case study is performed which consists on the numerical simulation of 2D moisture profiles measured using a non-intrusive method such as neutron radiography (Toropovs et al., 2015). This case study permits investigating some critical constitutive laws used in numerical modeling of concrete at high temperature, notably dehydration, water retention curves and permeability.

Finally, mesoscopic simulations, which have been performed in the framework of the master research project supervised by the author, are presented. The objective is the investigation of the influence of concrete's heterogeneity on the high temperature behavior.

Chapter 4 - In-situ neutron tomography of heated concrete

In Chapter 4, the first neutron tomography experiments of heated concrete performed at Institute Laue Langevin (ILL) are presented.

First, an introduction about of neutron imaging, which is necessary for understanding the methodology and the image analysis that follows, is given.

Then, an original experimental setup developed in this project, along with the specimen preparation, are described.

One of the big challenges of these tests was the temporal and spatial resolution. The tomography has to be fast enough to be able to follow the dehydration speed in concrete. The details the tomography acquisition speed are also given in this chapter.

Finally, the tomography results in terms of moisture migration in heated concrete, which are the first of their kind to the authors knowledge, are presented. Among them, the influence of the aggregate size on the drying of concrete is discussed. A special attention is dedicated to the moisture accumulation, a phenomenon which is directly linked to spalling.

Chapter 5 - Simulation of moisture distribution: from continuum towards a 3D mesoscopic approach

In Chapter 5, the numerical model, the constitutive law's of which has been improved thanks to the analyses presented in Chapter 3, is employed for simulating the moisture migration given by the neutron tomography.

First, a continuum model is used for predicting the drying front. Then, 3D mesoscopic simulations, for explaining the influence of the aggregate size on the drying front, are presented.

Chapter 6 - Conclusion and perspectives

The main findings in this PhD project are summarized in this chapter. Some new research perspectives driven from the outcomes of this thesis are also discussed.

Chapter 2

Numerical model for concrete behavior at high temperature

In this chapter, the numerical model that has been used in this thesis for simulating the high-temperature behavior of concrete is described. The starting point is the model based on the hybrid mixture theory in the mathematical formulation originally proposed in Hassanizadeh and Gray (1979a; 1979b; 1980) and then applied for geomaterials in (Lewis and Schrefler, 1998), and for building materials in (Gawin et al., 1999).

2.1 Conservation Equations

For sake of brevity only the final form of the macroscopic conservation equations are given here. The full development of the model equations starting from the local microscopic balance equations with successive volume averaging can be found in (Lewis and Schrefler, 1998; Pesavento, 2000; Schrefler et al., 2002; Gawin et al., 2003). The model is formulated as a coupled system of partial differential equations that describe the mass, energy, and momentum conservation.

2.1.1 Mass Conservation

The general form of a mass conservation equation is:

$$\frac{\partial}{\partial t} \text{density} + \nabla \cdot (\text{flux}) = \text{source} \quad (2.1)$$

The mass conservation of solid skeleton, liquid water, vapor water, and dry air are respectively:

$$\frac{\partial m_s}{\partial t} = \dot{m}_{dehyd} \quad (2.2)$$

$$\frac{\partial m_l}{\partial t} + \nabla \cdot (m_l \mathbf{v}_{l-s}) = -\dot{m}_{vap} - \dot{m}_{dehyd} \quad (2.3)$$

$$\frac{\partial m_v}{\partial t} + \nabla \cdot (m_v \mathbf{v}_{g-s}) + \nabla \cdot (m_v \mathbf{v}_{v-g}) = \dot{m}_{vap} \quad (2.4)$$

$$\frac{\partial m_a}{\partial t} + \nabla \cdot (m_a \mathbf{v}_{g-s}) + \nabla \cdot (m_a \mathbf{v}_{a-g}) = 0 \quad (2.5)$$

where $\mathbf{v}_{\pi-s}$ is the velocity of the liquid water ($\pi = l$) and gas mixture ($\pi = g$) with respect to the solid phase and $\mathbf{v}_{\pi-g}$ is the velocity of the vapor ($\pi = v$) and dry air ($\pi = a$) with respect to the gas mixture. Note that the fluid flow is given according to the Eulerian reference system. The source term \dot{m}_{vap} corresponds to the water mass per unit-volume of porous the

medium and per unit-time due to evaporation ($\dot{m}_{vap} > 0$) or condensation ($\dot{m}_{vap} < 0$). The source term $\dot{m}_{dehyd} < 0$ is the water mass per unit-volume of porous medium and per unit-time due to cement dehydration process. In the presented formulation, the dehydration mass rate \dot{m}_{dehyd} is treated as a negative source in the solid conservation equations and as a positive source in the liquid water conservation equation.

The mass density of the solid skeleton and the fluids depends on porosity ϕ . Furthermore, the partial density of the fluid species (gas and liquid) depends on the liquid saturation S_l . Thus, the mass of each phase can be expressed as:

$$m_s = (1 - \phi) \rho_s \quad (2.6)$$

$$m_l = \rho_l S_l \phi \quad (2.7)$$

$$m_v = \rho_v (1 - S_l) \phi \quad (2.8)$$

$$m_a = \rho_a (1 - S_l) \phi \quad (2.9)$$

where $\rho_s, \rho_l, \rho_v, \rho_a$ are the densities of solid, liquid, vapor, and air, respectively.

The fluids are assumed to flow under pressure according to Darcy's law. For the gas phase, the velocity is given by:

$$\mathbf{v}_{g-s} = -K \frac{k_{rg}}{\mu_g} \nabla p_g \quad (2.10)$$

and for the capillary water:

$$\mathbf{v}_{l-s} = -K \frac{k_{rl}}{\mu_l} \nabla p_l \quad (2.11)$$

where K is the intrinsic permeability; k_{rg} and k_{rl} are the phase permeabilities; μ_l and μ_g are the dynamic viscosities for the liquid and gaseous phase (see Section 2.2 on the constitutive equations of the model). The dry air and vapor in the gas mixture also diffuse according to Fick's law:

$$\mathbf{j}_v = -\rho_g D \nabla \left(\frac{\rho_v}{\rho_g} \right) = -\mathbf{j}_a \quad (2.12)$$

where D is the effective diffusivity of vapor in the air. Thus, the fluxes in Eq. 2.3 - 2.5 can be expressed as:

$$m_l \mathbf{v}_{l-s} = -K \frac{\rho_l k_{rl}}{\mu_l} \nabla p_l \quad (2.13)$$

$$m_v \mathbf{v}_{g-s} + m_v \mathbf{v}_{v-g} = -K \frac{\rho_v k_{rg}}{\mu_g} \nabla p_g - D \rho_g \frac{M_v M_a}{M_g^2} \nabla \left(\frac{p_v}{p_g} \right) \quad (2.14)$$

$$m_a \mathbf{v}_{g-s} + m_a \mathbf{v}_{a-g} = -K \frac{\rho_a k_{rg}}{\mu_g} \nabla p_g - D \rho_g \frac{M_v M_a}{M_g^2} \nabla \left(\frac{p_a}{p_g} \right) \quad (2.15)$$

We can therefore write, for conservation of liquid water, vapor water, and dry air, the following equations:

- Liquid water

$$S_l \rho_l \frac{\partial \phi}{\partial t} + S_l \phi \frac{\partial \rho_l}{\partial t} + \rho_l \phi \frac{\partial S_l}{\partial t} + \nabla \cdot \left(-K \frac{\rho_l k_{rl}}{\mu_l} \nabla p_l \right) = -\dot{m}_{vap} - \dot{m}_{dehyd} \quad (2.16)$$

- Vapor water

$$(1 - S_l)\phi \frac{\partial \rho_v}{\partial t} - \rho_v \phi \frac{\partial S_l}{\partial t} + (1 - S_l)\rho_v \frac{\partial \phi}{\partial t} + \nabla \cdot \left(-K \frac{\rho_v k_{rg}}{\mu_g} \nabla p_g - D \rho_g \frac{M_v M_a}{M_g^2} \nabla \left(\frac{p_v}{p_g} \right) \right) = \dot{m}_{vap} \quad (2.17)$$

- Dry air

$$(1 - S_l)\phi \frac{\partial \rho_a}{\partial t} - \rho_a \phi \frac{\partial S_l}{\partial t} + (1 - S_l)\rho_a \frac{\partial \phi}{\partial t} + \nabla \cdot \left(-K \frac{\rho_a k_{rg}}{\mu_g} \nabla p_g - D \rho_g \frac{M_v M_a}{M_g^2} \nabla \left(\frac{p_a}{p_g} \right) \right) = 0 \quad (2.18)$$

The conservation of water species is obtained by adding the conservation of liquid water (Eq. 2.16) and vapor water (Eq. 2.17). By doing this, the evaporation source term \dot{m}_{vap} is eliminated from the mass conservation equation.

- Water species (liquid+vapor)

$$S_l \rho_l \frac{\partial \phi}{\partial t} + S_l \phi \frac{\partial \rho_l}{\partial t} + \rho_l \phi \frac{\partial S_l}{\partial t} + (1 - S_l)\phi \frac{\partial \rho_v}{\partial t} - \rho_v \phi \frac{\partial S_l}{\partial t} + (1 - S_l)\rho_v \frac{\partial \phi}{\partial t} + \nabla \cdot \left(-K \frac{\rho_l k_{rl}}{\mu_l} \nabla p_l \right) + \nabla \cdot \left(-K \frac{\rho_v k_{rg}}{\mu_g} \nabla p_g - D \rho_g \frac{M_v M_a}{M_g^2} \nabla \left(\frac{p_v}{p_g} \right) \right) = -\dot{m}_{dehyd} \quad (2.19)$$

2.1.2 Energy Conservation

In the energy conservation equation of the multi-phase medium it is accounted for: heat accumulation by the material, conductive and convective heat flows as well as the heat effects of phase changes and dehydration process. The conservation of energy is expressed as:

$$\rho C_p \frac{\partial T}{\partial t} + (m_l C_l v_{l-s} + m_g C_g v_{g-s}) \cdot \nabla T + \nabla \cdot (-\lambda \cdot \nabla T) = -H_{vap} \dot{m}_{vap} + H_{dehyd} \dot{m}_{dehyd} \quad (2.20)$$

where H_{vap} and H_{dehyd} are the enthalpies related to evaporation and dehydration, respectively. The vapor source \dot{m}_{vap} , which is deduced from liquid water conservation (Eq. 2.16), reads:

$$\dot{m}_{vap} = -S_l \phi \frac{\partial \rho_l}{\partial T} \frac{\partial T}{\partial t} - \phi \rho_l \left(\frac{\partial S_l}{\partial T} \frac{\partial T}{\partial t} + \frac{\partial S_l}{\partial p_c} \frac{\partial p_c}{\partial t} \right) - S_l \rho_l \frac{\partial \phi}{\partial T} \frac{\partial T}{\partial t} + \nabla \cdot \left(K \frac{\rho_l k_{rl}}{\mu_l} (\nabla p_g - \nabla p_c) \right) - \dot{m}_{dehyd} \quad (2.21)$$

The heat capacities C_p (overall), C_l (liquid), C_g (gas) as well as the thermal conductivity are discussed in Section 2.2. After replacing the mass fluxes, the energy conservation equation reads:

$$\rho C_p \frac{\partial T}{\partial t} + \left(-K \frac{\rho_l k_{rl}}{\mu_l} \nabla p_l C_l + -K \frac{\rho_g k_{rg}}{\mu_g} \nabla p_g C_g \right) \cdot \nabla T + \nabla \cdot (-\lambda \cdot \nabla T) = -H_{vap} \dot{m}_{vap} + H_{dehyd} \dot{m}_{dehyd} \quad (2.22)$$

2.1.3 Momentum Conservation

By neglecting the inertial forces and considering the gravitational ones, the linear momentum conservation equation reads:

$$\nabla \cdot (\mathbf{t}^{Total}) + \rho \mathbf{g} = 0 \quad (2.23)$$

where \mathbf{g} stands for the acceleration of gravity and \mathbf{t}^{Total} is the total stress tensor. The density can be expressed as:

$$\rho = (1 - \phi)\rho_s + \phi (S_l \rho_l + (1 - S_l)\rho_g) \quad (2.24)$$

2.1.4 Final form of model equations

The model consist of 4 conservation equations: mass conservation of dry air, mass conservation of water species, energy conservation and linear momentum conservation. For describing the state of concrete at high temperature, 4 primary variables are chosen: gas pressure p_g , capillary pressure p_c , temperature T , and displacement vector \mathbf{u} . The model equations are now developed with respect to the state variables:

- Dry Air

$$\begin{aligned} & \phi(1 - S_l) \left(\frac{\partial \rho_a}{\partial T} \frac{\partial T}{\partial t} + \frac{\partial \rho_a}{\partial p_c} \frac{\partial p_c}{\partial t} + \frac{\partial \rho_a}{\partial p_g} \frac{\partial p_g}{\partial t} \right) - \phi \rho_a \left(\frac{\partial S_l}{\partial T} \frac{\partial T}{\partial t} + \frac{\partial S_l}{\partial p_c} \frac{\partial p_c}{\partial t} \right) \\ & + (1 - S_l) \rho_a \frac{\partial \phi}{\partial T} \frac{\partial T}{\partial t} - \nabla \cdot \left(K \frac{\rho_a k_{rg}}{\mu_g} \nabla p_g \right) - \nabla \cdot \left(D \rho_g \frac{M_v M_a}{M_g^2} \nabla \left(\frac{p_a}{p_g} \right) \right) = 0 \end{aligned} \quad (2.25)$$

- Water species

$$\begin{aligned} & (S_l \rho_l - (1 - S_l) \rho_v) \frac{\partial \phi}{\partial T} \frac{\partial T}{\partial t} + S_l \phi \frac{\partial \rho_l}{\partial T} \frac{\partial T}{\partial t} + \phi (\rho_l - \rho_v) \left(\frac{\partial S_l}{\partial T} \frac{\partial T}{\partial t} + \frac{\partial S_l}{\partial p_c} \frac{\partial p_c}{\partial t} \right) \\ & + (1 - S_l) \phi \left(\frac{\partial \rho_v}{\partial T} \frac{\partial T}{\partial t} + \frac{\partial \rho_v}{\partial p_c} \frac{\partial p_c}{\partial t} + \frac{\partial \rho_v}{\partial p_g} \frac{\partial p_g}{\partial t} \right) - \nabla \cdot \left(K \frac{\rho_l k_{rl}}{\mu_l} (\nabla p_g - \nabla p_c) \right) \\ & - \nabla \cdot \left(K \frac{\rho_v k_{rg}}{\mu_g} \nabla p_g \right) - \nabla \cdot \left(D \rho_g \frac{M_v M_a}{M_g^2} \nabla \left(\frac{p_v}{p_g} \right) \right) = -\dot{m}_{dehyd} \end{aligned} \quad (2.26)$$

- Energy

$$\begin{aligned} & \rho C_p \frac{\partial T}{\partial t} - K \left(C_l \frac{\rho_l k_{rl}}{\mu_l} (\nabla p_g - \nabla p_c) + C_g \frac{\rho_v k_{rg}}{\mu_g} \nabla p_g \right) \cdot \nabla T - \nabla \cdot (\lambda \cdot \nabla T) = \\ & - H_{vap} \dot{m}_{vap} + H_{dehyd} \dot{m}_{dehyd} \end{aligned} \quad (2.27)$$

- Linear momentum

$$\nabla \cdot (\mathbf{t}^{Total}) + \rho \mathbf{g} = 0 \quad (2.28)$$

2.2 Constitutive Equations

Constitutive relationships describe the high-temperature behavior of concrete. They are needed for expressing all the components of the model equations in terms of the state variables. These

relationships include equations of state for constituents of the medium and material functions describing certain physical properties and their evolution with temperature.

The constitutive relationships presented below have been collected from literature and mark the starting point in the numerical model implemented in this project. Some key constitutive laws are discussed and improved as a result of several numerical analyses presented in Chapter 3.

2.2.1 Density and pressure relationships

Gases are treated as ideal gases:

$$\rho_{\pi} = p_a \frac{M_{\pi}}{RT} \quad (2.29)$$

for $\pi = a, v$ and where M_{π} is the molar weight and R is the universal gas constant. By Dalton's law the gas pressure is the sum of the partial pressures:

$$p_g = p_a + p_v \quad (2.30)$$

For defining the vapor pressure an equilibrium formulation is adopted, *i.e.*, vapor pressure is provided by the Kelvin equation, obtained by imposing the equality of vapor water and liquid water enthalpies :

$$p_v = p_{vs} \exp \left(\frac{M_v}{\rho_l RT} (p_g - p_c - p_{vs}) \right) \quad (2.31)$$

where $p_{vs}(T)$ is the saturation vapor pressure. Liquid water is considered incompressible (*i.e.*, not pressure dependent) but its density varies with temperature. The following relationship is retained (Furbish, 1997):

$$\rho_l = \sum_{n=0}^5 b_n T^n + (p_{l-1} - p_{l-2}) \sum_{n=0}^5 a_n T^n \quad (2.32)$$

where $p_{l-1} = 10$ MPa and $p_{l-2} = 20$ MPa. Temperature is expressed in °C and the coefficients a and b are given in the following table:

a_0 $\left[\frac{\text{kg}}{\text{m}^3 \cdot \text{MPa}} \right]$	a_1 $\left[\frac{\text{kg}}{\text{m}^3 \cdot \text{MPa} \cdot ^\circ\text{C}} \right]$	a_2 $\left[\frac{\text{kg}}{\text{m}^3 \cdot \text{MPa} \cdot ^\circ\text{C}^2} \right]$	a_3 $\left[\frac{\text{kg}}{\text{m}^3 \cdot \text{MPa} \cdot ^\circ\text{C}^3} \right]$	a_4 $\left[\frac{\text{kg}}{\text{m}^3 \cdot \text{MPa} \cdot ^\circ\text{C}^4} \right]$	a_5 $\left[\frac{\text{kg}}{\text{m}^3 \cdot \text{MPa} \cdot ^\circ\text{C}^5} \right]$
$4.8863E - 7$	$-1.6528E - 9$	$1.8621E - 12$	$2.4266E - 13$	$-1.5996E - 15$	$3.3703E - 18$
b_0 $\left[\frac{\text{kg}}{\text{m}^3} \right]$	b_1 $\left[\frac{\text{kg}}{\text{m}^3 \cdot ^\circ\text{C}} \right]$	b_2 $\left[\frac{\text{kg}}{\text{m}^3 \cdot ^\circ\text{C}^2} \right]$	b_3 $\left[\frac{\text{kg}}{\text{m}^3 \cdot ^\circ\text{C}^3} \right]$	b_4 $\left[\frac{\text{kg}}{\text{m}^3 \cdot ^\circ\text{C}^4} \right]$	b_5 $\left[\frac{\text{kg}}{\text{m}^3 \cdot ^\circ\text{C}^5} \right]$
$1.0213E + 3$	$-7.7377E - 1$	$8.7696E - 3$	$-9.2118E - 5$	$3.3534E - 7$	$-4.4034E - 10$

Table 2.1: Coefficients for describing evolution of the density of water with temperature

Saturation vapor pressure, expressed in Pa, is approximated by a function of temperature, expressed in K, following Hyland-Wexler relationship (ASHRAE, 2001):

$$p_{vs}(T) = \exp [C_1/T + C_2 + C_3 T + C_4 T^2 + C_5 T^3 + C_6 \ln(T)] \quad (2.33)$$

where: $C_1 = -5800.2206$, $C_2 = 1.3915$, $C_3 = -4.864 \times 10^{-2}$, $C_4 = 4.1765 \times 10^{-5}$, $C_5 = -1.4452 \times 10^{-8}$, $C_6 = 6.546$

2.2.2 Mass transfer properties

2.2.2.1 Permeability

Permeability, which is a key parameter in the model, is based on the concept of intrinsic and relative permeability. The key point is the description of permeability evolution with temperature, gas pressure, and damage. For a thermo-hydral problem, the following relationship is proposed (Gawin et al., 1999):

$$K = K_0 \cdot 10^{A_T(T-T_0)} \left(\frac{p_g}{p_{atm}} \right)^{A_p} \quad (2.34)$$

where K_0 is the intrinsic permeability, $A_T = 0.005$ and $A_p = 0.368$. When damage of the material is considered, the following relation is used (Gawin et al., 2002b):

$$K = K_0 \cdot 10^{A_T(T-T_0)} \left(\frac{p_g}{p_{atm}} \right)^{A_p} \cdot 10^{A_d d} \quad (2.35)$$

where d is the total damage parameter. Liquid water and gas relative permeability are considered using the well-known Van Genuchten relationships (Van Genuchten, 1980). Liquid water relative permeability reads:

$$k_{rl} = \sqrt{S_l} \left(1 - \left(1 - S_l^{1/A_s} \right)^{A_s} \right)^2 \quad (2.36)$$

and gas relative permeability is:

$$k_{rg} = \sqrt{1 - S_l} \left(1 - S_l^{1/A_s} \right)^{2A_s} \quad (2.37)$$

where the parameter $A_s = 0.6$.

It is worth noting that there is a wide variation in measured values of intrinsic permeability. Moreover, there is considerable variation in the way that the evolution of permeability with temperature is described. One reason for such variation is the uncertainty and complexity surrounding such measurements at room temperature and even more at high temperature. This issue is discussed more in details in Section 3.2.4.

2.2.2.2 Diffusivity

The diffusivity of vapor into air at ambient temperature is given by the following relationship (Perre and Degiovanni, 1990):

$$D_{va}(T, p_g) = D_{v0} \left(\frac{T}{T_0} \right)^{B_v} \frac{p_{g0}}{p_g} \quad (2.38)$$

where $D_{v0} = 2.58 \times 10^{-5} \text{m}^2 \text{s}^{-1}$ is the diffusion coefficient at ambient conditions and $B_v = 1.667$. Since concrete porous network is tortuous, the so-called effective diffusivity is described by the following relationship:

$$D = (1 - S)^{A_v} \phi \tau D_{va}(T, p_g) \quad (2.39)$$

where A_v is a constant usually in the range [1,3] and the tortuosity is given by:

$$\tau(\phi, S_l) = \phi^{1/3} (1 - S_l)^{7/3} \quad (2.40)$$

2.2.3 Thermal properties

2.2.3.1 Thermal Conductivity

The thermal conductivity of a porous medium depends on the saturation S_l , the porosity ϕ , and the densities of the solid skeleton ρ_s and the liquid water ρ_l (Baggio et al., 1993):

$$\lambda = \lambda_d \left(1 + 4 \frac{S_l \phi \rho_l}{(1 - \phi) \rho_s} \right)$$

where λ_d is the thermal conductivity of the dried material depending on the temperature (Harmathy and Allen, 1973):

$$\lambda_d = \lambda_{d0} [1 + A_\lambda (T - T_0)]$$

and $\lambda_{d0} = 1.67 \frac{\text{W}}{\text{m}\cdot\text{K}}$ and $A_\lambda = -0.005 \text{ K}^{-1}$, and T_0 is the room temperature.

2.2.3.2 Thermal capacity

The thermal capacity of the porous medium is given by a combination of the thermal capacity of its constituents (Lewis and Schrefler, 1998):

$$\rho C_p = (1 - \phi) \rho_s C_{ps} + \phi [S_l \rho_l C_{pl} + (1 - S_l) (\rho_a C_{pa} + \rho_v C_{pv})]$$

The thermal capacities of the fluid phases are kept constant: $C_{pl} = 1005 \frac{\text{J}}{\text{K}\cdot\text{kg}}$, $C_{pv} = 1805 \frac{\text{J}}{\text{K}\cdot\text{kg}}$, $C_{pa} = 4181 \frac{\text{J}}{\text{K}\cdot\text{kg}}$ while the thermal capacity of the solid phase is provided by the linear relationship (Harmathy and Allen, 1973):

$$C_{ps} = C_{ps0} [1 + A_c (T - T_0)] \quad (2.41)$$

where $C_{ps0} = 940 \frac{\text{J}}{\text{K}\cdot\text{kg}}$ and A_c is a constant.

2.2.3.3 Enthalpy of evaporation

The enthalpy of evaporation is considered temperature dependent and is approximated by means of the Watson formula (Reid et al., 1987):

$$\Delta H_{vap} = 2.672 \cdot 10^5 (T_{crit} - T)^{0.38} \quad (2.42)$$

where T_{crit} , which is the critical temperature of water, equals 647 K.

2.2.4 Fluid viscosities

Fluid viscosities are typically temperature dependent. Their values/evolutions are well known in the literature (ASHRAE, 2001). The total gas viscosity depends on the concentration of each constituent:

$$\mu_g = \mu_v + (\mu_a - \mu_v) \left(\frac{p_a}{p_g} \right)^{0.608} \quad (2.43)$$

The viscosity of air and vapor are:

$$\mu_v = \mu_{v0} + \alpha_v (T - T_0) \quad (2.44)$$

$$\mu^a = \mu_{ga0} + \alpha_a (T - T_0) + \beta_a (T - T_0)^2 \quad (2.45)$$

where $\mu_{v0} = 8.85 \cdot 10^{-6} \text{ Pa}\cdot\text{s}$ and $\alpha_v = 3.53 \cdot 10^{-8} \text{ Pa}\cdot\text{s}\cdot\text{K}^{-1}$, $\mu_{a0} = 17.17 \cdot 10^{-6} \text{ Pa}\cdot\text{s}$, $\alpha_a = 4.73 \cdot 10^{-8} \text{ Pa}\cdot\text{s}\cdot\text{K}^{-1}$ and $\beta_a = 2.22 \cdot 10^{-11} \text{ Pa}\cdot\text{s}\cdot\text{K}^{-1}$.

The dynamic viscosity of water is strongly dependent on temperature (Reid et al., 1987) and has been approximated by means of the following formula (Thomas and Sansom, 1995):

$$\mu_l = 0.6612 \cdot (T - 229)^{-1.562} \quad (2.46)$$

2.2.5 Porosity

The micro-structure characteristics, in particular porosity, evolves with temperature. Schneider and Herbst (1989) showed that increasing temperature produces an increase in porosity:

$$\phi = \phi_0 + A_\phi(T - T_0) \quad (2.47)$$

where ϕ_0 and A_ϕ are material constants.

2.2.6 Dehydration

Dehydration is another key element in the model. The following relationship is commonly adopted:

$$\Delta m_{dehyd} = f_s \cdot f_m \cdot f_c \cdot f(T) \quad (2.48)$$

where f_s is a stoichiometric factor, f_m takes into account concrete's age, f_c is the cement mass per unit volume of concrete and $f(T)$ depends over the temperature:

$$f(T) = \begin{cases} 0 & \text{with } T < 105^\circ\text{C} \\ \frac{[1 + \sin(\pi/2(1 - 2\exp(-0.004(T - 105)))]}{2} & \text{with } T > 105^\circ\text{C} \end{cases} \quad (2.49)$$

It is worth noting that this relationship, proposed by Pesavento (2000), was originally obtained for a cement paste heated at a slow rate and the parameters do not have a clear meaning. Enhanced relationships, possibly taking into account the heating rate and the gas pressure, are needed for improving the model. This subject will be discussed more in detail in Section 3.3.3.

2.2.7 Retention curves: $S_l - p_c$ relationship

Another key element when modeling transport processes in heated concrete are the sorption isotherms also known as water retention curves. These curves relate the capillary pressure to the quantity of water that is retained by the solid matrix.

The sorption isotherms, which will be the starting point for the numerical analyses performed in this work, are the ones used by many state-of-art models (Pesavento, 2000; Gawin et al., 2002a; Dal Pont et al., 2007; Meftah et al., 2012). These isotherms are described in the following.

Van Genuchten (1980) proposed, a relation between the capillary pressure and the liquid saturation:

$$p_c = p_c(S) = a \left(S^{-b} - 1 \right)^{\left(1 - \frac{1}{b}\right)} \quad (2.50)$$

where a and b are material parameters. Baroghel-Bouny et al. determined this parameters experimentally for four different types of concrete at ambient temperature (Baroghel-Bouny et al., 1999): Normal Strength Concrete (NSC), High Performance Concrete (HPC), Normal Strength Mortar (NSM), High Performance Mortar (HPM). It is worth noting that hysteresis is neglected in this formulation.

Coefficients	Material			
	NSC	HPC	NSM	HPM
a [MPa]	18.6237	46.9364	37.5479	96.2837
b [-]	2.2748	2.0601	2.1684	1.9540

Table 2.2: $S_l - p_c$ parameters at T_0

When Eq.2.50 is inverted, it reads:

$$S_l = \left(\left(\frac{p_c}{a} \right)^{\frac{b}{b-1}} + 1 \right)^{-1/b} \quad (2.51)$$

Pesavento (2000) extrapolated the original formulation given by Equation 2.51 to take into account high-temperature influence on the microstructure and surface tension:

$$S_l = \left(\left(\frac{E}{a(T)} p_c \right)^{\frac{b}{b-1}} + 1 \right)^{-1/b} \quad (2.52)$$

in which the parameter b is constant, while the parameter a is modified by the temperature-dependent parameter E , which accounts for the surface tension:

$$E(T) = \begin{cases} \left[\frac{T_{crit} - T_0}{T_{crit} - T} \right]^N & \text{if } T < T_{crit} \\ \frac{N}{z} E_0 \theta + \left[E_0 - \frac{N}{z} E_0 (T_{crit} - z) \right] & \text{if } T > T_{crit} \end{cases} \quad (2.53)$$

The parameter a is also modified due to the changes in the pore structure of concrete above 100 °C. Pesavento proposes the following formulation for $a(T)$:

$$a(T) = \begin{cases} a & \text{if } T \leq 100^\circ\text{C} \\ q_1 + q_2 & \text{if } T > 100^\circ\text{C} \end{cases} \quad (2.54)$$

where q_2 is a constant parameter related to the water critical temperature T_{cri} and q_1 is given by:

$$q_1 = (a - q_2) \left(1 + 2 \left(\frac{T - T_B}{T_{cr} - T_B} \right)^3 - 3 \left(\frac{T - T_B}{T_{cr} - T_B} \right)^2 \right) \quad (2.55)$$

where T_B is the temperature triggering the microstructure change ($T_B = 100^\circ\text{C}$). It is worth noting that no experimental evidence exists supporting the influence of the micro-structure change. A more detailed discussion is provided in Section 3.3.4.

Coefficients	Value
b	see Table 2.2
q_2	$7 \cdot 10^6$
Z	5
N	1.2
E_0	1

Table 2.3: $S_l - p_c$ parameters at high temperature

2.2.8 Effective stress principle

Following the development from Lewis and Schrefler (1998), the constitutive law of the solid phase introduced through the concept of effective (Bishop's) stress is:

$$\sigma' = \sigma + \mathbf{I}p_s \quad (2.56)$$

where σ is the total stress tensor, \mathbf{I} is the second order unit tensor and p^s is the average pressure of both the water and air on the solid skeleton given by:

$$p^s = S_g p_g + S_w p_w \quad (2.57)$$

Under the hypothesis of a non-deformable solid skeleton, Eq. (2.56) becomes:

$$\sigma' = \sigma + \mathbf{I}(S_g p_g + S_w p_w) \quad (2.58)$$

For greater generality, a corrective term known as Biot's constant (α) has to be introduced to account for the deformability of the solid skeleton. Therefore, a more general expression of the effective stress is assumed as follows:

$$\sigma'' = \sigma + \mathbf{I}\alpha(S_g p_g + S_w p_w) \quad (2.59)$$

Considering that $p_w = p_g - p_c$, Eq. 2.59 takes the final form:

$$\sigma'' = \sigma + \mathbf{I}\alpha(p_g - S_w p_c) \quad (2.60)$$

2.2.9 Strain decomposition

When a mechanically loaded concrete element is exposed to high temperature, the strains are usually treated as a superposition of different strain components which can be classified into three categories according to their origin:

- *mechanical strains* induced by a mechanical load (e.g. elastic strain, creep strain etc.)
- *thermo-hygral strains* induced by the physical and chemical process such as drying, dehydration, temperature rise etc. occurring in mechanically unloaded concrete elements. The most important components in this category are the thermal dilation and capillary shrinkage.

Thermal dilation strains can be expressed as:

$$d\varepsilon_{th} = \beta_s(T)dT\mathbf{I} \quad (2.61)$$

where β_s is the thermal dilation coefficient which for concrete can be approximated by a linear function of temperature:

$$\beta_s(T) = A_{B1}(T - T_0) + A_{B0} \quad (2.62)$$

where A_{B0} and A_{B1} are material constants.

Capillary shrinkage strains are modeled by means of the effective stress principle which considers the interaction between the solid and the two fluids (gas and water) and takes into account pressures applied on the solid skeleton p_s :

$$d\varepsilon_{sh} = \frac{\alpha}{K_T} \frac{d(p_s)}{dt} \mathbf{I} \quad (2.63)$$

where K_T is the bulk modulus of the porous medium.

- *Interaction strains* are the ones generated when a mechanical and a thermal load is applied simultaneously on a concrete element. In this case, the overall measured strain differs from the sum of all strains induced by each single mechanism. An example of interaction strains, is the additional elastic strain coming from the decrease of Young modulus with temperature. Other example is the thermal creep which is a time dependent strain during transient thermal processes due to temperature increase.

2.2.10 Damage constitutive law

Mazars' continuum damage model (Mazars, 1986) is one of the most used in literature for modeling concrete damage. This model relies on a single scalar variable d describing damage in an isotropic manner. Nevertheless, it distinguishes damage in traction and compression. The damage variable follows an evolution law based on a strain criterion. This equivalent strain allows representing a triaxial state in a uniaxial state. As the tensile strains (positive strains) are dominant in the cracking phenomenon of concrete, this equivalent strain ε_{eq} introduced by Mazars is defined from the positive principal strains as below:

$$\varepsilon_{eq} = \sqrt{\sum_{i=1}^3 (\langle \varepsilon_i \rangle_+)^2} \quad (2.64)$$

If $\varepsilon_{eq} > \kappa$ where κ is the damage threshold then:

$$d = \alpha_t d_t + \alpha_c d_c \quad (2.65)$$

where

$$d_t = 1 - \frac{k_0(1 - A_t)}{\varepsilon_{eq}} - \frac{A_t}{\exp[B_t(\varepsilon_{eq} - \kappa)]} \quad (2.66)$$

$$d_c = 1 - \frac{k_0(1 - A_c)}{\varepsilon_{eq}} - \frac{A_c}{\exp[B_c(\varepsilon_{eq} - \kappa)]} \quad (2.67)$$

where parameters α_t and α_c are weighing functions of the principal strains.

This model is local in the sense that local damage is calculated without any interaction with the neighborhood. This local formulation poses difficulties for modeling strain localization in the softening phase of the material behavior. Upon finite element modeling the strains localize in the weakest finite elements or the most loaded. Therefore, a mesh dependent response appears. From an energy point of view, the dissipated energy decreases with the size of element and eventually approaches to zero if the mesh is very fine (Bažant, 1976).

To prevent softening and localization issues, stresses at a material point shall not be described locally, but must take into account the interaction between defects (pores, microcracks) at the microstructural level (Pijaudier-Cabot and Bažant, 1987). The nonlocal theory applied to damage mechanics consists of averaging a mechanical quantity in its neighborhood using weight functions (Gaussian ones are mostly used).

In the Mazars' model, the local equivalent strain is replaced by an averaged equivalent strain over a volume Ω (Giry et al., 2011):

$$\varepsilon_{eq}(\mathbf{x}) = \frac{\int_{\Omega} \phi(\mathbf{x}-\mathbf{s}) \varepsilon_{eq}(\mathbf{s}) d\mathbf{s}}{\int_{\Omega} \phi(\mathbf{x}-\mathbf{s}) d\mathbf{s}} \quad (2.68)$$

where $\phi(\mathbf{x}-\mathbf{s})$ is the weight function defining the interaction between the considered point located at \mathbf{x} and the neighboring point located at \mathbf{s} inside the volume of the structure Ω . The most

widely used nonlocal weight function is adopted as the Gauss distribution function:

$$\phi(\mathbf{x}-\mathbf{s}) = \exp\left(-\left(\frac{2\|\mathbf{x}-\mathbf{s}\|}{l_c}\right)^2\right) \quad (2.69)$$

where l_c is the internal length of the model and $\|\mathbf{x}-\mathbf{s}\|$ the distance between the points located at \mathbf{x} and \mathbf{s} . The characteristic size of the weighting domain depends on the characteristic length l_c which is generally linked to the size of material heterogeneity.

2.3 Model Parameters

One of the criticisms of the advanced THM numerical models found in literature (Gawin et al., 1999; Dal Pont and Ehrlacher, 2004; Davie et al., 2006), including the one presented here, is their complexity, particularly the high number of parameters that characterize the model. Therefore, this section is dedicated to summarize in a synthetic way in a single table all these parameters (see Table 2.4).

It is worth noting that the model uses 60 parameters among which:

- 37 parameters are related to **physical properties of fluid phases** such as density, viscosity, thermal capacity etc. and their evolution with temperature. These properties are well established in literature.
- 8 parameters depend on the **properties of concrete at ambient temperature**. Among these properties, intrinsic permeability (K_0) remains the most debatable due to the difficulty in assessing reliable measurements experimentally. For the rest of these concrete properties (*porosity, conductivity, solid density etc.*) the experimental techniques are better established and thus the parameters can be considered trustworthy. In addition, this last group of parameters is also less influential.
- 15 parameters are related to the **evolution of constitutive properties at high temperature**. Among them, 10 cannot be directly measured. They concern the parameters linked with 3 constitutive laws: i) the water retention curves (*i.e.*, $S_l - p_c$ evolution) at high temperature ii) dehydration of concrete iii) permeability evolution at high temperature. The significance of these constitutive laws and a methodology for improving these relationships is presented in the Chapter 3 of this thesis.

2.4 Finite element formulation

2.4.1 Spatial discretization

The weak form of Eqs (2.25 - 2.28) was obtained in (Lewis and Schrefler, 1998; Pesavento, 2000) and is then discretized using the finite element method. The unknown variables are expressed in terms of their nodal values as:

$$p_g(t) = \mathbf{N}_{p_g} \bar{\mathbf{p}}_g(t) \quad p_c = \mathbf{N}_{p_c} \bar{\mathbf{p}}_c(t) \quad T = \mathbf{N}_T \bar{\mathbf{T}}(t) \quad \mathbf{u}(t) = \mathbf{N}_u \bar{\mathbf{u}}(t)$$

where $\bar{\mathbf{p}}_g(t)$, $\bar{\mathbf{p}}_c(t)$, $\bar{\mathbf{T}}(t)$, $\bar{\mathbf{u}}(t)$ are vectors of the nodal values of the primary variables at the time instant t , and \mathbf{N}_{p_g} , \mathbf{N}_{p_c} , \mathbf{N}_T , \mathbf{N}_u are vectors of shape functions related to these variables. After the finite element discretization, the weak form of the final system of Eqs. (2.25 - 2.28) can be expressed in the following matrix form:

$$\mathbf{C}_{ij}(\mathbf{Y}) \frac{\partial \mathbf{Y}}{\partial t} + \mathbf{K}_{ij}(\mathbf{Y}) \mathbf{Y} = \mathbf{f}_i(\mathbf{Y}) \quad (2.70)$$

Constant	Description	Values	Reference
Physical parameters			
$a_{0...5}, b_{0...5}$ ρ_0^l $C_{1...6}$ $C_{pa}; C_{pv}; C_{pl}$ D_{v0}, A_v, B_v ΔH_{vap} ΔH_{dehyd} M_v, M_a μ_v, μ_v, μ_l $\alpha_v, \beta_v, \alpha_l$ R	Mass density evolution coefficients Water density at T_0 Saturating vapor pressure coefficients Air/Vapor/Liquid thermal capacity Diffusion coefficients at T_0 Enthalpy of evaporation Enthalpy of dehydration Vapor, Air molar mass Fluids' viscosity at T_0 Fluids' viscosity evolution coefficients Universal constant ideal gas	see Table 2.1 998[kg/m ³] see sec 2.2.1 1005, 1805, 4181 [J · kg ⁻¹ · K ⁻¹] 2.58 × 10 ⁻⁵ [m ² /s], 1.667[-] 1[-] 2.672 × 10 ⁵ [J/kg] 2.5 × 10 ⁶ [J/kg] 0.018016[kg/mol], 0.028964[kg/mol] 17.17 × 10 ⁻⁶ , 8.85 × 10 ⁻⁶ , 1.002 × 10 ⁻³ [Pa · s] 4.73 × 10 ⁻⁸ , 2.22 × 10 ⁻¹¹ , 3.53 × 10 ⁻⁸ , 0.6612 [Pa · s] · K ⁻¹ 8.317 [J · mol ⁻¹ · K ⁻¹]	(Furish, 1997) (Furish, 1997) (ASHRAE, 2001) (ASHRAE, 2001) (Perre and Degiovanni, 1990) (Reid et al., 1987) (Dal Pont, 2004) (ASHRAE, 2001) (ASHRAE, 2001) (ASHRAE, 2001) (ASHRAE, 2001)
Material parameters at ambient conditions			
a, b A_s C_{ps} ϕ K_0 λ_{a0} ρ_s	$S_I - p_c$ coefficients Relative permeability evolution coefficients Solid thermal capacity Porosity Intrinsic permeability Thermal conductivity at T_0 ; coefficient Solid density at T_0	Table 2.2 0.6[-] 940 [J · kg ⁻¹ · K ⁻¹] 0.1368[-] 10 ⁻¹⁷ ÷ 10 ⁻²⁰ [m ²] 1.67[W · m ⁻¹ · K ⁻¹] 2611[kg/m ³]	(Baroghel-Bouny et al., 1999) (Van Genuchten, 1980) (Harmathy and Allen, 1973) - (Harmathy and Allen, 1973) -
Material parameters at high temperatures			
q_2, q_3, z, N, E_0 f_c, f_s, f_m $A_T; A_p; A_d$ A_ϕ A_{ρ_s} A_c A_λ	$S_I - p_c$ high-temperature coefficients Dehydration law coefficients Intrinsic permeability evolution coefficients Porosity linear-law coefficient Solid density linear-law coefficient Thermal Capacity linear-law coefficient Thermal conductivity linear-law coefficient	Table 2.3 200[kg/m ³], 0.24[-], 0.4[-] 0.025[-]; 0.368[-]; 1 - 4[-] 0.72 × 10 ⁻³ [-] 0.2235[-] 0.35[-] -0.005[K ⁻¹]	(Pesavento, 2000) (Pesavento, 2000) (Gawin et al., 1999), (Gawin et al., 2002b) - (Harmathy and Allen, 1973) (Harmathy and Allen, 1973)
Reference values			
p_{atm} T_∞ T_B T_{cr} T_0	Atmospheric pressure Ambient temperature Water boiling temperature at p_{atm} ∞ Critical temperature Reference temperature	101325[Pa] 293.15[K] 373.15[K] 647.15[K] 293.15[K]	- - - - -

Table 2.4: Numerical model parameters and reference values

with:

$$\mathbf{K}_{ij} = \begin{pmatrix} \mathbf{K}_{gg} & \mathbf{K}_{gc} & \mathbf{K}_{gt} & 0 \\ \mathbf{K}_{cg} & \mathbf{K}_{cc} & \mathbf{K}_{ct} & 0 \\ \mathbf{K}_{tg} & \mathbf{K}_{tc} & \mathbf{K}_{tt} & 0 \\ \mathbf{K}_{ug} & \mathbf{K}_{uc} & \mathbf{K}_{ut} & \mathbf{K}_{uu} \end{pmatrix} \quad \mathbf{C}_{ij} = \begin{pmatrix} \mathbf{C}_{gg} & \mathbf{C}_{gc} & \mathbf{C}_{gt} & \mathbf{C}_{gu} \\ 0 & \mathbf{C}_{cc} & \mathbf{C}_{ct} & \mathbf{C}_{cu} \\ 0 & \mathbf{C}_{tc} & \mathbf{C}_{tt} & \mathbf{C}_{tu} \\ 0 & 0 & 0 & 0 \end{pmatrix} \quad \mathbf{f}_i = \begin{pmatrix} \mathbf{f}_g \\ \mathbf{f}_c \\ \mathbf{f}_t \\ \mathbf{f}_u \end{pmatrix}$$

where $\mathbf{Y} = \{\bar{\mathbf{p}}_g, \bar{\mathbf{p}}_c, \bar{\mathbf{T}}, \bar{\mathbf{u}}\}$ is the approximated solution. \mathbf{C}_{ij} , \mathbf{K}_{ij} , and \mathbf{f}_i operators are given in Appendix A.

2.4.2 Temporal discretization

The integration in the time domain is carried out using the Wilson- θ method (Bathe and Wilson, 1972) which leads to a generic, linear system in the form:

$$\tilde{\mathbf{K}}_{\alpha\alpha} \Delta \mathbf{Y}_{\alpha}^{n+1} + \mathbf{K}_{\alpha\alpha} \mathbf{Y}_{\alpha}^n = \mathbf{f}_{\alpha}^{n+\theta} \quad (2.71)$$

where:

$$\Delta \mathbf{Y}_{\alpha}^{n+1} = \mathbf{Y}_{\alpha}^{n+1} - \mathbf{Y}_{\alpha}^n \quad (2.72)$$

$$\tilde{\mathbf{K}}_{\alpha\alpha} = \frac{\mathbf{C}_{\alpha\alpha}}{\Delta t} + \theta \mathbf{K}_{\alpha\alpha} \quad (2.73)$$

where Δt is the time step, the superscript n refers to time t_n and $n + \theta$ to time $t_n + \theta \Delta t$. The equations are linearized by means of the Newton-Raphson method within each time step.

2.4.3 Initial and Boundary conditions

For model closure the initial and boundary conditions need to be defined. The initial conditions specify the full field of variables in the domain Ω and in its boundary $\Sigma = \partial\Omega$:

$$\begin{aligned} p_g(t=0) &= p_g^0 \\ p_c(t=0) &= p_c^0 \\ T(t=0) &= T^0 \\ \mathbf{u}(t=0) &= \mathbf{u}^0 \end{aligned} \quad (2.74)$$

The problem consists in solving the thermo-hydro-mechanical problem for the state variables T , p_g , p_c , and \mathbf{u} satisfying the conservation equations in the domain Ω and the boundary conditions imposed on $\Sigma = \partial\Omega$. The boundary conditions can be of the first kind or Dirichlet boundary conditions on Σ_i^1

$$p_g = \bar{p}_g \text{ on } \Sigma_g^1 \quad (2.75)$$

$$p_c = \bar{p}_c \text{ on } \Sigma_c^1 \quad (2.76)$$

$$T = \bar{T} \text{ on } \Sigma_T^1 \quad (2.77)$$

$$\mathbf{u} = \bar{\mathbf{u}} \text{ on } \Sigma_u^1 \quad (2.78)$$

of the second type or Neumann's condition on Σ_i^2 :

$$-m_a \mathbf{v}_{a-s} \cdot \mathbf{n} = \left(K \frac{\rho_a k_{rg}}{\mu_g} \nabla p_g + D \rho_g \frac{M_v M_a}{M_g^2} \nabla \left(\frac{p_a}{p_g} \right) \right) \cdot \mathbf{n} = \bar{q}_a \text{ on } \Sigma_g^2 \quad (2.79)$$

$$-m_l \mathbf{v}_{l-s} \cdot \mathbf{n} = K \frac{\rho_l k_{rl}}{\mu_l} (\nabla p_g - \nabla p_c) \cdot \mathbf{n} = \bar{q}_l \text{ on } \Sigma_c^2 \quad (2.80)$$

$$-(\mathbf{q} + H_{vap} m_l \mathbf{v}_{l-s}) \cdot \mathbf{n} = \left(\lambda \cdot \nabla T + H_{vap} K \frac{\rho_l k_{rl}}{\mu_l} (\nabla p_g - \nabla p_c) \right) \cdot \mathbf{n} = \bar{q}_T \text{ on } \Sigma_T^2 \quad (2.81)$$

and of the third kind or Cauchy's mixed boundary conditions on Σ_i^3 :

$$-m_v \mathbf{v}_{v-s} \cdot \mathbf{n} = \left(K \frac{\rho_v k_{rg}}{\mu_g} \nabla p_g + D \rho_g \frac{M_v M_a}{M_g^2} \nabla \left(\frac{p_v}{p_g} \right) \right) \cdot \mathbf{n} = \bar{q}_v - h_g (\rho_v - \rho_v^\infty) \text{ on } \Sigma_c^3 \quad (2.82)$$

$$\begin{aligned} -(\mathbf{q} + H_{vap} m_l \mathbf{v}_{l-s}) \cdot \mathbf{n} &= \left(\lambda \cdot \nabla T + H_{vap} K \frac{\rho_l k_{rl}}{\mu_l} (\nabla p_g - \nabla p_c) \right) \cdot \mathbf{n} \\ &= \bar{q}_T - h_T (T - T_\infty) - \epsilon \sigma (T^4 - T_\infty^4) \text{ on } \Sigma_T^3 \end{aligned} \quad (2.83)$$

where $\Sigma = \Sigma_i^1 \cup \Sigma_i^2 \cup \Sigma_i^3$ for $i = T, c, g, u$. The terms $\bar{q}_a, \bar{q}_v, \bar{q}_l, \bar{q}_T$ are the imposed air, vapor, liquid, and heat fluxes, respectively, with the unit outward normal vector \mathbf{n} . The terms $\rho_v^\infty, \rho_a^\infty, T_\infty$ are the ambient densities and temperature, while h_T and h_g are the convective mass and energy exchange coefficient. Finally, ϵ is the emissivity and σ is the Stefan-Boltzman constant.

2.5 Implementation

2.5.1 A new monolithic procedure for THM problems

The numerical implementation done in the presented work is based on an existing implementation for concrete subject to severe loading conditions proposed in (Dal Pont et al., 2007). In that work, the system of equations has been solved in Cast3M using a partitioned procedure, also known as staggered solution strategy. The latter implies that within one time step every single equation is solved for a given variable of the system while keeping the others constant. The algorithm of this solution strategy can be found in (Dal Pont et al., 2011) and a simplified scheme is given in Figure 2.1.

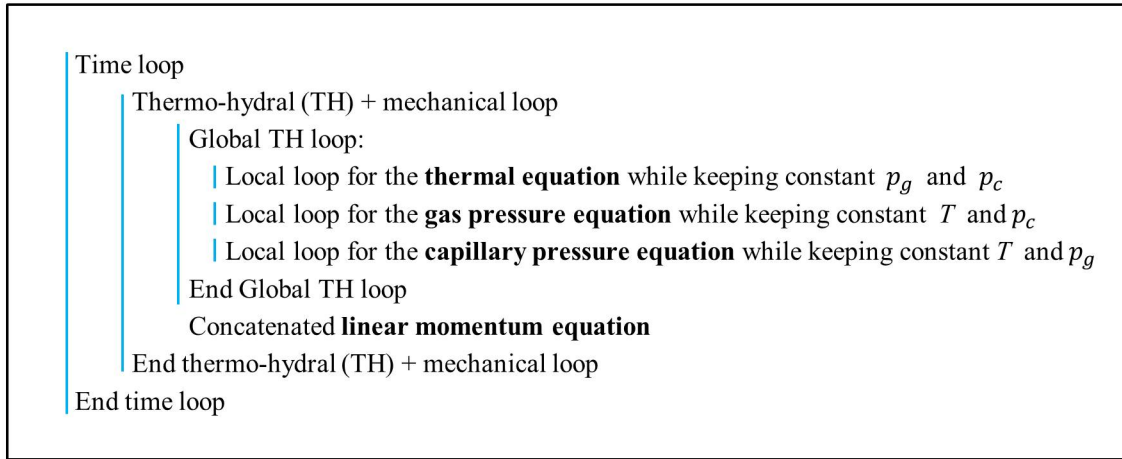


Figure 2.1: Scheme of the staggered solution strategy adopted in (Dal Pont et al., 2007)

While this iterative procedure is a relatively simple strategy to solve coupled problems, it has a high computational cost due to the nested iterations that characterize the procedure. The time efficiency becomes particularly important when considering 3D problems or mesoscopic scales. Inspired by the work of Sciumé (2013), a new solution strategy has been used in the present work for implementing the thermo-hydral numerical model in Cast3M. In this implementation, the solution of the system of equations of the TH part (thermo-hydral) is obtained by adopting a fully coupled monolithic approach. In contrast to the staggered approach, a new finite element (see Figure 2.2) allows computing the three state variables at each node at the same time loop, so only one level of iteration is required. A faster convergence is achieved thanks to the monolithic system. This reduces significantly the computational cost compared to the previous implementation. A numerical analysis for investigating the performance of the two approaches is presented in Chapter 3.

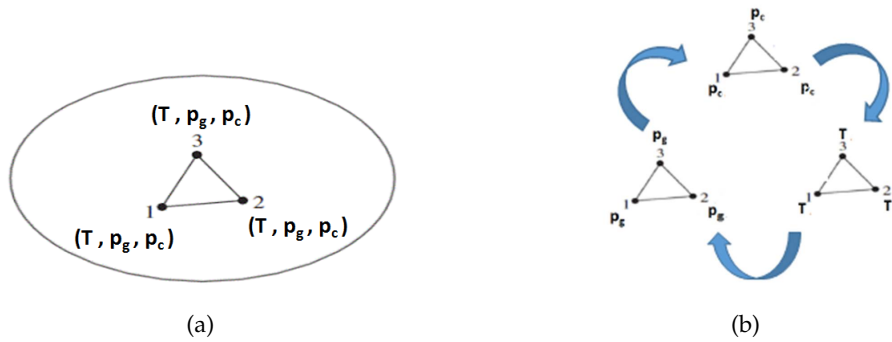


Figure 2.2: (a) Monolithic approach with a finite element with three unknowns in each node which are computed simultaneously, in contrast to (b) staggered approach where the sequential solution strategy is adopted

The linear momentum conservation equation can then be linked with the monolithic TH model (see Figure 2.3). In other words, the new computed TH solution can be used to compute the mechanical solution, which then gives a feedback to the hydral model (*i.e.*, damage-permeability coupling). This permits having a coupled thermo-hydro-mechanical model.

Some details of the numerical implementation in Cast3M are given in the next section.

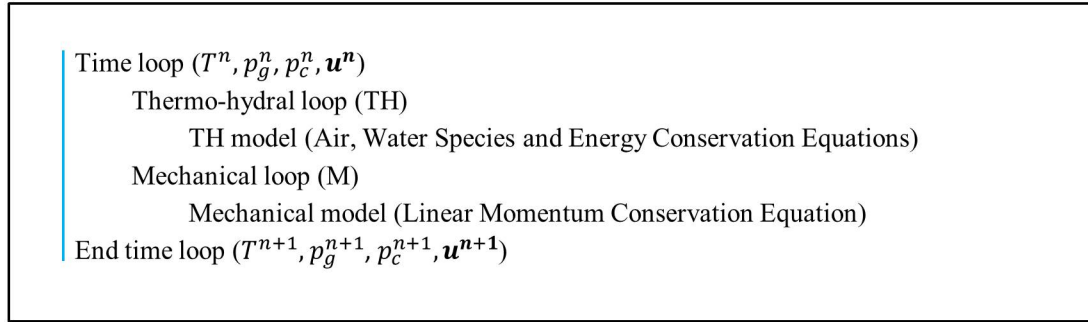


Figure 2.3: Scheme of the monolithic solution strategy proposed in this study

2.5.2 Cast3M Implementation

Cast3M is a computer code for the analysis of structures by the finite element method (FEM) and the Computational Fluid Dynamics (CFD) developed by French Atomic Energy Commission, CEA (2006). Cast3M has been originally developed for research in the mechanical domain in order to treat, design and analyze mainly nuclear structures, but also other industrial structures. In addition to its solver, Cast3M includes functions for model build-up (known as preprocessing) as well as functions for analyzing the results (post-processing).

Cast3M uses a high level macro-language, namely GIBIANE. The high flexibility that characterizes this language gives the opportunity to any user to adapt the GIBIANE script to the any kind of FE problem. More importantly, the sources of Cast3M are freely available for research purposes.

The implementation of the THM code has been done in version Cast3M 2015. A procedure file, namely MATETHM, was originally implemented in Cast3M based on a partitioned procedure developed by Dal Pont (2007) during his post-doctoral work at CEA. Even if the original MATETHM procedure was not fully operational, it allowed having the extra degrees of freedom on the finite element (see Figure 2.2(a)). In his PhD thesis, Sciumè (2013) made the procedure operational for using it in modeling the early age behavior of concrete and tumor growth.

Inspired by the work of Sciumè, a new monolithic procedure has been developed during this PhD for modeling the behavior of concrete at high temperature. The constitutive laws of the model, described in Section 2.2 are implemented in this new monolithic procedure. All the terms in Eq. 2.25 - 2.27, including the derivatives, are defined explicitly. Once all these terms are defined, matrices \mathbf{C} and \mathbf{K} , detailed in Appendix A, are built in the same procedure.

An important feature of Cast3M is the independence of each module (*i.e.*, thermo-hydral (TH), mechanical (M), fluid dynamics (CFD) etc.) which offers the user the chance to modify them individually. At the same time the user has the possibility to couple these modules. In the current study, this feature is useful for coupling the newly implemented TH procedure with the mechanical model. Given that Cast3M is naturally oriented to the solution of common problems encountered in nuclear/civil engineering, many mechanical constitutive laws (*e.g.* non-local damage, plasticity etc.) are available and can be coupled with the TH model. The mechanical model that has been used most in this project is the Mazars' damage model described in Section 2.2.10.

Cast3M standard procedure files such as TRANSNON, CHARTHER, PAS_DEFA, PASAPAS etc. have also been modified due to various issues and aspects of the coupled THM model implementation. An example of this kind of modifications is TRANSNON, which is a procedure in Cast3M used for solving the non-linear thermal problem. Originally, the procedure allowed only Dirichlet hydral boundary conditions. In the newly implemented code, the procedure has

been adjusted for being able to introduce mass flux boundary conditions as well, which is an important aspect in the THM model.

In addition to the newly created procedure files that describe the model and the adjusted procedure files that are related to boundary conditions, shape functions etc., Cast3M source files (*e.g.* idmatr.eso) have also been modified for achieving a more user-friendly code.

After having implemented the model, the THM analysis in Cast3M can be decomposed in 4 steps:

- (i) creating the geometry and choosing the mesh. Geometry and mesh can also be imported from another software, for example SALOME (<http://www.salome-platform.org/>)
- (ii) defining the input of the mathematical model (concrete properties, initial and boundary conditions etc.)
- (iii) problem solution using time and space discretization
- (iv) analysis and post treatment of the results. The results can be post-treated directly in Cast3M or exported in another post-processing software (Paraview, Matlab etc.)

While most of the numerical simulations presented in this work are performed using the implementation in Cast3M, the TH part of the numerical model has also been implemented in COMSOL Multiphysics (1998) in the framework of this research project. The details of this implementation are presented in the next section.

2.5.3 COMSOL Implementation

For verifying the Cast3M implementation, the same thermo-hydral numerical model has been implemented in another software, namely COMSOL, in the work presented in (Weber et al., 2016). The mechanical part of the model has not been implemented in COMSOL.

The software is capable of solving coupled physics phenomena simultaneously. In addition to conventional physics-based user interfaces, COMSOL also allows for entering coupled systems of partial differential equations (PDEs). The PDEs can be entered directly or using the so-called weak form. In the current study, the model has been implemented with the COMSOL weak form interface with dependent variables T , p_g , p_c . There are two main reasons for using the weak form interface in COMSOL. First, it provides full flexibility and second, the weak formulation was already existing from the implementation in Cast3M. The conservation equations 2.25 - 2.27, transformed to the weak form, are entered into the program. The closure equations were introduced as variables in the definition node. COMSOL substitutes recursively all variables and their derivatives in the conservation equations until they only depend on material parameters and primary variables. An alternative implementation using p_v instead of p_c as a primary variable was also implemented. For this implementation, the test functions in the weak form and the initial conditions need to be adapted. Boundary conditions are not affected. In the variables definitions, only the relation between p_v and p_c (Eq. 2.31) has to be inverted.

While both softwares, COMSOL and Cast3M, use a high-level implementation, COMSOL has the advantage of automatic recursive substitution of variables and evaluation of derivatives. On the other hand, Cast3M offers the possibility to choose among many existing mechanical models for concrete, including damage models, which can be easily coupled with the thermo-hydral model. Moreover, Cast3M is an open source software, free available for research.

2.6 Extension of the model to the mesoscale

2.6.1 Mesoscale modeling of concrete

In order to provide a more realistic description of concrete, the numerical model has been extended to mesoscale. This numerical modeling strategy goes to a lower observations scale considering separately the thermo-hydro-mechanical properties of each concrete constituent.

In the present work, concrete is treated as a bi-component material made of aggregates and cementitious matrix, occupying respectively the domain Ω_a and Ω_c with a perfect bond (Σ_{ac}) at the interface. The interfacial transition zone is neglected. The mesoscopic modeling scheme is presented in Figure 2.4.

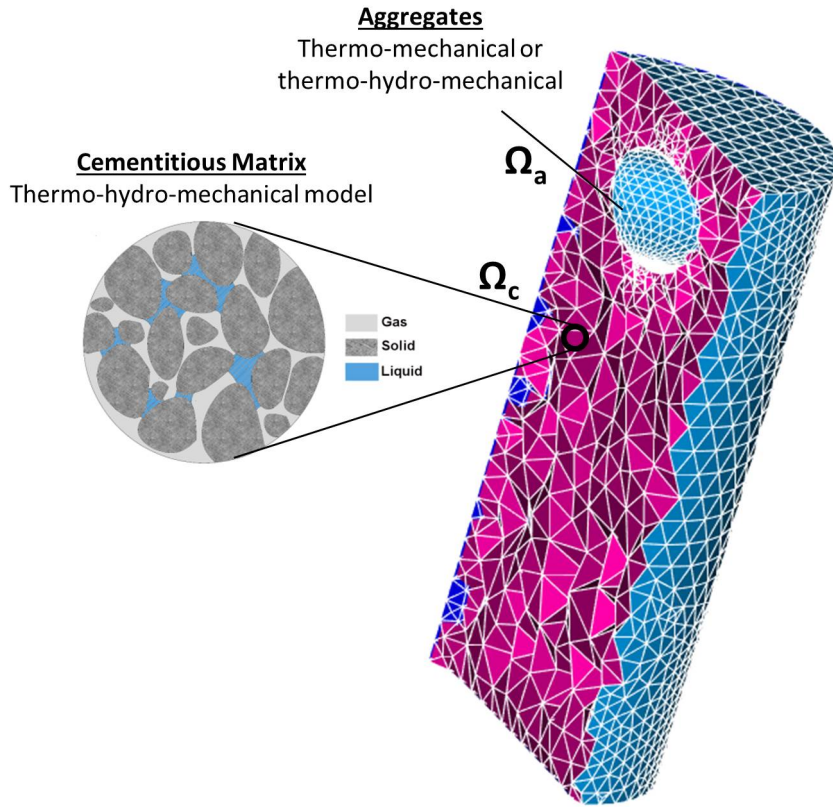


Figure 2.4: Mesoscale modeling scheme

Aggregates

For simplification, an aggregate can be modeled as an impermeable solid inclusion, so a thermo-mechanical model can be adopted for the description of its behavior at high temperature, neglecting hydal effects. However, in the case of permeable aggregates thermo-hydro-mechanical model can be easily considered for the aggregates. The heat transfer for the domain of the aggregates Ω_a is governed by the standard energy conservation equation:

$$\rho_a C_{p_{ag}} \frac{\partial T}{\partial t} - \nabla \cdot (\lambda_{ag} \cdot \nabla T) = 0 \quad (2.84)$$

where ρ_{ag} is the density, $C_{p_{ag}}$ is the thermal capacity, and λ_{ag} is the thermal conductivity of aggregates. Note that this energy conservation equation is the same as the one used for a porous medium (see Equation 2.27) if we neglect the hydal effects. This energy equation is coupled

with a mechanical model (linear elastic, damage etc), which describes aggregates' mechanical behavior at high temperature.

It is important to note here the differences in mechanical behavior at high temperature between aggregates and cement cementitious matrix (see Figure 1.7(b)). In contrast to the homogenized continuum models where the thermal dilation coefficient of concrete is approximated by a single linear function (see Equation 2.62), in mesoscopic modeling the thermal behavior of each constituent has been considered explicitly.

As the aggregates constitute 50-80% of the total volume of concrete, their thermal (β_s^{ag}) dilation has an impact on the thermal dilation of concrete (β_s). Aggregates used in a concrete mix come usually from sedimental rocks made of silicate or calcareous, metamorphic rocks like quartz or volcanic rocks like basalts, granites etc. All of this rocks exhibit a positive thermal dilation (*i.e.*, expansion) within the temperature range of a fire incident. The thermal expansion of aggregates depends mainly on the amount of silica. Rocks with a high percentage of silica, such as quartz, exhibit a high expansion. In contrast, rocks with low (or zero) percentage of silica, such as calcareous rocks, have a lower thermal expansion (Bažant and Kaplan, 1996). For the aggregates, the thermal dilation strains are expressed as:

$$d\varepsilon_{th}^{ag} = \beta_s^{ag}(T)dT \mathbf{I} \quad (2.85)$$

where $\beta_s^{ag}(T)$ is the evolution of the thermal dilation coefficient of aggregates with temperature.

Cementitious matrix

The cementitious matrix is considered as porous medium (solid skeleton, liquid, vapor, air), so the thermo-hydro-mechanical model described earlier in this chapter is used.

Concerning the thermal dilation, a study by Bažant and Kaplan (1996) on 4 different types of cement paste showed that the latter first expands, up to 150° and then shrinks beyond this temperature. The expansion is attributed to the volumetric expansion of water molecules and to the reduction of capillary forces at higher temperatures, whereas the shrinkage is attributed to the loss of free water (evaporation) and chemically bound water (dehydration) which induce important shrinkage strains.

The temperature, at which the cement paste changes behavior (*i.e.*, from expansion to shrinkage) depends on the heating rate. Hager (2004) found out that at a heating rate 1°C/min, this temperature is 120°C, whereas at a heating rate 0.5°C/min, this temperature increases to 180°C. This shows the dependence of the kinetics of dehydration on the thermal dilation of the cement paste.

Thus, the free thermal strains for cementitious matrix can be expressed as:

$$d\varepsilon_{th}^c = \beta_s^c(T)dT \mathbf{I} \quad (2.86)$$

where $\beta_s^c(T)$ is the evolution of the thermal dilation coefficient of cement with temperature.

2.6.2 Mesh Generation

For the generation of the finite element mesh two techniques have been used:

- 2D meshes are generated using a Fortran algorithm developed by Nguyen et al. (2010) and used in (Briffaut et al., 2013). The latter is able to generate the coordinates of the inclusions and their radius with a predefined grading curve. Then the aggregates are randomly distributed in the desired 2D space avoiding any possible overlapping. The center coordinates and radii of all the aggregates are loaded in Cast3M and used for the mesh generation of aggregates (see Figure 2.5(a)). Then the mesh of the cementitious matrix is generated (see Figure 2.5(b)) and finally the mesh of the two components is assembled

(see Figure 2.5(c)). In contrast to the original approach (Nguyen et al., 2010) where a diffuse mesh (material properties of each component projected on the shape functions of the finite element mesh) is used, in the present work an exact mesh is adopted.

- SALOME, which is an open source platform (<http://www.salome-platform.org/>), has also been used for mesh generation, especially for 3D cases. The mesh can then be imported in Cast3M.

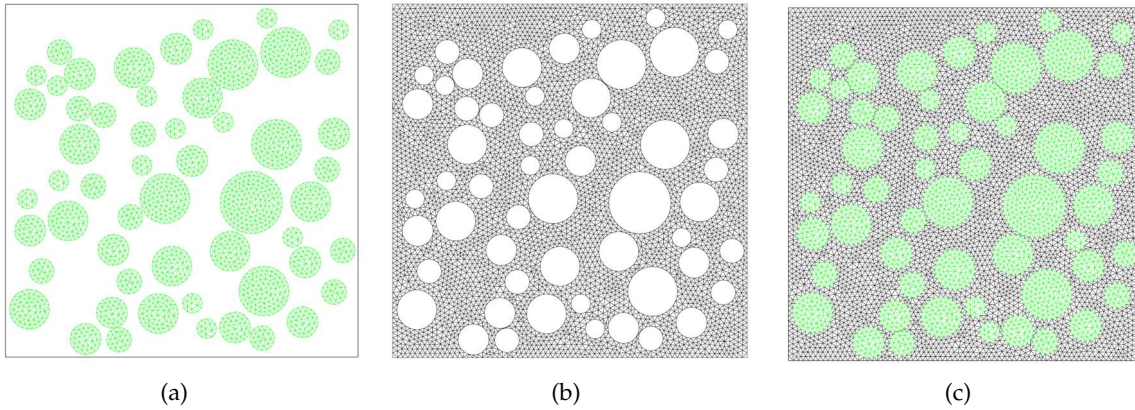


Figure 2.5: 2D mesh generation: (a) Center coordinates and radii of inclusions are used for their generation (b) After the inclusions, the cementitious matrix around it is meshed (c) Finally the mesh of the two components is assembled

Chapter 3

Application to experiments from literature

After the numerical implementation of the model, an important aspect to be evaluated is the time efficiency of the newly implemented codes (Cast3M and COMSOL) against the existing staggered procedure in Cast3M. Another important task is the validation of the numerical model. Similar to what is usually done in literature (Gawin et al., 2002a; Davie et al., 2006; Dal Pont et al., 2011; Meftah et al., 2012), the validation has been first based on standard measurements of temperature, gas pressure and/or global mass loss. Then, moisture migration measured in real time has been used for the first time for identifying and investigating some important constitutive laws. The above-mentioned issues have been treated through three case studies:

- Simulation of temperatures and gas pressures measured by Kalifa et al. (2000) presented in Section 3.1.
- Simulation of PTM tests by Mindeguia (2009) in the framework of RILEM TC256 presented in Section 3.2.
- Simulation of moisture migration measured by neutron radiography (Toropovs et al., 2015) presented in Section 3.3.

The experiments used in these three case studies have been mentioned earlier in this thesis (see Section 1.4.3) in the overview of the experiments on heated concrete. However, a more detailed description, necessary for feeding the numerical analysis, is presented for each case study.

After these three numerical analysis, 2D mesoscopic simulations for investigating the influence of concrete's heterogeneity are also presented in this chapter in Section 3.4.

It is important to note that all the numerical simulations presented in this thesis are performed on a standard laptop, i7-5500U CPU (2.4 GHz).

3.1 Simulation of temperature and gas pressure measurements

The objective in this case study is to verify the results of the newly implemented model against experimental measurements of temperature and gas pressure by Kalifa et al. (2000), as well as against the results of the already validated staggered approach (Dal Pont et al., 2007) in terms of numerical performance. A comparison with COMSOL implementation is also presented. In this first application, thermo-hydral (TH) simulations are performed and no mechanical calculation is involved.

3.1.1 Experiments by Kalifa et al. (2000)

In the study of Kalifa et al. (2000), a 300×300 mm concrete plate of 120 mm thickness is heated by a radiant heater placed 3 cm above the upper surface as shown in the experimental setup scheme in Figure 3.1. The lateral faces of the specimen are insulated with porous ceramic blocks. The specimen contains combined temperature and pressure sensors located at different depths. The concrete was a high performance concrete made with calcareous aggregates and with a compressive strength of 100 MPa. According to the reference, the heater had a temperature of 600°C . However, detailed information is not available. It is worth noting that not all the material parameters are provided in Kalifa et al. (2000). Therefore, the missing parameters are obtained from literature.

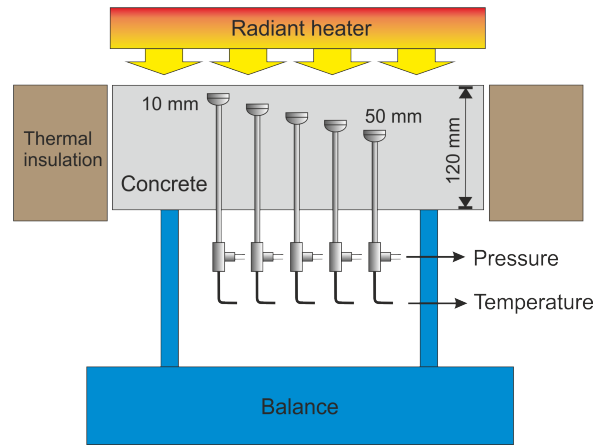


Figure 3.1: Experimental setup

3.1.2 Numerical Analysis

The simulations have been performed with a two-dimensional model consisting of 784 quadrilateral elements. The model setup is shown in Figure 3.2(a).

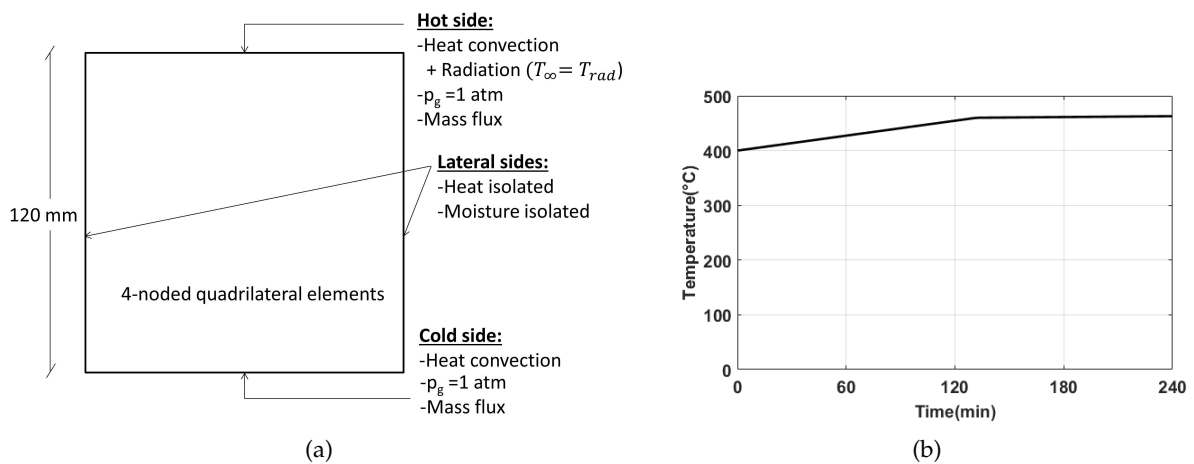


Figure 3.2: (a) Model setup and boundary conditions (b) Radiator temperature used in modeling

The lateral sides were closed to heat and mass transfer to simulate insulated conditions. To match the measured temperatures, it was necessary to use a radiator temperature as shown

in Figure 3.2(b). At the hot side, both convective and radiative heat exchange is considered simultaneously:

$$-\mathbf{n} \cdot (-k_{eff} \nabla T) = -h_T^{hot} (T - T_\infty) - \epsilon \sigma (T^4 - T_\infty^4) \quad (3.1)$$

At the cold side, heat exchange with the environment is considered:

$$-\mathbf{n} \cdot (-k_{eff} \nabla T) = -h_T^{cold} (T - T_\infty) \quad (3.2)$$

The heat transfer coefficient on the hot and cold side are respectively $h_T^{hot} = 8 \text{ W}/(\text{m}^2\text{K})$, $h_T^{cold} = 8.3 \text{ W}/(\text{m}^2\text{K})$, and $\epsilon = 0.85$. The heat transfer coefficients (h_T) are calibrated for fitting the temperature at 0 mm. For the hot side, the temperature T_∞ is the temperature of the radiant heater (see Figure 3.2(b)) and for the cold side side T_∞ corresponds to the room temperature. Mass transfer boundary conditions are the following. For the gas mixture, the pressure is fixed at atmospheric pressure.

$$p_g = p_{atm} \quad (3.3)$$

The vapor transport through the boundary is specified by the vapor flux and is expressed as:

$$-\mathbf{n} \cdot (m_v \mathbf{v}_{v-s} + m_l \mathbf{v}_{l-s}) = -h_g (\rho_v - \rho_v^\infty) \quad (3.4)$$

where the mass transfer coefficient is $h_g = 0.018 \text{ m/s}$. The ambient vapor density ρ_v^∞ is determined from the relative humidity.

It is worth noting that such kind of boundary condition was not possible in the original implementation and is not straightforward in Cast3M, as are the Dirichlet BC or the heat flux BC for instance. The modification of some Cast3M procedures, as mentioned in Section 2.5.2, made possible the application of a mass flux boundary condition in the newly implemented code.

3.1.3 Results and Discussion

Numerical results are compared with experimental results concerning gas pressure and temperature. The comparison of the temperature fields (see Figure 3.3) shows a good agreement with the experimental observations.

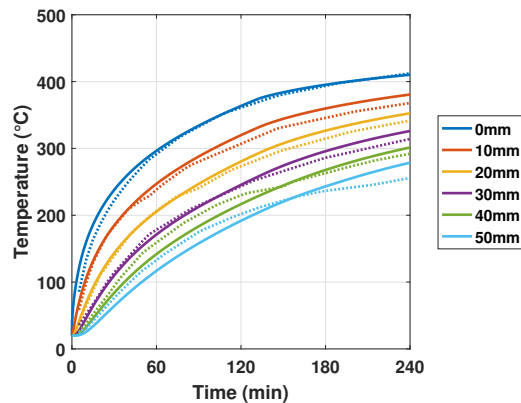


Figure 3.3: Simulation (solid lines) of temperature vs. experimental measurements (dotted lines) from Kalifa et al. (2000)

The pressure depends mainly on the vapor sources (evaporation, dehydration) and transport properties. Therefore the main constitutive laws of the model that have an influence on pressure are:

- *Evaporation/condensation* which is described by the water retention curves (see Section 2.2.7). Note that this is one of the main uncertainties of the model as there is no experimental evidence describing the behaviour at temperatures higher than 80 ° C (Poyet, 2016).
- *Dehydration* of the cement paste which is described by the constitutive law shown in Section 2.2.6.
- *Permeability* evolution adopted in these simulations is (Gawin et al., 1999):

$$K = K_0 \cdot 10^{A_T(T-T_0)} \left(\frac{p_g}{p_{atm}} \right)^{A_p} \quad (3.5)$$

where $K_0 = 7.5 \cdot 10^{-20} \text{ m}^2$, $A_T = 0.005$ and $A_p = 0.368$. Permeability, which is the main tuning parameter, has been found by calibrating the pressure curves.

When looking at the gas pressure profiles (see Figure 3.4), the position and the value of the peaks are in good agreement with the experiments, except for the pressure value at 30 mm (which is believed to be due to experimental anomalies as stated by the authors (Kalifa et al., 2000)). However, the width of the curves from the numerical results is wider. The pressure profiles from the experiments are narrower, most probably due to pressure post peak decrease coming from the formation of cracks, which is not contained in these numerical simulations.

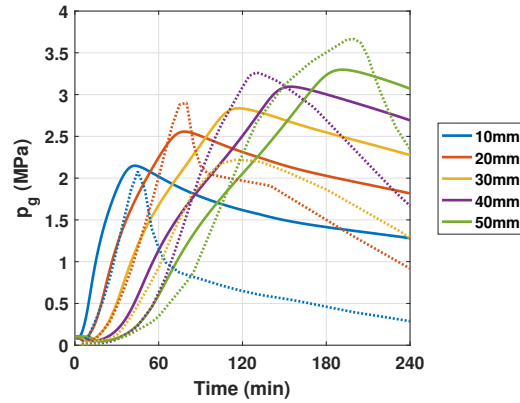


Figure 3.4: Simulation (solid lines) of gas pressure evolution vs. experimental measurements (dotted lines) from Kalifa et al. (2000)

3.1.3.1 Comparison: Monolithic vs. Staggered approach

The numerical analysis has also been validated against an existing numerical code using the staggered solution strategy (see Section 2.5 for more details on this existing code). The simulations are run using the same discretization in time and space for both codes. While the results are identical, the numerical performance of the newly implemented code (using the monolithic approach) is considerably better. The numerical simulations run on a standard laptop, i7-5500U CPU (2.4 GHz), lasted 35 min for the monolithic code and 15 hrs for the staggered one.

In other words, the newly implemented code is 20-30 times faster than the previous implementation (Dal Pont et al., 2007). This enhanced numerical performance makes the newly implemented code a powerful tool for performing 3D simulations, including mesoscopic geometries.

3.1.3.2 Comparison: Cast3M vs. COMSOL Multiphysics

The same thermo-hydral numerical model has been implemented in another software, namely COMSOL Multiphysics (1998), in the work presented in (Weber et al., 2016). As shown in Figure 3.5, the results from Cast3M compare well with COMSOL. In terms of computational efficiency, for a fixed time step the computational time of the two softwares is similar.

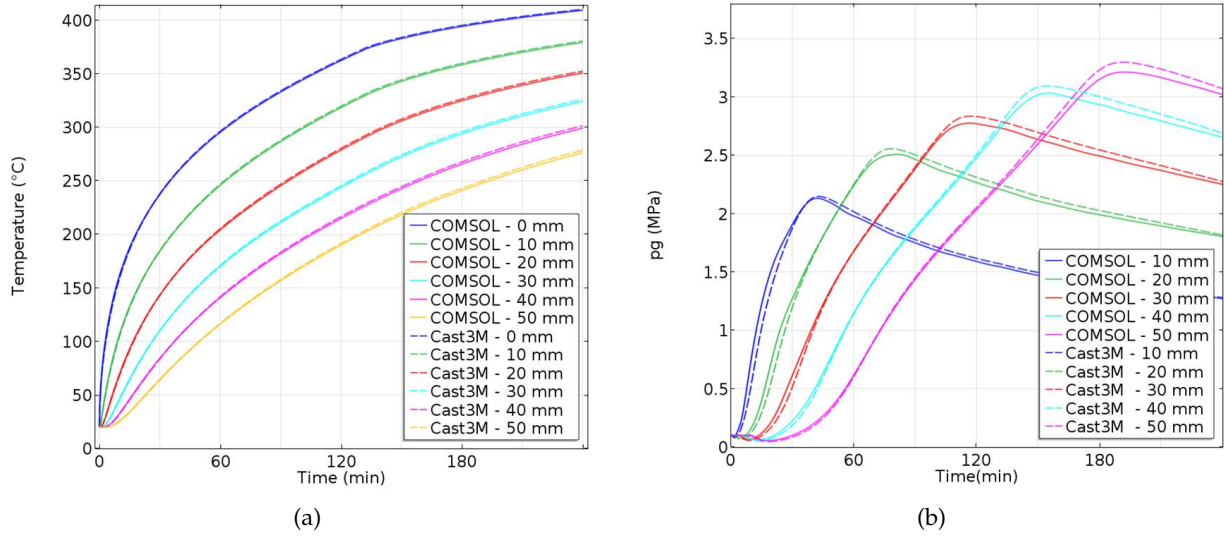


Figure 3.5: (a) Temperature and (b) Gas Pressure comparison between Cast3M and COMSOL

An alternative implementation using p_v instead of p_c as a primary variable was also implemented in COMSOL. The main objective was to check if the alternative state variable (p_v) would influence the results and the computational time. For this implementation, the initial conditions have to be adapted to the new state variable p_v and the relationship between p_v and p_c (see Equation 2.31) has to be inverted. The results are very similar as shown in the comparison for the gas pressure in Figure 3.6.

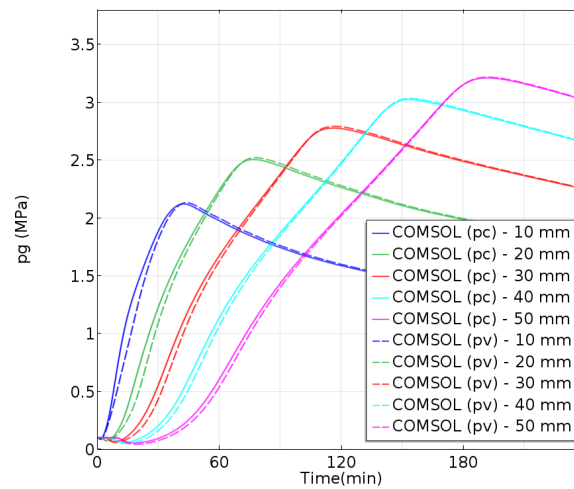


Figure 3.6: Gas pressure calculated from two different COMSOL implementations: one using p_c , the other p_v as state variable (Weber et al., 2016)

Given that there is no difference, neither in results, nor in computational time, the original implementation (with state variables p_g and p_c) has been retained in the following numerical simulations in this thesis.

3.1.4 Conclusions: Application 1

From this first application using a TH model, the following conclusions can be made:

- The numerical model implemented in this thesis in Cast3M, using a monolithic approach, is 20-30 times faster than the existing code which uses a staggered solution strategy.
- The model is able to predict the measured temperatures and pressures after the calibration of permeability which is the main tuning parameter.
- The analogous implementation of the same model in COMSOL gives the same results (as expected) with a similar computational time with respect to the newly implemented code in Cast3M. Changing the state variable p_c to p_v does not affect the results.

3.2 Simulation of PTM tests by Mindeguia (2009) in the framework of RILEM TC256

The objective of this study is to verify the results of the numerical model against a similar experiment as in (Kalifa et al., 2000) performed by Mindeguia (2009). The difference with the first application (Section 3.1) is that in this study more material properties, including their evolution with temperature are available. This limits the assumptions to be made on the material properties and gives the possibility to verify the prediction capabilities of the model.

This numerical study is a benchmark proposed by the Technical Committee (TC 256) of RILEM which focuses on fire spalling of concrete. This work has been presented in the 5th International Workshop on Concrete Spalling due to Fire Exposure (Dauti et al., 2017b).

3.2.1 Experiments by Mindeguia (2009)

The experimental setup is the same as in Figure 3.1. The tests were carried out on prismatic samples ($300 \times 300 \times 120 \text{ mm}^3$) heated on one side. Among different types of concrete tested, two of them are shown here. The reference concrete is an ordinary concrete (B40), which has been used for the construction of a tunnel in France in 2005. The second concrete is fabricated by only varying the w/c ratio (by increasing cement content and reducing water content) and by fixing the aggregates quantity constant. The two mixtures, as well as the main characteristics of the concretes at 20°C, are presented in Table 3.1.

	Unity	B40	B60
Cement CEM II/A-LL 42.5 R PM-CP2 (C)	kg	350	550
8/12.5 calcareous gravel (<i>Chalonnnes sur Loire</i>)	kg	330	330
12.5/20 calcareous gravel (<i>Chalonnnes sur Loire</i>)	kg	720	720
0/2 siliceous sand (<i>Chazé</i>)	kg	845	845
Water (W)	kg	188	165
Superplasticizer (PRELOM [®] 300)	% by mass of C	1	3
w/c ratio	/	0.54	0.30
28 days compressive strength	MPa	37	61
28 days modulus of elasticity	GPa	36	40
28 days tensile strength	GPa	2.4	3.8

Table 3.1: Concrete mixes studied in (Mindeguia, 2009)

The material properties such as porosity, permeability, young modulus, thermal conductivity etc. and their evolution with temperature have been measured experimentally (see Figure 3.7). In the first application, it was observed that the main model tuning parameter for predicting the measured pressures is the permeability. For that reason the permeability measurements obtained by Mindeguia (2009) and shown in Figure 3.7(b) are described below.

The gas permeability of concrete is measured through a constant pressure permeameter ("CEMBUREAU" device). The procedure consists in measuring the gas flow (di-nitrogen) percolating through a concrete disk (150 mm in diameter and 50 mm thick). For each measurement, two levels of gas pressure were applied in order to determine the intrinsic permeability of the material according to the Klinkenberg's approach (Klinkenberg, 1941). It should be mentioned that more levels of gas pressure are usually applied in literature when performing gas permeability measurements with the CEMBUREAU device, e.g. RILEM (1999) recommends at least 3 levels, Dal Pont (2004) uses 4 levels and 5 levels are suggested in (Kollek, 1989).

The evolution of the concrete gas permeability with temperature is estimated by applying the thermal cycles at 120, 250, 400 and 600 °C and then performing the measurement after 6 hrs of stabilization. Therefore, the permeability measurements are *residual* measurements.

The effect of the thermal loading was studied for B40 and B60 for three types of heating: slow, moderate and high heating. Inhere, only the moderate type of heating is considered. The latter is defined as following: the radiant panel is controlled in such a way that the temperature measured inside the panel reaches 600 °C as fast as possible. The temperature is then kept at 600 °C during 5 hours.

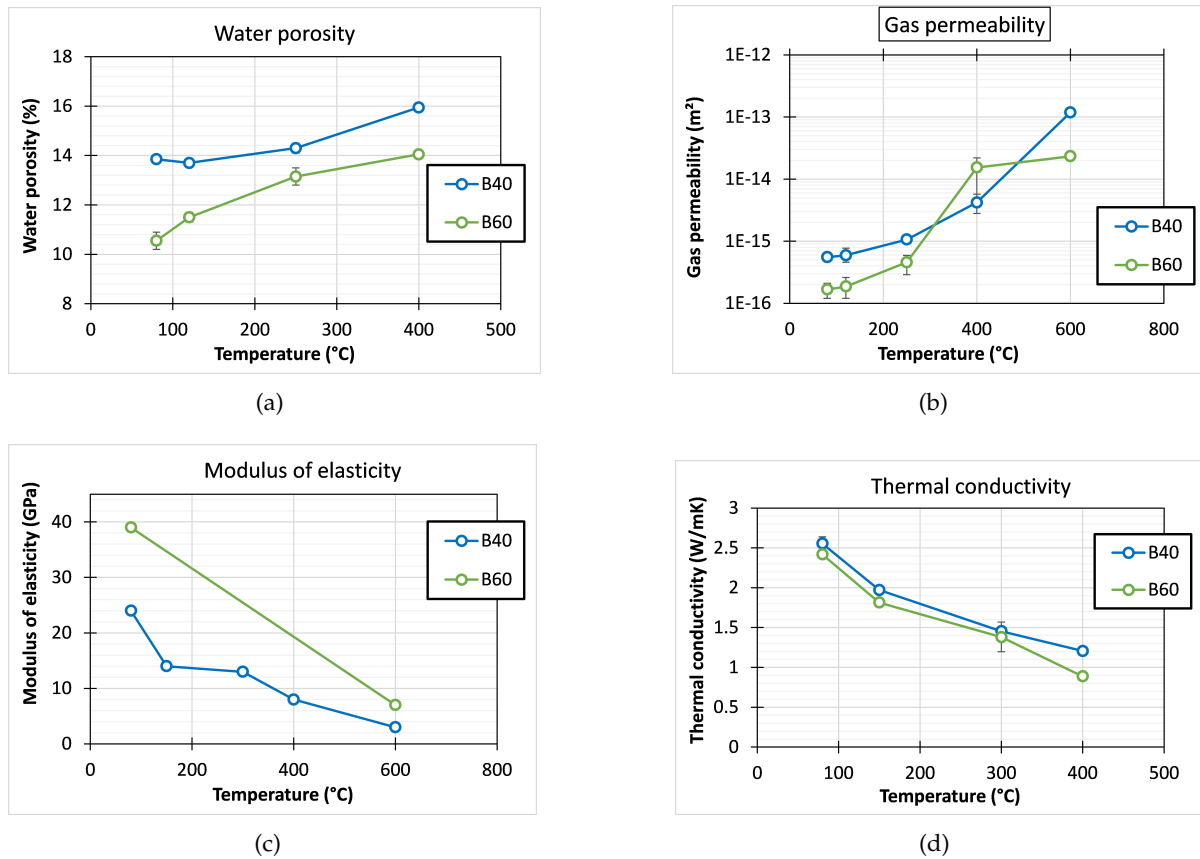


Figure 3.7: Evolution of material properties with temperature measured experimentally in (Mindeguia, 2009)

3.2.2 Numerical Analysis

The geometry adopted for the numerical simulations is 2D. The model setup is shown in Figure 3.8(a). The boundary conditions are the same as the first application (see Section 3.1.2). The radiator temperature has been adjusted as shown in Figure 3.8(b). The material properties conforming to the experiments have been adopted.

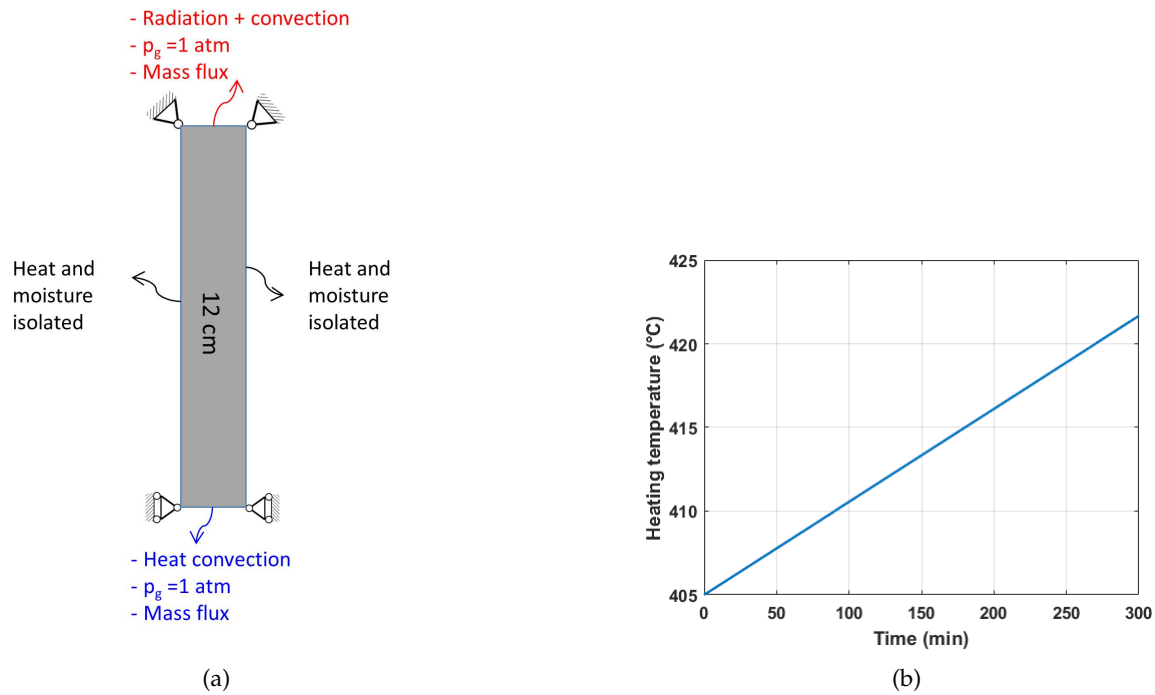


Figure 3.8: (a) Model setup and boundary conditions (b) Radiator temperature used in modeling

3.2.3 Results and discussion

In the following, the numerical results in terms of temperature, gas pressure, and mass loss will be compared with the experimental results.

3.2.3.1 Temperature evolution

In Figure 3.9 and the evolution of temperature at different positions is presented. The numerical results (solid lines) are in good agreement with the experimental observations (dotted lines) for both concretes.

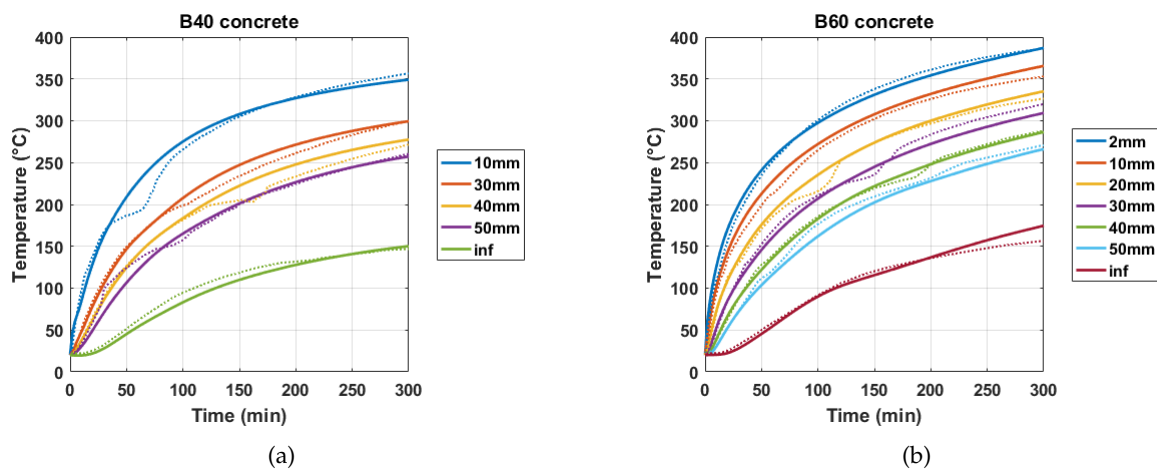


Figure 3.9: Comparison of predicted temperatures (solid lines) with experimental measurements (dotted lines) for (a) B40 and (b) B60 concrete

3.2.3.2 Gas pressure evolution

In Figure 3.10 the evolution of gas pressure at different positions is presented. In this numerical simulation, the permeabilities measured experimentally have been adopted. Under these conditions, the numerical results (solid lines) are not in good agreement with the experiments (dotted lines). The pressure results are about one order of magnitude lower than the experimental measurements.

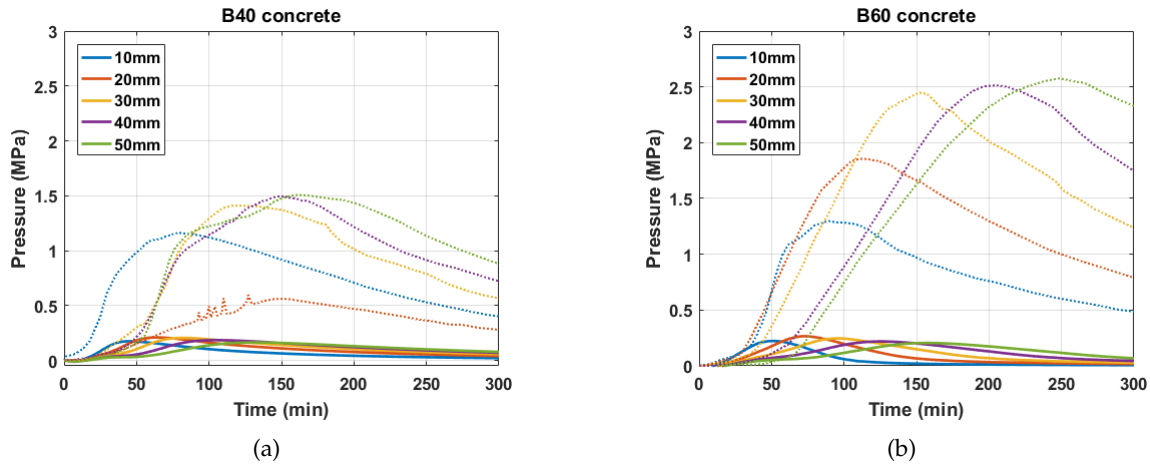


Figure 3.10: Comparison of predicted pressure profiles (solid lines) with experimental measurements (dotted lines) for (a) B40 and (b) B60 concrete using measured permeability

Permeability has been modified as in Figure 3.11 for a better agreement of pressures. Notice that the permeability has been plotted in logarithmic scale. The same evolution of permeability with temperature is maintained for B40 concrete, whereas for B60 concrete a different evolution is adopted. The rest of the material properties are as measured. In the modified permeability function, the initial value is $k_0 = 1.5 \times 10^{-17} \text{ m}^2$ for B40 concrete mix and $k_0 = 6 \times 10^{-18} \text{ m}^2$ for B60 concrete mix. Figure 3.12 presents the evolution of gas pressure at different positions. After having found out that the permeability has to be reduced for reaching the measured pressures, it is important to see the influence of permeability in terms of mass loss, presented in the next section.

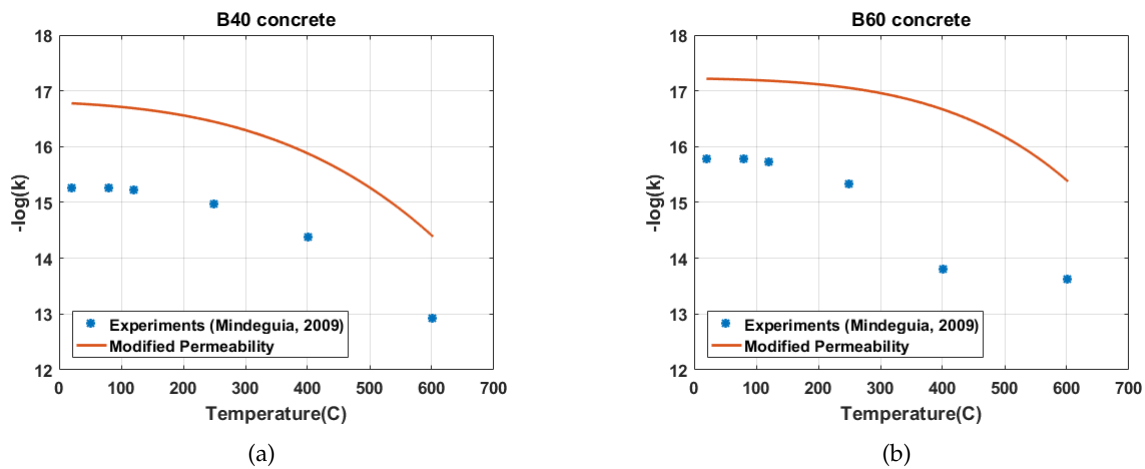


Figure 3.11: Permeability evolution for (a) B40 and (b) B60 concrete highlighting the reduced permeability (solid lines) in order to reach the measured pressure

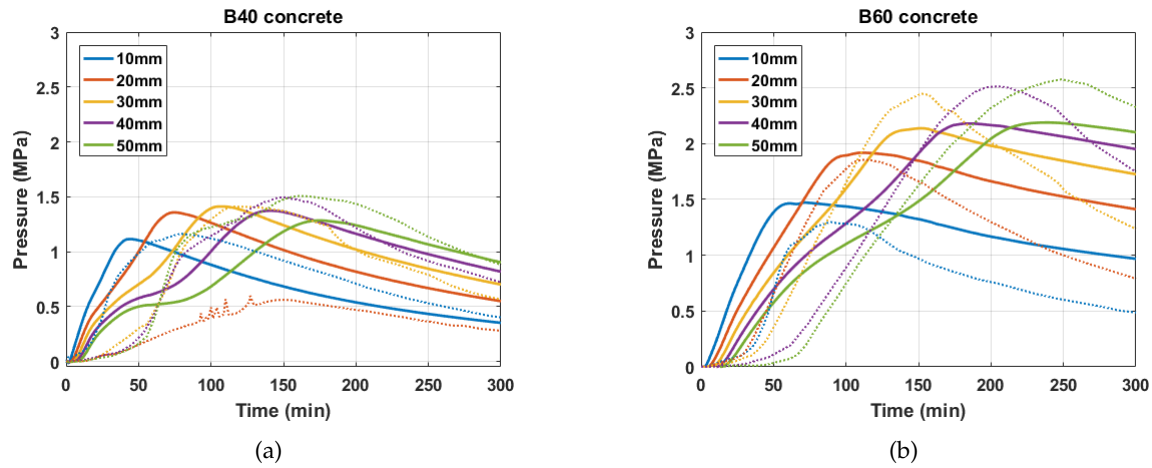


Figure 3.12: Comparison of predicted pressure profiles (solid lines) with experimental measurements (dotted lines) for (a) B40 and (b) B60 concrete using modified permeability

Before presenting the mass loss result, vapor pressure at different depths is plotted against temperature in Figure 3.13. It is observed that vapor pressure at all the depths follows the saturation vapor pressure until about 200°C and then a pressure drop is observed. Maximum pressure happening at 200°C have been observed in similar experimental and numerical studies in literature (Kalifa et al., 2000; Gawin et al., 2011a) for similar type of concrete.

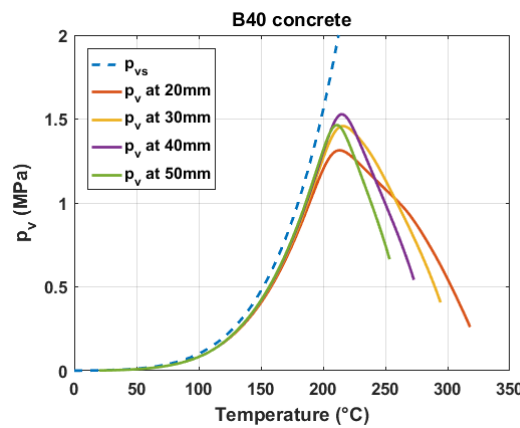


Figure 3.13: Dependence of vapor pressure on temperature

3.2.3.3 Mass loss evolution

In Figure 3.14, the mass loss for both concrete mixes is presented. The solid lines present the results when using the measured permeabilities given in the benchmark. Under these conditions, the numerical results are not in good agreement with the measured mass loss (dotted lines). When the modified permeability as in Figure 3.11 is used in the simulations, the results (dashed lines) are in better agreement with the measured mass loss.

Thus the modification of the permeability improved both the pressure and the mass loss.

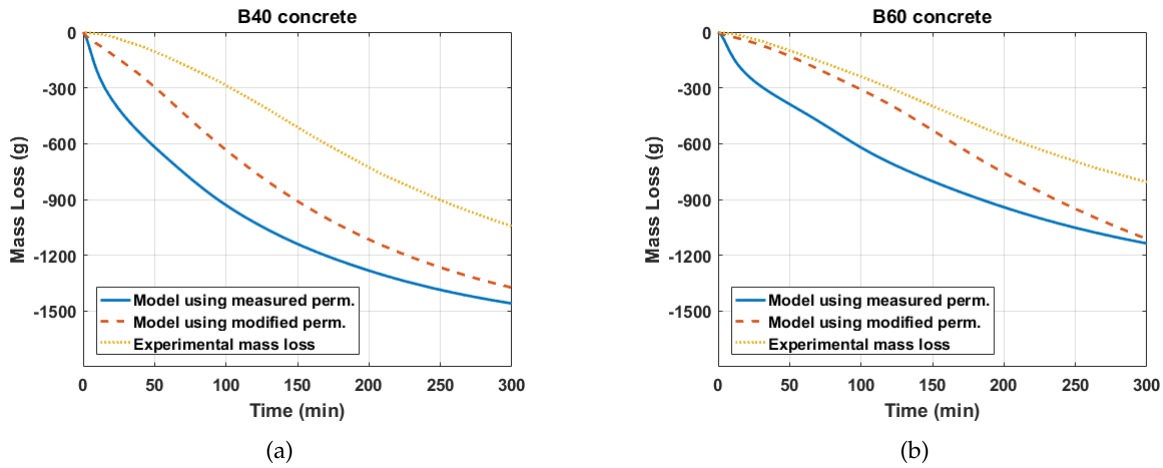


Figure 3.14: Comparison of predicted global mass loss (solid lines) with experimental measurements (dotted lines) for (a) B40 and (b) B60 concrete

3.2.4 Discussion on Intrinsic Permeability

A significant discrepancy on predicted and measured pressures is observed when the gas permeability measurements are used in the numerical model. The intrinsic permeability has to be reduced by a factor of 37 for B40 concrete and 28 for B60 concrete for a better comparison with temperatures.

The reason for the discrepancy can be attributed to the measurements of intrinsic permeability of concrete. The latter is dependent on the fluid (liquid water or gas) employed in the experimental procedure. Theoretically, if the fluid were neutral with respect to the material, the liquid-water intrinsic permeability (k_l) and the gas intrinsic permeability (k_g) should be the same because they correspond to intrinsic properties of the material and are only dependent on the pore structure. However, in (Baroghel-Bouny, 2007), experimental intrinsic gas permeabilities obtained in the case where $S_w = 0$ (i.e., for dry samples) have been compared with measured liquid water permeability (i.e., $S_w = 1$) and it was found out that the gas permeability is several orders of magnitude higher than the liquid water permeability. This has also been observed in other studies in literature (Bamforth, 1987; Loosveldt et al., 2002). Gas permeability measurements, can sometimes be influenced by cracking during the drying process prior to tests. On the other hand, liquid permeability measurements are affected by the water-solid interactions, such as ongoing hydration, crack healing, self-sealing or leaching, during the course of liquid water permeability testing in particular if the test takes a long time (Baroghel-Bouny, 2007).

In the experiments by Mindeguia (2009), the measured intrinsic gas permeability for B40 concrete and B60 concrete are between $10^{-15} - 10^{-16} \text{ m}^2$ (see Figure 3.7(b)). These values seem to be higher than other measurements of intrinsic gas permeability found in literature (Dal Pont and Ehrlicher, 2004; Baroghel-Bouny, 2007; Hamami et al., 2012; Zhang, 2014; Ezzedine El Dandachy et al., 2016) which report values between $10^{-16} - 10^{-17} \text{ m}^2$. The modified intrinsic permeabilities (see Figure 3.11) obtained from the numerical analysis presented above also fall in the latter range.

The numerical analysis presented in this section shows that intrinsic permeability is extremely important in controlling the pore pressure in heated concrete. It points out the need of assessing reliable measurements of permeability. More importantly, it points out the need of new experimental methods in

the context of spalling, as an alternative to pressure measurements, the prediction of which is strongly depended on permeability, a parameter difficult to asses.

3.2.5 Mechanics

Mazars' damage model, described in Section 2.2.10, has been used for describing the deterioration of the material. Thermal dilation strains as well as capillary shrinkage strains are considered in the mechanical model (see Section 2.2.9 for more details). Damage-dependent permeability has been adopted in the simulations for B40 concrete (Gawin et al., 2002b):

$$k = k_0 \cdot 10^{A_T(T-T_0)} \left(\frac{p_g}{p_{atm}} \right)^{A_p} \cdot 10^{A_d d} \quad (3.6)$$

where $A_T = 0.00025$, $A_p = 0.368$ and $A_d = 1$. The experimental-numerical comparison, shown in Figure 3.15(a), is satisfying when the same adjusted permeability $k_0 = 1.5 \cdot 10^{-17} \text{ m}^2$, is used. Damage is computed using the mechanical properties given in the benchmark and is presented in Figure 3.15(b). The damage of the material reaches about 70% at the heated surface after 5 hours of heating.

While there is no essential difference to the pressure results without the mechanical part presented in Figure 3.12(a), the numerical analysis presented in this section shows that the damage-dependent permeability function provides satisfying results.

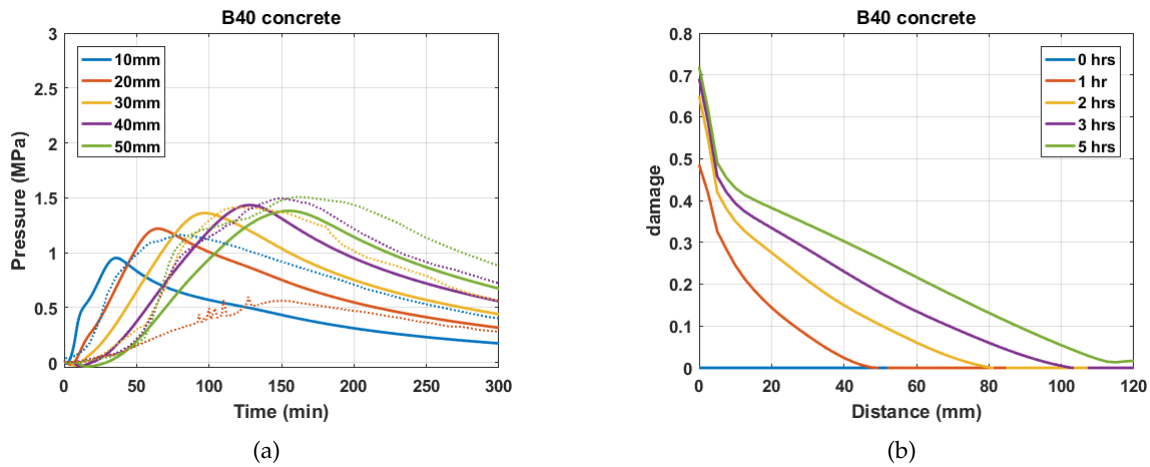


Figure 3.15: Results when using a mechanical model: (a) Pressures (b) damage

3.2.6 Conclusions: Application 2

From this second application, the following conclusions can be made:

- The measured permeability has to be reduced for both concretes to reach the measured pressures. The discrepancy might be explained by the gas permeability measurements reported in the experimental study employed in this numerical analysis which are higher than analogous measurements found in literature.
- Mass loss from the numerical model is larger. The reduced permeability also improves the mass loss results.

- A mechanical model has been used for computing damage in the concrete. The latter, when coupled with permeability, gives satisfying pressure results which are similar to the TH model.
- The numerical analysis shows the significance of permeability in predicting the pore pressures and mass loss in heated concrete. At the same time, it points out the need for alternative experimental techniques in the context of spalling for the validation of the numerical models.

3.3 Simulation of moisture migration measured by neutron radiography

In the first two applications, the numerical analyses are based on temperature, gas pressure and/or global mass loss results, as commonly done in literature (Gawin et al., 2002a; Davie et al., 2006; Dal Pont et al., 2011; Meftah et al., 2012). In the third application, data from neutron imaging experiments, which is a non-destructive method for measuring moisture content, have been used for the first time in investigating some critical constitutive laws adopted in modeling concrete at high temperature.

The experimental data used in this numerical analysis (neutron radiography, thermogravimetric analysis (TGA), porosity measurements (MIP) etc.) has been obtained in the framework of a project dealing with behaviour of concrete at high temperature by research scientists at Empa Laboratories in Switzerland. The details of the neutron radiography experiments can be found in (Toropovs et al., 2015), whereas some extra experimental data about TGA and MIP were presented later, along with the numerical analysis, in (Dauti et al., 2018a).

3.3.1 Experimental data from neutron radiography

In (Toropovs et al., 2015), a combination of measurements was performed simultaneously: moisture profiles via neutron radiography, temperature profiles with embedded thermocouples and pore pressure evolution with embedded pressure sensors. Different samples, with and without polypropylene (PP) or superabsorbent polymers (SAP) were tested. For the present analysis, a case of a plain high-performance concrete (HPC) sample is considered with dimensions $100 \times 100 \times 25 \text{ mm}^3$ and a mix composition given in Table 3.2. After casting, the samples were sealed in plastic bags and stored at $20 \pm 0.3^\circ \text{C}$ and $95 \pm 3\%$ RH until the age of about 3 weeks.

Cement CEM I 52.5 R	488
Silica fume	122
Aggregate 0–4 mm	1582
Superplasticizer Sika 20HE	8.54
Water	189.1
w/b total	0.31
Total density	2389.64

Table 3.2: Mix composition [kg/m^3]

Mercury Intrusion Porosimetry (MIP) tests were carried out on HPC after it was exposed to different temperatures. Larger samples of concrete were crushed into pieces of 2-5 mm after 28 d of sealed curing. Next, they were heated to a given temperature in an oven with a heating rate of $16.2^\circ \text{C}/\text{min}$ and kept at the desired temperature for 2 h. Afterwards they were left to cool down to room temperature while in the oven. In order to remove possible free water before the intrusion of mercury, the samples were immersed in isopropanol for 4 d and dried at 50°C for 2 d. MIP tests at pressure up to 200 MPa were run. Each test was run on about 1-1.2 g of small chunks (about 7-10 pieces) of mortar cut with pincers from the thermally-treated larger pieces. One MIP test was carried out for each exposure temperature. The total porosity accessed in the samples previously exposed to different temperatures is presented as a function of temperature in Figure 3.16. A linear fit (with $R^2 = 0.81$) gives the following temperature-dependent porosity function:

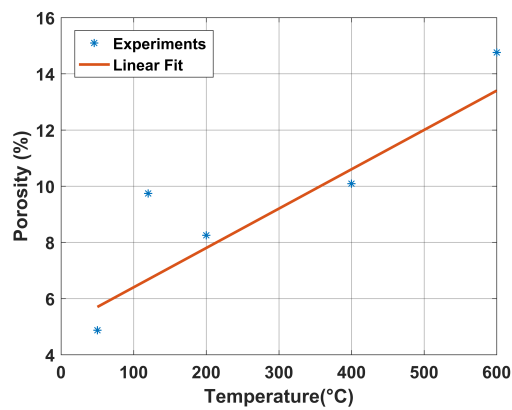


Figure 3.16: Porosity measurements

The arrangement of the sample during the neutron test is shown in Figure 3.17. The sample was heated from below and insulated against moisture and heat loss on the side walls. For the moisture insulation, high-temperature adhesive aluminium foil with working temperature up to 316°C was used. The heating plate was programmed to reach 550°C in 12 min and hold the temperature for the following 2 hours. Thermocouples have been embedded into the mortar at nominal distances of 5, 10, 15, 25, 35, 45, 55, 65, and 95 mm from the heated face. The exact position of the thermocouples has been determined from an X-ray scan.

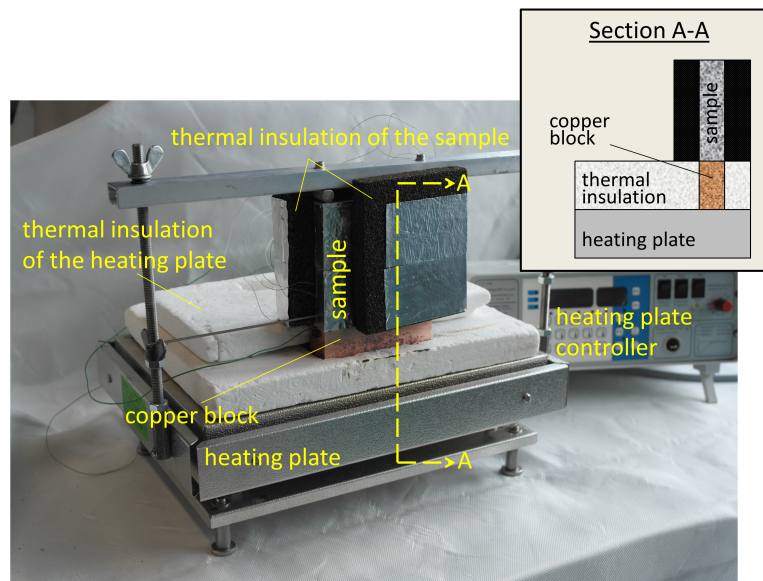


Figure 3.17: Arrangement of the sample (Toropovs et al., 2015)

The intensities in the neutron radiography permit the quantification of moisture loss during heating. In contrast to the original publication (Toropovs et al., 2015), a rigorous quantitative analysis according to Hassanein et al. (2005) has been performed, including a scattering correction. In addition, image registration was used to eliminate artefacts coming from the sample shift due to thermal expansion of the heating device. These corrections reveal a moisture accumulation behind the drying front not observed in the simpler analysis presented in (Toropovs et al., 2015). In Figure 3.18, the result of the experiment is shown in terms of water change profiles (expressed as equivalent water thickness) up to 60 minutes of heating.

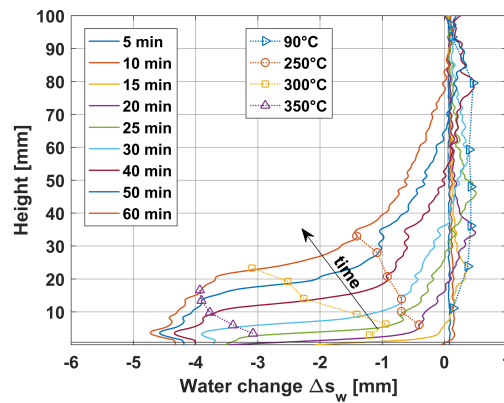


Figure 3.18: Water change profiles, HPC sample. Negative values correspond to water loss, positive to water gain

In this plot, the water change is the difference between the moisture content at a time t and t_0 . The profiles were obtained by averaging the change in moisture content across 70% of the width of the specimen in order to exclude the boundary effects. The latter were visible near the vertical edges of the sample due to imperfect sealing that led to faster drying at the boundaries (Toropovs et al., 2015). The thermocouples and in particular the pressure sensors can disturb the process locally, *e.g.* by creating cavities through which vapor can migrate (Dal Pont, 2004; Dauti et al., 2017a). However, the radiography provides results from the whole thickness of the slab, so this effect should be less pronounced.

The following observations can be made from the experimental results in Figure 3.18:

- The maximum water loss observed in terms of water thickness is about 4.7 mm. This corresponds to the initial water content calculated from the mixing water of 18.9% of the mortar volume (see Table 3.2), which for a sample thickness of 25 mm corresponds to an initial equivalent water thickness of 4.73 mm.
- The plateau on the profiles represents the dehydration front (*e.g.* after 30 min of heating the front is at a depth of around 10 mm).
- Moisture accumulation is observed behind the dehydration front as already postulated by Shorter and Harmathy in the context of spalling (Ashton and Bate, 1960) (positive values of water change in Figure 3.18). This accumulation extends into the colder region and reaches its maximum at some distance from the front. For instance, when the dehydration front is at 10 mm (after 30 min of heating), the accumulated moisture peak is at 60 mm. This distance between the front and the moisture accumulation is observed in the profiles at other times as well.

More information on the evolution of dehydration is found by plotting the water change at the thermocouples. The water change at the position of each thermocouple can be followed in time by neutron radiography. In addition, the temperature evolution in time is known from the thermocouple measurements. Combining the water change at the location of the thermocouples with temperature measurements provides the curves shown in Figure 3.19. One can observe a minor water loss between 150 and 250°C and major water loss around 300°C. The former can be interpreted as evaporation of free water, while the latter is associated with dehydration. Note that the evaporation temperature is higher than 100°C due to the increased vapor pressure. According to this interpretation, about 1 mm of water loss corresponds to evaporation of free water. This is $1.0/4.73 = 21\%$ of the mixing water or 39.7 kg/m^3 . The other 3.73 mm corresponds to the water release due to dehydration, which makes up for $3.5/4.73 =$

79% of the mixing water or 149.3 kg/m^3 . With an initial porosity of 5%, the free water content in the fully saturated state would be 50 kg/m^3 . The estimated water content of 39.7 kg/m^3 thus corresponds to 80% saturation.

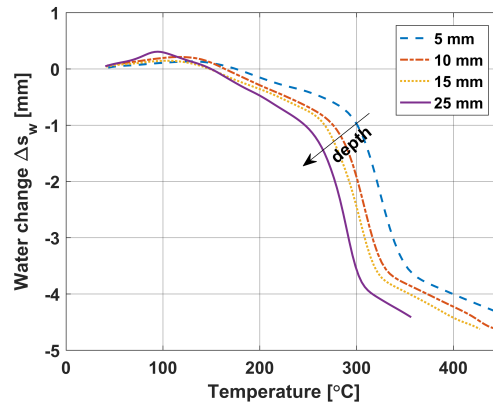


Figure 3.19: Water change vs. temperature

The water loss due to heating is usually determined by thermogravimetric analysis (TGA). For the HPC used in this thesis, the TGA is presented in Figure 3.20. This TGA has been performed on a concrete after 28 d of sealed curing. The larger sample was crushed into pieces of about 2 mm and 5 such pieces were used for the measurement. The sample was placed in a ceramic crucible and heated at a rate of $20^\circ\text{C}/\text{min}$ in dry nitrogen atmosphere. Note that the sample in the state directly after sealed curing was used, *i.e.*, containing also free water. The sample was heated from 20°C to 980°C ; only a part of the temperature range relevant to the experiment is presented in Figure 3.20. The total amount of mass loss given by the TGA until 450°C is 6.5% by mass. This is less but comparable to the results shown in Figure 3.19 according to which all the mixing water, which makes up 7.9% by mass, is lost. This curve is quite different from the ones shown in Figure 3.19 in that it does not exhibit the sudden mass loss at 300°C observed in the neutron radiography. The TGA resembles more to the experiments by Harmathy (1970) which are often employed for numerical analysis.

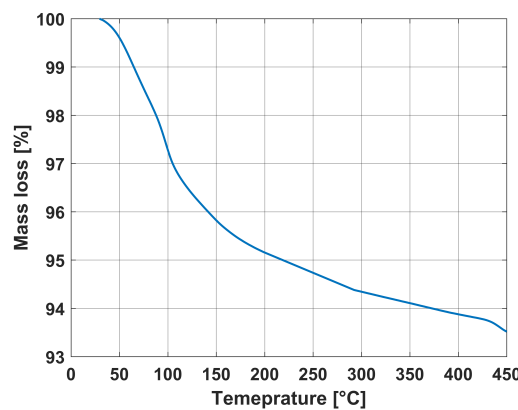


Figure 3.20: Thermogravimetric analysis for HPC used in neutron radiography

3.3.2 Numerical Analysis

A 2D model setup is adopted (see Figure 3.21), consisting of a 100 mm square concrete specimen heated on the bottom face and insulated on the side walls. The square geometry is discretized in quadrilateral finite elements with 4 mm size.

The lateral sides were closed to heat and mass transfer to simulate insulated conditions. At the heated side, the temperature measured on a heating element is specified directly as a boundary condition:

$$T = T_{hot\ face} \quad (3.7)$$

On the cold side, heat convection with the ambient temperature is considered. The effect of radiation is assumed negligible. The heat flux is:

$$-\mathbf{n} \cdot (-k_{eff} \nabla T) = -h_T (T - T_\infty) \quad (3.8)$$

where the heat transfer coefficient is $h_T = 8.3 \frac{W}{m^2 \cdot K}$, and $\epsilon = 0.85$. T_∞ corresponds to the room temperature.

For the gas mixture, at the cold side the pressure is fixed at atmospheric pressure:

$$p_g = p_{atm} \quad (3.9)$$

At the hot side, the copper block on which the sample is placed does not prevent the gas to circulate. Therefore, an atmospheric gas pressure can be assumed as well.

The boundary condition for the vapor transport through the hot and cold sides is specified by the vapor flux and is expressed as:

$$-\mathbf{n} \cdot (m_v \mathbf{v}_{v-s} + m_l \mathbf{v}_{l-s}) = -h_g (\rho_v - \rho_v^\infty) \quad (3.10)$$

where the mass transfer coefficient is $h_g = 0.018 \frac{m}{s}$. The ambient vapor density ρ_v^∞ is determined from the relative humidity.

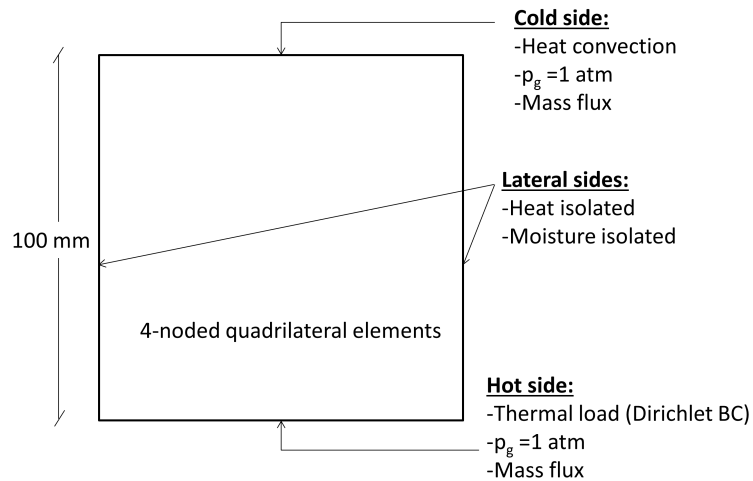


Figure 3.21: Model Setup

3.3.2.1 Temperature results

The first step in the comparison with the experiment described in Section 3.3.1 is the validation of temperature results. In Figure 3.22, a comparison between the temperature curves from the experiment and the numerical model is presented for the first 30 minutes of heating at different depths in the specimen. Although curves are labeled with the nominal position of the thermocouples, the numerical values are evaluated at their exact positions determined from an

X-ray scan. This is crucial because even a small change in depth causes a significant difference in the temperature results. For example, the thermocouple at the nominal position 15 mm is actually located 14.5 mm away from the heated surface. This difference of 0.5 mm, which is revealed from the X-ray scan, represents a temperature difference of 8°C.

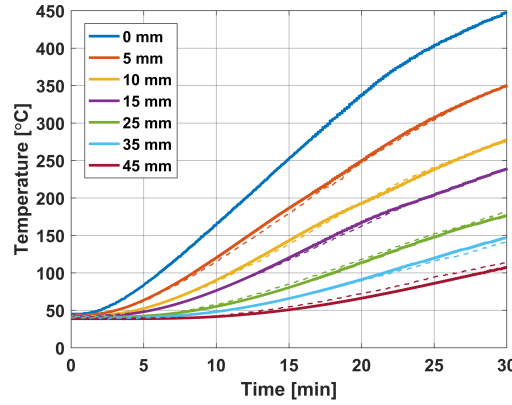


Figure 3.22: Comparison of predicted temperature profiles (solid lines) with experimental measurements (dotted lines)

3.3.2.2 Water loss profiles based on Harmathy dehydration evolution

An important parameter in simulating the water loss is the dehydrated mass, m_{dehyd} . The constitutive laws commonly used in the numerical models in literature (Dal Pont et al., 2011; Gawin et al., 2003; Pesavento, 2000) are based on the thermo-gravimetric results of Harmathy (1970). The kinetics of dehydration and the influence of vapor pressure are neglected in these models. This behavior is described by the following relation:

$$\Delta m_{dehyd} = m_{dehyd}^0 \cdot f(T) \quad (3.11)$$

where m_{dehyd}^0 is the total amount of mass which can be dehydrated and $f(T)$ is the degree of conversion of cement paste. Note that the amount of mass that can be dehydrated is usually expressed as a function of a number of factors (stoichiometric factor, ageing degree etc.) which do not have a clear meaning. In the current investigation m_{dehyd}^0 is retrieved from the experimental results presented in Figure 3.19. For the HPC under consideration, the amount of chemically bound water is 149 kg/m³ (see Section 3.3.1). This is used in Equation 3.11 as the total amount of mass which can be dehydrated. Different mathematical relations for $f(T)$ have been proposed in (Dal Pont et al., 2011; Gawin et al., 2011a) but they are all similar to the one reported in (Pesavento, 2000) which is plotted in Figure 3.23. This relation assumes that the dehydration starts at 105°C and increases continuously until 450°C.

The water loss, expressed in kg/m³, is calculated from the change in saturation of pores and the dehydration of cement paste:

$$w_{change} = (\phi S \rho_l)_0 - (\phi S \rho_l)_t + \Delta m_{dehyd} \quad (3.12)$$

This can be converted to an equivalent water thickness:

$$\Delta s_w = \frac{w_{change}}{\rho_l} \cdot d_{sample} \quad (3.13)$$

In Figure 3.24, the numerical results using the standard dehydration formulation (Equation 3.11) are shown. It is observed that the front of dehydration moves too fast compared to the

experiments and there is no plateau.

The disagreement in the numerical results suggests reconsidering the constitutive laws used in the numerical model. The constitutive laws that could potentially affect the dehydration front and the moisture accumulation in concrete are: the dehydration law and the water retention curves. In addition, permeability is also a model parameter that plays role in the moisture migration inside concrete.

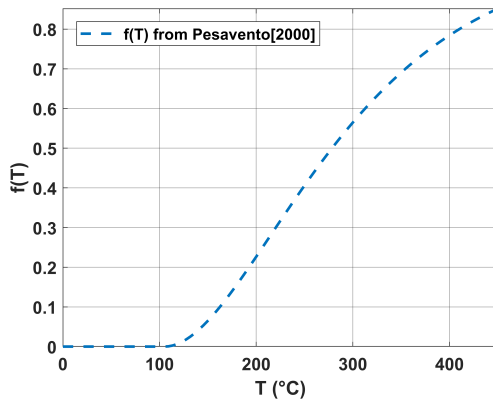


Figure 3.23: Dimensionless function of dehydration $f(T)$

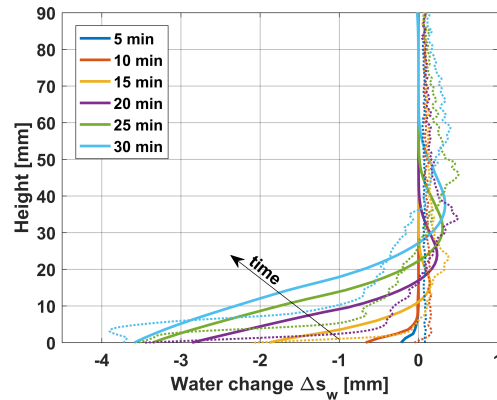


Figure 3.24: Water change with usual dehydration law

3.3.3 Influence of dehydration of concrete on water loss profiles

3.3.3.1 Dehydration of concrete

It is known that the dehydration temperatures determined by a TGA depend strongly on the heating rate, the sample size, and the vapor pressure (Scrivener et al., 2015). To minimize these influences, the TGA is usually run on pulverized samples after free water removal, in a flow of dry gas with relatively slow heating. However, the TGA experiment presented in Figure 3.20 was carried out on a sample directly after sealed curing and not pulverized in order to also resolve the free water loss and possible effect of moisture accumulation in the sample. These measures were applied in order to better correspond to the macroscopic concrete sample exposed to heating and studied here. However, the conditions in the neutron experiment were necessarily still quite different, in particular due to much larger sample in the latter. This explains the difference between the TGA measurement and the neutron measurements. The experimental observations shown in Section 3.3.1 clearly show that a TGA curve is not suitable as dehydration curve for modeling. To better understand this point, a more in depth discussion of the dehydration of concrete at high temperature is presented here. When hydrated cement paste in concrete is subjected to high temperature, chemically bound water, which is part of the solid skeleton, is released due to dehydration. Harmathy (1970) performed an experimental study about the thermal properties of concrete at high temperature, including the dehydration of cement paste. The degree and rate of conversion have been estimated with the aid of thermo-gravimetric and differential thermal analysis. He states that the dehydration starts as soon as (or even before) the desorption of evaporable water is completed (around 100°C) and proceeds uninterruptedly as the temperature increases. The influence of vapor pressure has been investigated in (Manns and Neubert, 1989). In their experiments they heated several concrete blocks slowly in an autoclave. When a certain pressure was reached, this pressure was kept constant by controlling a valve. The escaping vapor was condensed and its mass was determined. The experiments show that the dehydration temperature is always above the temperature of the vapor saturation curve at the given pressure. For instance, for a pressure of

4 MPa, dehydration starts only around 250°C. Once the pressure was kept constant, the water release was increasing rapidly with temperature.

Pasquero (2004) attempted to determine an evolution law of dehydration by taking into account its kinetics. Although no general law could be found, he explains that if for instance a heating rate of 5°C/min is assumed, the time to advance from 200°C to 250°C is a few minutes and in such a short interval it is possible that some of the hydrates that were supposed to be decomposed at 200°C will rather decompose at an accelerated rate at above 250°C. This idea is directly used in the dehydration law suggested in (Dal Pont and Ehrlacher, 2004).

In a more recent work, Zhang and Ye (2012) also studied kinetic effects of the Portland cement phases. Their experiments show a substantial increase of the dehydration temperature with the heating rate. In this reference, the influence of temperature on the reaction rate is described by an Arrhenius equation.

As confirmed by the experimental studies (Manns and Neubert, 1989; Zhang and Ye, 2012; Pasquero, 2004) mentioned above, the dehydration process is far from being an instant phenomenon. In contrary, the kinetics and pressure dependence of the associated chemical reactions play an important role and can result in a mass loss at temperatures different from what is usually assumed. This is in line with the observations obtained from the neutron radiography experiments described in Section 3.3.1.

3.3.3.2 Adjusted dehydration law

The analysis of the water loss profiles (Figure 3.18 and Figure 3.19) shows that a significant water loss starts only at 250°C. This observation suggests that the function f_T that describes the evolution of dehydration of cement paste with temperature needs to be modified. The new shape of the evolution of the dehydrated mass, f_T , is compared in Figure 3.25 against the standard formulation used by the majority of the models in the literature (Pesavento, 2000; Gawin et al., 2002b) (Dal Pont et al., 2011). The standard dehydration evolution (dashed curve) is consistent with the thermogravimetric analysis (Harmathy, 1970; Zhang and Ye, 2012) obtained on very small samples, low heating rates and in dry conditions (evacuation of released vapor with a flow of dry gas). However, what is not considered when using this law in numerical modelling is the kinetics of dehydration and the influence of high vapor pressures. In the experiments described in Section 3.3.1, no water loss appears below 250°C, but a sudden increase is observed above that temperature. Rapid increase of temperature or gas pressure might be the cause of shifting the decomposition of cement hydrates to temperatures higher than the reaction temperatures at ambient pressure and low heating rate. This explanation is also supported by the experimental studies (Manns and Neubert, 1989; Dal Pont et al., 2011; Zhang and Ye, 2012) mentioned in Section 3.3.3.1. In particular, the findings in (Manns and Neubert, 1989) confirm a dehydration temperature of 250°C at 4 MPa, a pressure that can be reached in high performance concrete according to Kalifa et al. (2000). Numerical simulations using the adjusted dehydration function (Figure 3.25) are shown in Figure 3.26. The speed and the shape of the dehydration front are well predicted by the numerical model. The results in terms of quantity of water loss are satisfactory as well. Comparing Figure 3.24 and Figure 3.26 with the corresponding dehydration functions in Figure 3.25, one can observe a similarity of shapes between the profiles and the dehydration curve. Indeed, assuming a linear increase of temperature with height, there is a direct mapping between the two. Moisture accumulation behind the front is also observed in the numerical results. However, this accumulation differs from the one observed in the experiments. The model gives lower moisture accumulation, whose peaks are located closer to the dehydration front compared to experiments. This point is addressed in the following section.

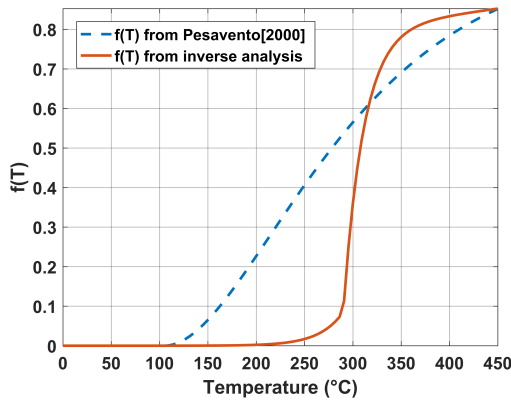


Figure 3.25: Dimensionless function of dehydration $f(T)$

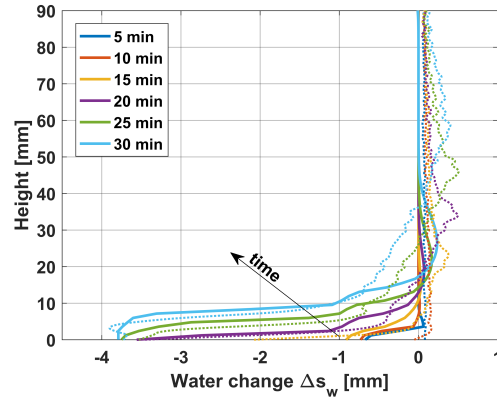


Figure 3.26: Water change profiles using adjusted dehydration law

3.3.4 Influence of retention curves on water loss profiles

3.3.4.1 Water retention curves

Another parameter that might affect the water loss profiles is the constitutive law that describes the moisture content in the pore structure of concrete, also known as water retention curves or sorption isotherms. These curves relate the water content, often formulated as saturation (S_l), to relative humidity (RH) or capillary pressure (p_c). The last two can be related to each other via the Kelvin equation (see Eq. 2.31), keeping in mind that:

$$RH = \frac{p_v}{p_{vs}} \quad (3.14)$$

The Young-Laplace equation, on the other hand, relates the capillary pressure to the surface tension (γ):

$$p_c = \frac{2\gamma \cos \theta}{r} \quad (3.15)$$

where θ is the wetting angle, and r is the characteristic pore radius.

For a given porous material, the liquid saturation can be found from sorption experiments. Based on the formulation by Van Genuchten (1980), Baroghel-Bouny et al. (1999) proposed an experimentally derived relationship between capillary pressure and saturation at the equilibrium state for concrete at ambient temperature:

$$p_c = p_c(S) = a \left(S^{-b} - 1 \right)^{\left(1 - \frac{1}{b}\right)} \quad (3.16)$$

where a and b are material-dependent coefficients (see Section 2.2.7 for more details).

The effect of moderate temperature (up to 80°C) on water retention in cement based materials has also been investigated in literature (Ishida et al., 2007; Poyet, 2009; Drouet et al., 2015). Based on such experimental results, Poyet (2016) proposed an analytical model which is based on the van Genuchten model parameters (Van Genuchten, 1980).

Unfortunately, the information in literature for sorption isotherms at temperatures higher than 80°C is limited. The first attempt for developing sorption isotherms at high temperature was the formulation by Bažant and Thonguthai (1978) for normal strength concrete. However these isotherms were formulated for one-phase fluid models and are not suitable for advanced numerical models which have evolved for considering separate liquid and vapor phases. In

addition, the discontinuous nature of the curves at high relative humidity (see Figure 3.27) is not convenient for numerical implementation.

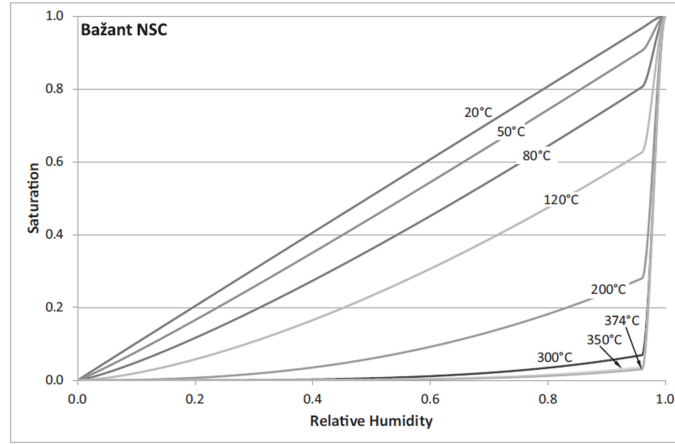


Figure 3.27: Bažant's sorption isotherms (plot taken from Davie et al. (2018))

In his PhD thesis, Pesavento (2000) extrapolated the original formulation of Baroghel-Bouny et al. (1999), given in Equation 3.16, to take into account high-temperature effects:

$$S_l(p_c, T) = \left(\left(\frac{E}{a(T)p_c} \right)^{\frac{b}{b-1}} + 1 \right)^{-1/b} \quad (3.17)$$

in which the parameter b is constant, while the parameter a is modified by the temperature-dependent parameter E which takes into account the effect of temperature on surface tension of water (Bažant and Thonguthai, 1978). This parameter defined below the critical temperature T_{crit} reads:

$$E(T) = \left[\frac{T_{crit} - T_0}{T_{crit} - T} \right]^N \quad \text{if } T < T_{crit} \quad (3.18)$$

where T_0 is the ambient temperature and $N = 1.256$. In Figure 3.28, the evolution of surface tension with water (Bažant and Thonguthai, 1978) is compared with the parameter E used in the water retention curves.

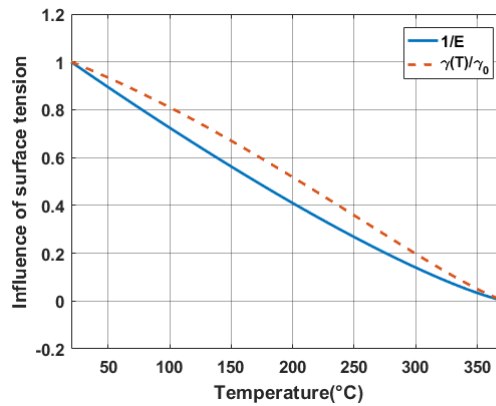


Figure 3.28: Influence of the temperature evolution of surface tension as given in (Bažant and Thonguthai, 1978) (shown in dashed lines) is taken into account by the parameter E , the inverse of which is shown in solid lines

The parameter a is also modified to consider changes in the pore structure of concrete above 100°C. This parameter is described by a cubic polynomial function monotonically decreasing with temperature (see Equation 2.55), which is proportional to the inverse of a characteristic pore radius).

The sorption isotherms, proposed by Pesavento, have been used extensively in numerical models in literature (Gawin et al., 2002a; Dal Pont and Ehrlacher, 2004; Zeiml et al., 2008; Mef-tah et al., 2012; Al Fadul and Mackie, 2018). Nevertheless, due to the lack of experimental data at elevated temperatures, the validation of this numerical formulation for sorption isotherms is missing.

Recently, Davie et al. (2018) proposed a formulation for sorption isotherms at elevated temperatures. Similar to Pesavento's formulation, the ambient temperature curves of Baroghel-Bouny et al. (1999) are used as a starting point. Then the work of Leverett (1941) is adopted to develop a model based on the material properties. Leverett (1941) showed that at ambient temperature, a relations exists between saturation (S_l) and capillary pressure (p_c) as a function of the micro-structure of the material (characterized by the porosity ϕ and the permeability k_0).

After merging the relation of Leverett (1941) with the original formulation of Baroghel-Bouny et al. (1999) and considering the evolution of the relevant properties (porosity, permeability, surface tension etc.) at high temperature, Davie et al. (2018) proposed:

$$S_l(p_c, T) = \left(\left(\frac{1}{a} p_c \frac{\gamma_0}{\gamma(T)} \sqrt{\frac{\phi_0}{K_0}} \sqrt{\frac{K(T)}{\phi(T)}} \right)^{\frac{b}{b-1}} + 1 \right)^{-1/b} \quad (3.19)$$

where γ_0 is the surface tension at ambient temperature and $\gamma(T)$ is its evolution with temperature. Recall that in Pesavento's formulation (Equation 3.17), the ratio $\frac{\gamma_0}{\gamma(T)}$ is considered by the parameter E , the inverse of which is plotted in Figure 3.28.

The formulation in Equation 3.19 has been validated (Davie et al., 2018) for temperatures up to 80°C with a set of experimental data from literature and then used for numerical analysis at more elevated temperatures. One of the most influential parameters in the formulation is permeability, for which Davie et al. (2018) have adopted functions which are obtained indirectly from numerical analyses, instead of direct experimental measurements. For instance, for moderate temperatures a back-calculated permeability (Drouet et al., 2015) is used, whereas for more elevated temperatures Bary's function (cited by Gawin et al. (2002b)) has been adopted. Thus, permeability, which is a parameter difficult to assess (especially when considering high temperatures), remains the main uncertainty in this formulation. Both formulations, Pesavento (2000) and Davie et al. (2018), are theoretically based on the micro-structural change of concrete at high temperature. In the former, this is considered by the pore radius evolution (parameter $a(T)$), in the latter by the evolution of material properties, notably permeability and porosity. However, none of this formulations has been directly validated for temperatures above 80°C due to lack of experimental evidence. In the next section, a new approach for investigating the validity of the sorption isotherms is presented. The sorption isotherms formulated by Pesavento (2000) are used in this investigation.

3.3.4.2 Adjusted water retention curves

In Figure 3.29, the formulation suggested in Pesavento (2000) is presented graphically in solid lines. The numerical-experimental comparison given in Figure 3.26 suggests that the sorption isotherms need to be adjusted so that higher saturation at lower temperature is obtained. In other words, the curves need to be shifted towards lower temperatures. This shift is controlled by the surface tension (parameter E) and pore structure evolution (parameter a) with temperature. While the former is known (Bažant and Thonguthai, 1978), the latter remains uncertain

since no experimental evidence exist beyond 80°C (Poyet, 2016) . The amount of the shift can be identified by inverse analysis of the experimental data. Note that this change only modifies the temperature dependency. The sorption curve at room temperature is not affected.

In Figure 3.30, the water change profiles using the modified sorption isotherms are shown.

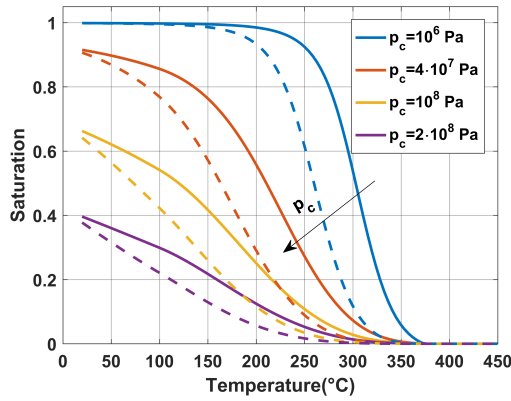


Figure 3.29: Original retention curves (solid lines) vs. modified retention curves (dashed lines)

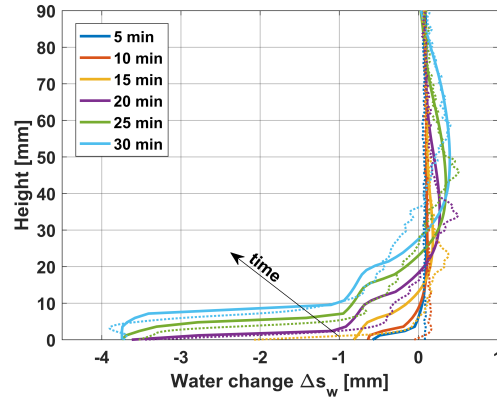


Figure 3.30: Water change profiles using the modified retention curves highlighting their impact on the moisture accumulation

It is observed that the modified sorption isotherms influence the moisture accumulation behind the front. The condensation is now shifted into the colder region behind the front. This is due to the fact that in the modified retention curves a specific saturation is reached at lower temperatures than in the original curves.

These results show that the retention curves play a key role on the moisture accumulation behind the drying front, i.e., one of the possible mechanisms related to concrete spalling as illustrated by the "pore pressure build-up theory" (Harmathy, 1965). Experiments using neutron imaging represent an effective way for improving water retention curves by inverse analysis. Such an approach, becomes particularly important when considering the fact that sorption isotherms at high temperature are difficult to obtain, and consequently missing in literature.

3.3.5 Role of permeability on water loss profiles

Permeability is an important parameter in modeling the transport phenomena in concrete. When modeling concrete at high temperature, not only intrinsic permeability, but also its evolution with temperature matters. Hot permeability measurements at high temperature are missing in the literature and residual measurements come with the risk of parasite effects such as crack healing, crack breathing, different external ambient conditions (Rastiello et al., 2014). Furthermore, the numerical benchmark of experiments of Mindeguia (2009), presented in Section 3.2, showed that even the permeability measured at ambient temperature has typically to be reduced to match experimentally measured pressures (Dauti et al., 2017b; Wang et al., 2017). Due to lack of reliable experimental values for permeability, the strategy in this study is to explore the influence of the permeability on the dehydration front in a reasonable range of values. A numerical parametric study using different values of intrinsic permeability has been performed. The permeability function used in the numerical model is taken from Gawin et al. (1999) (see Equation 2.34).

In Figure 3.26, results obtained using an intrinsic permeability $k_0 = 10^{-19} \text{ m}^2$ are shown. In Figure 3.31(a) and Figure 3.31(b), the results for higher and lower intrinsic permeabilities are presented, respectively.

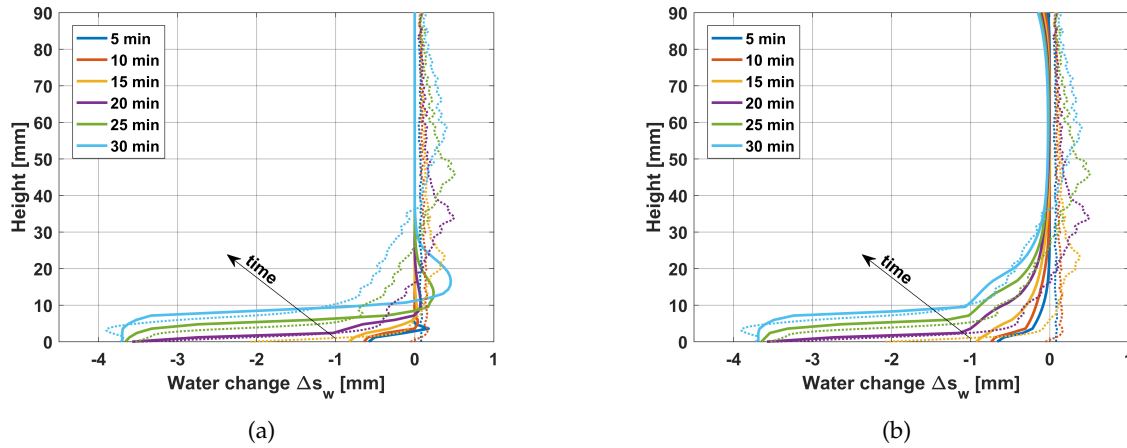


Figure 3.31: Comparison of water change profiles (solid lines) with experimental measurements (dotted lines) using (a) $k_0 = 10^{-18} \text{ m}^2$ and (b) $k_0 = 10^{-20} \text{ m}^2$

The results show that the intrinsic permeability does not affect the speed and the shape of the dehydration front, *i.e.*, the evolution of the front for different k_0 is the same. However, the initial intrinsic permeability affects the moisture accumulation behind the front. When the intrinsic permeability is increased (Figure 3.31(a)), no moisture accumulation is observed. This is probably because a higher permeability leads to a lower pressure, which is below the vapor saturation pressure. When the intrinsic permeability is decreased (Figure 3.31(b)), sharper and higher peaks of water gain are formed behind the front.

3.3.6 Conclusions: Application 3

- Moisture change profiles obtained from neutron imaging on heated concrete suggest that the commonly used numerical law for concrete dehydration based of thermogravimetric analysis needs to be reconsidered.
- A modified dehydration curve, in which the cement decomposition is shifted towards higher temperatures based on the experimental data, is presented. Implementing this adjusted constitutive law in the numerical model gives a better prediction of the speed and the shape of the dehydration front
- The front is mainly determined by the dehydration constitutive law whereas the water accumulation behind the front is determined by the retention curve and the permeability. This allows for calibrating the constitutive laws for the two parts, the dehydration front and the water accumulation, independently.
- Parameter identification in standard constitutive laws via inverse analysis as done in this thesis has proved to be an effective method for improving the state-of-the-art numerical models on heated concrete.

3.4 Mesoscale Modeling

The numerical simulations presented above, for the purpose of validating the implemented code and investigating the constitutive laws, are performed using a homogenized continuum model, as commonly done in literature (Gawin et al., 2002b; Davie et al., 2006; Dal Pont et al., 2007).

In this section, a mesoscopic analysis has been performed for identifying the differences (if any) with the homogenized continuum model results presented earlier in this chapter (see Section 3.1). The numerical analysis is based on the experiments of Kalifa et al. (2000).

This study has been performed in the framework of the master project of Gramegna (2017), for which the author of this doctoral thesis acted as the project advisor.

3.4.1 Numerical Analysis

The simulations have been performed with a 2D model consisting of 120 mm square geometry discretized in 7330 triangular elements. The finite element (FE) mesh, shown in Figure 3.32 has been generated using the technique described in Section 2.6.2. The numerical concrete used in this simulations contains 55% of aggregates per unit volume. The smallest aggregate size taken into account is 4 mm. The cementitious matrix represents the cement paste and the aggregates smaller than this limit. The biggest aggregate size taken into account in the grading curve is 25 mm.

Given the lack of experimental measurements on each component of concrete used in (Kalifa et al., 2000), the material properties are gathered from literature, mainly from (Harmathy, 1970). In this simulations, aggregates are modeled as a solid material (no permeability, no porosity). Thus the aggregate will transfer heat but not mass.

The boundary conditions, also shown in Figure 3.32, are the same as for the macroscopic homogenized continuum model. The computation time was 25 min.

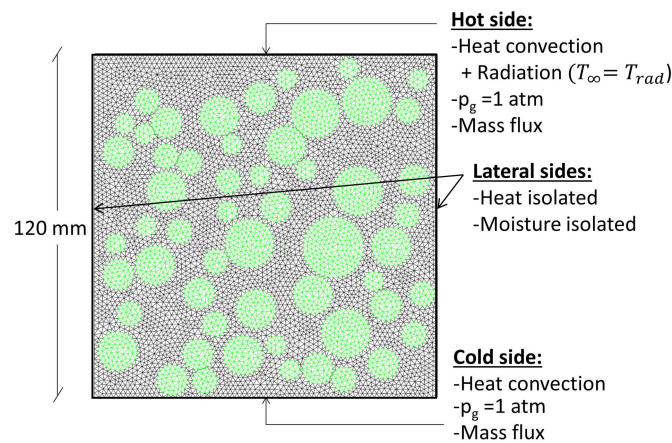


Figure 3.32: Mesoscopic model setup showing the FE mesh and the TH-boundary conditions

3.4.2 Results

The temperature and gas pressure fields after 60 min of heating are shown in Figure 3.33. In contrast to the homogenized continuum models where these fields are homogeneous, a clear

influence of the aggregates can be seen in the mesoscopic analysis. This influence is more pronounced for the pressure field (see Figure 3.33(b)).

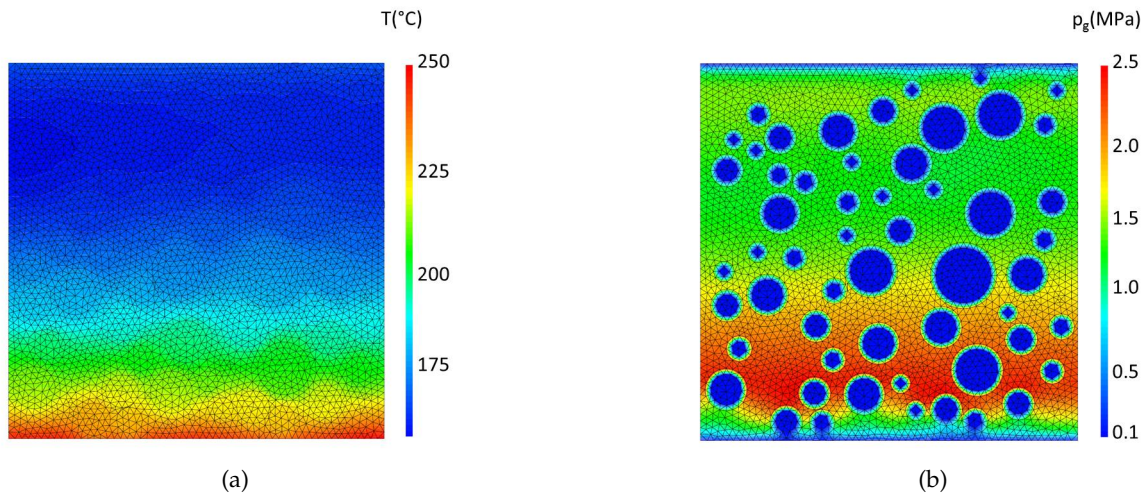


Figure 3.33: Temperature and gas pressure fields after 60 min of heating as given by the mesoscale TH model

For having a closer look at the quantitative comparison of the pressure fields, in Figure 3.34 the pressures at several points, which are all equidistant (10 mm) from the heated surface given by the mesoscopic model (solid lines) are plotted and compared against homogenized continuum model results (dashed lines). The comparison at three different times (*i.e.*, 30 min, 60 min, 120 min) is presented. Note that the pressures given by the homogenized continuum model are straight lines (as expected), whereas the results of the mesoscopic model show significant fluctuations.

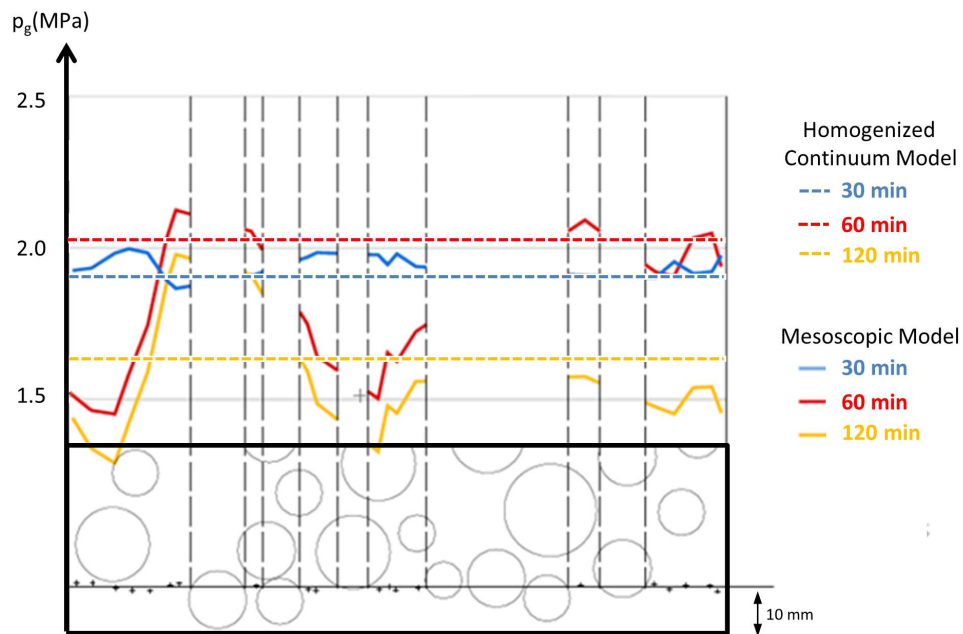


Figure 3.34: Comparison of the pressure results at a distance 10 mm from the heated surface, highlighting the importance of considering mesoscopic geometries in THM modeling (Gramegna, 2017)

This 2D mesoscopic analysis shows the importance of considering the heterogeneity of concrete in numerical models.

Nevertheless, it is important to mention that the results presented here are obtained using a single mesostructure and others should be added in the analysis for a stronger conclusion. Moreover, mesoscopic simulation requires material characterization of the concrete under consideration for avoiding the use of material properties from literature performed on aggregates and cement paste which are not always the same as the case under consideration. In addition, 3D simulations and mechanical behaviour should also be taken into account.

In Chapter 5, the third dimension and the mechanical part have been included in the model for investigating and confronting with experimental measurements the influence of heterogeneity on the behaviour of heated concrete.

3.5 Chapter Conclusions

In this chapter, numerical analyses have been performed for predicting the measurements obtained in three experiments in literature. The study showed that, the existing state-of-the-art numerical models in literature rely on some critical constitutive laws (e.g. permeability, dehydration, water retention curves) whose formulation is based on experiments that are not always reliable (e.g. gas permeability) and representative (e.g. TGA) or that are missing and simply extrapolated numerically (e.g. sorption isotherms at high temperature).

The validation of these numerical models in literature is mostly based on pressure measurements. The latter can be influenced by the measurement technique. Moreover, it has been shown that for predicting the pressure measurements, permeability plays an extremely important role. As it was discussed in Section 3.2.4, this parameter is difficult to assess at room temperature and only residual measurements at high temperature are available in literature.

This points out the need for assessing reliable permeability measurements at ambient and also high temperature. More importantly, it brings up the need for performing alternative measurements, which are non-intrusive and more reliable.

It has been shown in the third application, that neutron radiography experiments complemented with numerical modeling is an effective approach for shedding light and identifying the parameters of some critical constitutive laws.

However, the neutron radiography provides information only in 2D. This is because the 2D image obtained from radiography contains the attenuation properties of the material integrated over the thickness of the sample. This does not permit having local information, which is essential for considering the heterogeneity of concrete. The mesoscopic analysis, presented in Section 3.4 showed that heterogeneity of concrete plays a significant role. Spalling is intrinsically a three dimensional process, since it locally depends on the heterogeneity of concrete. This heterogeneity has to be taken into account, in order to capture in its fullness the complex mechanisms of spalling.

For having information in 3D, neutron tomography experiments are necessary. Such experiments, performed for the first time in literature during this PhD project, are presented in the next chapter.

Chapter 4

In-situ neutron tomography of heated concrete

An overview of experiments on heated concrete has been presented in Section 1.4 of this thesis. For the purpose of better understanding the spalling mechanisms, most of these experiments rely on temperature and gas pressure measurements using embedded elements. The latter often disturbs the tested concrete specimen, resulting in measurements that are not always reliable. Other experiments have been performed for measuring moisture content by using neutron radiography or NMR. However, these experiments yielded one dimensional moisture profiles. The information in 3D, which is pivotal for understanding spalling, is missing.

In this PhD project, neutron tomography, which is a non-intrusive method, has been used for measuring in real time the 3D moisture distribution in heated concrete. This novel experiment has been performed at the Institute Laue Langevin (ILL) that has the most powerful neutron flux in the world. The high flux is vital for obtaining fast 3D scans in order to capture the fast dehydration process in concrete.

The neutron tomography experiments on heated concrete are presented in this chapter. First some general information about neutron imaging such as its basic principles, the components of neutron facility and the mathematics of image analysis are given in Section 4.1. This information is useful for understanding the methodology employed in these experiments including image reconstruction. After the general introduction, the material and methods employed in these experiments are detailed in Section 4.2. Among others, this section details the heating cell developed during this PhD, the sample preparation, the neutron tomography setup etc. Finally, the results are presented and discussed in Section 4.3.

4.1 Neutron imaging

4.1.1 X-ray vs. neutron radiography

Transmission radiography measures the attenuation of ionising radiation passing through a body in order to visualize its internal structure. The type of radiation can be X-rays, γ -rays, electrons, neutrons etc. The main advantage of such measuring technique is its non-destructive nature. The technique has been exploited extensively in many fields since the discovery of X-rays by the German physicist Wilhelm Rontgen in the end of the 19th century. The discovery particularly transformed Medicine which has also been the driving force behind the development of X-ray imaging. X-rays interact with the electron cloud of the matter via electromagnetic effects (see Figure 4.1(a)). Thus the interactions are strongly related with the atomic number of the elements (Z). In other words, X-rays are relatively insensitive to light elements such as hydrogen, while heavier elements such as lead are difficult to penetrate. Figure 4.2(a) presents the different X-ray attenuation coefficients (cm^{-1}) for 125 kV X-rays for the full spectrum of elements in the periodic table showing the increase in absorption of X-rays (darker shading) at higher atomic number.

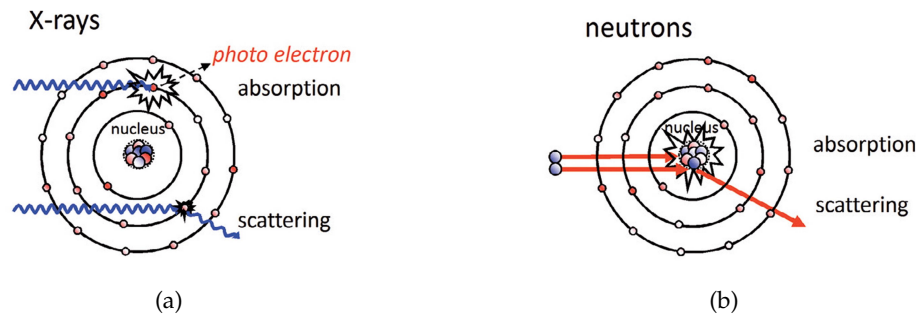


Figure 4.1: (a) X-rays interact with the electrons and (b) neutron interact with the nucleus of atoms (Kardjilov et al., 2011)

Attenuation coefficient for 125 kV x-rays (cm ⁻¹)																	
1a	2a	3b	4b	5b	6b	7b	8			1b	2b	3a	4a	5a	6a	7a	0
H 0.02																	He 0.02
Li 0.06	Be 0.22											B 0.28	C 0.27	N 0.11	O 0.16	F 0.14	Ne 0.17
Na 0.13	Mg 0.24											Al 0.38	Si 0.33	P 0.25	S 0.30	Cl 0.23	Ar 0.20
K 0.14	Ca 0.26	Sc 0.48	Ti 0.73	V 1.04	Cr 1.29	Mn 1.32	Fe 1.57	Co 1.78	Ni 1.96	Cu 1.97	Zn 1.64	Ga 1.42	Ge 1.33	As 1.50	Se 1.23	Br 0.90	Kr 0.73
Rb 0.47	Sr 0.86	Y 1.61	Zr 2.47	Nb 3.43	Mo 4.29	Tc 5.06	Ru 5.71	Rh 6.08	Pd 6.13	Ag 5.67	Cd 4.84	In 4.31	Sn 3.98	Sb 4.28	Te 4.06	I 3.45	Xe 2.53
Cs 1.42	Ba 2.73	La 5.04	Hf 19.70	Ta 25.47	W 30.49	Re 34.47	Os 37.92	Ir 39.01	Pt 38.61	Au 35.94	Hg 25.88	Tl 23.23	Pb 22.81	Bi 20.28	Po 20.22	At	Rn 9.77
Fr	Ra 11.80	Ac 24.47	Rf	Ha													
Lanthanides	Ce 5.79	Pr 6.23	Nd 6.46	Pm 7.33	Sm 7.68	Eu 5.66	Gd 8.69	Tb 9.46	Dy 10.17	Ho 10.91	Er 11.70	Tm 12.49	Yb 9.32	Lu 14.07			
Actinides	Th 28.95	Pa 39.65	U 49.08	Np	Pu	Am	Cm	Bk	Vf	Es	Fm	Md	No	Lr x-ray			

(a)

Attenuation coefficient for thermal neutrons (cm ⁻¹)																										
1a	2a	3b	4b	5b	6b	7b	8			1b	2b	3a	4a	5a	6a	7a	0									
H 3.44																		He 0.02								
Li 3.30	Be 0.79																				B 101.60	C 0.56	N 0.43	O 0.17	F 0.20	Ne 0.10
Na 0.09	Mg 0.15																				Al 0.10	Si 0.11	P 0.12	S 0.06	Cl 1.33	Ar 0.03
K 0.06	Ca 0.08	Sc 2.00	Ti 0.60	V 0.72	Cr 0.54	Mn 1.21	Fe 1.19	Co 3.92	Ni 2.05	Cu 1.07	Zn 0.35	Ga 0.49	Ge 0.47	As 0.67	Se 0.73	Br 0.24	Kr 0.61									
Rb 0.08	Sr 0.14	Y 0.27	Zr 0.29	Nb 0.40	Mo 0.52	Tc 1.76	Ru 0.58	Rh 10.88	Pd 0.78	Ag 4.04	Cd 115.11	In 7.58	Sn 0.21	Sb 0.30	Te 0.25	I 0.23	Xe 0.43									
Cs 0.29	Ba 0.07	La 0.52	Hf 4.99	Ta 1.49	W 1.47	Re 6.85	Os 2.24	Ir 30.46	Pt 1.46	Au 6.23	Hg 16.21	Tl 0.47	Pb 0.38	Bi 0.27	Po	At	Rn									
Fr	Ra 0.34	Ac	Rf	Ha																						
	Ce 0.14	Pr 0.41	Nd 1.87	Pm 5.72	Sm 171.47	Eu 94.58	Gd 1479.04	Tb 0.93	Dy 32.42	Ho 2.25	Er 5.48	Tm 3.53	Yb 1.40	Lu 2.75												
*Lanthanides	Th 0.59	Pa 8.46	U 0.82	Np 9.80	Pu 50.20	Am 2.86	Cm	Bk	Cf	Es	Fm	Md	No	Lr neut.												
**Actinides																										

(b)

Figure 4.2: Periodic table with attenuation coefficients for (a) X-rays and (b) neutrons highlighting the high interaction of X-rays with high-atomic-number elements and the relatively high interaction of neutrons with hydrogen (De Beer, 2015)

Neutrons are weakly interacting neutral particles which have on average high penetration capabilities into matter. The first one to put forward the idea of a neutral particle was Rutherford (1920) who postulated that such a particle would "move freely through the matter" and because it is uncharged and interacts primarily with nuclei the penetration would be non-destructive. After the "proof of existence" of neutron by Chadwick (1932), for which he received the Nobel prize in 1935, neutron radiography also began to be used in similar research activities as X-ray imaging. Although the latter has been driving the advances in transmission imaging, due to the role of diagnostic medicine and the comparatively simpler instrumentation, neutron imaging has also been widely applied in many diverse fields such as earth sciences (Perfect et al., 2014), material science (Kardjilov et al., 2011), nuclear science (De Beer, 2015) etc. Similar to X-rays, attenuation of neutrons is a combined process of adsorption (total removal of particles) and scattering (deflection of the particle). However, in contrast to X-rays, neutrons interact with the nuclei of atoms rather than its orbital electrons 4.1(b). So usually the neutron attenuation (see Figure 4.2(b)) is not linked with the density of the material but rather with its elemental composition. Some elements show an opposite neutron and X-ray attenuation capability. For instance, hydrogen will be easy to detect and clearly visible on a neutron radiograph but can not be detected on the X-ray radiograph.

The complementary properties of X-ray and neutron imaging in the context of concrete can be shown by presenting horizontal slices obtained by each method (see Figure 4.3). In the X-ray image, mortar and aggregates are hard to distinguish due to their comparable density, whereas pores can be easily identified. This is why X-rays are usually adopted for investigating porosity, cracking or deformation of cementitious materials. Conversely, in the neutron image, the moisture content of the mortar stands out considerably from the silica aggregates and the pores due to higher attenuation of hydrogen with respect to the rest of the sample. For this reason, neutron imaging is a very effective method for studying the evolution of the moisture content.

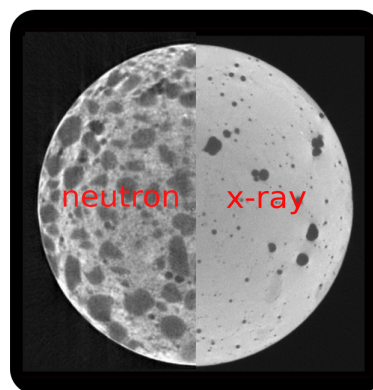


Figure 4.3: Joint halves of two horizontal slices of neutron (on the left) and X-ray (on the right) tomographies of the same cylindrical sample of concrete (70 mm in diameter) acquired in comparable conditions ($\sim 100 \mu\text{m}$ resolutions, polychromatic beams). From <https://next-grenoble.fr/>

4.1.2 Basic components of a neutron imaging facility

Figure 4.4 presents the basic components of a neutron imaging facility, namely: neutron source, collimator, investigated object, scintillator screen and CCD camera.

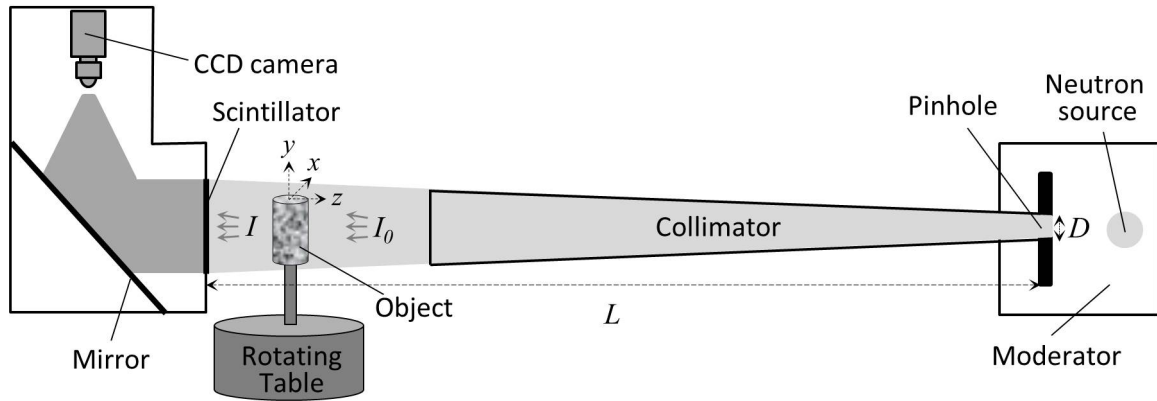


Figure 4.4: Layout of a neutron imaging system

Neutrons are typically produced either by fission in nuclear reactors or by spallation in which a high energy proton beam impinges a heavy metal target and neutrons are ejected from the resulting excited nuclei. In both these cases, neutrons have spectra of energies that are too high to be useful for either neutron scattering or imaging. Moderators are employed to cool the neutron spectrum to lower energies that depend on the temperature of the moderating medium, often hydrogen or hydrogenous materials (Anderson et al., 2009). Once the low energy neutrons are produced, they enter a collimator tube, the interior walls of which are made of a material with high neutron absorption cross section (e.g. boron). This technique prevents the stray neutrons and allows only the neutrons which are more or less parallel with the axis of the collimator. In order to maximize the flux and to have a larger field at the imaging plane (which permits imaging larger objects) the collimators are usually divergent (small entrance aperture, known as pinhole, and larger exit). The divergence (d) of the neutron beam (also known as unsharpness) which has a direct influence on the spatial resolution of the resulting image, depends on the diameter of the pinhole (D) and on the collimator tube length (L), referred to as the L/D ratio. From Figure 4.5, d can be expressed as:

$$d = \frac{i}{L/D} \quad (4.1)$$

where i is the distance of the object from the imaging plane. A compromise between the amount of flux and the geometric unsharpness d has to be made when optimizing the L/D ratio. A low L/D provides a higher neutron flux, but comes at cost of a higher geometrical unsharpness.

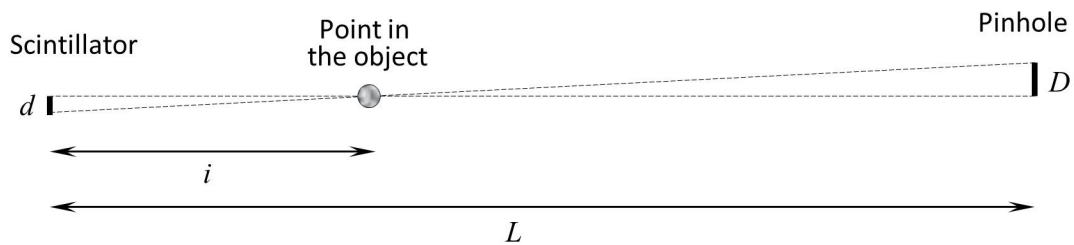


Figure 4.5: Evaluation of the divergence of the neutron beam

After the neutrons exit the collimator, they penetrate the sample and are then captured by the detector. The detector is composed by a converter (also known as scintillator), which, after capturing the neutrons, emits energy in the form of light (photons) and an image recorder. An ideal converter would be one with large neutron absorption cross section in order to capture

neutrons with different kinetic energy and minimal γ -ray cross section (for not capturing them) and high light production in order to reduce the noise of the produced signal. Lithium-6 (^6Li) is a very efficient scintillation converter and appears in the most widely used thermal neutron scintillators. Nowadays the primary detection technique for most neutron (and also X-ray) imaging facilities is the high-performance charge-coupled device (CCD) or sCMOS cameras which have revolutionized the recording procedure into a competitive high resolution imaging system that can collect and read out images far faster than film. A typical system consists of a scintillator screen, a 45° front surface mirror, a focusing lens, and a camera.

An optimization of all the components mentioned above is necessary for maximizing the quality of the produced images. A list of the most well-known neutron imaging facilities, along with their beamline parameters can be found in (Perfect et al., 2014).

Recently, a new neutron and X-ray facility (NeXT) has become operational in Grenoble, France. NeXT-Grenoble was born in 2016 from a collaboration between Université Grenoble Alpes and the Institute Lau-Langevin (<https://next-grenoble.fr/>). The neutrons are generated by a nuclear reactor and ILL is nowadays the worlds most powerful neutron source with a flux of 1.5×10^{15} neutrons per second per cm^2 (n/s/cm^2). Initially, the instrument, namely D50, had pinholes ranging from 10 mm to 1.5 mm, a collimation tube length of 10 m, and a detector allowing for up to $30 \mu\text{m}$ spatial resolution. For an $L/D = 660$, the flux was $5 \times 10^7 \text{ n/s/cm}^2$. After an upgrade in 2017, the size of the pinhole can be increased up to 30 mm, allowing a maximum flux of $3.5 \times 10^8 \text{ n/s/cm}^2$ for an $L/D = 330$. In addition, a high resolution detector which can reach up to $7 \mu\text{m}$ spatial resolution has been developed. The average neutron wavelength is 2.3 \AA . The instrument also features a polychromatic, divergent X-ray radiography setup aimed at bimodal tomography (Tengattini et al., 2017).

4.1.3 Mathematics of neutron imaging

4.1.3.1 Neutron radiography

The detection of the transmitted neutron beam intensity in a plane perpendicular to the beam propagation (xy-plane in Figure 4.4) is called a neutron radiography. The resulting 2D-image represents information about the attenuation properties of the material traversed by the neutrons. In other words, the information is integrated over the thickness of the object, τ , along the beam propagation path (z-axis in Figure 4.4). These attenuation properties can then be directly related with the morphology or chemical composition of the object. Assuming homogeneous material, the neutron beam intensity, I (n/s/cm^2), recorded by the camera can be described by the Beer-Lamber law:

$$I(x, y) = I_0(x, y) \cdot e^{-\Sigma_i \cdot \tau} \quad (4.2)$$

where I_0 (n/s/cm^2) is the intensity of the incident neutrons (before encountering the target material), Σ_i (cm^{-1}) is the effective attenuation cross section which depends on the object material (see Figure 4.2(b) and τ (cm) is the thickness of the object. When studying the moisture content, a two layer model, in which one layer represents the water and the other represents all the other material, can be considered (Weber et al., 2013). Thus the Equation 4.2 becomes:

$$I(x, y) = I_0(x, y) \cdot e^{-\Sigma_w \cdot \tau_w(x, y) - \Sigma_{oth} \cdot \tau_{oth}(x, y)} \quad (4.3)$$

where Σ_w and Σ_{oth} are the attenuation cross sections for the water layer and for the other layer (depending on the material under study the other layer might be cement, concrete, paper, wood etc.) and τ_w and τ_{oth} are equivalent thicknesses of these layers. Assuming that among this layers only water is lost during the experiment ($\Delta\tau_{oth}(x, y, t) = 0$), the change in water thickness at a

time t can be described as:

$$\Delta\tau_w(x, y, t) = -\frac{1}{\Sigma_w} \ln \frac{I(x, y, t)}{I_0(x, y, t_0)} \quad (4.4)$$

where

$$\Delta\tau_w(x, y, t) = \tau_w(x, y, t) - \tau_w(x, y, t_0) \quad (4.5)$$

For expressing the change in water thickness $\Delta\tau_w(x, y, t)$ as a change in water content (kg/cm^3) or vice-versa the following relation is used:

$$w_{\text{change}}(t) = \Delta\tau_w(x, y, t) \frac{\rho_l}{\tau} \quad (4.6)$$

where ρ_l is the water density in (kg/cm^3) and τ is the thickness of the object in cm. For quantitative analysis, the artefacts arising from the camera dead pixels, gamma rays, scintillator degradation and burning have to be taken into consideration. Such artefacts are corrected by preprocessing the raw images using dark current correction, flat field correction etc.

As shown in Figure 4.1(b), neutrons are attenuated by the nuclei by absorption and scattering. However, scattering should be distinguished from absorption, since the neutrons, after being scattered, can reach the detector, contributing to the recorded intensity (I). In such cases, the beam intensity is not reduced but merely redistributed. This can lead to a measured intensity higher than expected in the regions where the scattered neutrons hit the detector. The amount of scattering strongly depends on the distance of the sample with the detector: the smaller the distance, the higher the number of scattered neutrons impinging the detector. Scattering can be corrected by algorithms (Hassanein et al., 2005) or can be reduced by using specific neutron collimators (Tremisn et al., 2015).

4.1.3.2 Neutron tomography

Although radiography provides useful data about the internal structure, a lot of information is lost due to the fact that the three-dimensional object is projected along two dimensions. This lost information can be retrieved by a technique known as computed tomography (CT). Radiograms (also known as projections) are taken at different directions in small successive steps over 180° or 360° around the sample. A parallel beam or a beam with a very low beam divergence, requires only 180° rotation, since a projection at an angle θ will be an exact mirror image of the projection at an angle $\theta + 180^\circ$. The series of projections can then be used to computationally reconstruct a three-dimensional image (also known as tomogram) by using reconstruction algorithms.

In Figure 4.6 a simple example of a reconstruction of a 2D object (square and circle) is shown (Anderson et al., 2009). The projections taken at different angles are represented as line integrals (see Figure 4.6(a)). For a 3D reconstruction all projections are rearranged into a sinogram by applying Radon transform. A sinogram, whose name comes from its characteristic sinusoid shape, contains all the attenuation information for all angles. In Figure 4.6(b) the sinogram of Figure 4.6(a), containing all the line integrals of a certain number of projections taken around the 2D geometry, is shown. Each vertical line in the sinogram represents one projection at θ and is plotted in gray levels as a function of the pixel number. To reconstruct the image from the sinogram, the inverse Radon transform is applied. There are several techniques by which the inverse transform can be calculated but the most common is filtered back projection (FBP). Figure 4.6(c) shows four different reconstructions using filtered back projection technique, with different number of projections. As the number of projections increases, so does overlapping. Consequently the number of artifacts is reduced. The derivations of the FBP algorithm can

be found in (Kak and Slaney, 2001; Herman, 2009). Other methods, based in iterative reconstruction algorithms, exist in literature (Hutton et al., 2006). As the name "iterative" suggests, the estimated image is progressively refined in a repetitive calculation of projection and back-projection operations. Thus, they can require substantially greater computation time than FBP (Lalush, 2004). The principal trade-off between iterative techniques and FBP is one of accuracy versus efficiency.

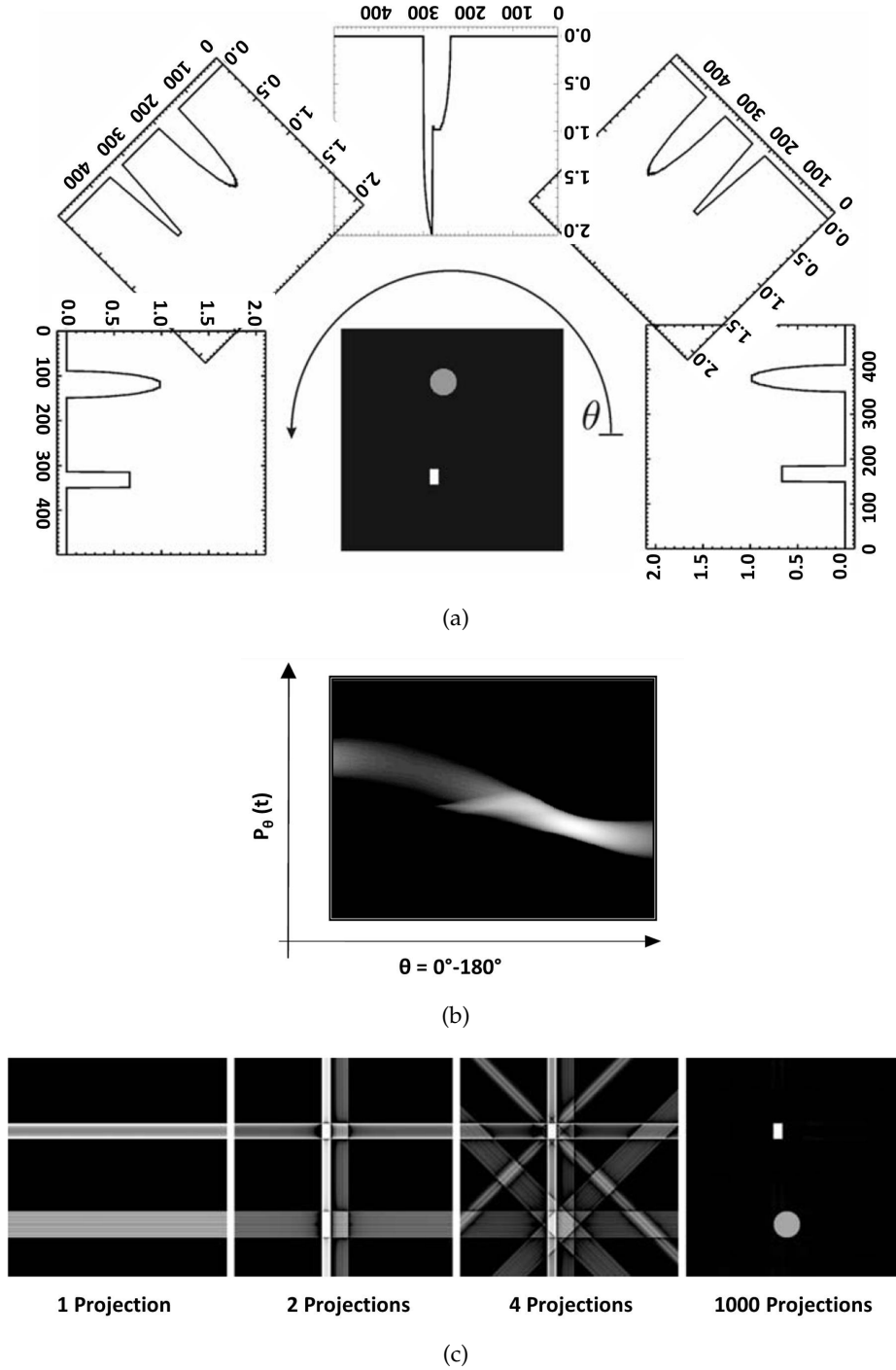


Figure 4.6: Example of an image reconstruction taken from (Anderson et al., 2009) where in (a) projections from the scanning of the 2D object are represented by line integrals and then assembled in a sinogram shown in (b). Next, in (c) filtered back projection algorithm is used to calculate the inverse transform. The higher the number of projections, the better the quality

Following the technique described above and illustrated in Figure 4.6 for a simple 2D geometry, 3D images can be made by stacking together all the reconstructed slices. Each pixel of each reconstructed slices is actually a finite volume, a so called voxel, whose value represents the attenuation coefficient of the corresponding voxel in the sample.

4.2 Material and methods

In the previous section, the principles of neutron imaging, including the mathematics of the image analysis have been described. These aspects are important for understanding the passage from the assembly of neutron radiographies to the local 3D attenuation coefficient. The latter can be directly linked with the moisture content. Taking advantage of this property of neutron imaging, the method has been employed in this PhD thesis, for analyzing the moisture migration in concrete exposed to high temperature.

The experiments performed in this PhD thesis, consist on neutron tomography scans on cylindrical concrete samples heated unidirectionally. This section presents the details of the experimental campaign, starting from the preparation of the concrete samples (section 4.2.1) to the design of the dedicated testing equipment (section 4.2.2). Finally section 4.2.3 presents the neutron tomography setup at NeXT and details the passages necessary to reconstruct a 3D image of the sample starting from the acquired radiograms.

4.2.1 Sample preparation

In this experimental campaign, cylindrical specimens were used. This choice optimizes the quality of the tomography for a given imaging setup. For the diameter, two criteria were considered. In order to investigate the effect of the aggregates, the diameter should be large enough to enclose a representative number of aggregates. On the other hand, there is a maximum thickness that can be penetrated by neutrons, before having a non-attenuated signal too close to the background noise. In order to determine the optimal contrast, there was a need for pretests. They showed that a diameter of 3 to 5 cm yields an optimal contrast. Although the heating setup has been designed for specimens of up to 5 cm diameter, most tests were performed with 3 cm specimens. Commercial plastic containers were used for the molds (Figure 4.7). In some specimens, three thermocouples type K were embedded for temperature measurement at distances 3 mm, 10 mm, and 20 mm from the heated surface (Figure 4.8). The two wires of the thermocouples enter the concrete radially from two sides and are welded together at the center. The location of the embedded thermocouples, especially the exact position of the welding point, was determined afterwards from the tomograms. In order to end up with a representative concrete heating surface at the top with a minimal amount of air bubbles, the samples were cast upside down. The thermocouples were thus located at the bottom during casting. To remove any entrapped air, the samples were vibrated on a vibrating table. This task is particularly important for avoiding large pores in the samples.

The samples, which will be heated, were sealed in plastic containers which were stored in 97% RH and 20°C. After demolding, the heated surface was ground to minimize reflection of the heat. To prevent the vapor from escaping and to obtain a 1D movement of moisture within the heated sample, the lateral surface of the samples were covered with self-adhesive aluminium tape (virtually invisible to neutrons because of their very low interaction with aluminium) before the test, as shown in Figure 4.8. The aluminium tape used in the tests (3M™ High-Temperature Aluminium Foil Tape 433) has a working temperature up to 316°C which is higher than the maximum temperature experienced by the sample (~310°C). As one of the objectives was to see the influence of aggregate size, two mixes (see Table 4.1) containing alluvial aggregates (sandstone, dolomites, and metamorphic rocks) with different sizes have been used. The two mixtures, HPC 8 mm and HPC 4 mm, have maximum aggregates sizes of 8 mm

and 4 mm, respectively. The aggregate volume fraction for both mixtures was of 60% (of the *total* volume). In addition, a sample HPC 4 mm with a single aggregate $d \cong 10$ mm near the heated surface was cast for a more direct investigation of the influence of the aggregates on moisture migration.

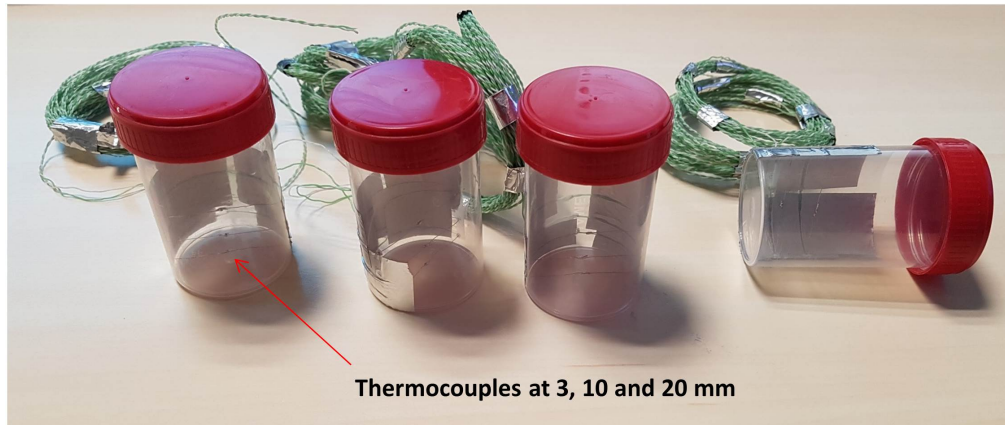


Figure 4.7: Plastic molds with thermocouple wires



Figure 4.8: Specimen wrapped with adhesive aluminium tape

	HPC 4 mm	HPC 8 mm
Cement CEM I 52.5 R	488	488
Silica fume	122	122
Aggregate 0–1 mm	632.8	400
Aggregate 1–4 mm	949.2	600
Aggregate 4–8 mm	0	582
Superplasticizer SIKA 20HE	8.54	8.54
Water	189.1	189.1
w/b total	0.31	0.31

Table 4.1: Concrete mixtures [kg/m^3]

4.2.2 Heating Cell

The heating cell has been designed and developed in the framework of this PhD project. A drawing of the heating cell is shown in Figure 4.9(a).

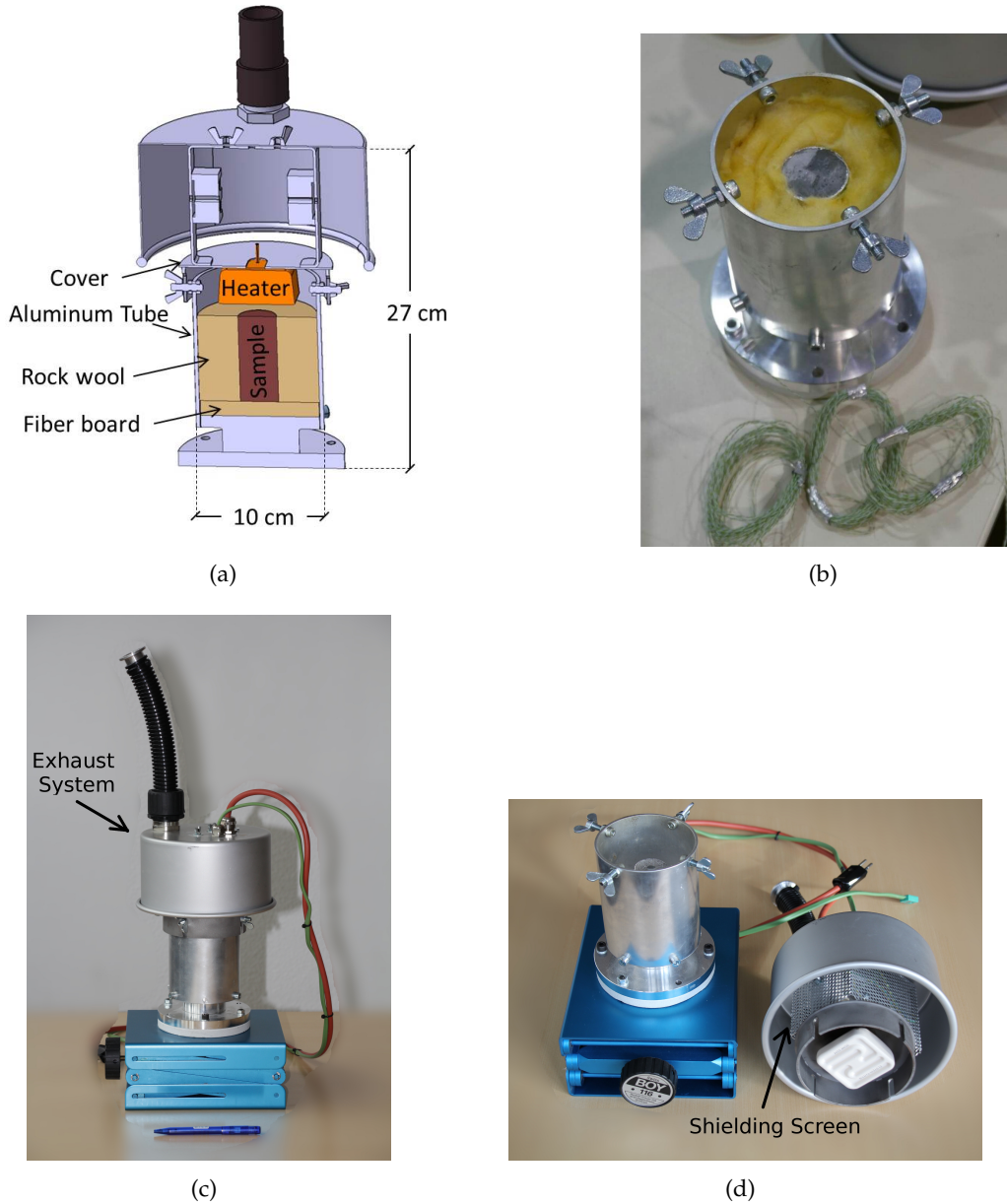


Figure 4.9: Experimental setup: (a) 3D rendering of the CAD drawing of the cell; (b) specimen inside the setup wrapped laterally with aluminium tape for moisture insulation and rockwool for heat insulation; (c) complete setup highlighting the gas and dust evacuation system; (d) disassembled setup highlighting the shielding screen for electrical protection

During a test, the concrete cylinder is heated on the top face with a ceramic infrared radiator (Elstein) with a surface of $6 \times 6 \text{ cm}^2$ and a power of 250 W. For all the tests, the radiator is heated up to 500°C within 3 minutes and kept at constant temperature by a controller connected to the thermocouple built in the radiator. The latter is placed in a cover on top of the cell consisting of an aluminium tube, which is rather transparent to neutrons. At the bottom of the heating cell, the specimen stands on a cement fiberboard, which is also used for thermal insulation. The bottom aluminium plate contains some outlet for thermocouples. Another fiber board

is also placed between the base and the stand, which allows for the vertical positioning. To maximize the uniformity of one-dimensional heating, the space between the concrete cylinder and the aluminium tube is filled with rock wool (Figure 4.9(b)). The complete device is shown in Figure 4.9(c). The disassembled system is shown in Figure 4.9(d).

Besides the proper heating, a main issue was safety. Although the radiator was heated up to 500°C and the concrete up to 300°C, the temperature on the aluminium tube did not exceed 60°C. The cell is not only constructed for heating but it also serves as a protection against possible spalling, which however did not actually occur. Since gases which are released at high temperature can become radioactive, they were sucked out by an exhaust evacuation system. The system consists of a hood covering the outlet between the aluminium tube and the cover and a plastic tube, which is connected to a vacuum system (Figure 4.9(c)). This system would also be able to collect possible radioactive dust in the case of spalling. The electrical wires for the power supply and the built-in thermocouple were protected from touching by a shielding screen (Figure 4.9(d)).

Materials for the heating cell were carefully selected. Not only is the transparency to neutrons of concern, but also the radioactive activation. All materials after being a certain time in the neutron beam are activated depending on their chemical composition. This results in a waiting time after the test until the setup and the sample can be handled safely. Therefore low-impurity aluminium was taken as much as possible. When steel was used, as for screws and the cover, stainless alloys were avoided. The careful design allowed for optimal use of beam time and adherence to safety requirements.

4.2.3 Neutron tomography setup and image reconstruction

Neutron tomography was performed at the NeXT(D50) beamline (Tengattini et al., 2017) at the Institute Laue Langevin (ILL) in Grenoble, France. For this test a pinhole of 15 mm was used, placed at 10 m from the sample, yielding a collimation ratio of ~ 650 , corresponding to a neutron flux of $7.9 \times 10^7 \text{ ns}^{-1} \text{ cm}^{-2}$. This configuration choice was dictated by the shielding exiting at the time of the testing, which limited the maximum pinhole diameter to 15 mm. The sample was placed at ~ 100 mm from the detector to minimize the effect of scattering, yielding a maximum resolution *on the neutron side* of 150 μm . The detector employed a 100 μm scintillator made of $^6\text{LiF}/\text{ZnS}$, yielding a maximum theoretical resolution above 100 μm . The camera used was a Hamamatsu Orca 4.0V2 sCMOS with 2048×2048 pixels, mounting a 50 mm lens adopting an aperture of $f/1.4$. This detector allows for any field of view below $170 \text{ mm} \times 170 \text{ mm}$, and was in this case calibrated to 100 mm, to match the sample height, yielding a pixel size of $\sim 50 \mu\text{m}$. From the above follows that the effective spatial resolution of the images was determined in this setup by the settings of the camera (notably its binning). This was set differently for lower temporal resolution and higher spatial resolution tomographies aimed at sample characterization, and the higher temporal resolution with lower spatial resolution tomographies aimed at capturing the fast drying processes induced by thermal loading.

One of the big challenges was in fact optimizing a sufficient temporal and spatial resolution. Despite the world-leading neutron flux at the ILL, the exposure time needed for a single high-contrast projection is still in the order of 2.5 seconds. For comparison, in previous tests in a different facility (Toropovs et al., 2015) the exposure time for a sample with 25 mm thickness was around 15 seconds. An exposure time of 2.5 seconds implies that a single tomography comprising 500 projections, adds up to about 20 minutes. While this is more than acceptable for initial and final characterization of the sample, it is too slow for in-situ testing. As it turned out from the tests, the front moved 0.2 mm per minute. This would correspond to a 4 mm variation of the front during a 20 min lasting scan. Such movement would cause a blurring deemed unacceptable for the purpose of this study.

The exposure time can be reduced through binning, *i.e.* grouping the pixels (sensors) of the camera, which allows reducing the acquisition time at the cost of a lower spatial resolution. For the fast tomography presented here, 4×4 binning was used, which leads to a pixel size of $200\text{ }\mu\text{m}$ but reduces the exposure time by a factor of 16, meaning an exposure time of ~ 0.15 seconds. Based on preliminary images an even shorter exposure time of 0.12 seconds was deemed acceptable and selected to perform the in-situ rapid tomographies. This corresponds to tomograms comprising 500 projections acquired in one minute. The rotating table was set to rotate continuously by 180° in one direction in one minute and reverse during the next minute. The angular blur induced by the continuously rotating (rather than stopping-and-starting) was in this case below the resolution of the images. The speed at the surface of the cylinder is in fact of 0.79 mm/s meaning that the surface moves of about $95\text{ }\mu\text{m}$ within the exposure time, which is about half of the pixel size of $200\text{ }\mu\text{m}$.

Acquiring one tomogram in one minute was found to be sufficient for the purposes of this study, *i.e.*, capturing the dehydration front. The front moved in fact about $200\text{ }\mu\text{m}$, *i.e.*, one pixel during a scan. This leads to some negligible blurring in the tomogram, since the reconstruction of the 3D image assumes stable sample conditions. It should be noted that this blurring only affects the mortar on the drying front; the aggregates are in fact not moving and show sharp boundaries.

For the test, the heating cell with the specimen was placed on the rotation table in the beamline (Figure 4.10), where it can be observed that the cables and exhaust pipe are hanging from the ceiling to minimize mechanical interactions. They were selected to be flexible enough to allow rapid rotations of the setup by 180° .

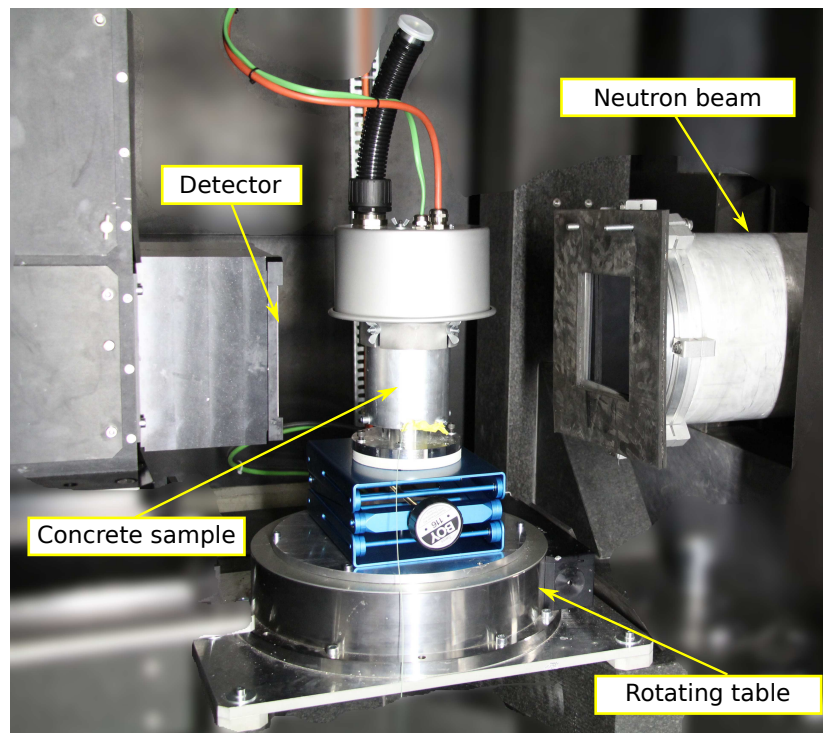


Figure 4.10: Setup in the NeXT(D50) beamline at Institute Laue Langevin (ILL)

A total of 11 heating tests were completed within two days. During each test, a sample was heated during one hour and real-time tomographies were performed every minute. On four samples, 'post-mortem' higher resolution scans were taken for a better description of the morphology. They were taken after the sample cooled down to a stable state at around 100°C .

to make sure that the process has stopped. The high-resolution tomograms were taken with the table rotating 360° , without binning and with a larger number of projections, yielding an effective resolution closer to the optimal $50\ \mu\text{m}$. This chapter focuses on the detailed analyses of three tested samples: HPC 4 mm, HPC 8 mm and HPC 4mm with a single aggregate near the heated surface, for exploring the physics involved, notably the effect of aggregate size. The remaining tests are employed as validation of the statistical representativity of the reported study.

The acquired radiograms are normalized by the so called "flat field" and "dark field" (*i.e.*, by the radiograms of the unencumbered beam and by the background noise of the camera). This allows for accounting for any inhomogeneity of the neutron beam and of the scintillator screen and electronic noise. The so obtained normalized radiogram represents maps of the attenuation of the neutron beam accumulated along its path through the concrete sample. In Figure 4.11(a), one such projection for a given angle and at a given time is reported, which highlights the portion of the sample where drying has occurred. The radiogram also shows the heater at the top as well as the fiber board at the base. The rock wool and aluminium are instead practically invisible, as by design. Starting from the radiographies acquired at different angular position it is possible to reconstruct a 3D field of neutron attenuation. In this work, projections in 500 angular stations at regularly spaced intervals between 0° to 180° are used. The reconstructions are performed employing a commercial software (X-act, from RX Solutions) which employs filtered back projection algorithm, one of the classic standards employed in the domain. The software also allows compensating for any misalignment of the setup such as the rotation axis (*i.e.*, its center and inclination) relative to the image coordinate system. Once the correct parameters for the correction are selected, a reconstruction of a $250 \times 250 \times 340$ voxels takes less than one minute. A "remove outliers" filter has also been employed to account for any spurious high-energy gamma received by the detector. A representative 3D rendering of the reconstruction is shown in Figure 4.11(b), where it is cut in half to highlight the drying front around the aggregates.

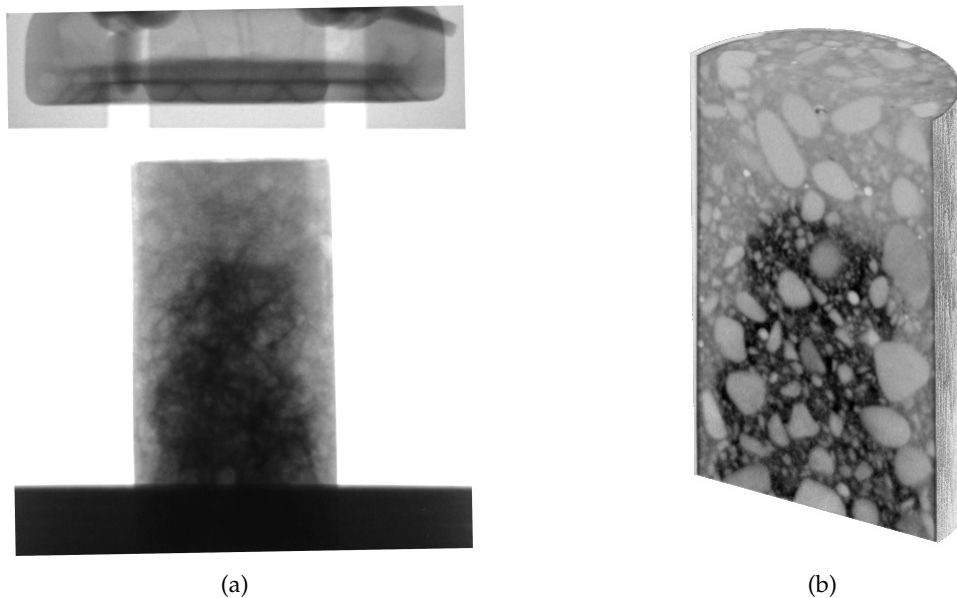


Figure 4.11: Example of the neutron images acquired in this work: (a) the radiograms are projections of the attenuation field of the concrete to neutrons. When enough of such projections are acquired at different angles, the Radon transform can be employed to reconstruct the full three-dimensional volume of attenuation coefficients, as that in (b). The drying front is evident in both thanks to the high attenuation coefficient of water

4.3 Results and discussion

This section analyses the different measurements gathered by the reported experimental campaign, starting from the classic ones (temperature, in Section 4.3.1), moving onto the position of the drying front and the effect of aggregate size (Section 4.3.2) and exploring eventually the moisture profiles of the sample (Section 4.3.3 and Section 4.3.4). In the end some important observations such as thermocouple-induced air bubbles (Section 4.3.5), influence of a crack on the drying front (Section 4.3.6), additional drying at the boundaries (Section 4.3.7) are discussed.

4.3.1 Temperature measurements

In Figures 4.12(a) and 4.12(b) the temperature profiles for the samples HPC 8 mm and HPC 4 mm measured between 0 mm and 20 mm from the heating surface are reported. These profiles were determined by fitting second-order polynomials to the readings of the embedded thermocouples. In Figure 4.13, these temperatures are compared, highlighting in a first approximation identical behavior. The temperatures measured at the same nominal distance from the heated surface are slightly higher on the sample HPC 8 mm. The biggest difference (about 15°C) is observed at the nominal distance 10 mm from the heated surface.

When comparing the measurements for each specimen, the exact position of the thermocouples as well as the distance of the radiator to the heated surface has to be taken into account. The exact position is determined via neutron tomography scans (see Figure 4.14) thanks to the higher resolution tomographies acquired at the end of both heating tests. The thermocouple welding point can be in fact clearly identified on the reconstructed tomograms. The exact position of each thermocouple is reported in Table 4.2. There it can be observed how all the thermocouples on sample HPC 4 mm are a bit further from the heated surface compared to HPC 8 mm. This fact could explain the small discrepancies observed in Figure 4.13. Note that the largest gap in temperatures at TC2 corresponds to the highest gap in distance. From the images it was observed that the distance between the heated surface and the radiator was almost the same for both cases, with the HPC 4 mm being only 0.5 mm closer.

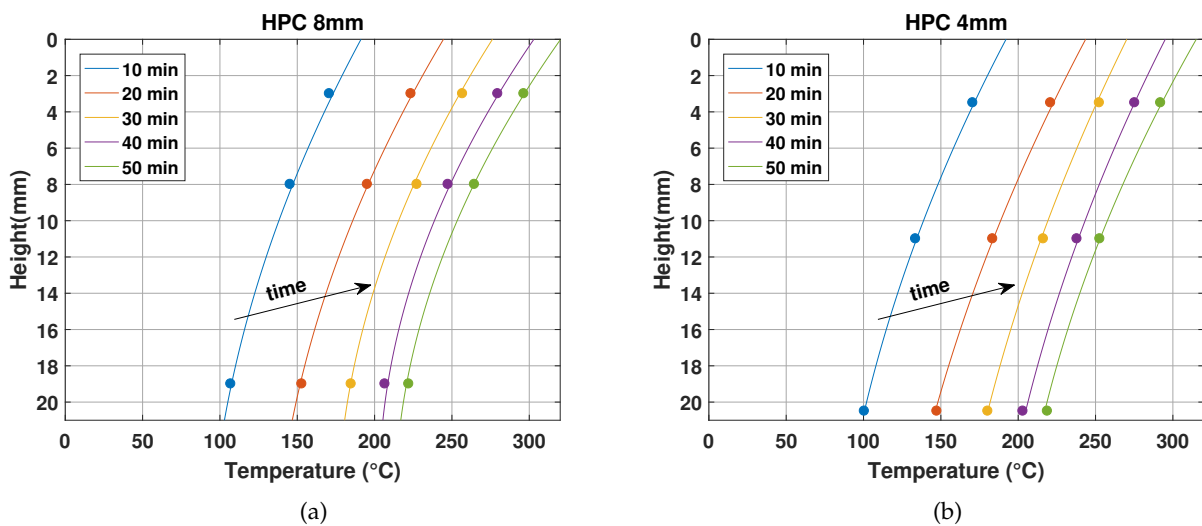


Figure 4.12: Temperature profiles measured during the heating tests as a function of their vertical position measured from the heated surface for tests HPC 8 mm (a) and HPC 4 mm (b)

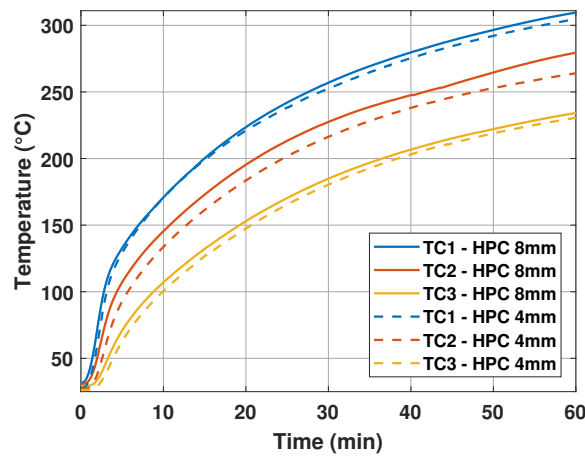


Figure 4.13: Comparison of the temperature profiles across time for two tests with different aggregate sizes as measured by the three thermocouples (TC1, TC2, TC3) placed at three nominal positions (3, 10, and 20 mm from the heated surface), highlighting the analogous thermal response of the two

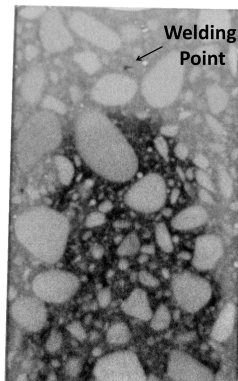


Figure 4.14: Welding point of thermocouple

	HPC 8 mm	HPC 4 mm
TC1	3 mm	3.5 mm
TC2	8 mm	11 mm
TC3	19 mm	20.5 mm

Table 4.2: Distance of the thermocouples from the heated surface determined via neutron tomography scans

4.3.2 Global dehydration speed: HPC 8 mm vs HPC 4 mm

Having established that the aggregate size has a negligible effect on the temperature profiles, it is important to understand whether this is also true for the drying front. In order to investigate this, vertical slices containing the sample's axis of rotation from tests on two concrete samples with different aggregate size are shown in Figure 4.15. The slices on the left-hand side correspond to the sample with a maximum aggregate size of 4 mm, whereas the slices on the right-hand side correspond to the sample with a maximum aggregate size of 8 mm. Due to the strong attenuation of the wet cement paste, the evolution of the drying front is evident in the images. These results show qualitatively how the drying front moves *faster* in the sample with bigger aggregates. Additional samples tested at ILL also confirm this observation. Another information highlighted is that in all tested samples, drying progressed faster at the lateral boundaries despite the use of heat and moisture insulation detailed above and aimed at maximizing the uni-dimensionality of the flow. This boundary effects are discussed more in detail in Section 4.3.7.

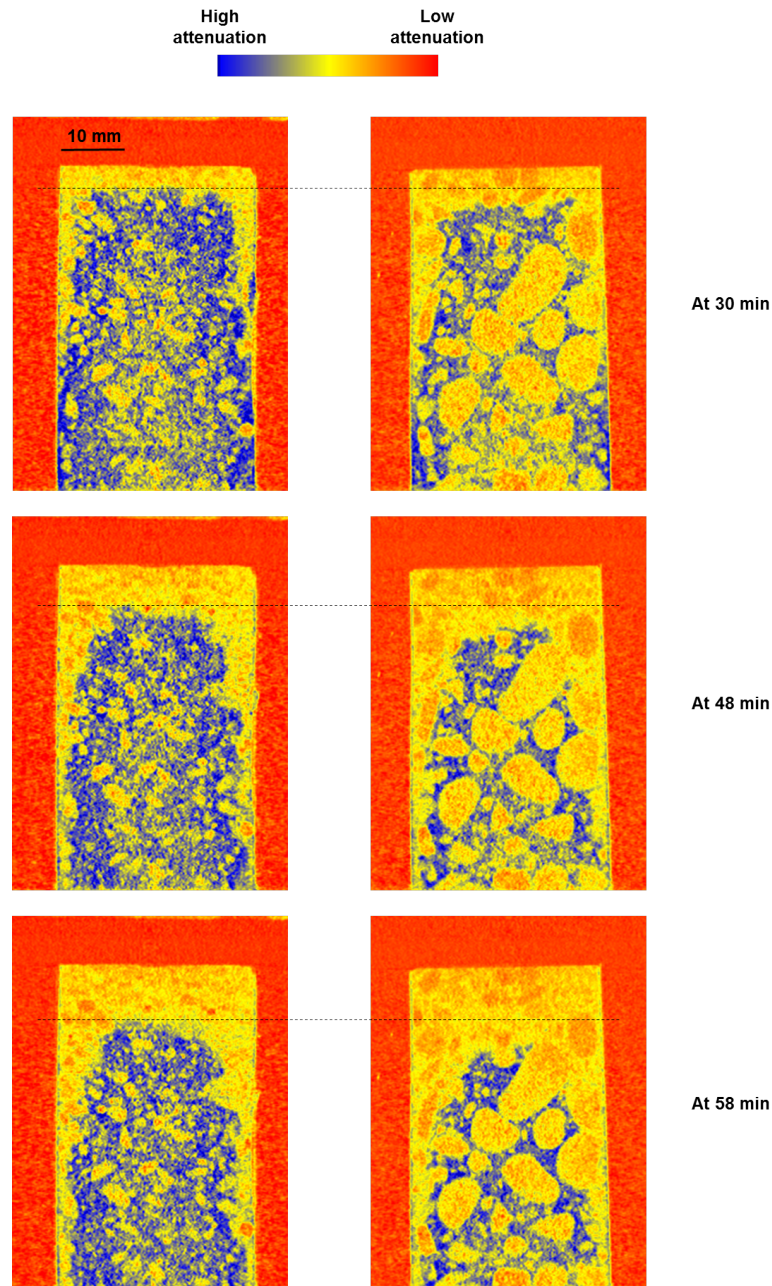


Figure 4.15: Sequence of vertical slices from reconstructed 3D volumes showing the evolution of the drying front at different heating times in HPC 4 mm (on the left) and HPC 8 mm (on the right)

4.3.2.1 Segmentation of aggregates and cement paste

To overcome the qualitative nature of these observations it is necessary firstly to discern or "segment" the aggregates from the cement paste. Due to their difference in neutron attenuation, aggregates and cement paste can be separated using thresholding techniques. This is a classic tool in image processing, in which voxels (the 3D pixels constituting the image) are classified based on whether their gray value, *i.e.*, their attenuation coefficient, is above or below a given user-defined threshold (hence the name). The procedure followed in this study for performing the segmentation is described below.

Step 1: Average the initial 10 tomograms

To compensate for the *relatively* high random noise existing in the rapid tomographies, which could cause an incorrect assignment of some pixels, multiple tomograms in comparable states can be averaged together. In our case the first ten tomograms (where the drying process has not started yet) are median filtered together in order to achieve a higher quality reference dataset yielding a more accurate thresholding. Median-filtering operation is done using a script written in the macro language in ImageJ. The new stack of images (Figure 4.17) has noticeably less noise compared to the fast tomograms in Figure 4.16.

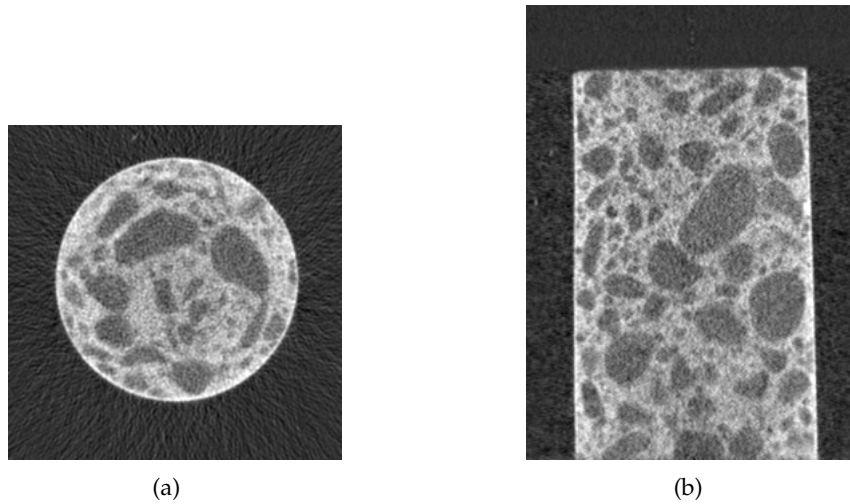


Figure 4.16: (a) Horizontal and (b) vertical slice from 1st fast tomography of sample HPC 8 mm

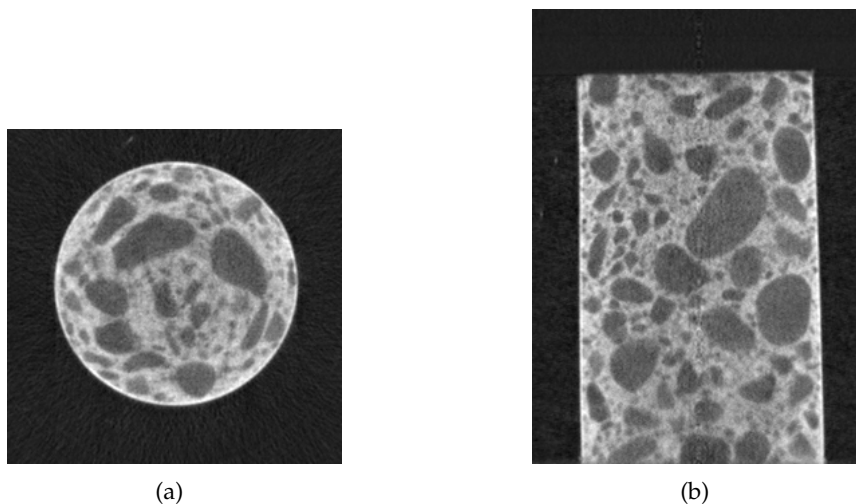


Figure 4.17: (a) Horizontal and (b) vertical slice from the stack of images obtained by averaging the first 10 tomograms

Step 2: Mask for the volume outside the sample

The histogram of the horizontal slice in Fig. 4.17(a) is shown in Figure 4.18(a). The peak enclosed in the red box belongs to the volume outside the sample. But the contrast between

aggregates and cement paste is not evident from the histogram. Therefore, first a mask is created to get rid of the useless volume outside the sample. The mask is obtained by thresholding in ImageJ. A binary image in which value 0 is assigned for the volume outside the sample and value 1 for the sample (see Figure 4.18(b)). This mask is applied to the medianed slices (Figure 4.17(a)). The resulting image and its histogram is shown in Figure 4.19. In this image the gray value of the volume outside the sample is 0. In contrast to the histogram in Figure 4.18(a), in which the contrast between the cement paste and aggregate was hidden, the new histogram clearly shows two peaks which correspond to aggregates and cement paste (assuming that the volume occupied by the pores is negligible).

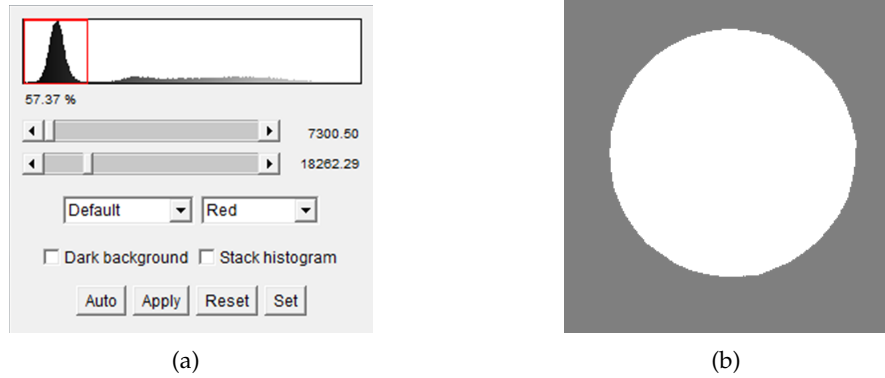


Figure 4.18: (a) Histogram of the image in Figure (a) and mask obtained by thresholding the peak enclosed in red which belongs to the volume outside the sample

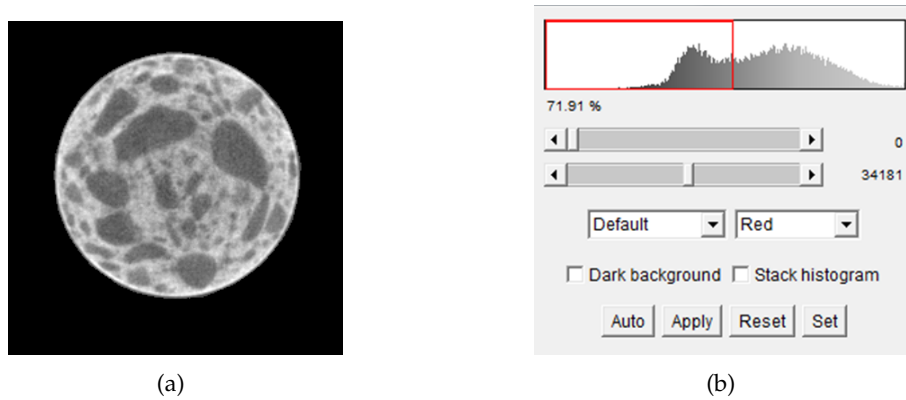


Figure 4.19: (a) Image after removing the outside part and (b) its histogram highlighting the peaks corresponding to cement paste and aggregate

Step 3: Separating the aggregates from the cement paste

The next step after masking out the volume outside the sample is segmenting the concrete components (aggregates and cement paste) by applying a threshold. The result of the segmentation is shown in Figure 4.20(b). White pixels have been assigned to the aggregates and a black ones to the cement paste. Obviously a key parameter in this process is the threshold value, which affects the measured percentage of "white" and "black" voxels. It can be shown that for reasonable threshold ranges the measure of the phases only fluctuates by $\pm 3\text{-}4\%$ in volume.

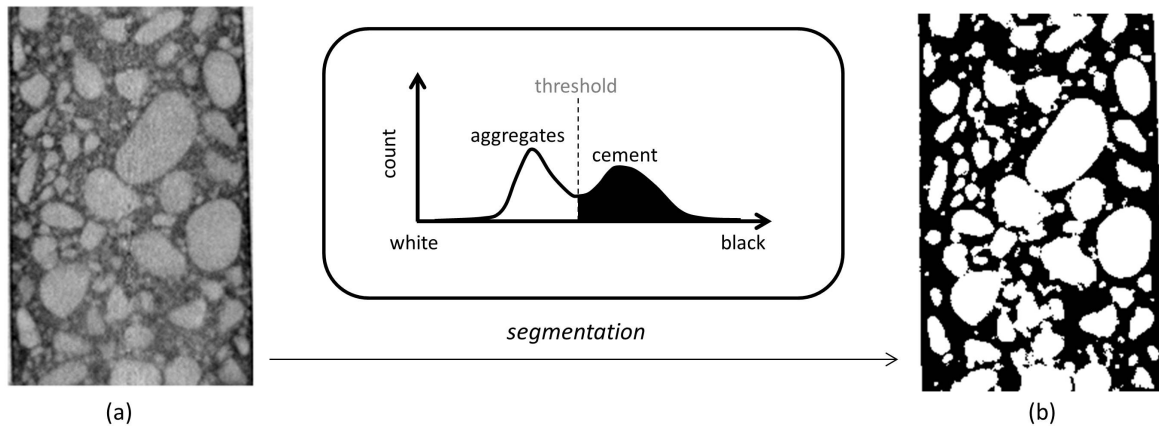


Figure 4.20: Example of the segmentation through thresholding: (a) A vertical slice of the tomogram obtained by median filtering the first ten (and substantially stationary) tomograms in order to minimize the effect of random noise. Through thresholding it is possible to automatically discern (and thus quantify) the two phases as highlighted in (b) where the "aggregate" voxels have been arbitrarily assigned a white color, while the cement ones have been assigned a black color

The volumes occupied by each phase together with the corresponding uncertainties are summarized in Table 4.3. These values are different for the two mixes which were produced using 60% of aggregates by volume (see Table 4.1). This discrepancy can be ascribed to the image resolution: the tomograms acquired with a pixel size of $200\ \mu\text{m}$ do not allow the detection of the smaller aggregates. The aggregates with size $0\text{--}1\ \text{mm}$ occupy 15% of the volume of HPC 8 mm and 24% of the volume of HPC 4 mm. This corresponds approximately to the difference in volume of aggregates in the whole sample between the results of image analysis (43% and 33% respectively) and the volume fraction imposed in the concrete mixtures (60% for both). This resolution was nonetheless deemed sufficient for tracking the drying front.

	$V_{\text{Aggregates}}\ (\%)$	$V_{\text{Cement Paste}}\ (\%)$
HPC 8 mm (whole sample)	43 ± 3	57 ± 3
HPC 4 mm (whole sample)	33 ± 4	67 ± 4
HPC 8 mm (only the core)	54 ± 3	46 ± 3
HPC 4 mm (only the core)	48 ± 4	52 ± 4

Table 4.3: Volume fractions of the aggregates and cement paste as measured from the image after segmentation for the whole sample and for the core of the sample

4.3.2.2 Computing the volume of the dried cement paste

In Figure 4.15, the dehydration speed of HPC 4 mm was qualitatively compared with HPC 8 mm. In this section, it is shown how a quantitative comparison can be obtained.

As the front progresses, and the water (main contributor to the neutron beam attenuation) contained in the cement paste migrates, the contrast between cement paste and aggregates reduces, hindering their discernment. Nonetheless, the spatial distribution of the aggregates, measured in the initial state, can be assumed not to change throughout the test. Consequently, it is possible to subtract the aggregates from every tomogram (a process generally named "masking"), leaving behind only the cement paste, which can be in a dry state (after losing all the free and chemically bound water) or in a wet state. Figure 4.21(a) reports a vertical slice of one such masked tomograms, which already highlights the dry part of the cement paste. From this point it is straightforward to isolate through thresholding the dry cement paste, as shown in

Figure 4.21(b). This operation allows then quantifying the volume fractions of the two states of cement as the tests progresses.

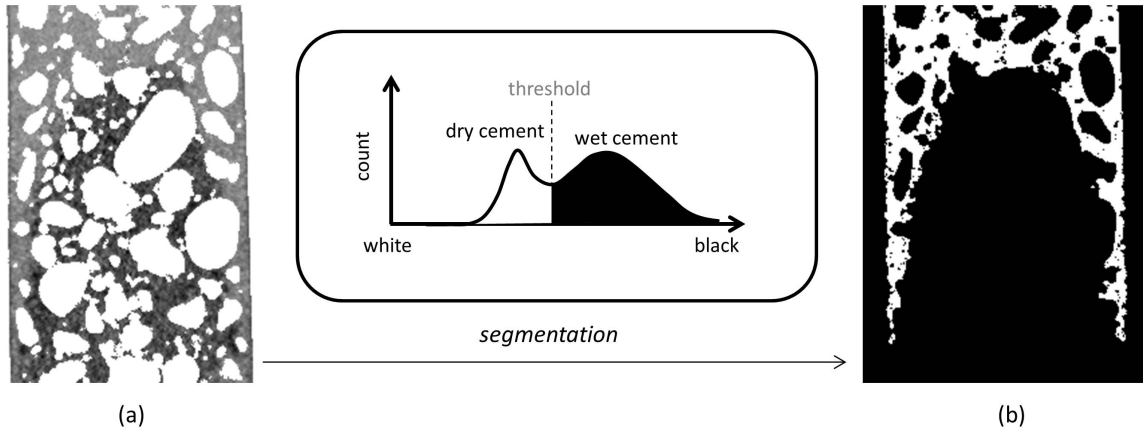


Figure 4.21: Quantification of the drying process through segmentation. In (a) the aggregates, obtained in the initial state are removed, leaving behind only dry and wet cement. (b) these two phases can then be separated through segmentation

The procedure is repeated for all the tomograms of two tests identical in conditions but containing different aggregate sizes. This allows for following the volume of dry cement paste in time for both samples. In Figure 4.22(a), the amount of dry cement with respect to initial cement ($V_{dry}/V_{initial}$), where it can be observed how the sample with bigger aggregate size dries faster, is shown. After 58 min, about 55% of the cement of HPC 8 mm and only 35% of the cement of HPC 4 mm is dried. Drying starts after about 10 min for both samples when the temperature at 3 mm from the surface is around 170°C. The region in gray represents the uncertainty induced by the choice of the threshold when separating the wet and dry cement, implying that this large discrepancy cannot be imputed to the segmentation process.

The drying curve for HPC 8 mm exhibits some discontinuities, in the form of plateaus which are linked to the averaging method employed in the analysis. Since the diameter of aggregates is about half of the diameter of the core used for averaging, the relative contribution of mortar is not homogenous but varies with depth. At heights where the cross-section has a large portion of aggregates and a small portion of cement paste, the contribution of mortar is growing less with depth, which produces a small plateau. Note that in the sample with smaller aggregates, this effect is not observed.

It is clear from the images (e.g. Figure 4.15) that, despite the several precautions paid to maximize the uni-dimensionality of the process, only the core part respects this ideal condition. Therefore, to analyze the 1D behavior, the boundaries of the sample are excluded and only the core, (half of the sample diameter), where the front is more uniform will be considered henceforth. The volume fractions of aggregates and cement paste for the core of the sample are reported in Table 4.3. The partial volume of aggregates increases, i.e 54% in the core vs. 43% in the whole sample for HPC 8 mm. This is due to the natural tendency of bigger aggregates to be in the middle when casting.

In Figure 4.22(b), the ratio of the dehydrated volume in the core to the total core volume is shown at different time steps. Similar to the previous case where the whole sample is considered (Figure 4.22(a)), the drying front is faster for HPC 8 mm, implying that the observed difference cannot be ascribed to the boundary effect.

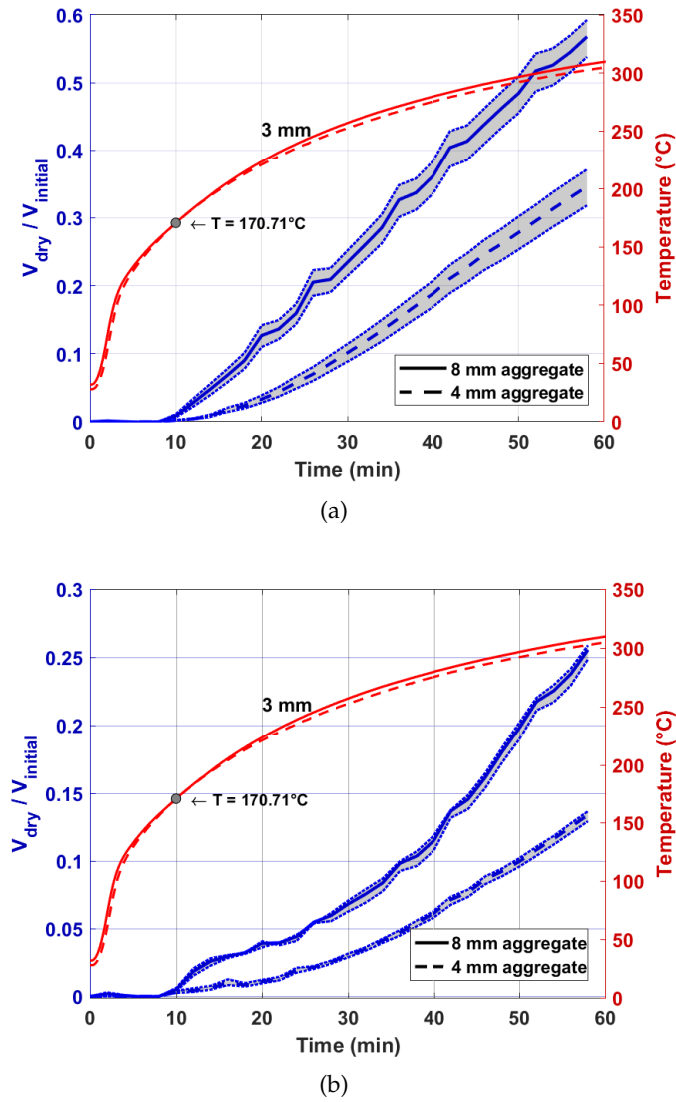


Figure 4.22: Evolution of the drying front across time measured in terms of dry volume fraction obtained through segmentation for test with comparable boundary conditions and similar measured temperature profiles. This large difference is observed both when the entire sample is considered (a) and when only the core part, closer to the uni-dimensional ideal, is considered (b)

Recall that the temperature measurements (see Figure 4.13) showed that the thermal field is very similar in both samples. Despite the fact that the thermocouples make point-wise measurements, the similarity in temperature profiles indicates that the temperature cannot be the driving force of the observed difference in the dehydration front.

A possible explanation for this difference is the more pervasive crack network induced by the bigger aggregates, which results in a considerably higher permeability and in the release of gas pressure. On one side, the higher permeability can lead to a faster moisture migration. On the other side, the sudden release of gas pressure might trigger the dehydration reactions as it has been postulated in (Manns and Neubert, 1989) where the influence of the gas pressure on the dehydration of concrete is discussed.

The direct proof of this more pervasive fracture network in HPC 8 mm was not possible by neutron imaging since the spatial resolution $200\ \mu\text{m}$ is not sufficient for detecting micro cracks. However, this can be explained by the influence of the aggregate size on:

- the cracks formed by the thermal incompatibility of the concrete components at high temperature. While the aggregates expand with increasing temperature, the cement paste exhibits first expansion and then shrinkage (Mindeguia et al., 2013b). This thermal mismatch in the behavior of concrete components results in the development of local micro cracks (Mindeguia et al., 2013a), particularly around the aggregates.
- the shrinkage cracks at constant temperature during concrete hardening. Cement paste exhibits shrinkage strain during hardening and the restraint of this strain by the aggregates can cause shrinkage cracks (Mindess and Diamond, 1982). Various studies in literature found out that a larger aggregate diameter increases shrinkage cracking (Lura et al., 2009; Grassl et al., 2010; Idiart et al., 2012; Wu et al., 2015).

To further investigate the influence of the aggregates on the drying front, another sample with 4 mm aggregates but containing a single $d \cong 10$ mm aggregate at the top was also tested in the same conditions. Vertical slices of the tomographies acquired during this tests are reported in Figure 4.23. It is clear that this aggregate severely affects the test, accelerating the drying process (which progresses faster around the aggregate) and modifying its shape. Most of the acceleration of the process happens while the front is grazing the sides of the macro aggregate where the fracture network is likely to be more pervasive.

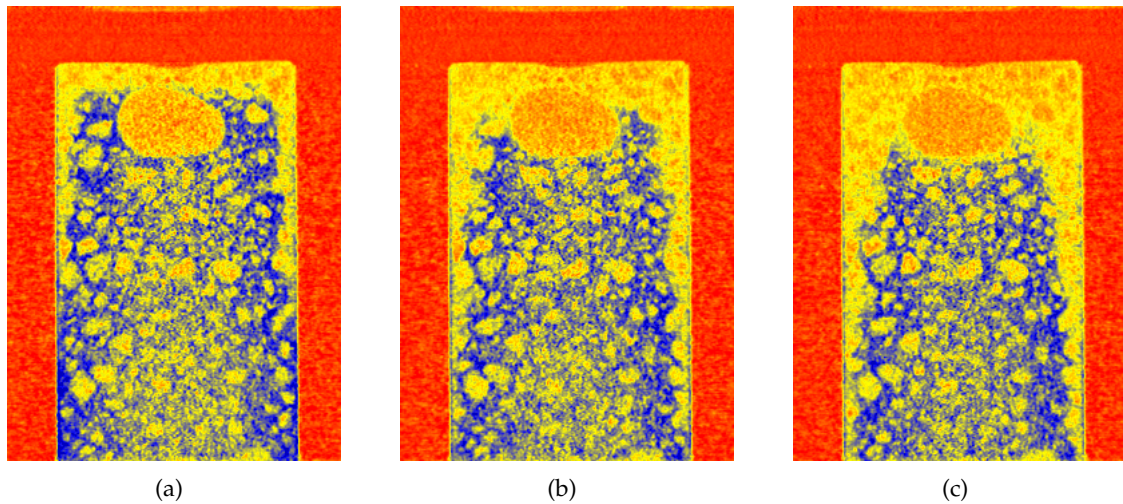


Figure 4.23: Vertical slices of the tomograms acquired while testing a concrete sample containing 4 mm aggregates as well as a bigger, 10 mm aggregate at different time steps: (a) 30 minutes, (b) 44 minutes and, (c) 54 minutes. It is evident that the process is accelerated by this bigger aggregate

4.3.3 Evolution of moisture content

At high temperatures, the moisture content in the cement paste evolves due to the physical processes of dehydration, evaporation, and condensation. The variation of water content can be investigated looking at the attenuation coefficients of the cement paste in space and time. The attenuation coefficient (perceived in the images as a gray value) is in fact directly linked to water content: a high gray value means a high water content. To remove the boundary effect, only the core of the specimen is considered in this analysis, where the front is more uniform (see Figure 4.24). For a given depth (distance from the top), the attenuation coefficient of the cement paste is thus sampled and averaged over a disc. The aggregates are removed using the aggregate masking procedure detailed in Section 4.3.2.1.

The evolution of the average gray value of the disc is then computed for every time step. Results at different depths of the sample HPC 8 mm are shown in Figure 4.25(a). Therein, the gray values are normalized by their initial average value (*i.e.*, before drying). Recall that the normalized average gray value is related to the water content. A decrease in gray value corresponds to a loss in water content, *e.g.* at 3 mm from the heated surface, a major water loss starts after 10 minutes of heating. This is associated to the time when the drying front arrives at the position 3 mm.

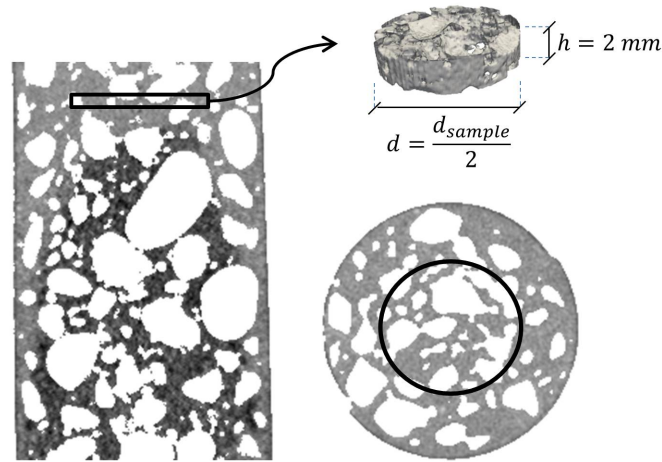


Figure 4.24: Region of interest used for averaging the attenuation coefficient in order to compute the evolving gray value. The region is selected so as to remove the boundary effect (hence only the center of the sample is used) and to have a temporal resolution comparable to the acquisition time (2 mm in height)

By using the thermocouple readings at 3, 8, and 19 mm from the heated surface, the results in Figure 4.25(a) can be re-plotted against temperature as shown in Figure 4.25(b). The profiles with markers correspond to the position of the thermocouples. Additional profiles can be obtained by interpolating the thermocouple readings. The results show that no major water loss occurs until $\sim 200^\circ\text{C}$. The temperature of the water loss varies between $200\text{--}250^\circ\text{C}$ depending on the position in the sample. These variations can be associated with the kinetics of dehydration and the influence of vapor pressure. The kinetics and pressure dependence of the chemical reactions driving the dehydration process play a key role and can result in a mass loss at temperatures different from what is usually assumed as already shown in Section 3.3.3 and presented in (Dauti et al., 2018a). The same analysis is performed for sample HPC 4 mm and the results are shown in Figure 4.26. Once again, the faster drying of HPC 8 mm can be clearly seen when comparing Figure 4.25(a) with Figure 4.26(a). Furthermore, the comparison of Figure 4.25(b) with Figure 4.26(b), shows that the major water loss is shifted to higher temperatures for HPC 4 mm. This shift is about 20°C , *e.g.* at a depth 5 mm from the surface, the waterloss in HPC 8 mm starts at around 220°C , whereas in HPC 4 mm it starts at 240°C .

The disc defined in Figure 4.24 is also used to scan the depth of the sample at several instances in time. This yields the vertical profiles shown in Figure 4.27 for HPC 8 mm and HPC 4 mm. The horizontal plateau in the profiles correspond to the position of the drying front at each time step. These graphs can be interpreted as a quantitative representation of the images shown in Figure 4.15. Beyond the plateau of the drying front, an increase in gray value is observed (normalized average gray value above 1) which seems to be a moisture accumulation behind the drying front. However, before drawing any premature conclusions, one has to verify that this increase in the gray value is not merely due some well-known CT artifacts such as

scattering and beam hardening. This question is discussed in more depth in the next section.

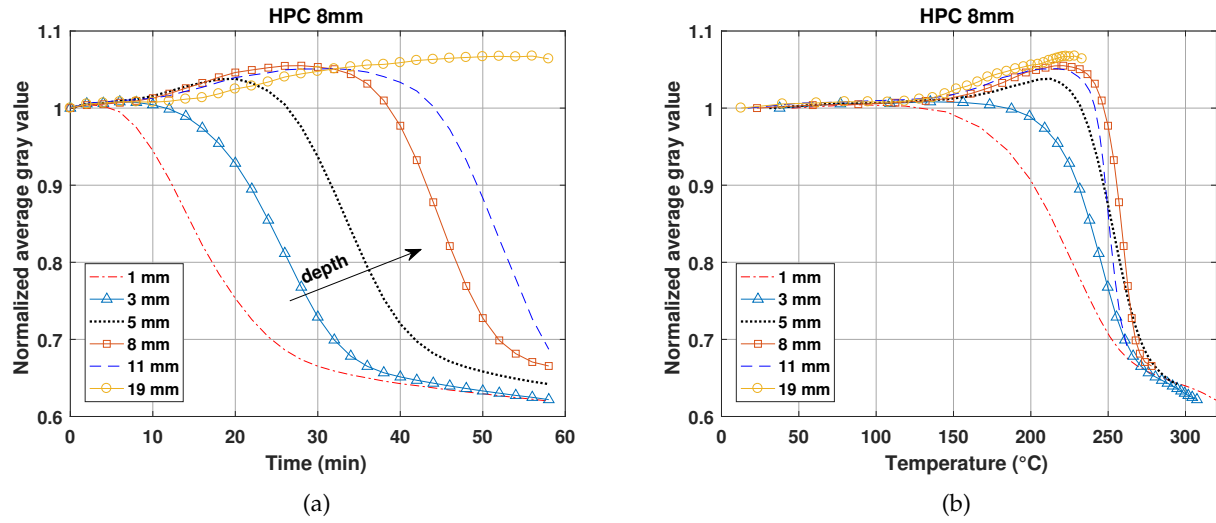


Figure 4.25: Moisture profile evolution at different depths for HPC 8 mm, evaluated through the normalized attenuation coefficient to which they are directly proportional. (a) water content evolution against time and (b) water content evolution against temperature (interpolated from the thermocouples)

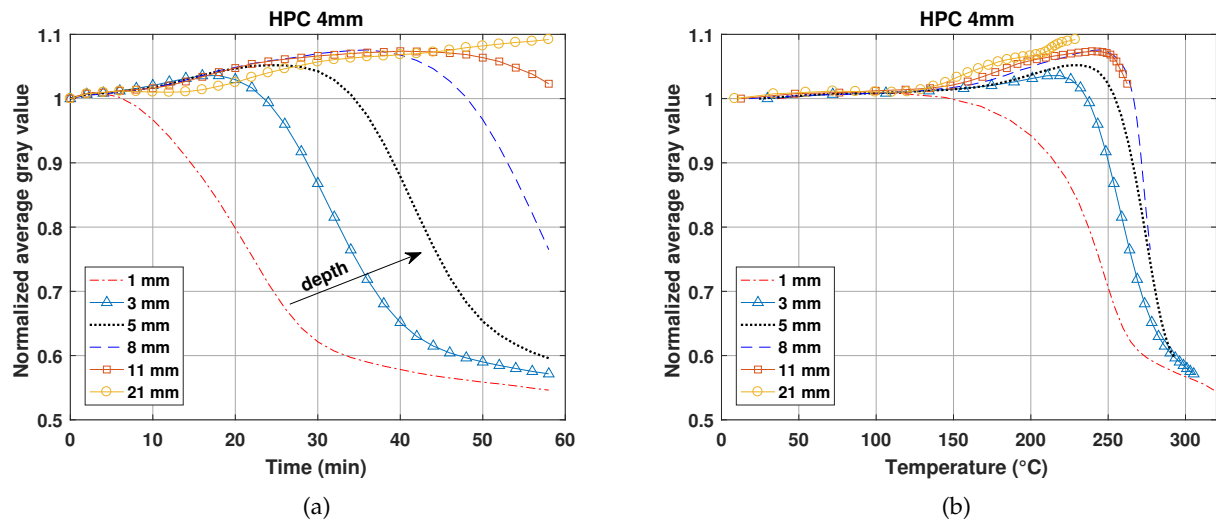


Figure 4.26: Moisture profile at different depths for HPC 4 mm plotted (a) against time and (b) against temperature, similar to what was shown in Figure 4.25 for HPC 8 mm

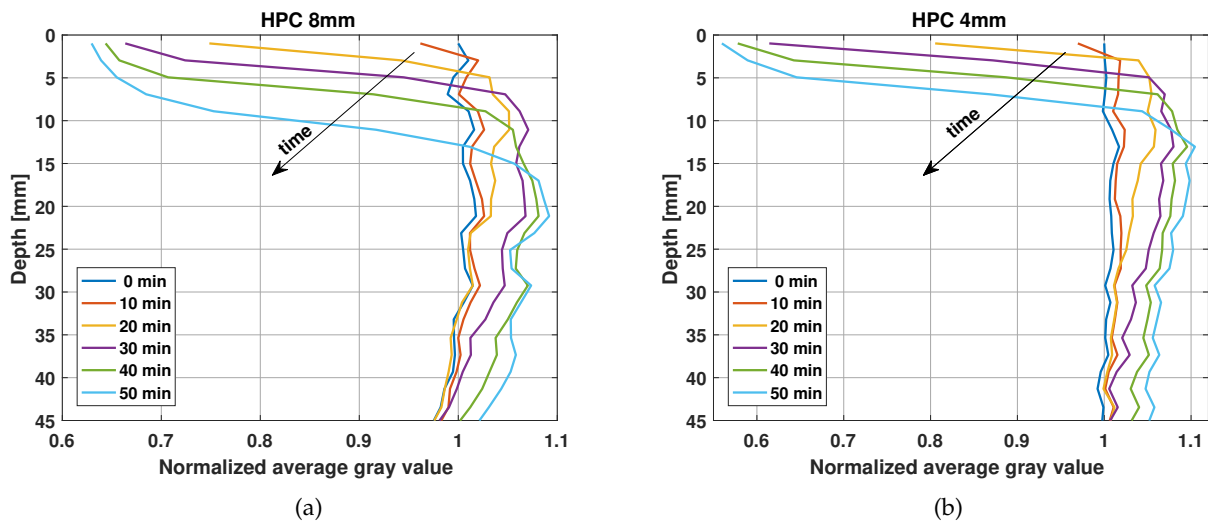


Figure 4.27: Moisture profile evolution vs. depth for (a) HPC 8 mm (b) HPC 4 mm

4.3.4 Discussion on the moisture accumulation

One of possible mechanisms of spalling is related to the vapor pressure build up due to the moisture clog formation. To explore this hypothesis, a more thorough analysis of the moisture profile in two representative tests is performed in this section.

A synthetic way to analyze the moisture profile evolution during a test is to average the attenuation coefficient across the transverse section (xy -plane), more specifically in the sample core, where it is more homogeneous and to plot this value as a function of the depth from the exposed face (z -position) and the elapsed time (t). The resulting representation is reported in Figure 4.28 for the sample HPC 8 mm. For example, point a is the average gray value in the xy -plane at 15 mm from the top of the sample and at time $t = 30$ minutes. Three distinct zones are evident in this representation: Zone I, having the lowest attenuation which corresponds to drying, Zone II, having the highest attenuation which could be associated to a moisture accumulation and Zone III having an attenuation intermediate between the first two, corresponding to the initial, wet state of the concrete.

The contrast between the zones allows tracking in time and space the drying front as well as the end of the apparent moisture accumulation zone, which can be computed by finding the transition point in terms of averaged gray value. Figure 4.29 shows these two interface fronts for HPC 8 mm and HPC 4 mm respectively. Polynomial curves are used to fit the raw data. The shaded space between the curves represents the depth of the moisture accumulation zone. When comparing the results, it can be seen that the moisture accumulation extends on a larger zone in sample HPC 8 mm. This is more clear when looking at the evolution of the moisture accumulation depth with time (see Figure 4.30(a)). In Figure 4.30(b) the evolution of the moisture accumulation peak with time is shown for both samples. The peak reaches a slightly higher value in HPC 4 mm.

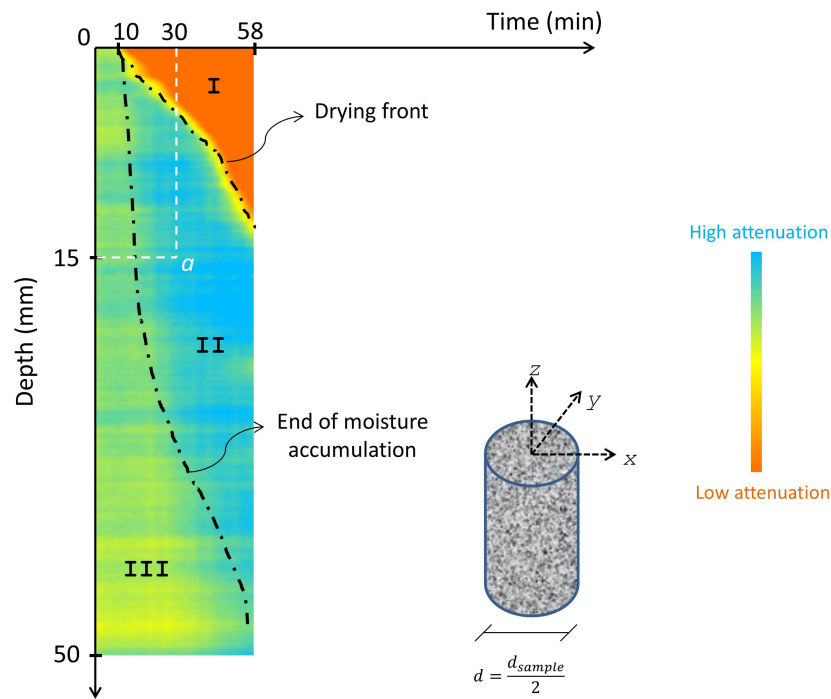


Figure 4.28: Schematic representation for the moisture profiles for HPC 8 mm. Each value in the graph (scaled to a color bar), represents the averaged attenuation in xy-plane. Such representation allows tracking the interface front i.e drying front and moisture accumulation in space and time

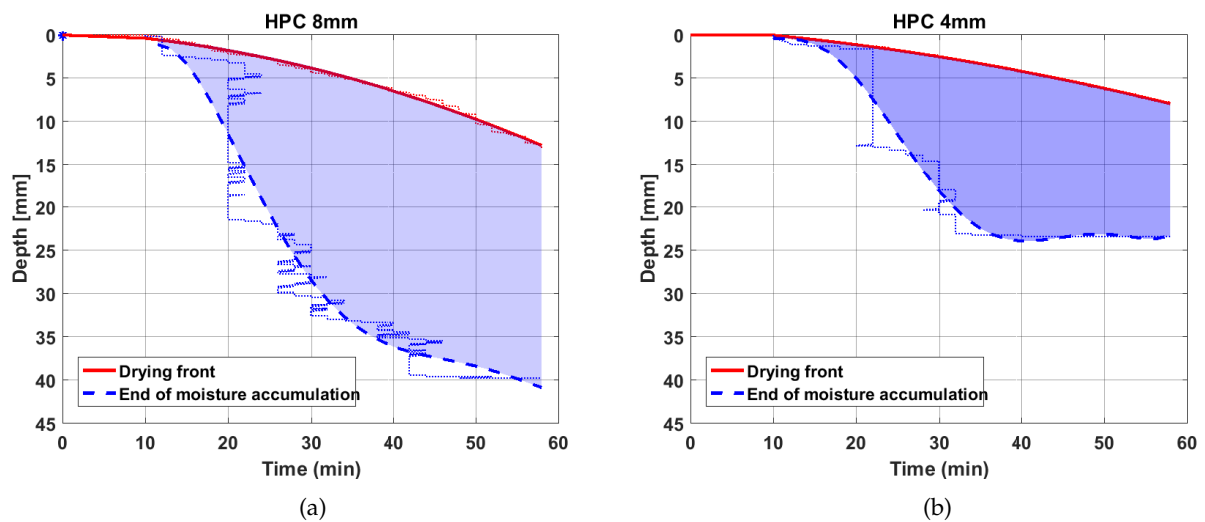


Figure 4.29: Depth of moisture accumulation zone as given by image analysis for tested sample (a) HPC 8 mm and (b) HPC 4 mm

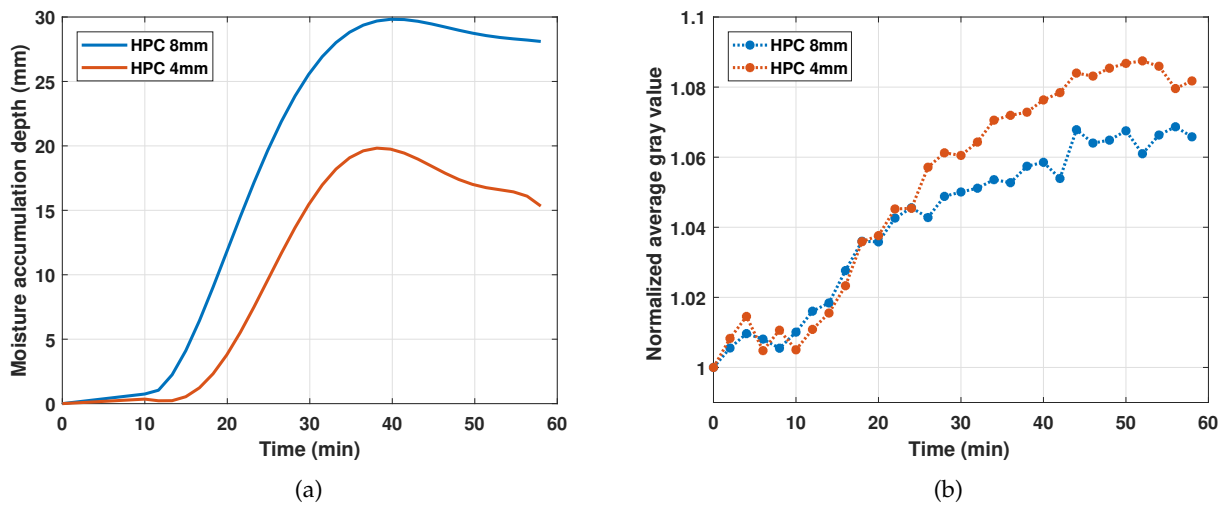


Figure 4.30: Characteristics of moisture accumulation zone: (a) depth (b) and peak evolution for both HPC 8 mm and HPC 4 mm

The accumulation of water behind the drying front is a pivotal hypothesis for one of the principal theories on the mechanisms of spalling. This theory speculates that the vapor produced at the dehydration front moves ahead and condenses in the colder region, causing a so-called "moisture clog", which in turn blocks the vapor transport into the specimen, causing the pressure build-up which provokes spalling (Harmathy, 1965; Jansson, 2013). While some numerical simulations (Gawin et al., 2002b) corroborate this hypothesis there is a substantial lack of experimental observations and quantification. The results presented in this contribution might therefore be the first direct proof and quantification of this phenomenon.

However, it is important to consider the influence of any neutron imaging artefact before drawing a conclusive observation. The two main effects that are known to introduce artefacts in neutron imaging are scattering and beam hardening. While these artefacts can be removed for single images by standard image processing techniques, a more physics-based correction is needed to follow the evolution of quantitative values.

Scattering is a process where a part of the neutrons is forced to deviate from their straight trajectory. This results in blurring of the radiograph by scattered neutrons. The intensity of a point in the image is therefore not only determined by neutrons arriving directly on the projection line but also by neutrons scattered from neighboring points of the sample. Neutrons scattered in a region near the lateral boundary can thus, in principle, increase the detected intensity in the core of the sample. Drying in the boundary region would diminish this effect and result in a decreasing intensity in the core, which would be wrongly interpreted as water accumulation. Since neutrons are scattered by hydrogen atoms uniformly in all directions, the recorded intensity decreases with the distance between the sample and the detector squared. The large detector-sample distance adopted (10 cm) should allow for reduced effect of global scattering in the presented test, as confirmed when studying the areas surrounding the sample (which should also suffer from scattering). Correcting for scattering effects is somewhat cumbersome and requires additional information about the exact water content and a calibration within a specific beamline (Hassanein et al., 2005).

Beam hardening, on the other hand, is a spectral effect, observed with polychromatic neutron sources. As the beam passes through the sample, its mean energy increases (i.e., it becomes "harder") because the lower-energy neutrons are preferentially absorbed, leaving behind only

the higher energy neutrons (Hassanein et al., 2005; Perfect et al., 2014). The effect of beam hardening is that the water content is underestimated near the axis relative to the boundary. This phenomenon can be observed *e.g.* in Figure 4.15, particularly on the left-hand-side images where the sample seems to be dryer near the axis. In our specific case, beam hardening (which is in the order of a 3-4% fluctuation) can be easily compensated at the beginning of the tests, but as the water evaporates from the sides because of the sub-optimal boundary conditions, a spurious increase of the attenuation coefficient (and therefore of the perceived water content) is imaginable. Unfortunately, while this effect is minimal in terms of variation of the gray value, so is the sought-after water accumulation variation (in the order of 3-5 %). As such it is hard to conclusively prove that all the observed increase is caused by water accumulation. A possible approach is to model analytically the interaction of neutrons with water in our specific geometry. An example of such modeling can be found in (Dauti et al., 2018b). This simplified modeling shows that the water accumulation is less than the one observed before the beam hardening correction.

However further data analysis, which go beyond the purpose of this work, would be required to draw a conclusive observation. The current strategy is in fact to run a second experimental campaign in the future aimed at improving boundary conditions which would altogether remove the need for such post-processing. It is important to note that beam hardening only affects the water accumulation analysis and does not in any form influence the reported study of the water front movement and the effect of aggregates over it.

4.3.5 Thermocouple-induced cavities

A certain disturbance of the samples by the presence of thermocouples was also observed. Figure 4.31 shows a horizontal slice at the position of the thermocouple located 20 mm from the heated surface of a sample with HPC 4 mm concrete mix (see Table 4.1). This image is a high-resolution tomogram with no binning and an exposure time of 2.5 seconds taken at the end of the test. Air voids are observed around the thermocouple wire (type K) which has a diameter of only 0.25 mm. It appears that air bubbles rose during casting when vibrating and were trapped at the wires.

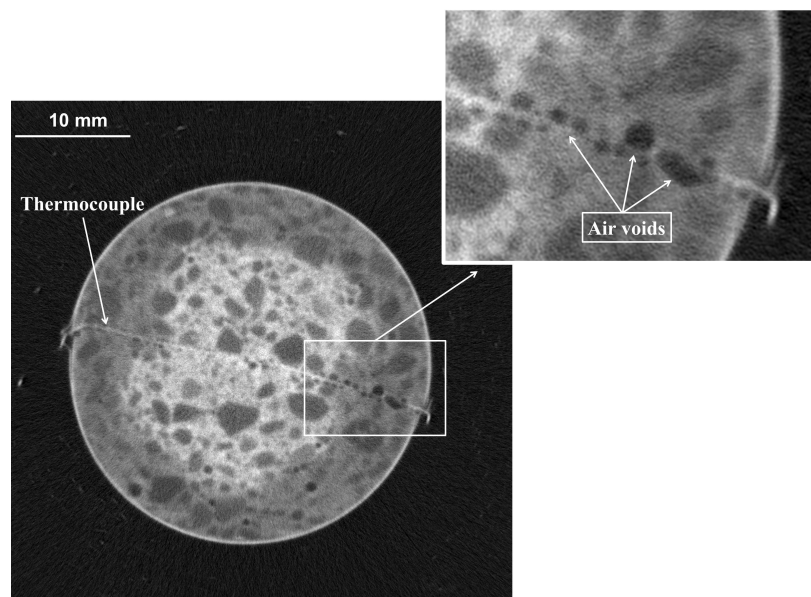


Figure 4.31: Air voids around a thermocouple in a high resolution image

This is an important observation for the experimental community on heated concrete which indicates that even very thin embedded elements such as a thermocouple can be intrusive and can affect locally the material properties and eventually the measurement that is being performed. Such an artefact becomes even more substantial when considering other embedded measurement elements such as pressure sensors, (see Figure 1.16) the size of which can range from 2 mm (metallic tube) to 12 mm (cup with sintered material). Similarly to what is observed for the thermocouples in Figure 4.31, air voids around a pressure sensor could build an escape channel for vapor and potentially affect the pressure measurements. The latter are then directly used for the validation of the existing numerical models presented in Section 1.3.2.

The neutron tomography images shown in this study are the first insight to the perturbations that embedded elements (in this case a thermocouple) can induce inside a concrete sample. On the one hand they suggest that the measurements (temperature and gas pressure) from embedded elements have to be used with precaution and on the other hand they emphasize the need of non-intrusive experimental methods in the context of spalling. In this sense, the non-destructive nature of neutron tests becomes even more relevant.

4.3.6 Influence of a crack on the drying front

As mentioned in Section 4.3.2 when discussing the physical reasons for a faster drying of HPC 8 mm, cracks may influence the evolution of the drying front. A case, in which a preexisting macro-crack has been observed to influence the drying front, is presented in the following. In this case, a sample HPC 4 mm equipped with thermocouples has been tested.

Vertical slices of the sample, obtained in real time, at different time stations are shown in Figure 4.32. A diagonal crack initiated at the position of the thermocouple, possibly due to the surrounding air voids, created a diagonal drying path on its way.

This important observation, firstly, points out once again the significant perturbation that can be induced in the material from embedded elements. Secondly, it shows the influence that such a perturbation, which in the considered case was a macro crack, can have on the drying front. Finally, this observation demonstrates the importance of 3D nature of tomography, which reveals information which is impossible to capture and therefore neglected by other experimental methods discussed in the overview of experiments on heated concrete (see Section 1.4).

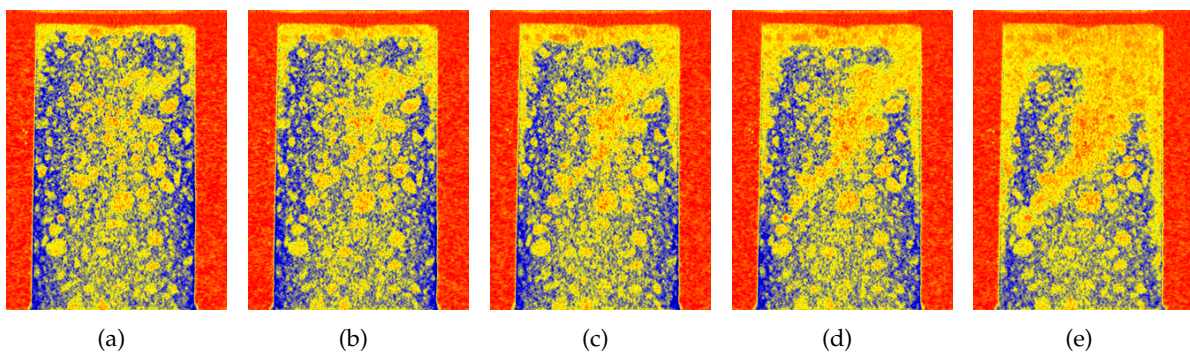


Figure 4.32: Vertical cut at (a) 20min (b) 22min (c) 26min (d) 30min (e) 42min

4.3.7 Additional drying at the boundary

4.3.7.1 Heat and moisture insulation

One of the challenges when performing experiments on heated concrete is maximizing the uni-dimensionality of the heat and moisture flow by adopting the appropriate lateral heat and moisture insulation.

For the heat insulation, in (Kalifa et al., 2000; Mindeguia et al., 2010) lateral side of the prismatic concrete samples were insulated by porous ceramics blocks. Van der Heijden et al. (2012) insulated their sample with mineral wool. Toropovs et al. (2015) used a 20 mm-thick glass foam layer in their neutron radiography tests of heated concrete. In (Mugume and Horiguchi, 2013; Felicetti et al., 2017) authors covered their samples with ceramic fibre board.

For the moisture insulation, self-adhesive aluminium foil was used in (Toropovs et al., 2015). Felicetti et al. (2017) tried two different sealing systems: I) carbon fibers placed on a high-temperature silicon layer previously smeared on the concrete surface II) aluminium foil placed on the concrete surface after being both smeared with epoxy resin. The second system turned out to be a better insulator according to the mass loss results of a 120°C drying test in a ventilated oven.

In the current study, rock wool and self-adhesive aluminium tape have been used as a common practice adopted for thermal and moisture insulation respectively. Despite these precautions, an additional drying at the boundaries was observed in all the tested samples (see for instance Figures 4.15, 4.23, 4.32). Once again it is worth noting that the observation of the boundary effect is only possible due to the 3D-measurements of moisture content by neutron tomography.

The exact observation of the boundary effect opens new perspectives for investigating and eventually improving the current experimental procedures on heat and moisture insulation for achieving a uni-dimensional heat and mass flow. This uni-dimensionality is not only important in terms of representing as close as possible the case of a concrete element submitted to fire, but its also critical in quantifying important physical phenomena such as moisture accumulation. The aspects of the interaction of the boundary effect with the quantification of the moisture accumulation have been discussed in Section 4.3.4.

4.3.7.2 Radiography vs. Tomography

In a situation where the drying front is not uniform, 3D measurements of moisture content by neutron tomography become even more relevant and 1D or 2D measurements (*i.e.*, neutron radiography and NMR) have to be used with precaution. For instance, in neutron radiography experiments, the recorded intensity is related to the neutron attenuation through the thickness of the sample parallel to the neutron source. The projection in a radiography is the sum in the direction of the beam. The 1D profile is then evaluated by averaging the projection perpendicular to the beam (see (Toropovs et al., 2015)). The boundary effects perpendicular to the the neutron beam can be eliminated by considering only an interior region of the radiography. The boundary effect in the beam direction, however, is inherently included in the radiography. This can give misleading results.

As an example, the averaging process as obtained from radiography is compared to the averaging obtained from tomography. The two processes correspond to two different regions: (see Figure 4.33(a)):

- The first region is a disc which excludes the boundaries and represents a region where the front is uniform.

- The second region is a slice in which we exclude the boundaries only in one direction. Such a region would be representative of the one dimensional moisture profiles usually obtained from neutron radiography experiments.

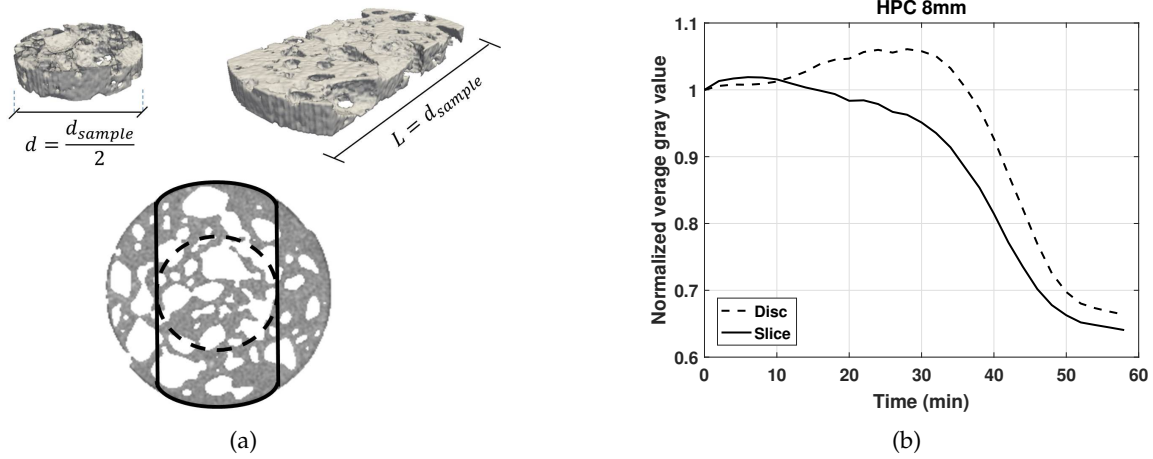


Figure 4.33: Moisture profiles for two regions: a disc (representing the analysis performed in the current study using the neutron tomography results) and a slice (representing the analysis usually performed using neutron radiography results), both represented schematically in (a). The results, given in (b) show how the 1D-profiles obtained from neutron radiography (solid line) can be misleading due to the boundary effect which is not visible in the direction of the beam

In Figure 4.33(b), the evolution of the average gray value in time for the two regions is compared. A clear difference between the two is observed. In the disc, an increase in the gray value is seen. On the other hand, the gray value in the slice doesn't exhibit such an increase due to the boundary effect which still exists in one direction. An increase in the core is hidden by a decrease near the boundary. This simple example highlights another aspect of the importance of 3D measurements .

4.4 Chapter Conclusions

In this chapter novel experiments on heated concrete, using neutron tomography, have been presented. An experimental setup adapted for neutron imaging and high-temperature testing has been developed in the framework of this PhD project. For the first time in literature, the local moisture distribution in concrete cylinders heated on the top face up to 300°C has been followed by the aid of neutron tomography. The world leading flux at ILL and the use of optimized acquisition parameters allowed capturing one tomogram per minute, which is an order of magnitude faster than any other neutron tomography test reported in literature. Such a fast acquisition speed was sufficient to follow the dehydration speed in concrete.

The main findings are listed below:

- The aggregate size has an influence on the global dehydration speed. Samples with 8 mm maximum aggregate size dried faster than samples with 4 mm maximum aggregate size. This can be attributed to a more pervasive crack network induced by bigger aggregates, which would accelerate the drying process.
- The direct observation of moisture profiles in 3D while monitoring the thermal field, allowed for relating the evolution of the moisture content with temperature. Such information is essential for investigating the constitutive behavior of heated concrete. For

example, the observation of a clear drying front at temperatures around 250°C improves the current knowledge on the dehydration of concrete.

- A more detailed analysis of the moisture profiles showed a moisture accumulation behind the front. This accumulation, known also as moisture clog, is directly linked to spalling. A special attention is dedicated in identifying the possible imaging artefacts (*e.g.* scattering, beam hardening) that might affect the results on the moisture accumulation. A simplified beam hardening correction model (presented in (Dauti et al., 2018b)) showed that, due to the non-uniformity of the drying front, the moisture accumulation appears to be higher than it actually is. More experiments, with improved boundary conditions, are needed for conclusive proof on this matter.
- Moreover, the 3D information provided by the tomography revealed some important and useful information for the experimental community on heated concrete. Some of this observations and recommendations emerging from the neutron tomography experiments are listed below:
 - (i) the embedded elements, such as thermocouples and pressure gauges, need to be used with precaution. Tomography images, have shown that air voids can form around such elements, resulting in a perturbation of the monitored parameters. This is particularly important when monitoring pressure inside concrete, as the validation of many state-of-art models on heated concrete are based on such measurements.
 - (ii) boundary effects are observed when adopting common methods for heat and moisture insulation (*e.g.* rockwool, self-adhesive aluminium tape). Improvements of insulation methods are necessary for a perfect unidimensional front.

The findings in this chapter demonstrate that neutron tomography is a powerful tool for performing experiments on heated concrete. The results obtained from rapid neutron tomography tests provide valuable information for understanding and modeling the underlying process.

In the next chapter, the neutron tomography results have been used for modeling the observed phenomena, notably the speed of the drying front, the faster lateral drying, the influence of an aggregate on the drying front etc.

Chapter 5

Simulation of moisture content: from continuum towards a 3D mesoscopic approach

5.1 Introduction

In Section 3.1 and 3.2, the numerical model has been used for simulating the standard measurements of temperature, gas pressure, and mass loss. It was observed that the model gives satisfying results provided the right input parameters and constitutive laws are introduced. For further investigation of the constitutive laws of the model, the use of a more reliable measurement technique such as neutron radiography has been presented (see Section 3.3). This approach proved to be very effective in adjusting some important constitutive laws, such as dehydration and sorption isotherms, for which the direct experimental measurement is missing or misinterpreted in literature.

The latest developments using neutron tomography, *i.e.*, measurements of 3D moisture distribution, are not only a milestone in the experimental techniques for heated concrete, but also a powerful tool for further improvement of the numerical models. In Section 5.2, the model is used for predicting the front speed and the moisture accumulation in a similar manner as done in Section 3.3. The objective is to verify if, after the adjustment of the constitutive laws, the model is capable of predicting the moisture migration. In addition, motivated by the boundary effects observed experimentally thanks to tomography, a study is dedicated to the investigation of the boundary conditions. 2D simulations will be performed for the investigation of the above mentioned aspects (*i.e.*, front speed, moisture accumulation, boundary effects).

The neutron tomography experiments presented in the previous chapter, showed an impact of the aggregates on the moisture distribution. For a numerical investigation of this phenomenon, modeling in mesoscopic scale is crucial. 3D simulations, both in a homogenized continuum and in a mesoscopic scale are presented and compared against experimental data in Section 5.3.

5.2 Front speed, moisture accumulation and boundary effects

5.2.1 Numerical Analysis

The numerical model implemented in Cast3M is used for the simulation of temperatures and moisture profiles obtained from neutron tomography tests at ILL. The case that is considered here is the test of the sample with maximum aggregate size 4 mm (HPC 4 mm). The experimental results of this tested sample are presented in Section 4.3.

The concrete mix used for this sample (see Table 4.1) is the same as the one used at neutron radiography experiments of Toropovs et al. (2015). Therefore, the same material properties as

for the simulations of the radiography tests (see Section 3.3) are used in here. Recall that the adjustment of dehydration and water retention curves was necessary for predicting the moisture profiles of the neutron radiography tests (see Section 3.3.3.2 and 3.3.4.2). These adjusted constitutive laws, given in Figure 5.1, have been adopted, for predicting the moisture profiles obtained at ILL.

It is important to emphasize here that the neutron tomography test of HPC 4 mm showed that the water loss starts at around 250°C (see Figure 4.26(b)), a fact which support the use of a dehydration curve as in Figure 5.1(a).

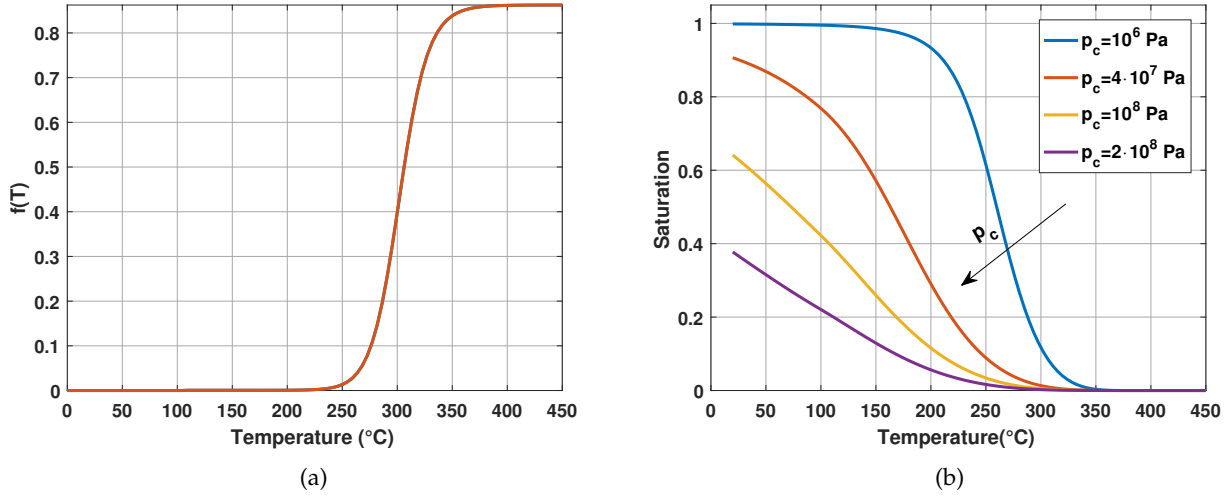


Figure 5.1: (a) Dehydration curve (b) Water retention curves

The permeability used in these simulations is:

$$k = k_0 \cdot 10^{A_T(T-T_0)} \cdot \left(\frac{p_g}{p_{atm}} \right)^{A_p} \quad (5.1)$$

where $k_0 = 10^{-20} \text{ m}^2/\text{s}$, $A_T = 0.005$, and $A_p = 0.368$.

For capturing the boundary conditions, observed experimentally, 2D simulations are sufficient. The rectangular geometry shown in Figure 5.2 represents the cylindrical specimen with $d = 30 \text{ mm}$ and $h = 60 \text{ mm}$. The geometry is discretized in quadrilateral finite elements with 1.5 mm size.

On the hot side, the heat flux due to radiation and convection is:

$$-\mathbf{n}(-k_{eff} \nabla T) = h_T^{hot}(T_{ext} - T) + \sigma \epsilon (T_{ext}^4 - T^4) \quad (5.2)$$

whereas on the cold side, heat convection with the ambient air is considered but the effect of radiation is assumed negligible:

$$-\mathbf{n}(-k_{eff} \nabla T) = h_T^{cold}(T_{ext} - T) \quad (5.3)$$

The averaged heat exchange coefficients, assumed to be constant during the simulations, are: $h_T^{hot} = 18 \frac{\text{W}}{\text{m}^2 \cdot \text{K}}$ for the hot side and $h_T^{cold} = 8 \frac{\text{W}}{\text{m}^2 \cdot \text{K}}$ for the cold side, as in (Gawin et al., 1999; Gawin et al., 2002b; Gawin et al., 2002a; Schrefler et al., 2002; Pesavento, 2000).

For the test, the radiator was heated up to 500°C within 3 min and kept at constant temperature until the end of the test. When such a heating curve is used as an external heating (T_{ext}) in Equation 5.2, the temperature is overestimated and a reduction of T_{ext} to 400°C is required for

obtaining reasonable results with respect to measurements. In another numerical study in literature with similar boundary conditions (Gawin et al., 2002a), the authors also had to reduce T_{ext} for reproducing the measured temperature. The reason behind the need for reducing the external temperature is related to some complexities at the hot boundary *e.g.*, limited surface of radiator, interaction between radiator and concrete surface (emissivity of radiator), complex air movement in the gap between the radiator and concrete surface, which are not fully considered by the boundary condition in Equation 5.2. However, such a thermal boundary condition that captures all the complex thermal processes falls outside the scope of this study.

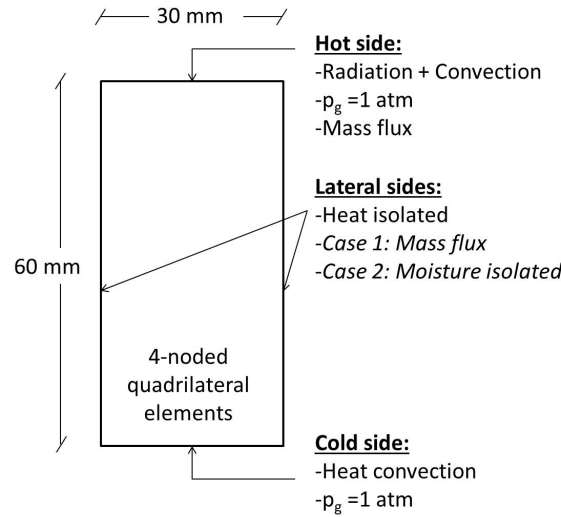


Figure 5.2: 2D model setup

For the gas mixture, the pressure is fixed at atmospheric pressure on the hot and cold sides:

$$p_g = p_{atm} \quad (5.4)$$

Natural boundary conditions are assumed at the lateral sides (no air flux).

The boundary condition for the vapor transport through the hot side is specified by the vapor flux as:

$$-\mathbf{n}(\rho_v \mathbf{v}_v + \rho_l \mathbf{v}_l) = h_m(\rho_v^{amb} - \rho_v) \quad (5.5)$$

where h_m is the mass transfer coefficient equal to 0.018 m/s as in (Gawin et al., 2002b; Pesavento, 2000; Dal Pont et al., 2011).

For investigating the boundary effect observed in the experiments, two cases are considered:

1. Moisture leak on the sides. A boundary condition as in Equation 5.5 with a lower mass transfer coefficient ($h_m = 0.009$ m/s) is applied on the lateral sides.
2. Perfect moisture insulation on the sides (1D mass flow).

5.2.2 Case 1: Moisture escape from the lateral boundaries

5.2.2.1 Temperature and gas pressure results

The temperature and pressure fields at different times are shown in Figure 5.3. The applied boundary condition results in a release of pressure at the lateral sides (see Figure 5.3(b)).

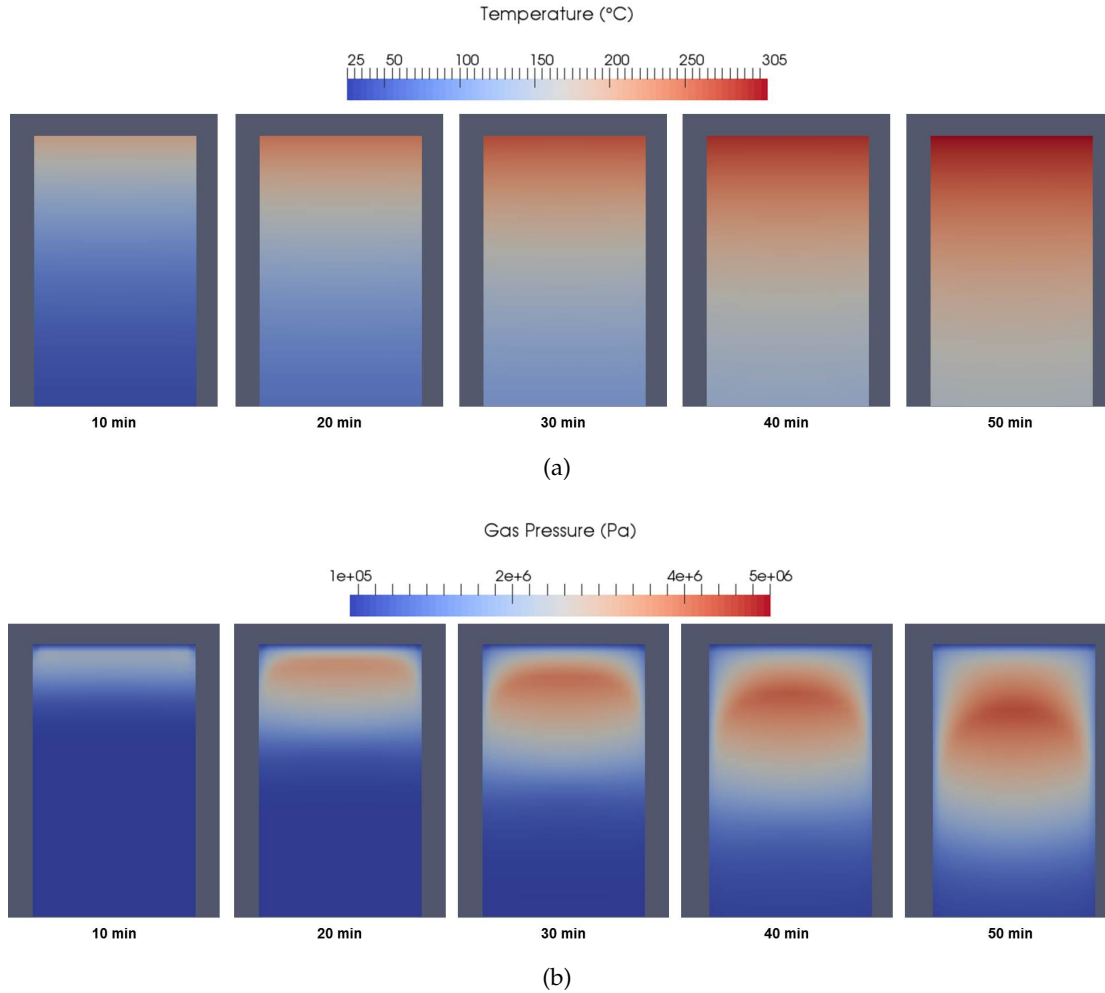


Figure 5.3: Case study 1: (a) Temperature field (b) Pressure field highlighting its non-uniformity

In Figure 5.4, the temperatures obtained from the numerical model (solid lines) are compared with the experimental measurements (dashed lines) using the three thermocouples located at nominal distances 3, 10, and 20 mm from the heated surface. Note that the numerical values are evaluated at the exact position of the thermocouple welding point determined from the neutron tomography. These exact positions are given in Table 4.2.

After the good agreement of temperatures, the next step is numerical simulation of the evolution of the moisture content.

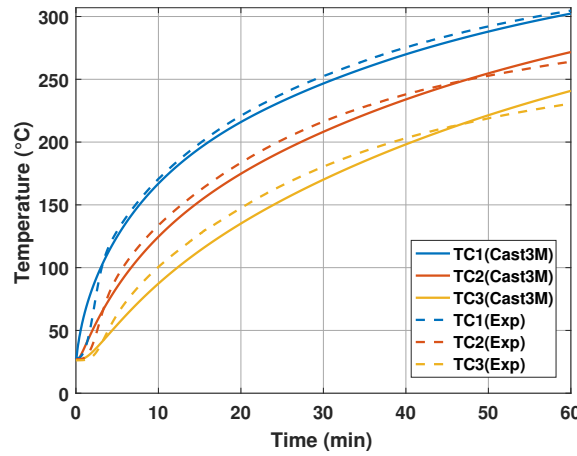


Figure 5.4: Case study 1: Simulation of the temperature profiles across time measured by the three thermocouples (TC1, TC2, TC3) placed at three nominal positions (3, 10, and 20 mm from the heated surface)

5.2.2.2 Moisture profiles

In the moisture profiles obtained through neutron tomography experiments, the attenuation coefficient (perceived in the images as a gray value) is directly related to the water content (see Section 4.3.3).

In numerical modeling, the variation in water content (w_{change}) is calculated from the change in the saturation of pores and from dehydration of the cement paste:

$$w_{change} = (\phi S \rho_l)_0 - (\phi S \rho_l)_t + \Delta m_{dehyd} \quad (5.6)$$

The variation of the water content is normalized to the initial water content ($w_i = 189 \text{ kg/m}^3$ from the concrete mix) for direct comparison with the experimental results:

$$\hat{w}_{change} = \frac{w_i - w_{change}}{w_i} \quad (5.7)$$

The normalized water change, \hat{w}_{change} , is computed at the core of the specimen (for avoiding any boundary effect).

The comparison of the moisture profiles is shown in Figure 5.5.

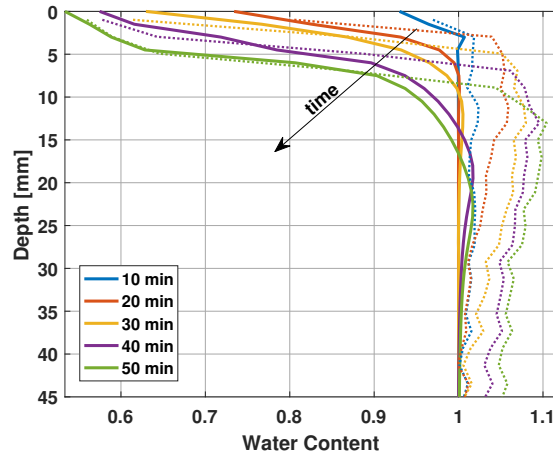


Figure 5.5: Case study 1: Moisture profile evolution : experimental (dotted lines) vs. numerical (solid lines)

It is observed that:

The numerical model gives good results in terms of the speed and shape of the drying front. Despite some small discrepancies, the plateau of the drying front is well predicted.

A moisture accumulation is observed behind the plateau of the drying front. This accumulation is more pronounced for profiles at 40 and 50 minutes. Quantitatively speaking, this moisture accumulation is much smaller than the one obtained by the neutron tomography images. However, as it was pointed out in Section 4.3.4, imaging artefacts such as beam hardening might affect the quantity of the moisture accumulation obtained from image analysis.

Discrepancies in the moisture accumulation

In Section 4.3.4, a special attention has been dedicated to the neutron tomography results regarding the moisture accumulation, for the simple reason that this phenomenon is directly linked to spalling of concrete. The experimental results showed a significant moisture accumulation behind the drying front. However, before drawing premature conclusions, the influence of imaging artefacts, notably beam hardening, has been considered.

A simplified model, for estimating the influence of beam hardening, given in (Dauti et al., 2018b), showed that this artefact complemented with the additional lateral drying, makes the moisture accumulation appear more pronounced than it actually is in reality. As shown in Figure 5.6, after the beam hardening correction, the water accumulation is less.

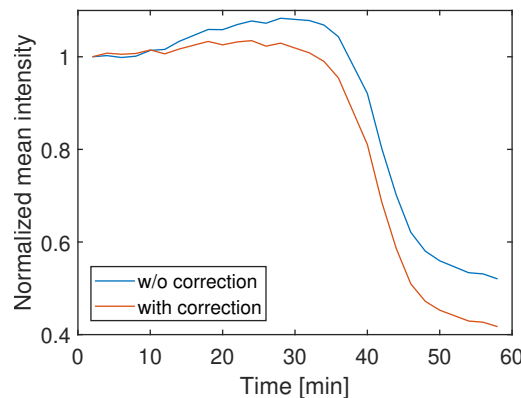


Figure 5.6: Evolution of intensity for sample with 8 mm aggregates before and after beam hardening correction as given by a simplified model presented in (Dauti et al., 2018b)

While the numerical model predicts very well the speed of the drying front, the moisture accumulation is considerably less than the one given by the neutron images. However, the results of the model are supported by the simplified correction model for beam hardening which suggests that the latter contributes in the amplification of the moisture accumulation given by the neutron images. Moreover, the model gives a more localized moisture accumulation, which seems to be more realistic than the one of the neutron images which appears to extend almost through the whole depth.

In order to have a conclusive proof on the quantity of the moisture accumulation, more experiments are needed with improved boundary conditions. A perfect one dimensional front, would diminish the apparent increases in the moisture accumulation due to beam hardening, thus removing the need for correction.

5.2.2.3 Boundary effect

In Figure 5.7(a) the variation of the water content at different time steps obtained experimentally is visualized and compared with the numerical results presented in Figure 5.7(b).

The numerical model is able to capture the additional drying at the boundaries observed experimentally. The moisture escape on the lateral sides results in an increased water loss on the sides.

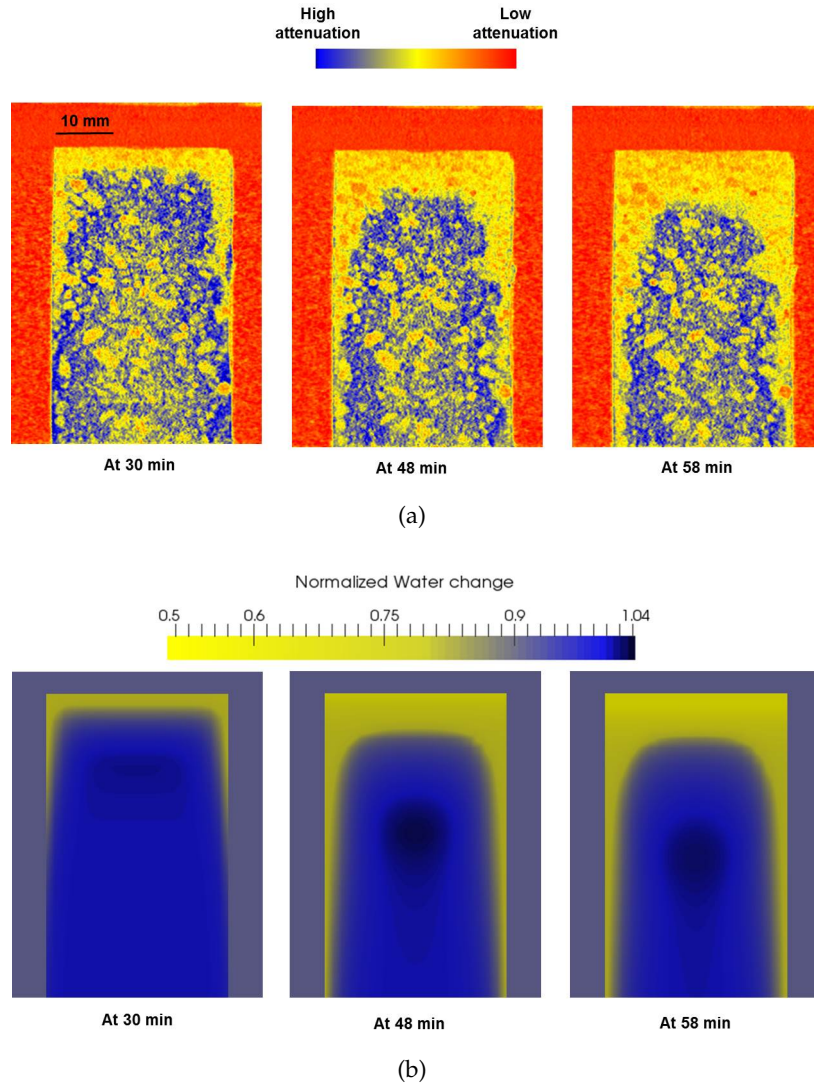


Figure 5.7: Case study 1: (a) Visualization of the variation of the water content measured by neutron imaging (b) Results of numerical simulations highlighting shape of the drying front and the moisture accumulation

The moisture accumulation observed in the plots in Figure 5.5 can also be visually seen in Figure 5.7(b) when looking at the core of the specimen (darker color).

In this first case study, moisture escape from the lateral sides was considered. In the next case study, a perfect moisture insulation (no mass flux on the lateral sides) is assumed in order to investigate the importance of sample's lateral insulation.

5.2.3 Case 2: Perfect moisture insulation

5.2.3.1 Temperature and gas pressure results

The temperature results, plotted in Figure 5.8, are not different from the Case 1 (see Figure 5.3(a)).

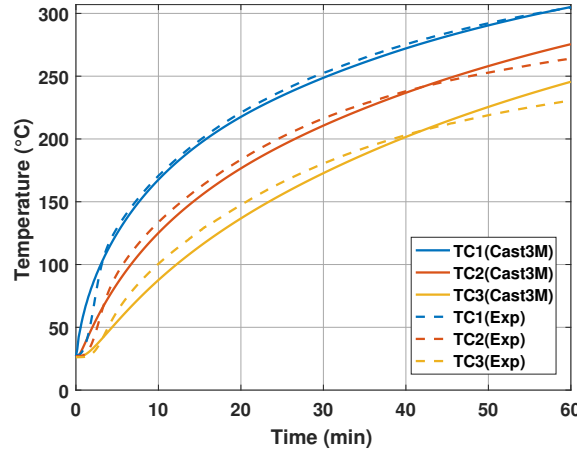


Figure 5.8: Case study 2: Simulation of the temperature profiles across time measured by the three thermocouples (TC1, TC2, TC3) placed at three nominal positions (3, 10, and 20 mm from the heated surface)

The pressure field shown in Figure 5.9, in contrast to Case Study 1 (see Figure 5.3(b)), is uniform due to the fact that vapor is not allowed to escape on the sides.

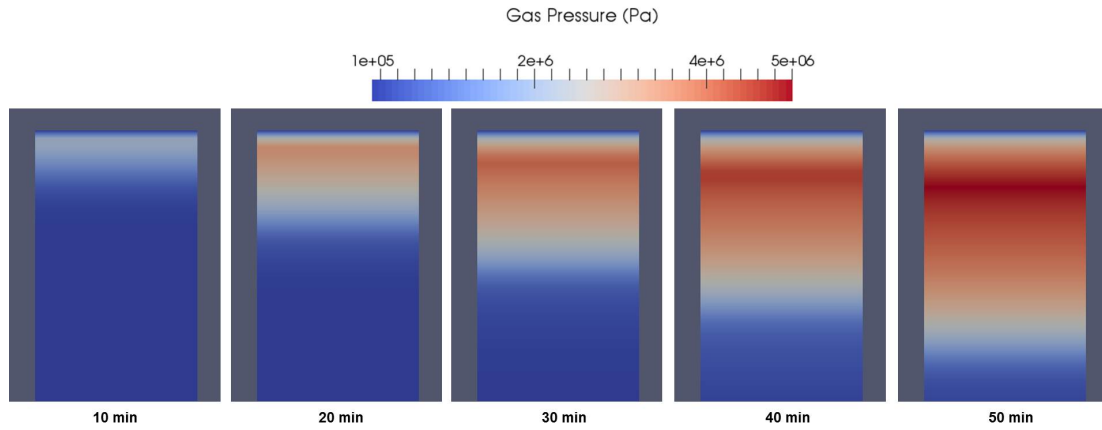


Figure 5.9: Case Study 2: A uniform pressure field observed at different times

5.2.3.2 Moisture profiles

In Figure 5.10, the moisture profiles obtained from the case with perfect boundaries are compared with the ones obtained in the case of lateral moisture leak.

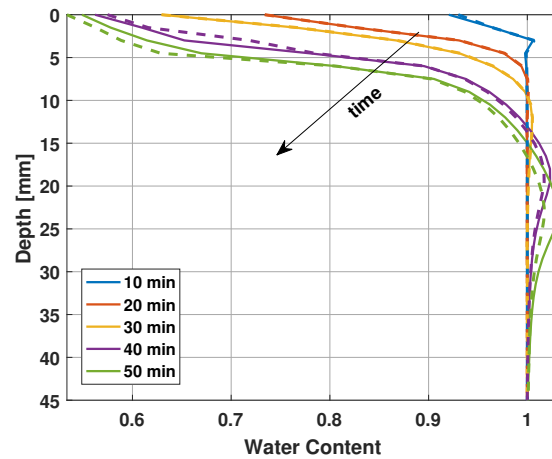


Figure 5.10: Numerical comparison of moisture profile evolution : perfect boundary (solid lines) vs. lateral moisture leak (dashed lines) highlighting the influence of sample's lateral insulation

The boundary conditions do not have an important impact on the speed of the drying front, which is similar for the two cases. However, they influence the moisture accumulation behind the front, which is more pronounced in the case of perfect boundary conditions.

The water change at different times is shown in Figure 5.11. As one would expect, the front in this case is uniform. As observed in the profiles in Figure 5.10, insulation of the mass transfer on the sides results in a higher moisture accumulation. The latter does not concentrate only in the core of the sample, as in the first Case study (see Figure 5.7(b)), but extends to the lateral sides of the specimen.

This numerical analysis shows the importance of having a better insulation in the experiments in order to obtain a unidimensional drying front for being as representative as possible to the real conditions in a heated structural element (e.g. wall, column etc.). It has been demonstrated numerically that the insulation has a direct influence on the quantity of the moisture accumulation, which is an important phenomena linked with the mechanisms of spalling.

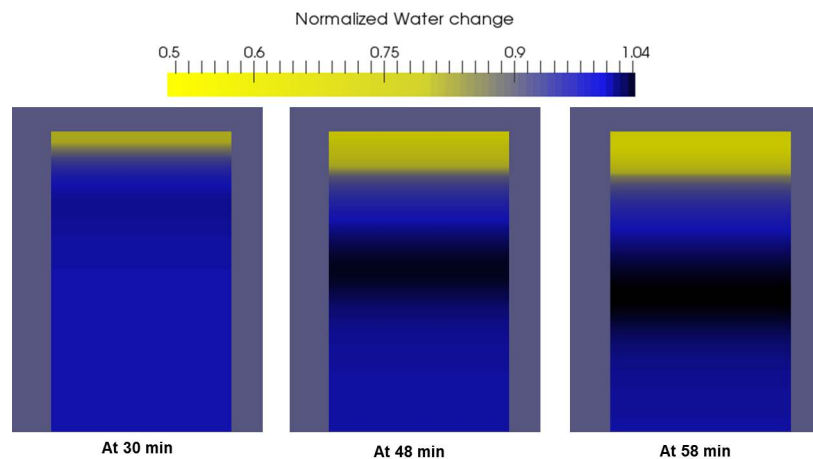


Figure 5.11: Case study 2: Numerical simulation with no mass flux on the sides highlighting the uniformity of the drying front and higher moisture accumulation compared with Case study 1

5.3 Simulations in 3D of moisture distribution

In the previous section, 2D simulations have been performed for simulating the front speed, the boundary effect and the moisture accumulation using a homogenized continuum model. In the next section 3D simulations have been performed for two reasons:

- First, for checking whether the 2D simulations, which have been performed in the previous section for simulating the front speed, the boundary effect and the moisture accumulation, are a good approximation or not. This numerical analysis is shown in Section 5.3.1, where 3D simulations of HPC 4 mm, treated as a homogenized continuum, are performed (same as in 5.2.2, but in 3D).
- Second, 2D simulations are not enough for simulating the problem in mesoscale. 3D simulations are needed for predicting the moisture profiles measured experimentally in a simplified case of a concrete sample HPC 4 mm with a single big aggregate. The objective is to use this simplified case to investigate the physical reasons for the additional lateral drying front observed in concrete samples with bigger aggregates.

5.3.1 Homogeneous HPC 4 mm

A cylindrical geometry with $d = 30$ mm and $h = 60$ mm is discretized in 2 mm tetrahedral elements of first order (TET4) as shown in Figure 5.12. For building the FE mesh, Salome (<http://www.salome-platform.org/>) which is an open source platform, has been used. Then the mesh is imported in Cast3M. The computational time on a standard laptop is about 6 hrs.

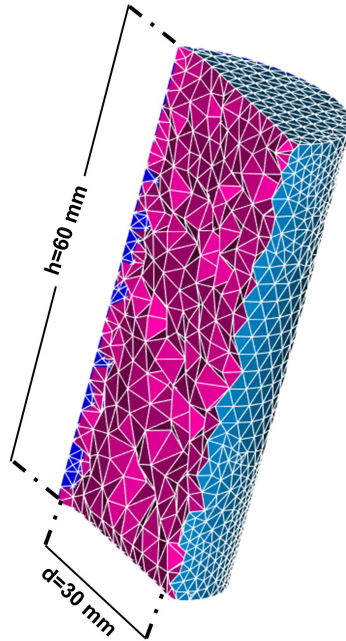


Figure 5.12: Finite element mesh generated in Salome

The temperature and pressure fields are shown in Figure 5.13. The variation of the water content is visualized in Figure 5.14.

The results of this study are very similar (not to say identical) with the 2D simulations of the same study (see Section 5.2.2). Therefore it can be concluded that a 2D model is sufficient for the simulations of temperature, gas pressure and moisture content when a homogenized continuum model is adopted.

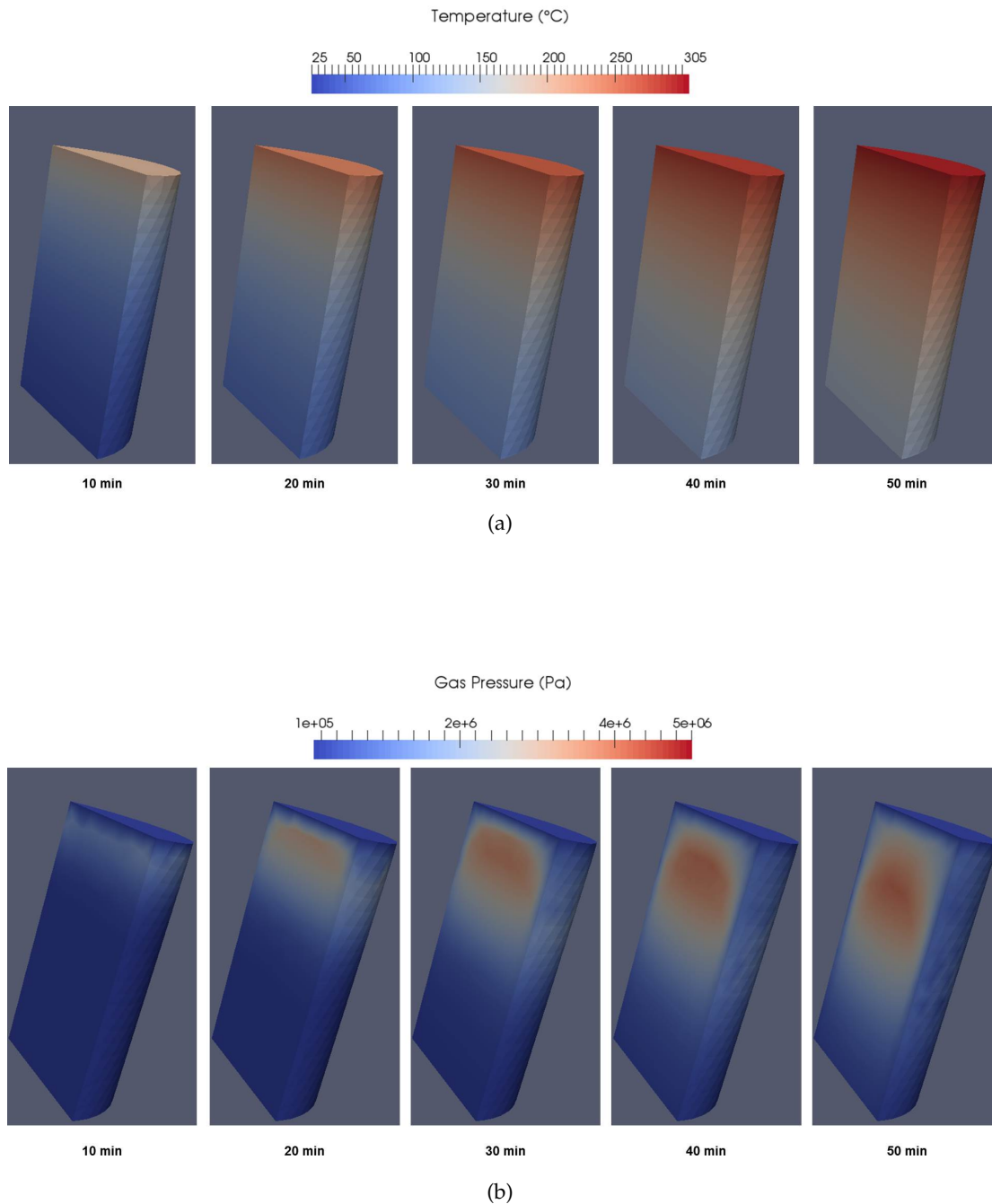


Figure 5.13: 3D simulations of HPC 4mm: (a) Temperature field (b) Pressure field

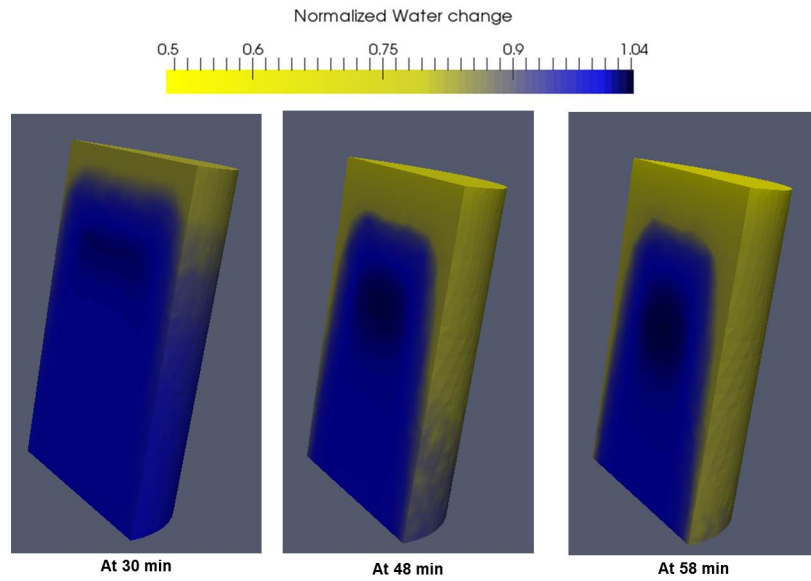


Figure 5.14: Water Content from 3D simulations

5.3.2 Simplified mesoscopic approach

In this section, mesoscopic modeling of the moisture distribution in HPC 4 mm with a single aggregate at the top is presented. For the sample under consideration, the moisture distribution has been measured experimentally by neutron tomography (see Section 4.23). In contrast to the analysis presented in Section 5.3.1 where a homogenized continuum model is used, a mesoscopic approach is adopted here. In other words, the single aggregate and cementitious matrix are considered explicitly in the numerical model. First, only the thermo-hydral behavior is considered (Section 5.3.2.1). Then the mechanical behavior is also included in the simulations (Section 5.3.2.2).

5.3.2.1 TH simulations

The single aggregate inside the HPC 4 mm sample has the shape of a spheroid. The dimensions and the exact position of the aggregate have been measured from the images and used for constructing the geometry to be used in the numerical model. The dimensions of the spheroid representing the aggregate are shown in Figure 5.15. The aggregate is modeled as a solid material (no permeability, no porosity) with a higher thermal conductivity (about 3 times) with respect to the cementitious matrix ($\lambda_a = 6.28 \frac{W}{m \cdot K}$ as measured in (Harmathy, 1970)). Thus the aggregate will transfer heat but not mass. It should be noted that the experimental characterization of the constituents (*i.e.*, aggregates and cementitious matrix) of the tested concrete is missing. Therefore, the thermo-hydral material properties of each constituent has been retrieved from literature, mainly from Harmathy (1970).

The computational time on a standard laptop is 7 hrs. Recall that the simulations using the homogenized continuum model lasted 6 hrs. So the presence of an aggregate, slightly increases the computational time. However, the latter can be considered similar for both cases.

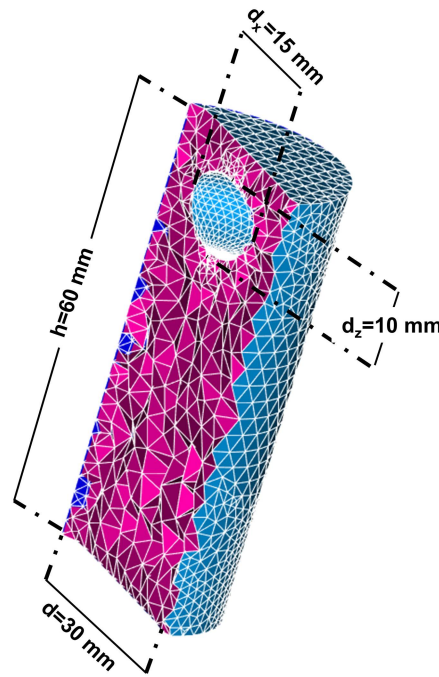


Figure 5.15: Finite element mesh highlighting the single aggregate at the top

Temperature and gas pressure

The temperature is shown in Figure 5.16. The temperature field is very similar to the homogeneous case (see Figure 5.13(a)).

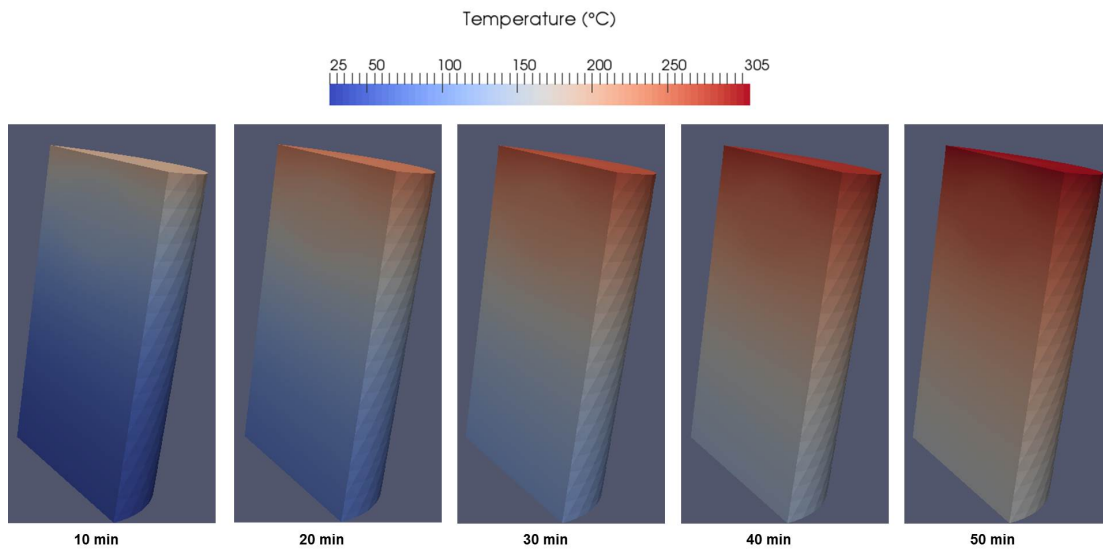


Figure 5.16: 3D simulations of temperature field in HPC 4 mm with a single big aggregate

In order to have a closer look at the influence of the aggregate on the thermal field, the temperatures along the width of the sample at 20 mm from the heated surface, just below the single aggregate, are compared in Figure 5.17.

For the homogeneous case (solid line), it is observed that the temperature is slightly higher at the core than at the outside. This is due to the drying at the boundaries which influences

the temperature field through the latent heat. As more water is evaporated near the boundary, the temperature propagation is delayed due to the consumption of energy which takes place in evaporation. However, quantitatively this effect is negligible (less than 1°C). When looking at the same profile in HPC 4 mm with a single aggregate, a more pronounced increase of temperature at the core of the specimen is observed. This is due the higher conductivity of aggregate compared to the cementitious matrix. The difference between the two cases is less than 4°C .

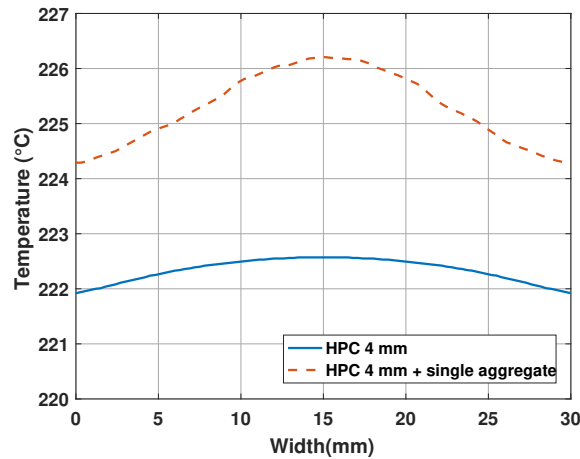


Figure 5.17: Temperature along the width of the specimen at a distance 20 mm from the heated surface (just below the aggregate) after 60 min of heating

The pressure field is presented in Figure 5.18 and pressure profiles at 20 mm from the heated surface are compared in Figure 5.19. Similar to what was observed in the 2D mesoscopic simulations presented in Section 3.4, there is some influence of the aggregates on the developed pressure.

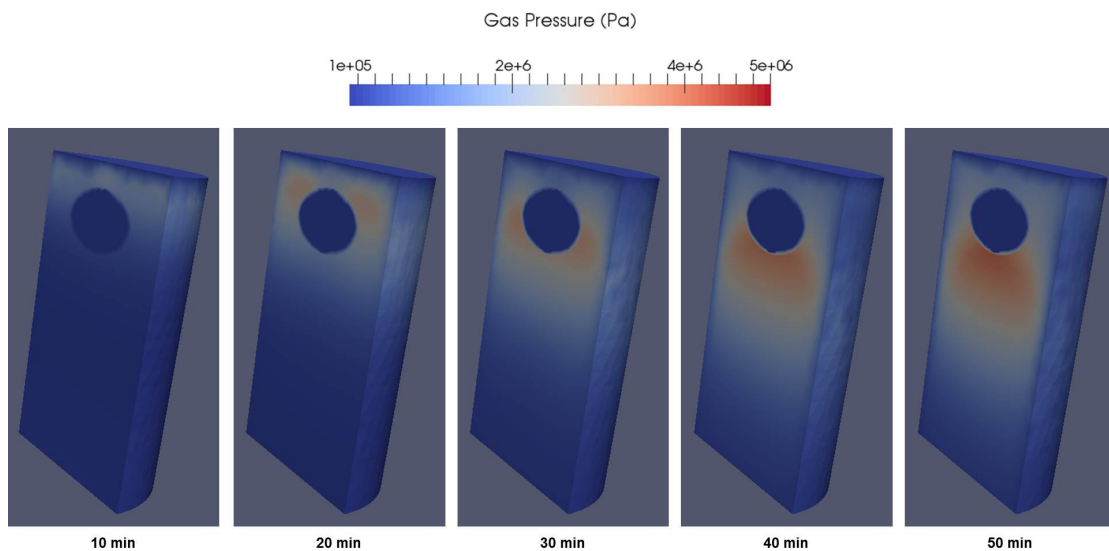


Figure 5.18: 3D simulations of pressure field in HPC 4 mm with a single big aggregate

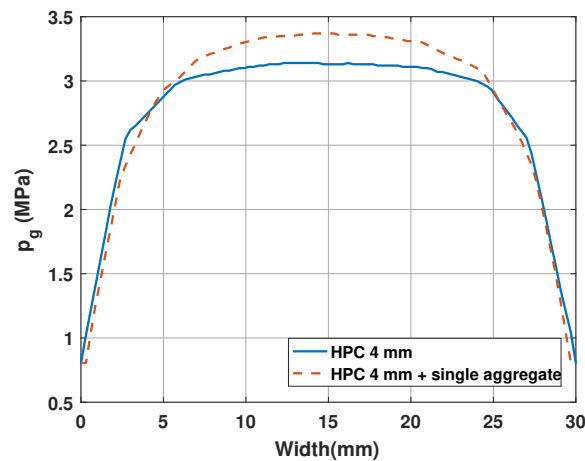


Figure 5.19: Pressure along the width of the specimen at a distance 20 mm from the heated surface (just below the aggregate) after 60 min of heating

Moisture content

The evolution of the moisture content given by the neutron tomography is shown in Figure 5.20(a) and the results from the numerical simulations in Figure 5.20(b).

In these numerical results it is observed that:

- The speed of the drying front is the same as in the homogeneous case (see Figure 5.14). In contrast to the experiment, no direct influence of the aggregate on the drying front can be seen. In the experiments (see Figure 5.20(a)), the drying process is accelerated around the aggregate. This phenomenon is not captured by the numerical model. Indeed, the fracture network, which is likely to be more pervasive around the aggregate, may result in a faster drying around the aggregate. This physical process is considered in the next section.
- A smaller water accumulation with respect to the homogeneous case is observed (see Figure 5.14). Due to the presence of the big aggregate, the vapor source coming from phase changes of cement is lower. Therefore, the vapor condensation toward the cooler side is less.

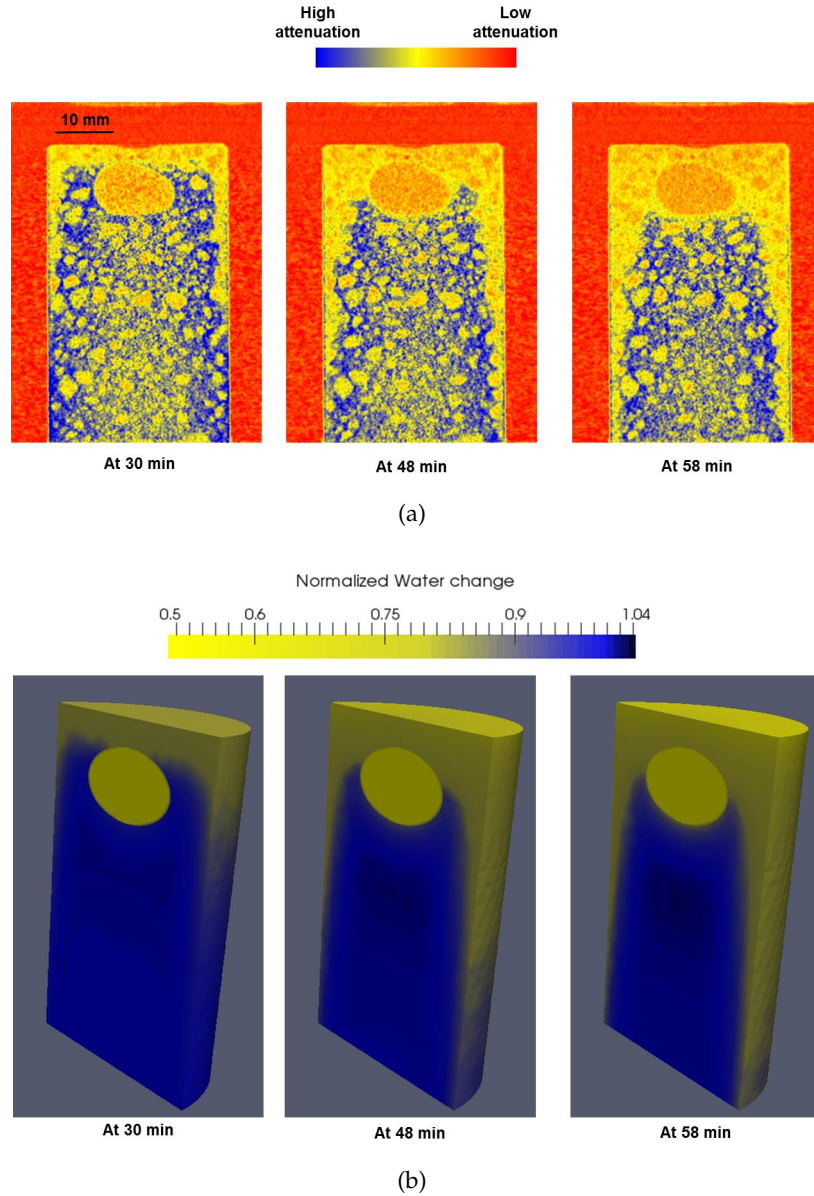


Figure 5.20: Evolution of moisture content: (a) Experiments (b) Numerical Model

5.3.2.2 THM simulations with damage-permeability coupling

To capture the faster drying around the aggregate, which is likely to be caused by a more pervasive fracture network around the aggregate, THM simulations are performed in this section. A non-local damage mechanical model (Pijaudier-Cabot and Bažant, 1987), described in Section 2.2.10 is used for the mechanical part. The characteristic length used in these simulations is three times the diameter of the aggregate ($l_c = 3d_a$) as in (Pijaudier-Cabot and Bažant, 1987).

The damage parameter is coupled with the permeability of the material as in (Gawin et al., 2002b):

$$k = k_0 \cdot 10^{A_T(T-T_0)} \cdot \left(\frac{p_g}{p_{atm}} \right)^{A_p} \cdot 10^{A_d d} \quad (5.8)$$

where $k_0 = 10^{-20} \text{ m}^2$, $A_T = 0.005$, $A_p = 0.368$, and $A_d = 1$.

The mechanical properties of the cementitious matrix such as compressive and tensile strength, young modulus, thermal dilation and their evolution with temperature, which have been adopted in the numerical model, have been measured experimentally by research scientists at Empa. For the single aggregate, mechanical properties from (Hager, 2004) have been adopted.

When the mechanical part is added to the model, the computational time on a standard laptop, increases from 7 to 9 hrs.

Damage and drying front

The damage field is presented in Figure 5.21(a). Similar to what has been already postulated in literature (Mindeguia et al., 2013a), damage in the cementitious matrix around the aggregate is observed due to the different thermal behavior of the concrete components at high temperature.

The evolution of the moisture content is presented in Figure 5.21(b). The much higher permeability induced by damage seems to influence the shape of the drying front.

Such a results can be used for the interpretation of the faster drying of samples with bigger aggregates (see Section 4.3.2). In a case where a number of big aggregates are found in a concrete sample, such as in HPC 8 mm (see Figure 4.15), it can be imagined that the damage induced in the cementitious matrix around the assembly of aggregates, influences the global speed of the drying front.

However, the example with the single aggregate is not enough as a conclusive proof for explaining the faster drying front observed experimentally on samples with bigger aggregate size. Nevertheless, the analysis of the single aggregate remains a good proof of concept and is an important first step towards 3D mesoscopic numerical analysis that considers the full particle size distribution of concrete.

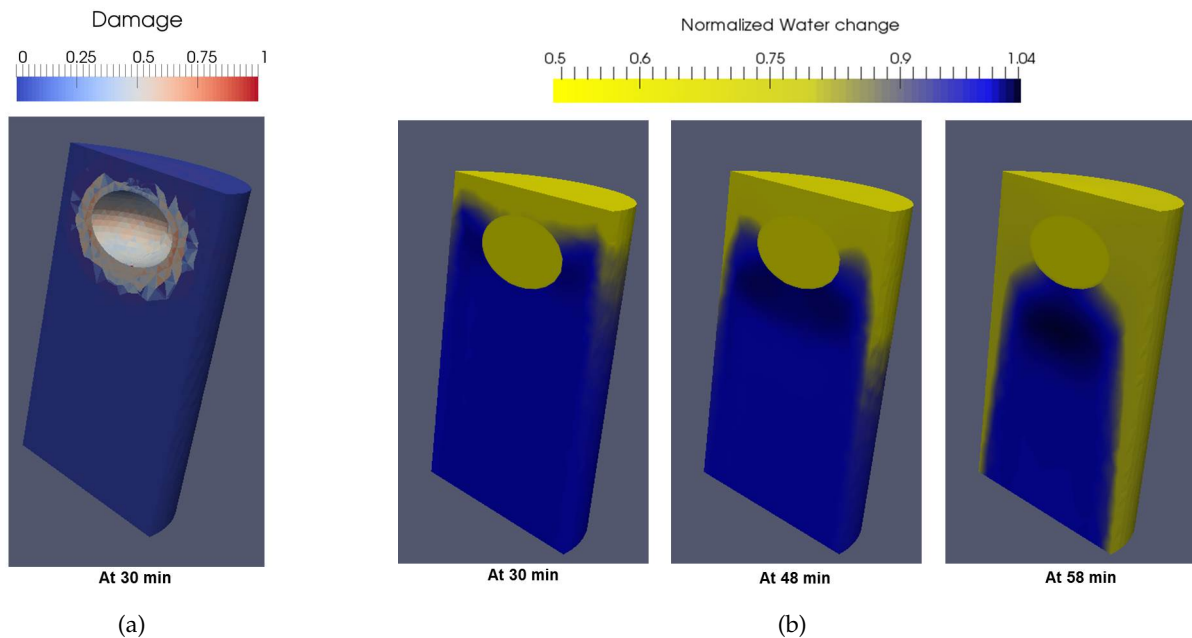


Figure 5.21: (a) Damage field and (b) evolution of water content highlighting the influence of single aggregate

5.4 Chapter Conclusions

In this chapter, the numerical model implemented in Cast3M has been used for simulating the neutron tomography experiments on heated concrete performed in this thesis.

The model uses adjusted constitutive laws from previous neutron radiography tests performed on the same concrete material, but on a sample with different geometry and size, as well different heating method (*i.e.*, radiator vs. thermal plate).

The model gives a good prediction of the drying speed. It also predicts a moisture accumulation, which is, however, less than the one observed in the neutron images. But one has to keep in mind that neutron images can be altered by artefacts. Indeed, a simplified image analysis has shown that, due to the additional lateral drying, beam hardening makes the moisture accumulation appear more pronounced than it actually is. However, more experiments with improved boundary conditions are needed for conclusive proof on the quantity of the moisture accumulation.

When a mass flux boundary condition is applied laterally, the model is also able to capture the additional lateral drying observed experimentally. This result suggests that the reason for the boundary effect is due to the insufficient moisture insulation in the lateral surface.

The importance of boundary conditions has been investigated through a numerical analysis comparing two cases: perfect vs. imperfect moisture insulation. It was found out that there is no difference in the speed of the drying front. However, lateral moisture escape results in a lower moisture accumulation.

The predictive capabilities of the model, after having calibrated the constitutive behavior of the material from a previous different experiment (see Section 3.3), with no additional parameter tuning involved, shows that it can be a useful tool for investigating the physical phenomena in heated concrete.

A 3D mesoscopic simulation of the experiment with a single big aggregate at the top has been performed for the purpose of investigating the influence of the aggregate size on the drying front. Thermo-hydro-mechanical simulations showed that the damage of the cementitious matrix around the aggregates influences the shape of the drying front. No influence of the aggregate on the drying front was observed, when damage was excluded from the model. Such a result is an important step towards the physical interpretation of the faster drying in samples with bigger aggregate size, but can not be considered as a conclusive proof. Nevertheless, it opens the way to 3D THM mesoscopic numerical analysis that considers a real concrete mesoscopic structure, which could possibly confirm the difference in drying speed.

Chapter 6

Conclusions and Perspectives

6.1 Summary of this doctoral work

The objective of this doctoral work was to contribute to understanding of the spalling mechanisms of concrete exposed to fire. Despite being an important subject of research over the last decades, the physics behind the fire spalling are not yet fully understood. The strategy followed in this thesis is a combined numerical-experimental approach, *i.e.* neutron imaging, complemented with advanced numerical modeling at the adequate scale, for a quantitative verification of assumptions used in different fire spalling theories. The work performed during this PhD project, concerning the numerical and the experimental investigation is described below.

6.1.1 Numerical model for concrete at high temperature

The diverse and coupled thermo-hydro-mechanical phenomena in concrete at high temperature, necessitate advanced numerical models, that can take into account all the relevant physical processes. The state-of-the art models on heated concrete are mainly based on the continuum approach of Lewis and Schrefler (1998).

Given the complexity of such models, a big effort has been dedicated to the numerical implementation. The starting point was an existing implementation by Dal Pont et al. (2007), which relies on a staggered solution strategy. In order to have a numerically efficient model, a new implementation, based on a monolithic solution strategy, has been done in this thesis. The newly implemented code is 20-30 times faster than the existing one.

The coupled thermo-hydro-mechanical model has been implemented in the finite element software Cast3M. In the framework of this PhD project, a parallel implementation, that considers only the thermo-hydral behavior of concrete has also been implemented in the finite element software COMSOL Multiphysics.

The numerical model has been applied to several experiments from literature. First, standard verification with PTM (pressure, temperature, mass loss) tests has been performed. Then the model has been verified for the first time against 2D moisture profiles given by the neutron radiography results obtained from (Toropovs et al., 2015). This numerical analysis allowed the improvement of the model in terms of material laws such as dehydration and water retention curves. The experimental methods employed for the determination of these material laws are either missing (no data for water retention curves at high temperature), or are not representative of the real conditions (*e.g.*, Thermo-Gravimetric Analysis not adequate for the dehydration law). In this sense, the effectiveness of the presented approach, *i.e.*, numerical analysis complemented with results from neutron imaging, becomes even more evident.

The numerical model has also been extended to the mesoscale. The newly implemented mesoscopic THM model has been used for 2D simulations of gas pressure. These simulations have shown the importance of considering the heterogeneous nature of concrete in numerical models.

Finally, the numerical model with improved material laws has been used for simulating the neutron tomography experiments performed in this thesis. Among others, 3D mesoscopic THM simulations are presented and verified against experimental results.

The developments in numerical modeling of heated concrete are schematically shown in Figure 6.1. The author hopes that the modeling work performed in this doctoral thesis, which is based on the previous developments, notably on the theoretical formulation by Gawin et al. (1999), contributes to the advancement of numerical models for concrete at high temperature.

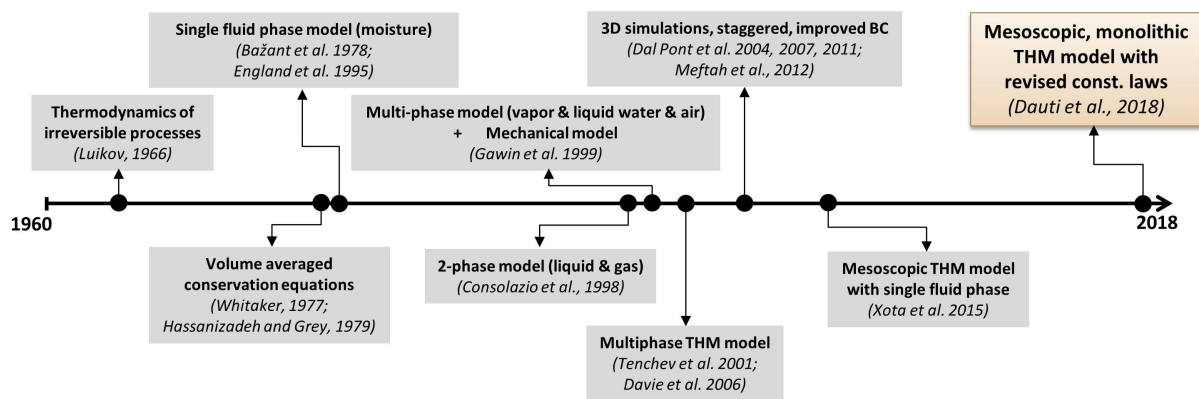


Figure 6.1: Contribution of this doctoral work to the advancement of numerical models for concrete at high temperature

6.1.2 Neutron tomography experiments on heated concrete

For what concerns the experimental investigation, the first ever neutron tomography on concrete during simultaneous heating has been successfully performed during this doctoral work. The aim was to obtain local information about the moisture content in 3D and in real time, for shedding light on the behavior of concrete at high temperature with respect to spalling. Such information was not possible using the existing experimental methods in literature.

For performing such experiments, a setup, adapted for neutron imaging and high temperature testing, has been developed. The world leading flux at ILL and the use of optimized acquisition parameters allowed capturing one tomogram per minute. Such a fast tomography (one order of magnitude faster than any other neutron tomography test reported in literature), was sufficient for following the fast dehydration process in concrete.

One of the objectives of the experiments was studying the influence of the aggregate size on the drying front. For this purpose, samples with different concrete mixtures *i.e.*, maximum aggregate size 4 mm (HPC 4 mm) and 8 mm (HPC 4 mm) have been prepared and tested.

A big effort has been dedicated to the analysis and post treatment of neutron tomography scans. 3D images are first obtained through image reconstruction, using a filtered back projection algorithm. Then, image analysis is performed for obtaining the moisture migration in three dimensions. Among others, the image analysis involves discerning the aggregates from

the cement paste by segmentation for extra information on the morphology of the tested samples.

The neutron tomography tests mark a significant contribution to the overall picture of experiments on heated concrete, shown in Figure 6.2.

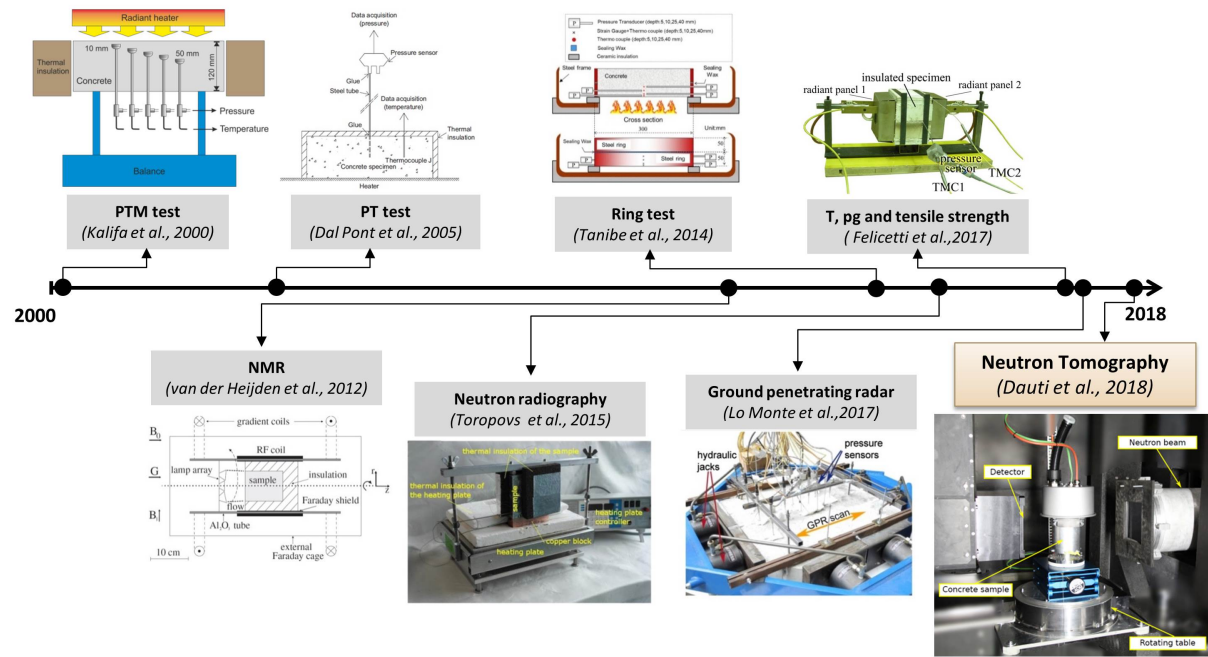


Figure 6.2: Contribution of this doctoral work to the development of experiments for concrete at high temperature

It is important to emphasize that the interaction between experiments (*i.e.* neutron imaging) and numerical modeling helps in improving both of them, as it has been shown in this thesis. The author strongly believes that a combined experimental-numerical approach is indispensable for understanding the behaviour of concrete at high temperature with respect to spalling.

6.2 Main Findings

The main results obtained from the experimental and numerical work performed in this thesis are summed below:

- *Neutron imaging complemented with numerical analysis is an effective approach for improving the constitutive laws such as dehydration and water retention curves.*

The constitutive laws of the numerical model have been improved thanks to a numerical analysis of moisture profiles obtained from neutron radiography tests performed in literature.

- *An important experimental finding is that drying is faster for samples with bigger aggregate size.*

A possible explanation can be the more pervasive fracture network around bigger aggregates. 3D mesoscopic THM simulations of an experiment with a single aggregate at the top have been performed. The model predicts a damage on the cementitious matrix

around the aggregate which changes the shape of the drying front. These mesoscopic simulations are an important step on explaining the physical reasons behind the faster drying front on samples with bigger aggregates.

- *The neutron tomography results show the existence of the moisture accumulation behind the drying front, a phenomenon directly linked to spalling.*

While many studies in literature have postulated the existence of a moisture clog, its quantification wasn't possible due to the lack of experimental methods. The moisture accumulation results presented in this thesis demonstrate the potential of neutron tomography method for quantifying the moisture clog.

- *The neutron tomography tests have shown that an important water loss occurs at temperatures around 250°C.*

This is an important observation for the numerical community on heated concrete which commonly adopts a dehydration constitutive law based on thermo-gravimetric analysis. The latter, which is performed on crushed samples, is not always representative of the real conditions.

- *Despite the employment of common heat and moisture insulation methods for a unidimensional front, an additional lateral drying has been observed.*

This result, which was revealed from tomography images, suggests that some commonly adopted thermal and moisture insulators are not enough for achieving a unidimensional drying front and, therefore, have to be used with precautions. Due to this boundary effect, it was found out that imaging artefacts such as beam hardening can influence the quantity of the moisture accumulation computed from image analysis.

- *Tomography images have revealed useful information for the experimental community, such as: thermo-couple induced cavities, influence of a crack on the drying front etc.*

Such result is the first insight to the perturbations that embedded elements can induce inside a concrete sample. They suggest that measurements from such embedded elements (temperature, gas pressure) might be influenced by these perturbations.

- *Continuum model results show a good agreement with the neutron tomography results performed in this thesis.*

The model with improved constitutive laws is able to predict the speed of the drying front. It also shows the existence of a moisture accumulation, which, in quantity, is less than the neutron images. However, the model results, seem to be more realistic and are supported by the fact that beam hardening can influence the quantity of the moisture accumulation given by the images.

6.3 Perspectives

While the results obtained in this thesis are a big progress towards the understanding of the drying process at high temperature with respect to spalling, they are not sufficient for providing a definitive explanation on the mechanisms of this phenomenon. Here's a list of research perspectives rising from the obtained results:

Numerical Modeling

- A numerical analysis of moisture profiles obtained from neutron radiography experiments proved to be successful in improving some important constitutive laws in concrete such as dehydration and water retention curves. A further step would be to look closer at the physics, so that these laws would be more general and apply to more cases.
- The mesoscopic thermo-hydro-mechanical model for concrete at high temperature developed in this thesis should be exploited. The esteemed numerical performance of the model, allows performing more simulations involving mesoscale geometries. Different particle size distributions for analyzing the moisture distribution can be performed. Such analysis would help in better understanding the physics behind the faster front speed observed in samples with bigger aggregates. Moreover, a stress analysis, along with a spalling criterion, can be applied to investigate the influence of heterogeneous nature of concrete on the mechanical behavior.

Experiments

- The quantification of the moisture clog, a phenomenon directly linked to spalling, is essential. Due to the imperfect boundary conditions, beam hardening can influence the quantity of the moisture clog given by the neutron images. Therefore, improved boundary conditions are necessary for achieving a 1D drying front. A second experimental campaign, has been already launched for the investigation of different methods of thermal and moisture insulation.
- Concrete with various types of fibers (polypropylene, recycled fiber polymers etc.) can be tested for identifying the differences (if any) in the drying front speed, and more importantly in the moisture accumulation. This would contribute in understanding the mechanisms of these fibers that are believed to reduce spalling.

Appendix A

Operators C and K

The operators **C** et **K** and the vectors **f** that derive from the weak-form of conservation equations read:

$$\mathbf{C}_{cc} = \int_{\Omega} \phi \left((1 - S_l) \frac{\partial \rho_v}{\partial p_c} + (\rho_l - \rho_v) \frac{\partial S_l}{\partial p_c} \right) \mathbf{N}^T \mathbf{N} d\Omega \quad (\text{A.1})$$

$$\mathbf{C}_{cg} = \int_{\Omega} (1 - S_l) \phi \frac{\partial \rho_v}{\partial p_g} \mathbf{N}^T \mathbf{N} d\Omega \quad (\text{A.2})$$

$$\begin{aligned} \mathbf{C}_{cT} = \int_{\Omega} & \left((1 - \phi) \left(S_l \frac{\rho_l}{\rho_s} + (1 - S_l) \frac{\rho_v}{\rho_s} \right) \frac{\partial \rho_s}{\partial T} + (1 - S_l) \phi \frac{\partial \rho_v}{\partial T} + S_l \phi \frac{\partial \rho_l}{\partial T} \right. \\ & \left. - \left(S_l \frac{\rho_l}{\rho_s} + (1 - S_l) \frac{\rho_v}{\rho_s} - 1 \right) \frac{\partial m_{dehyd}}{\partial T} + \phi (\rho_l - \rho_v) \frac{\partial S_l}{\partial T} \right) \mathbf{N}^T \mathbf{N} d\Omega \quad (\text{A.3}) \end{aligned}$$

$$\mathbf{K}_{cc} = - \int_{\Omega} \left(K \frac{\rho_l k_{rl}}{\mu_l} + D \frac{M_v M_a}{M_g RT} \frac{\rho_v}{\rho_l} \right) \mathbf{B}^T \mathbf{B} d\Omega \quad (\text{A.4})$$

$$\mathbf{K}_{cg} = \int_{\Omega} \left(K \left(\frac{\rho_l k_{rl}}{\mu_l} + \frac{\rho_v k_{rg}}{\mu_g} \right) + D \frac{M_v M_a}{M_g RT} \left(\frac{\rho_v}{\rho_l} - \frac{p_v}{p_g} \right) \right) \mathbf{B}^T \mathbf{B} d\Omega \quad (\text{A.5})$$

$$\mathbf{K}_{cT} = \int_{\Omega} D \frac{M_v M_a}{M_g RT} \frac{\partial p_v}{\partial T} \mathbf{B}^T \mathbf{B} d\Omega \quad (\text{A.6})$$

$$\mathbf{C}_{gg} = \int_{\Omega} (1 - S_l) \phi \frac{\partial \rho_a}{\partial p_g} \mathbf{N}^T \mathbf{N} d\Omega \quad (\text{A.7})$$

$$\mathbf{C}_{gc} = \int_{\Omega} \left((1 - S_l) \phi \frac{\partial \rho_a}{\partial p_c} - \rho_a \phi \frac{\partial S_l}{\partial p_c} \right) \mathbf{N}^T \mathbf{N} d\Omega \quad (\text{A.8})$$

$$\begin{aligned} \mathbf{C}_{gT} = \int_{\Omega} & \left((1 - S_l) (1 - \phi) \frac{\rho_a}{\rho_s} \frac{\partial \rho_s}{\partial T} - \rho_a \phi \frac{\partial S_l}{\partial T} + (1 - S_l) \phi \frac{\partial \rho_a}{\partial T} \right. \\ & \left. - (1 - S_l) \frac{\rho_a}{\rho_s} \frac{\partial m_{dehyd}}{\partial T} \right) \mathbf{N}^T \mathbf{N} d\Omega \quad (\text{A.9}) \end{aligned}$$

$$\mathbf{K}_{gg} = \int_{\Omega} \left(K \frac{\rho_a k_{rg}}{\mu_g} - D \frac{M_v M_a}{M_g RT} \left(\frac{\rho_v}{\rho_l} - \frac{p_v}{p_g} \right) \right) \mathbf{B}^T \mathbf{B} d\Omega \quad (\text{A.10})$$

$$\mathbf{K}_{gc} = \int_{\Omega} D \frac{M_v M_a}{M_g R T} \frac{\rho_v}{\rho_l} \mathbf{B}^T \mathbf{B} d\Omega \quad (\text{A.11})$$

$$\mathbf{K}_{gT} = - \int_{\Omega} D \frac{M_v M_a}{M_g R T} \frac{\partial p_v}{\partial T} \mathbf{B}^T \mathbf{B} d\Omega \quad (\text{A.12})$$

$$\begin{aligned} \mathbf{C}_{TT} = \int_{\Omega} & \left(\rho C_p - H_{vap} \left((1 - \phi) S_l \frac{\rho_l}{\rho_s} \frac{\partial \rho_s}{\partial T} + S_l \phi \frac{\partial \rho_l}{\partial T} \right) \right. \\ & \left. - \left(H_{vap} \left(1 - S_l \frac{\rho_l}{\rho_s} \right) + H_{dehyd} \right) \frac{\partial m_{dehyd}}{\partial T} - H_{vap} \rho_l \phi \frac{\partial S_l}{\partial T} \right) \mathbf{N}^T \mathbf{N} d\Omega \end{aligned} \quad (\text{A.13})$$

$$\mathbf{C}_{Tc} = - \int_{\Omega} H_{vap} \rho_l \phi \frac{\partial S_l}{\partial p_c} \mathbf{N}^T \mathbf{N} d\Omega \quad (\text{A.14})$$

$$\mathbf{C}_{Tg} = \mathbf{0} \quad (\text{A.15})$$

$$\begin{aligned} \mathbf{K}_{TT} = \int_{\Omega} & \left(\lambda - K \left(\left(C_l + \frac{\partial H_{vap}}{\partial T} \right) \frac{\rho_l k_{rl}}{\mu_l} + C_g \frac{\rho_g k_{rg}}{\mu_g} \right) \mathbf{N}^T \mathbf{p}_g^T \right. \\ & \left. + \left(C_l + \frac{\partial H_{vap}}{\partial T} \right) K \frac{\rho_l k_{rl}}{\mu_l} \mathbf{N}^T \mathbf{p}_c^T \right) \mathbf{B}^T \mathbf{B} d\Omega \end{aligned} \quad (\text{A.16})$$

$$\mathbf{K}_{Tc} = \int_{\Omega} H_{vap} K \frac{\rho_l k_{rl}}{\mu_l} \mathbf{B}^T \mathbf{B} d\Omega \quad (\text{A.17})$$

$$\mathbf{K}_{Tg} = - \int_{\Omega} H_{vap} K \frac{\rho_l k_{rl}}{\mu_l} \mathbf{B}^T \mathbf{B} d\Omega \quad (\text{A.18})$$

$$\mathbf{f}_c = \int_{\bar{\Sigma}_p} \mathbf{N}^T (\bar{q}_l + \bar{q}_v - h_g (\rho_v - \rho_v^\infty)) d\Sigma \quad (\text{A.19})$$

$$\mathbf{f}_g = \int_{\bar{\Sigma}_p} \mathbf{N}^T (\bar{q}_a - h_g (\rho_a - \rho_a^\infty)) d\Sigma \quad (\text{A.20})$$

$$\mathbf{f}_T = \int_{\bar{\Sigma}_T} \mathbf{N}^T \left(\bar{q}_T - h_T (T - T_\infty) - \epsilon \sigma (T^4 - T_\infty^4) \right) d\Sigma \quad (\text{A.21})$$

Bibliography

- Akashi, K., Ozawa, M., Fujimoto, K., and Parajuli, S. S. (2016). "Numerical analysis for a fire-related spalling failure model of high-strength Concrete". In: *The 2016 World Congress on Structures*.
- Al Fadul, M. A. and Mackie, K. R. (2018). "Numerical analysis of coupled heat and mass transfer phenomena in concrete at elevated temperatures". In: *Transport in Porous Media* 122.2, pp. 437–458.
- Anderberg, Y. (Jan. 1997). "Spalling phenomena of HPC and OC". In: *Proceedings of International Workshop on Fire Performance of High-Strength Concrete*, pp. 69–73.
- Anderson, I., McGreevy, R., and Bilheux, H. (2009). *Neutron Imaging and Applications*. Springer US.
- ASHRAE (2001). *ASHRAE Handbook: Fundamentals*. International Metric System. ASHRAE.
- Ashton, L. A. and Bate, S. C. C. (1960). "The fire resistance of prestressed concrete beams". In: *Proceedings of the Institution of Civil Engineers* 17.1, pp. 15–38.
- Baggio, P., Bonacina, C., and Strada, M. (1993). "Trasporto di calore e massa nel calcestruzzo cellulare". In: *La Tremotecnica* 12, pp. 53–60.
- Bamforth, P. B. (1987). "The relationship between permeability coefficients for concrete obtained using liquid and gas". In: *Magazine of Concrete Research* 39.138, pp. 3–11.
- Baroghel-Bouny, V., Mainguy, M., Lassabatere, T., and Coussy, O. (1999). "Characterization and identification of equilibrium and transfer moisture properties for ordinary and high-performance cementitious materials". In: *Cement and Concrete Research* 29.8, pp. 1225–1238.
- Baroghel-Bouny, V. (2007). "Water vapour sorption experiments on hardened cementitious materials. Part II: Essential tool for assessment of transport properties and for durability prediction". In: *Cement and Concrete Research* 37.3, pp. 438–454.
- Bathe, K. J. and Wilson, E. L. (1972). "Stability and accuracy analysis of direct integration methods". In: *Earthquake Engineering & Structural Dynamics* 1.3, pp. 283–291.
- Bažant, Z. P. (1976). "Instability, ductility, and size effect in strain-softening concrete". In: *Journal of the engineering mechanics division* 102.2, pp. 331–344.
- Bažant, Z. and Thonguthai, W. (Oct. 1978). "Pore pressure and drying for concrete at high temperature". In: *Journal of Engineering Mechanics - ASCE* 104.5, pp. 1059–1079.
- Bažant, Z. P. and Thonguthai, W. (1979). "Pore pressure in heated concrete walls: theoretical prediction". In: *Magazine of Concrete Research* 31.107, pp. 67–76.
- Bažant, Z. P. (1997). "Analysis of pore pressure, thermal stresses and fracture in rapidly heated concrete". In: *International Workshop on Fire Performance of High-Strength Concrete*, pp. 1487–1499.
- Bažant, Z. and Kaplan, M. (1996). *Concrete at High Temperatures: Material Properties and Mathematical Models*. Concrete design and construction series. Longman.
- Boström, L. and Robert, J. (2008). "Self-compacting concrete exposed to fire". In: *Report in SP Technical Research Institute of Sweden*.
- Boström, L., Wickström, U., and Adl-Zarrabi, B. (Apr. 2007). "Effect of specimen size and loading conditions on spalling of concrete". In: *Fire and Materials* 31, pp. 173–186.
- Briffaut, M., Benboudjema, F., Laborderie, C., and Torrenti, J.-M. (2013). "Creep consideration effect on mesoscale modeling of concrete hydration process and consequences on the mechanical behavior". In: *Journal of Engineering Mechanics* 139.12, pp. 1808–1817.

- Carré, H., Pimienta, P., La Borderie, C., Pereira, F., and Mindeguia, J.-C. (2013). "Effect of compressive loading on the risk of spalling". In: *MATEC Web of Conferences* 6, p. 01007.
- CEA (2006). *Cast3M, Finite Element Software*. Version 15.0.
- Chadwick, J. (1932). "Possible Existence of a Neutron". In: *Nature* 129, p. 322.
- Chen, B. and Liu, J. (June 2004). "Residual strength of hybrid-fiber-reinforced high-strength concrete after exposure to high temperatures". In: *Cement and Concrete Research* 34, pp. 1065–1069.
- Chung, J. H., Consolazio, G. R., and McVay, M. C. (2006). "Finite element stress analysis of a reinforced high-strength concrete column in severe fires". In: *Computers & Structures* 84.21, pp. 1338–1352.
- COMSOL (1998). *COMSOL Multiphysics® v. 5.2. www.comsol.com*. COMSOL AB, Stockholm, Sweden.
- Connolly, R. J. (1995). "The spalling of concrete in fires". PhD thesis. Aston University.
- Consolazio, G., McVay, M., and Rish III, J. (Sept. 1998). "Measurement and prediction of pore pressures in saturated cement mortar subjected to radiant heating". In: *ACI Materials Journal* 95, pp. 525–536.
- Dal Pont, S. and Ehrlacher, A. (2004). "Numerical and experimental analysis of chemical dehydration, heat and mass transfers in a concrete hollow cylinder submitted to high temperatures". In: *International Journal of Heat and Mass Transfer* 47.1, pp. 135–147.
- Dal Pont, S., Colina, H., Dupas, A., and Ehrlacher, A. (2005). "An experimental relationship between complete liquid saturation and violent damage in concrete submitted to high temperature". In: *Magazine of Concrete Research* 57.8, pp. 455–461.
- Dal Pont, S., Durand, S., and Schrefler, B. (2007). "A multiphase thermo-hydro-mechanical model for concrete at high temperatures—Finite element implementation and validation under {LOCA} load". In: *Nuclear Engineering and Design* 237.22, pp. 2137–2150.
- Dal Pont, S., Meftah, F., and Schrefler, B. (2011). "Modeling concrete under severe conditions as a multiphase material". In: *Nuclear Engineering and Design* 241.3, pp. 562–572.
- Dal Pont, S. (2004). "Lien entre la perméabilité et l'endommagement dans les bétons à haute température". PhD thesis.
- D'Aloia, L., Robert, F., Rougeau, P., Moreau, B., Flahault, N., and Collignon, C. (2013). "Improving the behavior of concrete exposed to fire by using an air entraining agent (AEA): Assessment of spalling". In: *MATEC Web of Conferences* 6, p. 02007.
- Dauti, D., Dal Pont, S., Weber, B., Briffaut, M., Toropovs, N., Wyrzykowski, M., and Sciumé, G. (2018a). "Modeling concrete exposed to high temperature: Impact of dehydration and retention curves on moisture migration". In: *International Journal for Numerical and Analytical Methods in Geomechanics* 42.13, pp. 1516–1530.
- Dauti, D., Weber, B., Dal Pont, S., Tengattini, A., Toropovs, N., and Briffaut, M. (2017a). "First results on fast neutron tomography of heated concrete". In: *5th International Workshop on Concrete Spalling due to Fire Exposure in Borås, Sweden*, pp. 249–258.
- Dauti, D., Dal Pont, S., Briffaut, M., and Sciumé, G. (2017b). "Numerical benchmark of experiments on heated concrete". In: *5th International Workshop on Concrete Spalling due to Fire Exposure in Borås, Sweden*, pp. 197–203.
- Dauti, D., Tengattini, A., Dal Pont, S., Toropovs, N., Briffaut, M., and Weber, B. (2018b). "Analysis of moisture migration in concrete at high temperature through in-situ neutron tomography". In: *Cement and Concrete Research* 111, pp. 41–55.
- Davie, C. T., Pearce, C. J., and Bićanić, N. (2006). "Coupled heat and moisture transport in concrete at elevated temperatures - Effects of capillary pressure and adsorbed water". In: *Numerical Heat Transfer, Part A: Applications* 49.8, pp. 733–763.
- Davie, C., Pearce, C., Kukla, K., and Bićanić, N. (2018). "Modelling of transport processes in concrete exposed to elevated temperatures – An alternative formulation for sorption isotherms". In: *Cement and Concrete Research* 106, pp. 144–154.

- De Beer, F. (Oct. 2015). "Neutron- and X-ray radiography/ tomography: Non-destructive analytical tools for the characterization of nuclear materials". In: *Journal of the Southern African Institute of Mining and Metallurgy* 115, pp. 913–924.
- Diederichs, U., Jumppanen, U.-M., and Penttala, V. (June 1989). "Behavior of high strength concrete at high temperatures". In: *Report number 92 in Helsinki University of Technology, Department of Structural Engineering*.
- Drouet, E., Poyet, S., and Torrenti, J.-M. (2015). "Temperature influence on water transport in hardened cement pastes". In: *Cement and Concrete Research* 76, pp. 37–50.
- England, G. and Khoylou, N. (1995). "Moisture flow in concrete under steady state non-uniform temperature states: experimental observations and theoretical modelling". In: *Nuclear Engineering and Design* 156.1, pp. 83–107.
- Ezzedine El Dandachy, M., Briffaut, M., Dal Pont, S., and Dufour, F. (Oct. 2016). "Induced anisotropic gas permeability of concrete due to coupled effect of Drying and Temperature". In: *Concrete under Severe Conditions - Environment and Loading*. Vol. 711. Key Engineering Materials. Trans Tech Publications, pp. 871–878.
- Feldkamp, L. A., Davis, L. C., and Kress, J. W. (1984). "Practical cone-beam algorithm". In: *Journal of the Optical Society of America* 1.6, pp. 612–619.
- Feldman, R. F. and Sereda, P. J. (1968). "A model for hydrated Portland cement paste as deduced from sorption-length change and mechanical properties". In: *Matériaux et Construction* 1.6, pp. 509–520.
- Felicetti, R. and Lo Monte, F. (2013). "Concrete spalling: Interaction between tensile behaviour and pore pressure during heating". In: *MATEC Web of Conferences* 6, p. 03001.
- Felicetti, R., Lo Monte, F., and Pimienta, P. (2017). "A new test method to study the influence of pore pressure on fracture behaviour of concrete during heating". In: *Cement and Concrete Research* 94, pp. 13–23.
- Figueiredo, F., Rickard, I., Shah, A. H., Huang, S.-S., Angelakopoulos, H., Bisby, L., Burgess, I., and Pilakoutas, K. (2017). "Recycled tyre polymer fibres to mitigate heat-induced spalling of concrete". In: *5th International Workshop on Concrete Spalling due to Fire Exposure in Borås, Sweden*, pp. 359–364.
- Furbish, D. (1997). *Fluid Physics in Geology: An Introduction to Fluid Motions on Earth's Surface and Within Its Crust*. OUP USA.
- Gagg, C. R. (2014). "Cement and concrete as an engineering material: An historic appraisal and case study analysis". In: *Engineering Failure Analysis* 40, pp. 114–140.
- Gawin, D., Majorana, C., and Schrefler, B. (1999). "Numerical analysis of hygro-thermal behaviour and damage of concrete at high temperature". In: *Mechanics of Cohesive-frictional Materials* 4.1, pp. 37–74.
- Gawin, D., Pesavento, F., and Schrefler, B. A. (2002a). "Modelling of hygro-thermal behaviour and damage of concrete at temperature above the critical point of water". In: *International Journal for Numerical and Analytical Methods in Geomechanics* 26.6, pp. 537–562.
- Gawin, D., Pesavento, F., and Schrefler, B. A. (2002b). "Simulation of damage-permeability coupling in hygro-thermo-mechanical analysis of concrete at high temperature". In: *Communications in Numerical Methods in Engineering* 18.2, pp. 113–119.
- Gawin, D., Pesavento, F., and Schrefler, B. (2003). "Modelling of hygro-thermal behaviour of concrete at high temperature with thermo-chemical and mechanical material degradation". In: *Computer Methods in Applied Mechanics and Engineering* 192.13–14, pp. 1731–1771.
- Gawin, D., Pesavento, F., and Schrefler, B. A. (2011a). "What physical phenomena can be neglected when modelling concrete at high temperature? A comparative study. Part 1: Physical phenomena and mathematical model". In: *International Journal of Solids and Structures* 48.13, pp. 1927–1944.

- Gawin, D., Pesavento, F., and Schrefler, B. A. (2011b). "What physical phenomena can be neglected when modelling concrete at high temperature? A comparative study. Part 2: Comparison between models". In: *International Journal of Solids and Structures* 48.13, pp. 1945 – 1961.
- Gens, A. and Olivella, S. (2001). "THM phenomena in saturated and unsaturated porous media". In: *Revue Française de Génie Civil* 5.6, pp. 693–717.
- Giry, C., Dufour, F., and Mazars, J. (2011). "Stress-based nonlocal damage model". In: *International Journal of Solids and Structures* 48.25–26, pp. 3431 –3443.
- Gramegna, L. (2017). "Numerical approach to study the influence of heterogenities in pressure measurements on concrete under high temperature". MA thesis. Université Grenoble Alpes.
- Grassl, P., Wong, H. S., and Buenfeld, N. R. (2010). "Influence of aggregate size and volume fraction on shrinkage induced micro-cracking of concrete and mortar". In: *Cement and Concrete Research* 40.1, pp. 85 –93.
- Grondin, F., Dumontet, H., Hamida, A. B., Mounajed, G., and Boussa, H. (2007). "Multi-scales modelling for the behaviour of damaged concrete". In: *Cement and Concrete Research* 37.10, pp. 1453 –1462.
- Guerrieri, M. and Fragomeni, S (Sept. 2013). "An experimental investigation into the influence of specimen size, in-situ pore pressures and temperatures on the spalling of difference size concrete panels when exposed to a hydrocarbon fire". In: *MATEC Web of Conferences* 6, p. 01002.
- Hager, I. (2004). "Comportement à haute température des bétons à haute performance: évolution des principales propriétés mécaniques". PhD thesis. Marne-la-Vallée, ENPC.
- Hamami, A., Turcry, P., and Aït-Mokhtar, A. (2012). "Influence of mix proportions on microstructure and gas permeability of cement pastes and mortars". In: *Cement and Concrete Research* 42.2, pp. 490 –498.
- Harmathy, T. (1965). *Effect of Moisture on the Fire Endurance of Building Elements*. Research paper 385. ASTM Special Technical Publication, pp. 74 –95.
- Harmathy, T. (1970). *Thermal Properties of Concrete at Elevated Temperatures*. Research paper. National Research Council of Canada.
- Harmathy, T. and Allen, L. (Feb. 1973). "Thermal properties of selected masonry unit concretes". In: *Journal of American Concrete Institute* 70.
- Hassanein, R., Lehmann, E., and Vontobel, P. (2005). "Methods of scattering corrections for quantitative neutron radiography". In: *Nuclear Instruments and Methods in Physics Research Section A: Accelerators, Spectrometers, Detectors and Associated Equipment* 542.1, pp. 353 –360.
- Hassanizadeh, M. and Gray, W. G. (1979a). "General conservation equations for multi-phase systems: 1. Averaging procedure". In: *Advances in Water Resources* 2, pp. 131 –144.
- Hassanizadeh, M. and Gray, W. G. (1979b). "General conservation equations for multi-phase systems: 2. Mass, momenta, energy, and entropy equations". In: *Advances in Water Resources* 2, pp. 191 –203.
- Hassanizadeh, M. and Gray, W. G. (1980). "General conservation equations for multi-phase systems: 3. Constitutive theory for porous media flow". In: *Advances in Water Resources* 3.1, pp. 25 –40.
- Herman, G. T. (2009). *Fundamentals of Computerized Tomography: Image Reconstruction from Projections*. 2nd. Springer Publishing Company, Incorporated.
- Hertz, K. (July 1992). "Danish investigations on silica fume concrete at elevated temperatures". In: *ACI Materials Journal* 89, pp. 345–347.
- Hertz, K. and Sørensen, L. (2005). "Test method for spalling of fire exposed concrete". In: *Fire Safety Journal* 40.5, pp. 466–476.

- Hutton, B. F., Nuyts, J., and Zaidi, H. (2006). "Iterative Reconstruction Methods". In: *Quantitative Analysis in Nuclear Medicine Imaging*. Ed. by H. Zaidi. Boston, MA: Springer US, pp. 107–140.
- Ichikawa, Y. and England, G. (2004). "Prediction of moisture migration and pore pressure build-up in concrete at high temperatures". In: *Nuclear Engineering and Design* 228.1, pp. 245–259.
- Idiart, A., Bisschop, J., Caballero, A., and Lura, P. (2012). "A numerical and experimental study of aggregate-induced shrinkage cracking in cementitious composites". In: *Cement and Concrete Research* 42.2, pp. 272–281.
- Ingberg, S., Griffin, H., Robinson, W., and Wilson, R. (Jan. 1921). "Fire tests of building columns". In: *Journal of The Franklin Institute-engineering and Applied Mathematics* 191, pp. 823–827.
- Iravani, A. and Anders, S. (2017). "Effects of cement type, aggregate type and concrete age on the mass loss of concrete exposed to elevated temperature". In: *5th International Workshop on Concrete Spalling due to Fire Exposure in Borås, Sweden*, pp. 63–72.
- Ishida, T., Maekawa, K., and Kishi, T. (2007). "Enhanced modeling of moisture equilibrium and transport in cementitious materials under arbitrary temperature and relative humidity history". In: *Cement and Concrete Research* 37.4, pp. 565–578.
- Jansson, R. (2013). "Fire spalling of concrete : Theoretical and experimental studies". PhD thesis. KTH, Concrete Structures, pp. xvi, 134.
- Jansson, R. and Boström, L. (2013). "Factors influencing fire spalling of self compacting concrete". In: *Materials and Structures* 46.10, pp. 1683–1694.
- Kak, A. and Slaney, M. (2001). *Principles of Computerized Tomographic Imaging*. Society for Industrial and Applied Mathematics.
- Kalifa, P., Menneteau, F.-D., and Quenard, D. (2000). "Spalling and pore pressure in HPC at high temperatures". In: *Cement and Concrete Research* 30.12, pp. 1915–1927.
- Kalifa, P., Chéné, G., and Gallé, C. (2001). "High-temperature behaviour of HPC with polypropylene fibres: From spalling to microstructure". In: *Cement and Concrete Research* 31.10, pp. 1487–1499.
- Kardjilov, N., Manke, I., Hilger, A., Strobl, M., and Banhart, J. (2011). "Neutron imaging in materials science". In: *Materials Today* 14.6, pp. 248–256.
- Khoury, G. A., Anderberg, Y., Both, K., Fellingner, J., Peter, N., and Majorana, C. (2007). *FIB 38: Fire design of concrete structures - materials, structures and modelling*. Vol. 38. FIB - The International Federation for Structural Concrete (fib - fédération internationale du béton).
- Klinkenberg, L. (Jan. 1941). "The permeability of porous media to liquids and gases". In: *American Petroleum Institute on Drilling and Production Practice*. Vol. 2, pp. 200–213.
- Kollek, J. J. (1989). "The determination of the permeability of concrete to oxygen by the Cembureau method-a recommendation". In: *Materials and Structures* 22.3, pp. 225–230.
- Krzemień, K. and Hager, I. (2015). "Assessment of Concrete Susceptibility to Fire Spalling: A Report on the State-of-the-art in Testing Procedures". In: *Procedia Engineering* 108, pp. 285–292.
- La Borderie, C., Lawrence, C., and Menou, A. (2007). "Approche mésoscopique du comportement du béton". In: *Revue Européenne de Génie Civil* 11.4, pp. 407–421.
- Lalush, D. S. (2004). "Iterative Image Reconstruction". In: *Emission tomography. The fundamentals of PET and SPECT*. Ed. by J. N. A. Miles N. Wernick. Elsevier. Academic Press, pp. 443–472.
- Le, T. T. H. (May 2011). "On a morphological approach of the mesostructure for the multi-scale analysis of the thermo-hydro-mechanical behaviour of cementitious materials". PhD thesis. Université Paris-Est.
- Leverett, M. (1941). "Capillary behavior in porous solids". In: *Society of Petroleum Engineers*, pp. 152–168.
- Lewis, R. W. and Schrefler, B. A. (1998). *The Finite Element Method in the Static and Dynamic Deformation and Consolidation of Porous Media*. John Wiley.

- Liu, X., Ye, G., Schutter, G. D., Yuan, Y., and Taerwe, L. (2008). "On the mechanism of polypropylene fibres in preventing fire spalling in self-compacting and high-performance cement paste". In: *Cement and Concrete Research* 38.4, pp. 487–499.
- Lo Monte, F. and Felicetti, R. (2017). "Heated slabs under biaxial compressive loading: a test set-up for the assessment of concrete sensitivity to spalling". In: *Materials and Structures* 50.4, p. 192.
- Lo Monte, F., Lombardi, F., Felicetti, R., and Lualdi, M. (2017). "Ground-Penetrating Radar monitoring of concrete at high temperature". In: *Construction and Building Materials* 151, pp. 881–888.
- Long William G., M. H. H. (Dec. 1983). "Rapid-fire refractories". Patent US 4419454A (US).
- Loosveldt, H., Lafhaj, Z., and Skoczylas, F. (2002). "Experimental study of gas and liquid permeability of a mortar". In: *Cement and Concrete Research* 32.9, pp. 1357–1363.
- Lu, F. and Fontana, M. (2017). "Intumescent coating against explosive spalling of HPC in fire". In: *5th International Workshop on Concrete Spalling due to Fire Exposure in Borås, Sweden*, pp. 365–374.
- Luikov, A. V. (1966). *Heat and Mass Transfer in Capillary-Porous Bodies*. Elsevier Ltd.
- Luikov, A. (1975). "Systems of differential equations of heat and mass transfer in capillary-porous bodies (review)". In: *International Journal of Heat and Mass Transfer* 18.1, pp. 1–14.
- Lura, P. and Terrasi, G. P. (2014). "Reduction of fire spalling in high-performance concrete by means of superabsorbent polymers and polypropylene fibers: Small scale fire tests of carbon fiber reinforced plastic-prestressed self-compacting concrete". In: *Cement and Concrete Composites* 49, pp. 36–42.
- Lura, P., Jensen, O., and Weiss, J. (2009). "Cracking in cement paste induced by autogenous shrinkage". In: *Materials and Structures* 42.8, pp. 1089–1099.
- Manns, W. and Neubert, B. (1989). "Wassergehalt von Beton bei Temperaturen von 100C bis 500C im Bereich des Wasserdampfpartialdruckes von 0 bis 5,0 MPa". In: *Deutscher Ausschuss für Stahlbeton*.
- Mazars, J. (1986). "A description of micro- and macroscale damage of concrete structures." In: *Engineering Fracture Mechanics*. Vol. 25. 5. Lab. de Mecanique et Technol., Paris VI Univ., France, pp. 729–737.
- McDonald, P., Rodin, V., and Valori, A. (2010). "Characterisation of intra- and inter-C-S-H gel pore water in white cement based on an analysis of NMR signal amplitudes as a function of water content". In: *Cement and Concrete Research* 40.12, pp. 1656–1663.
- Meftah, F., Dal Pont, S., and Schrefler, B. A. (2012). "A three-dimensional staggered finite element approach for random parametric modeling of thermo-hygral coupled phenomena in porous media." In: *International Journal for Numerical and Analytical Methods in Geomechanics* 36.5, pp. 574–596.
- Mindeguia, J.-C. (July 2009). "Experimental contribution to the understanding of the thermal instability risk of concrete". Theses. Université de Pau et des Pays de l'Adour.
- Mindeguia, J.-C., Pimienta, P., Noumowé, A., and Kanema, M. (2010). "Temperature, pore pressure and mass variation of concrete subjected to high temperature — Experimental and numerical discussion on spalling risk". In: *Cement and Concrete Research* 40.3, pp. 477–487.
- Mindeguia, J.-C., Pimienta, P., Carré, H., and La Borderie, C. (2013a). "Experimental analysis of concrete spalling due to fire exposure". In: *European Journal of Environmental and Civil Engineering* 17.6, pp. 453–466.
- Mindeguia, J.-C., Hager, I., Pimienta, P., Carré, H., and La Borderie, C. (2013b). "Parametrical study of transient thermal strain of ordinary and high performance concrete". In: *Cement and Concrete Research* 48.Supplement C, pp. 40–52.
- Mindess, S. and Diamond, S. (1982). "The cracking and fracture of mortar". In: *Matériaux et Construction* 15.2, pp. 107–113.

- Mugume, R. and Horiguchi, T. (2013). "Prediction of fire spalling in fibre-reinforced high strength concrete". In: *MATEC Web of Conferences* 6, p. 03002.
- Mugume, R. B. and Horiguchi, T. (2011). "Effect of the measurement technique on the amount of maximum pore pressures measured inside concrete subjected to high temperatures". In: *2nd International RILEM Workshop on Concrete Spalling due to Fire Exposure*, pp. 87–94.
- Neville, A. M. (2012). *Properties of Concrete*. 5th ed. Trans-Atlantic Publications, Inc.
- Nguyen, D., Lawrence, C., La Borderie, C., Matallah, M., and Nahas, G. (2010). "A mesoscopic model for a better understanding of the transition from diffuse damage to localized damage". In: *European Journal of Environmental and Civil Engineering* 14.6-7, pp. 751–776.
- Ortiz, M. (1985). "A constitutive theory for the inelastic behavior of concrete". In: *Mechanics of Materials* 4.1, pp. 67–93.
- Pasquero, D. (2004). "Contribution à l'étude de la déshydratation dans les pâtes de ciment soumise à haute température". PhD thesis. ENPC.
- Pereira, F., Pistol, K., Korzen, M., Weise, F., Pimienta P. and Carré, H., and Huismann, S. (2011). "Monitoring of fire damage processes in concrete by pore pressure and acoustic emission measurements". In: *2nd International RILEM Workshop on Concrete Spalling due to Fire Exposure*, pp. 369–77.
- Perfect, E., Cheng, C.-L., Kang, M., Bilheux, H., Lamanna, J., Gragg, M., and Wright, D. (2014). "Neutron imaging of hydrogen-rich fluids in geomaterials and engineered porous media: A review". In: *Earth-Science Reviews* 129, pp. 120–135.
- Perre, P. and Degiovanni, A. (Nov. 1990). "Simulation par volumes finis des transferts couplés en milieux poreux anisotropes: Séchage du bois à basse et à haute température". In: *International Journal of Heat and Mass Transfer*, pp. 2463–2478.
- Pesavento, F. (2000). "Nonlinear modelling of concrete as a multiphase material in high temperature conditions". PhD thesis. Università degli Studi di Padova.
- Phan, L. (Jan. 2002). "High-strength concrete at high temperature-An Overview". In: *Utilization of High Strength/high Performance Concrete, 6th International Symposium. Proceedings* 1.
- Pijaudier-Cabot, G. and Bazant, Z. (1987). "Nonlocal damage theory". In: *Journal of Engineering Mechanics - ASCE* 113.10, pp. 1512–1533.
- Poyet, S. (June 2016). "Describing the influence of temperature on water retention using van Genuchten equation". In: *Cement and Concrete Research* 84, pp. 41–47.
- Poyet, S. (2009). "Experimental investigation of the effect of temperature on the first desorption isotherm of concrete". In: *Cement and Concrete Research* 39.11, pp. 1052–1059.
- Rastiello, G., Boulay, C., Dal Pont, S., Tailhan, J., and Rossi, P. (Feb. 2014). "Real-time water permeability evolution of a localized crack in concrete under loading". In: *Cement and Concrete Research* 56, pp. 20–28.
- Reid, R., Prausnitz, J., and Poling, B. (Jan. 1987). *The properties of gases and liquids*.
- Richter, E. (2004). "Fire tests on single-shell tunnel segments made of a new high-performance fireproof concrete". In: *Fire Design of Concrete Structures: What now? What next?*
- RILEM-TC-116 (1999). "Tests for gas permeability of concrete". In: *Material and Structures* 32, pp. 174–179.
- Rutherford, E. (1920). "Bakerian Lecture: Nuclear constitution of atoms". In: *Proceedings of the Royal Society of London A: Mathematical, Physical and Engineering Sciences* 97.686, pp. 374–400.
- Saito, H. (Jan. 1966). "Explosive Spalling of Prestressed Concrete in Fire". In: *Bulletin of Japan Association for Fire Science and Engineering* 15, pp. 23–30.
- Schneider, U. and Herbst, H. J. (1989). "Permeabilität und Porosität von Beton bei hohen Temperaturen." In: *Deutscher Ausschuss fuer Stahlbeton*, pp. 23–52.
- Schrefler, B. A., Majorana, C. E., Khoury, G. A., and Gawin, D. (2002). "Thermo-hydro-mechanical modelling of high performance concrete at high temperatures". In: *Engineering Computations* 19.7, pp. 787–819.

- Sciumè, G. (2013). "Thermo-hygro-chemo-mechanical model of concrete at early ages and its extension to tumor growth numerical analysis". PhD thesis.
- Scrivener, K., Snellings, R., and Lothenbach, B. (Dec. 2015). *A Practical Guide to Microstructural Analysis of Cementitious Materials*.
- Tanibe, T., Ozawa, M., Kamata, R., and Rokugo, K. (2014). "Steel ring-based restraint of HSC explosive spalling in high temperature environments". In: *Journal of Structural Fire Engineering* 5.3, pp. 239–250.
- Tenchev, R, Ly, L., and Purkiss, J. (May 2001). "Finite element analysis of coupled heat and moisture transfer in concrete subjected to fire". In: *Numerical Heat Transfer Part A-applications* 39, pp. 685–710.
- Tenchev, R. and Purnell, P. (2005). "An application of a damage constitutive model to concrete at high temperature and prediction of spalling". In: *International Journal of Solids and Structures* 42.26, pp. 6550–6565.
- Tengattini, A., Atkins, D., Giroud, B., Ando, E., Beaucou, J., and Viggiani, G. (2017). "NeXT-Grenoble, a novel facility for Neutron and X-ray Tomography in Grenoble". In: *3rd International Conference on Tomography of Materials and Structures*.
- Thomas, H. R. and Sansom, M. (Mar. 1995). "Fully coupled analysis of heat, moisture, and air Transfer in unsaturated soil". In: *Journal of Engineering Mechanics-ASCE* 121.
- Toropovs, N., Lo Monte, F., Wyrzykowski, M., Weber, B., Sahmenko, G., Vontobel, P., Felicetti, R., and Lura, P. (2015). "Real-time measurements of temperature, pressure and moisture profiles in High-Performance Concrete exposed to high temperatures during neutron radiography imaging". In: *Cement and Concrete Research* 68, pp. 166–173.
- Tremsin, A. S., Lehmann, E. H., McPhate, J., Vallerger, J., Siegmund, O., White, B., White, P., Feller, W., de Beer, F., and Kockelmann, W. (2015). "Quantification of cement hydration through neutron radiography with scatter rejection". In: *IEEE Transactions on Nuclear Science* 62.3, pp. 1288–1294.
- Van der Heijden, G., Huinink, H., Pel, L., and Kopinga, K. (2011). "One-dimensional scanning of moisture in heated porous building materials with NMR". In: *Journal of Magnetic Resonance* 208.2, pp. 235–242.
- Van der Heijden, G., Pel, L., and Adan, O. (2012). "Fire spalling of concrete, as studied by NMR". In: *Cement and Concrete Research* 42.2, pp. 265–271.
- Van Genuchten, M. T. (1980). "A closed-form equation for predicting the hydraulic conductivity of unsaturated soils". In: *Soil science society of America journal* 44.5, pp. 892–898.
- Wang, J., Davie, C., and Masoero, E. (2017). "Rilem TC256 - Numerical benchmark of experiments on heated concrete". In: *5th International Workshop on Concrete Spalling due to Fire Exposure in Borås, Sweden*, pp. 185–196.
- Weber, B., Wyrzykowski, M., Griffa, M., Carl, S., Lehmann, E., and Lura, P. (2013). "Neutron radiography of heated high-performance mortar". In: *MATEC Web of Conferences* 6, p. 03004.
- Weber, B., Dauti, D., and Dal Pont, S. (2016). "Implementation of a porous media model for simulating pressure development in heated concrete". In: *COMSOL Conference, Munich*.
- Werner, S. and Rogge, A. (2015). "The effect of various fire-exposed surface dimensions on the spalling of concrete specimens". In: *Fire and Materials* 39.5, pp. 545–556.
- Whitaker, S. (1977). "Simultaneous Heat, Mass, and Momentum Transfer in Porous Media: A Theory of Drying". In: *Advances in Heat Transfer*. Ed. by J. P. Hartnett and T. F. Irvine. Vol. 13. Elsevier, pp. 119–203.
- Wu, Z., Wong, H., and Buenfeld, N. (2015). "Influence of drying-induced microcracking and related size effects on mass transport properties of concrete". In: *Cement and Concrete Research* 68.Supplement C, pp. 35–48.
- Wyrzykowski, M., McDonald, P. J., Scrivener, K. L., and Lura, P. (2017). "Water redistribution within the microstructure of cementitious materials due to temperature changes studied with ¹H NMR". In: *The Journal of Physical Chemistry C* 121.50, pp. 27950–27962.

- Xotta, G., Mazzucco, G., Salomoni, V., Majorana, C., and Willam, K. (2015). "Composite behavior of concrete materials under high temperatures". In: *International Journal of Solids and Structures* 64-65, pp. 86 –99.
- Zeiml, M., Leithner, D., Lackner, R., and Mang, H. A. (2006). "How do polypropylene fibers improve the spalling behavior of in-situ concrete?" In: *Cement and Concrete Research* 36.5, pp. 929 –942.
- Zeiml, M., Lackner, R., Pesavento, F., and Schrefler, B. A. (2008). "Thermo-hydro-chemical couplings considered in safety assessment of shallow tunnels subjected to fire load". In: *Fire Safety Journal* 43.2, pp. 83 –95.
- Zhang, Q. and Ye, G. (2012). "Dehydration kinetics of Portland cement paste at high temperature". In: *Journal of Thermal Analysis and Calorimetry* 110.1, pp. 153–158.
- Zhang, Z. (2014). "Modelling of sorption hysteresis and its effect on moisture transport within cementitious materials". PhD thesis.